Towards 3D Dosimetry with Optical Fluorescence Tomography Using a Radiofluorogenic Material: Setup and Data Processing

Sanders, Nicolai Højer

Publication date:
2017

Document Version
Publisher's PDF, also known as Version of record

Towards 3D Dosimetry with Optical Fluorescence Tomography Using a Radiofluorogenic Material: Setup and Data Processing

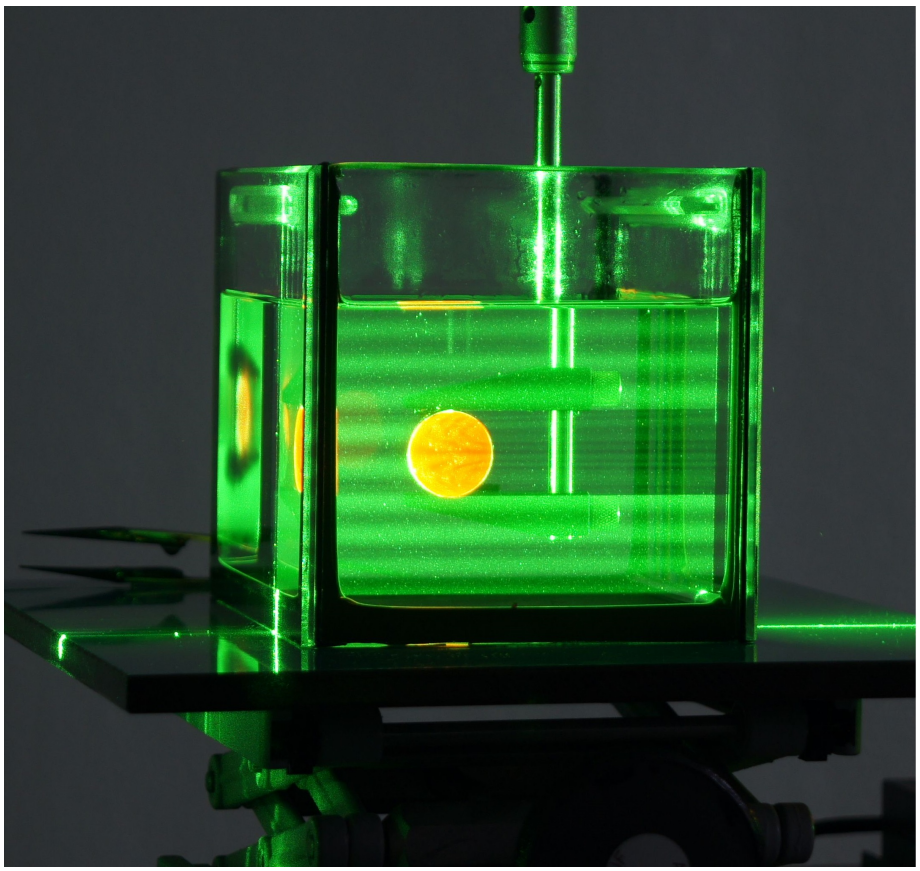

Nicolai Sanders
Technical University of Denmark
Center for Nuclear Technologies

14 December 2017

Abstract

In this project, a system for 3D readout of the absorbed dose in a radiofluorogenic and radiochromic solid-state polymer dosimeter has been developed. Optical fluorescence tomography is used to readout the 3D dosimeter. A sheet of laser light is used to excite fluorescence in the dosimeter, and a camera then acquires 2D images of the resulting fluorescent emission. 3D information is obtained by moving the dosimeter sample through the light sheet. The main features are that the readout only takes 1.5 minute per cm of sample length to complete, and the spatial resolution is 0.1 x 0.1 x 1 mm, limited by the optics in the system.

In this project, a system for 3D readout of the absorbed dose in a solid-state polymer dosimeter has been developed. Optical fluorescence tomography is used to readout the radiofluorogenic dosimeter. A sheet of laser light is used to excite fluorescence in the dosimeter, and a camera then acquires 2D images of the resulting fluorescent emission. 3D information is obtained by moving the dosimeter sample through the light sheet. The main features are that the readout only takes 1.5 minute per cm of sample length to complete, and the spatial resolution is 0.1 x 0.1 x 1 mm, limited by the optics in the system.

The measured data are fluorescence images excited by the a sheet of laser light. The calculation of the absorbed dose 3D distribution from the fluorescence images is complicated by the fact that the dosimeter material is both radiofluorogenic and significantly radiochromic: The fluorescence response is linear with the absorbed dose and the intensity of the excitation light, but the excitation light is absorbed by the sample in a locally dose-dependent manner. An analytical solution to this problem has been derived for calculating the 3D distribution of the absorbed dose from the 3D readout fluorescence images. Two interesting special cases of this solution have been highlighted. The impact of uncertainty in the dosimeter material parameters and boundary conditions was illustrated.

An alternative algorithmic solution to the dose reconstruction was made. It works by fitting dose images represented by Fourier components to the observed data, and then optimizing the Fourier components to improve the fit. This solution was demonstrated to converge uniformly towards the true dose solution, if the given material parameters and boundary conditions for the dosimeter are correct. This solution method is relatively computationally intensive, and it could benefit from better optimization.

A complete list of design recommendations and considerations for the 3D setup has been compiled; A diode laser at 520 nm is suitable for excitation of the pararosaniline dye used in the dosimeter. A cylindrical lens is used to generate a light sheet. The vertical intensity line profile of the light sheet must be characterized for each readout series in order to perform the data analysis. This can be done with a fluorescence reference in the field of view of the camera. The refractive index matching fluid should match the dosimeter at the fluorescence emission wavelengths, but be slightly higher, to prevent total internal reflection of the emitted light.

A list of material properties required for the dosimeter to function ideally has been established. The decadic attenuation coefficient at the wavelength of the excitation laser should be at most 0.007 cm^{-1}. The decadic radiochromic response at the excitation wavelength should not exceed 0.0036 $cm^{-1}Gy^{-1}$. The ratio of the fluorescence before irradiation and the radiofluorogenic response should not exceed 2 Gy. The radiochromic and radiofluorogenic response should be stable over time and homogeneous within a dosimeter sample. Some experiments with a radiofluogenic dosimeter material have been made. The dosimeter used in this project did not fulfil these requirements mentioned above and further work on the polymer material is required to meet the requirements.

Some dosimeter readouts with the 3D setup were made, and it was demonstrated that the dose reconstruction algorithm can work with data from the 3D readout setup.

Resumé

I dette projekt blev der udviklet et system til 3D udlæsning af den absorberede dosis i et radiokromisk og radiofluorogent solidt polymer dosimeter. Optisk fluorescenstomografi bruges til at udlæse den absorberede dosis i 3D. Et tæppe af laserlys bruges til at excitere fluorescens i dosimeteret, og et kamera optager 2D billeder af den resulterende emission. 3D information opnås ved at bevæge dosimeterprøven gennem lystæppet. Udlæsningen tager maksimalt 5 minutter, med en rumlig opløsning på 0.1x0.1x1 mm. Den rumlige opløsning er begrænset af optikken i systemet.
De udlæste data er fluorescensbilleder exciteret af lystæppet.
Udregningen af den absorberede dosisfordeling fra fluorescensbillederne er kompliceret, fordi dosimeteret er både radiofluorogent og radiokromt. Dette betyder, at fluorescensresponsen stiger lineært med både absorberet dosis og intensiteten af excitationslyset. Samtidig bliver excitationslyset absorberet i prøven, igen lineært med dosen. En analytisk løsning på dette problem er blevet udledt, og løsningen bruges til at udregne 3D dosisfordelingen ud fra de opsamlede fluorescensdata. To interessante specialtilfælde af denne løsning bliver også blevet undersøgt. Nogle estimater af konsekvensen af usikkerheder i dosimetermaterialets optiske konstanter og grænsebetingelser er blevet udført.
En alternativ algoritmisk løsning til dosisudregningen blev også lavet. Denne løsning virker ved at fitte kandidater af dosisfordelingen, repræsenteret ved Fourierkomponeneter, til de observerede fluorescensdata. Fourierkomponenterne kan så optimeres til at minimere afvigelsen. Denne metode konvergerer uniformt mod den rigtige dosis, hvis de givne materialeparametre og grænsebetingelser er korrekte. Metoden er for beregningsintensiv til at blive brugt i praksis, men en bedre optimeret implementering kunne gøre den interessant.
En udførlig liste med designanbefalinger og overvejelser for 3D udlæsningssetuppet er blevet samlet. En diodelaser ved 520 nm er passende til at excitere farvestoffet, pararosanilin, i dosimeteret. En cylindrisk linse bliver brugt til at lave et lystæppe. Den vertikale intensitetsprofil af lystæppet skal karakteriseres for hver udlæsning for at udføre førnævnte dataanalyse. Dette gøres bedst med en fluorescensreference i kameraets synsfelt. Indeksmatchingsvæsken børe matche dosimetermaterialet ved fluorescensemissionsbølgelængden. Væskens indeks skal være en anelse højere for at forhindre total intern refleksion af det udsendte lys.
En liste med krav til dosimetermaterialets egenskaber er blevet lavet. Den dekadiske attenuationskoefficient ved bølgelængden for excitationslyset bør maksimalt være 0.007 cm^{-1}. Den dekadiske radiokromiske respons ved excitationsbølgelængden bør højst være 0.0036 $cm^{-1}Gy^{-1}$. Ratioen af fluorescensen før bestråling og den radiofluorogene respons bør højst være 2 Gy. Den radiokrome og den radiofluorogene respons børe være homogene i et dosimeter og stabile over tid. Nogle eksperimenter med det radiokrome dosimetermateriale blev udført, og dosimetermaterialet opfylder ikke disse krav. Derfor er mere udviklingsarbejde med materialet påkrævet.
Nogle udlæsninger med 3D setuppet blev udført, og det blev demonstreret, at dosisrekonstruktionsalgoritmen virker med de udlæste data.

Contents

1 Outline

The structure of this thesis is as follows:

- Introduction to the motivation and context for this project.
- Introduction to the radiofluorogenic solid state polymer dosimeter.
- Introduction to the fluorescence measurement setup used to characterize the fluorescence response of this dosimeter.
- Introduction to the setup used to read out the 3D distribution of the fluorescence response in the polymer.
- Mathematical derivation of the analytical equation used to calculate the 3D distribution of the absorbed dose from the fluorescence images from the 3D readout setup.
- Description of an alternative algorithmic method for calculating the 3D distribution of the absorbed dose.
- Detailed description of the components in the 3D readout setup, and the relevant design considerations.
- Detailed description of the components in the fluorescence measurement setup, and the relevant design considerations.
- Some examples of the irradiation and 3D readout experiments performed with the polymer.
- An overall conclusion to the thesis.

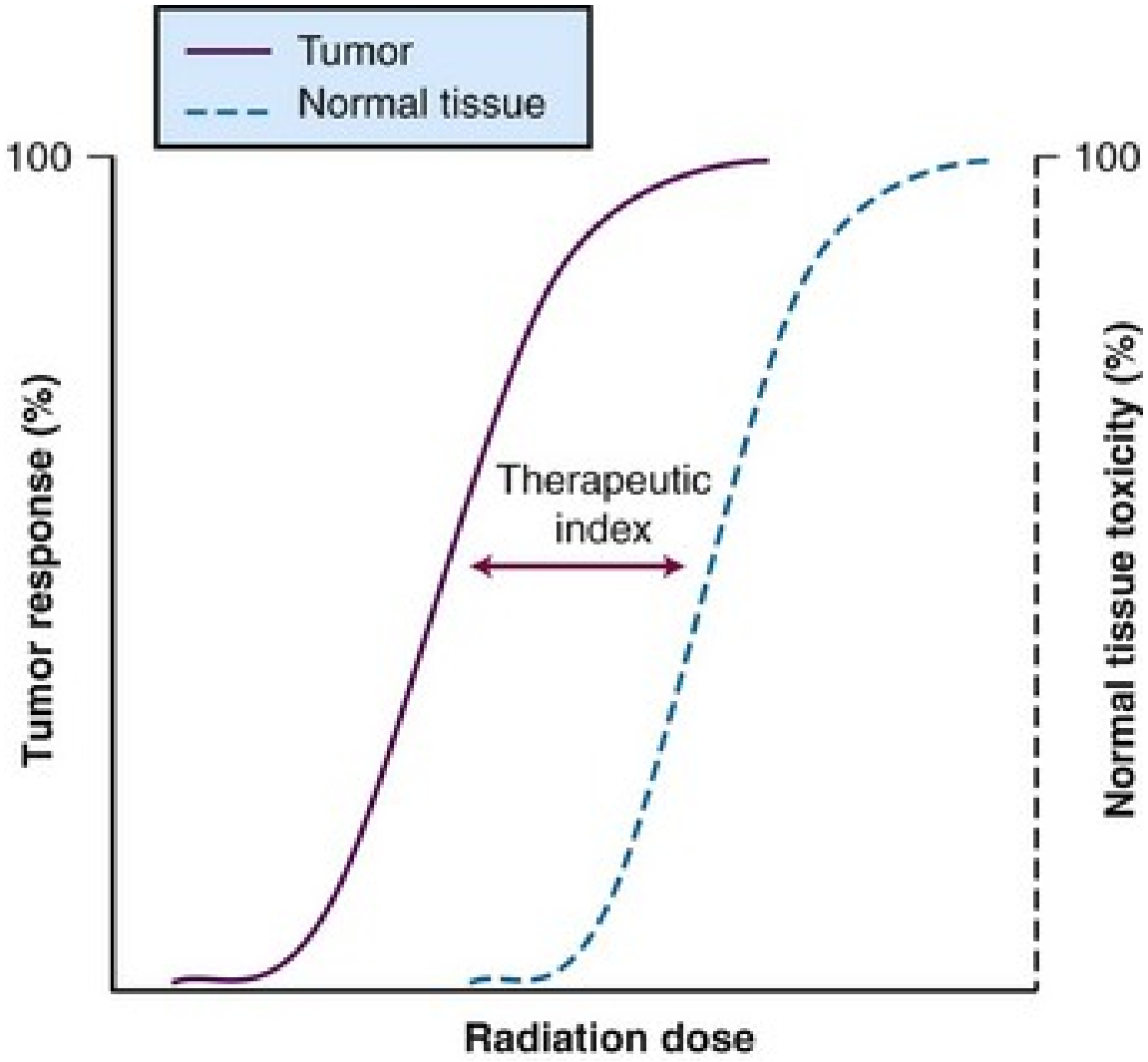

Figure 1: An idealized therapeutic index curve[2].

2 Introduction

Ionizing radiation is often used to treat cancer. This is because the cancer cells are often more vulnerable to the genetic damage from the radiation than the surrounding normal tissue. Figure 1 shows an idealized therapeutic index curve. The gap between the tumor response and the toxicity of normal tissue is the therapeutic window. This difference in radiation resistance is called the therapeutic window/index, and it broadly determines whether and how any radiation therapy should be delivered. Expanding the therapeutic index is an area of active research.[9]
Common to all radiation therapy methods is that the absorbed dose to the cancer cells should be high enough to ensure total elimination, while the absorbed dose to all other tissues should be as low as reasonably achievable.
It is particularly important to minimize the absorbed dose to life-critical organs with high metabolic activity.
These demands are obviously in opposition to each other, and the only way to reconcile them is to know the position and shape of all solid tumors with great precision, and to be able to deliver the necessary radiation with the same degree of precision and control.

Diagnostic imaging has been developed to the point where most tumors can be located and delineated with good precision and accuracy.
The methods for delivering the required radiation have also become increasingly sophisticated, in particular for external beam radiation therapy. By irradiation from multiple angles, and carefully choosing the type and energy of the radiation particles, it is possible to achieve high contrast in received absorbed dose between the treatment volume and the surrounding tissue.
The three main challenges with these methods are to ensure that the treatment volume and the tumor coincide, to ensure that the absorbed dose calculation in the treatment planning is accurate and to ensure that the treatment machine can execute the plan accurately.

2.1 Motivation

There is currently a need for better methods for 3D dosimetry[12][25].
It is the intention of this project to examine the possibility of using radiation induced changes in the fluorescence of a polymer matrix to perform 3D dosimetry with high spatial resolution. Beyond the basic research interest of exploring a new dosimetry method, a high resolution dosimetry method would also allow for easier quality assurance of the various radiation therapy machines and softwares that are currently in use. Right now, the doses delivered to patients are calculated using treatment planning softwares and delivered by whatever machine the treatment was planned for. The accuracy of the absorbed dose calculations are verified through Monte Carlo model simulations[32] and through regular testing with point dosimeters and film dosimeters. In this context, a reliable and easy way to perform 3D dosimetry with high resolution would serve as another way to evaluate and ensure the agreement between the planned treatments and the delivered radiation. There is a particular need for this in proton beam therapy.
To reap the full potential advantages of proton therapy, the depth of the Bragg peak[19] must be controllable with very high precision. This requires complete agreement between simulation and delivery, and a reliable 3D method would be helpful for this.
There already exist other 3D dosimetry methods, based on optical tomography of radiochromic materials, rotating/moving arrays of point detectors, and gels that scatter light when irradiated. None of these systems fit perfectly for the role of quality assurance in a clinical setting. Low resolution, low absorbed dose precision, and impractical readout requirements are the most pressing problems[25].
There are systems which utilize arrays of dosimeters to obtain spatial information beyond 2D. For example, the ScandiDos Delta^4 phantoms[5] use two orthogonal arrays of photodetectors to obtain information for treatment plan verification. The resolution is 5x5 mm, limited by the size of the detectors. There is also the PTW OCTAVIUS® which uses a rotating array of ionization chambers to obtain information beyond simple 2D. The resolution is 2.5x2.5 mm. Sun Nuclear makes the ArcCHECK®, which uses an array of diode photodetectors wrapped around a cylinder. The center of the cylinder is open, for phantom inserts. The array resolution is 10x10 mm. All of these systems are in clinical use, because they are relatively fast and easy to use for treatment plan verification. None of them offer full 3D information, since they are based on arrays of detectors.
Therefore, true 3D dosimetry is still not in common clinical use, although there is a clear agreement that there is a necessity for developing better methods[16].

2.2 Intensity Modulated Radiation Therapy State of the Art

Radiotherapy has a long history, starting as early as 1896, just one year after the discovery of x-rays.
At first, radiotherapy was only successfully used to treat various skin conditions, including lupus and skin cancer. Due to the novelty of radioactivity and a lack of knowledge and oversight there were also many harmful treatments in use.
Around 1934 the radiologist Henri Coutard had developed the method of fractionated radiation exposure that is still the basis of radiotherapy today. Today, there is a lot of emphasis on delivering

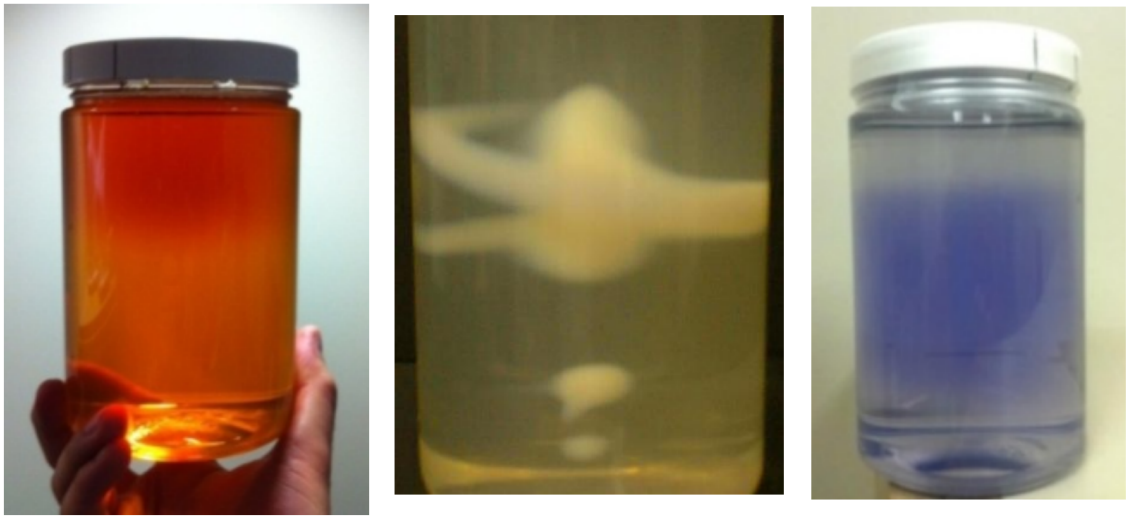

Figure 2: Images and text from[25]: Illustration of the 3D absorbed dose information captured in three different gel dosimeters. (left) The Fricke-xylenol-orange-gelatin dosimeter shows a colour change in the volume irradiated with 12 MeV electron beams. (centre) The polyacrylamide polymer gel dosimeter shows increased scatter in the high absorbed dose areas radiated using a Cobalt-60 tomotherapy IMRT delivery. (right) A VMAT prostate irradiation of a Leuco-crystal-violet micelle gel dosimeter.

the radiation in a controlled, precise and quantifiable manner, in order to spare healthy tissues while still irradiating the tumor(s) sufficiently.
In order to follow this principle, the methods for planning the treatments and delivering the radiation have become increasingly sophisticated. Rotating gantries and programmable collimators allow for irradiation from multiple angles with fields that conform the tumor while avoiding organs at risk. Innovations in imaging allow for rapid or even simultaneous adaptations of the treatment plans to the patient geometry. Precise point and 2D dosimetry confirms that the complex machines deliver the programmed absorbed dose at the programmed positions. However, there is still a place for easy and reliable 3D dosimetry, since it would streamline the verification and calibration process for the machines. 3D dosimetry would also be a valuable research tool, if it was sufficiently simple to use. At the time of writing, the field of candidates for 3D dosimetry is rather narrow, and all of the methods have various disadvantages that keep them from clinical use.

2.3 State of the Art for 3D Dosimetry

3D dosimetry is still not in common clinical use. The reason is primarily that the current mature 3D dosimetry systems are impractical to use. The preparation of the dosimetric materials is often time-sensitive, and the optical readouts before and after irradiation can take a long time, from 30 minutes to several hours. Optical CT scans are sensitive to artifacts, such as bubbles or particles, in the samples. If these artifacts are not identified they could lead to erroneous interpretations. Therefore, it takes both a long time and expert knowledge to use the current 3D dosimetry systems. Figure 2 shows images of a 3 different 3D dosimeters based on gels with radiochromic responses and radiation induced scattering of light. These dosimeters can all be read out with optical CT and, for the Fricke gel and Polyacrylamide gel, nuclear magnetic resonance imaging. Figure 3 shows a diagram and an image of an optical CT system for 3D readout of radiochromic samples of the PAGAT gel dosimeter. The galvo scanner moves the laser beam through the sample, while the photodetector reads out the amount of light not absorbed by the sample through any given line.

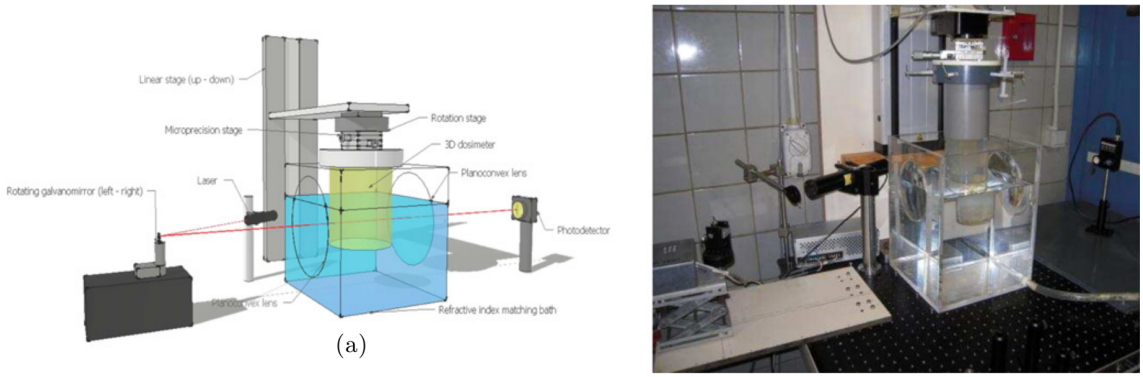

(a)

Figure 3: Diagram and image[29] of an optical CT system for radiochromic samples.

The sample is also slowly rotated in order to obtain absorbance measurements from every possible angle. This data set can then be reconstructed into a 2D profile of the optical density through an inverse Radon transform[4]. This procedure can be repeated for each 2D slice of the sample, to obtain a complete 3D absorbed dose profile. The use of a rotating stage and a galvo scanner is necessary in order to obtain accurate estimation of the optical density of the sample. This is why the optical readout can take a long time for these systems. If the radiochromic dye can diffuse through the gel, then this can cause some problems for readouts over multiple hours. The output from optical CT scans can also be sensitive to imperfections in the samples or method[10], leading to artifacts in the reconstructed absorbance distributions.
One of the most important radiochromic dosimeter materials for optical CT is PRESAGE^{TM}. This material is composed of leucodyes and halogenated hydrocarbons dissolved in a rigid polyurethane matrix[11]. This rigid matrix has the twin advantages of preventing diffusion of the dye and it allows the material to be shaped into inserts for phantoms without the need for a container. The most common dye used is leucomalachite green, since this dye has an absorbance peak at 633 nm, which is close to the 639 nm absorbance peak for GAFChromic EBT films. It has a linear dose response up to about 100 Gy, and with proper cold storage the radiochromic response will only fade slowly and consistently over time. Figure 4 shows an image of a 3D dosimeter based on radiation induced fluorescence response in the material. Figure 5 shows an image of the setup used to readout the samples shown in figure 4. This setup uses the same basic concept as the one described in this thesis, optical fluorescence tomography, but with a few significant differences. The excitation light is at 381 nm and comes from ultraviolet lamps, rather than a laser. The light sheet was formed by shining the lamps through slits of 2 mm. This limits how thin the light sheet can be, and therefore also their spatial resolution. They use a dye suspended in a gel, which leads to diffusion of the irradiated dye over time. This is not a problem for the relatively short time during irradiation and imaging, but does make it impossible to re-image a sample a few days after irradiation.

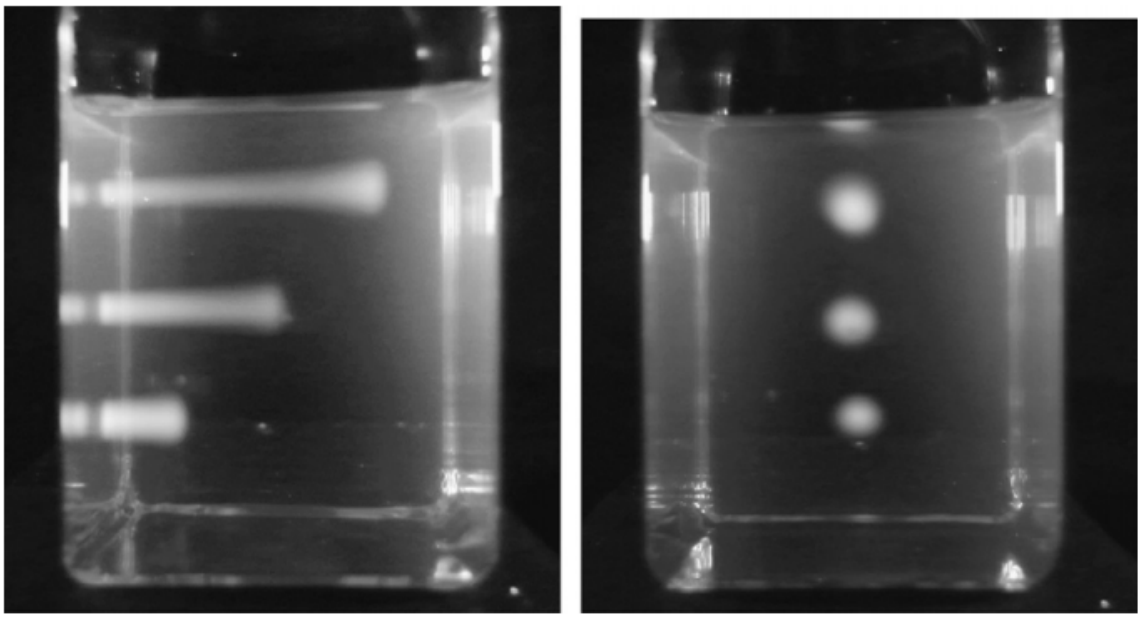

Figure 4: Fluorescence from a radiofluorogenic and radiochromic 3D dosimeter material[30]. It was irradiated with a 80 MeV proton beam with different amount of blocking material in front of the dosimeter. The Bragg peak is clearly visible.

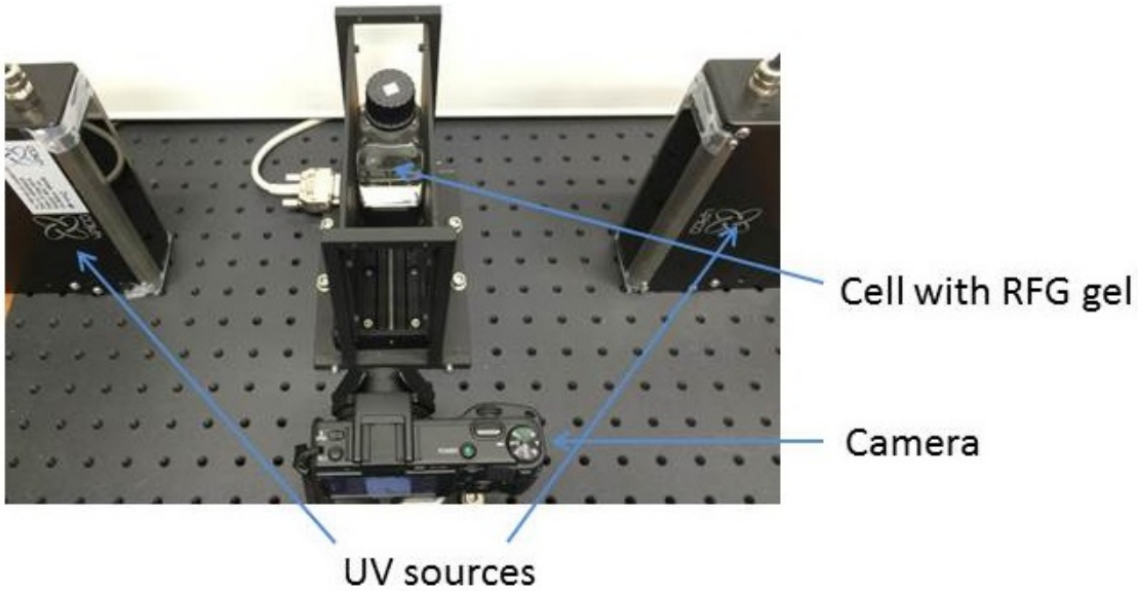

Figure 5: Readout setup[33] for the radiofluorogenic samples in figure 4.

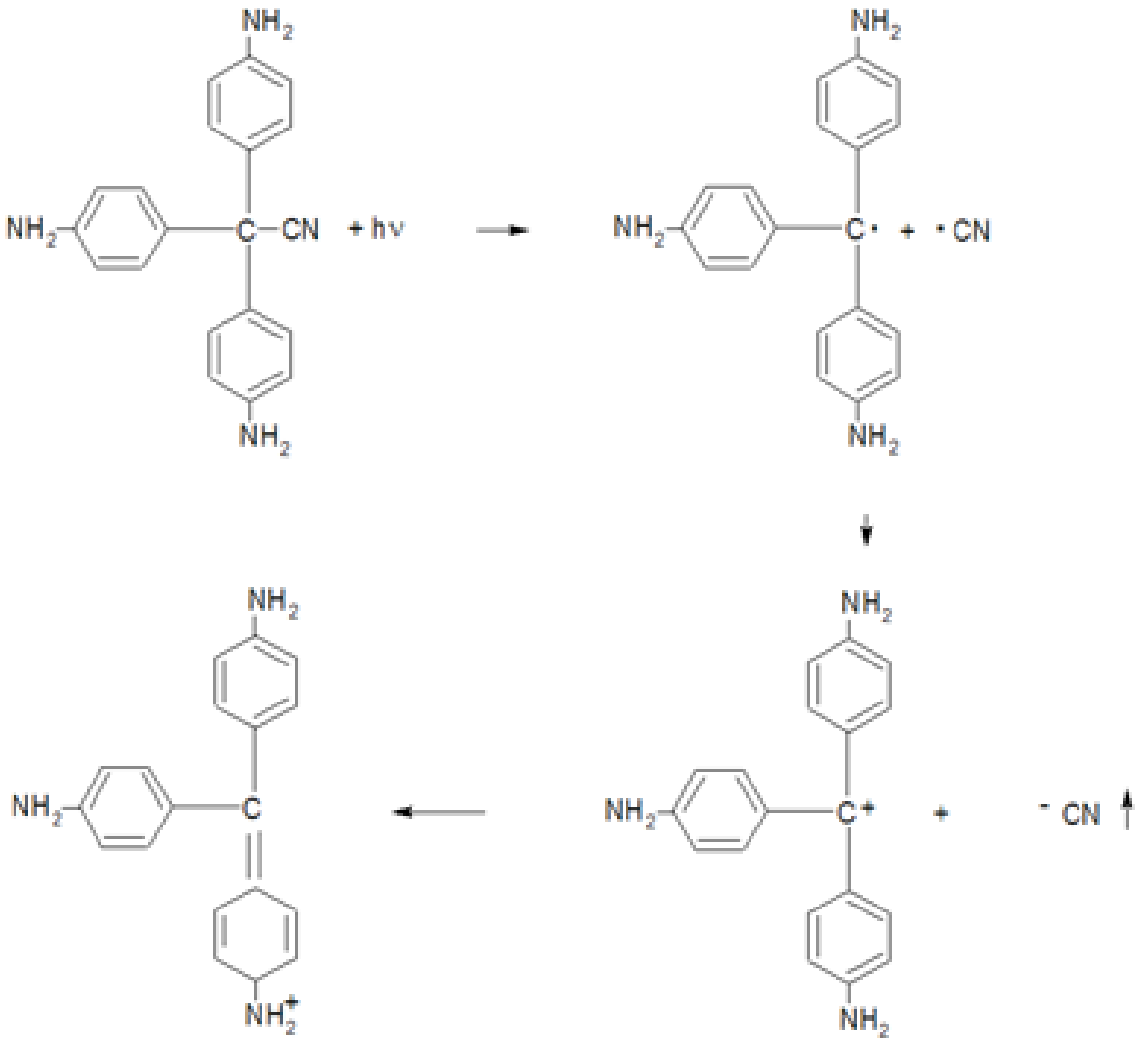

Figure 6: The chemical reaction changes the dye from its leuco form to its exposed form.

3 The Radiofluorogenic Polymer

In this project, a radiofluorogenic polymer ([8] and [7]) was used as the basis for the development of the 3D setup and the fluorescence measurent setup. The polymer used is composed of polyethylene glycol diacrylate with a molecular weight of 550 g/mol.
It is mixed with a photo initiator, Diphenyl(2,4,6-trimethylbenzoyl)phosphine oxide, which enables it to be cured with UV light with wavelengths around 385 nm to 395 nm.
The radiochromic property comes from the dye, leuco-pararosaniline, which turns magenta when exposed to radiation. This dye has previously been used for dosimetry in radiochromic B3-films, particularly for high-dose applications.[18] Figure 6 shows the chemical reaction that exposes the dye in the polymer. Initially, the dye molecules are transparent to visible light. When a dye molecule is hit by ionizing radiation, it releases the cyano group. The cyano group is then passivated by some other free radical present in the polymer composition. One of the aniline groups in the dye forms a double bond with the central carbon atom. In this form, the dye has a magenta color.
This dye is normally not fluorescent when in solution, but when it is fixed inside a stiff polymer, the dye becomes fluorescent. This is because the rigid environment leaves fewer vibrational states

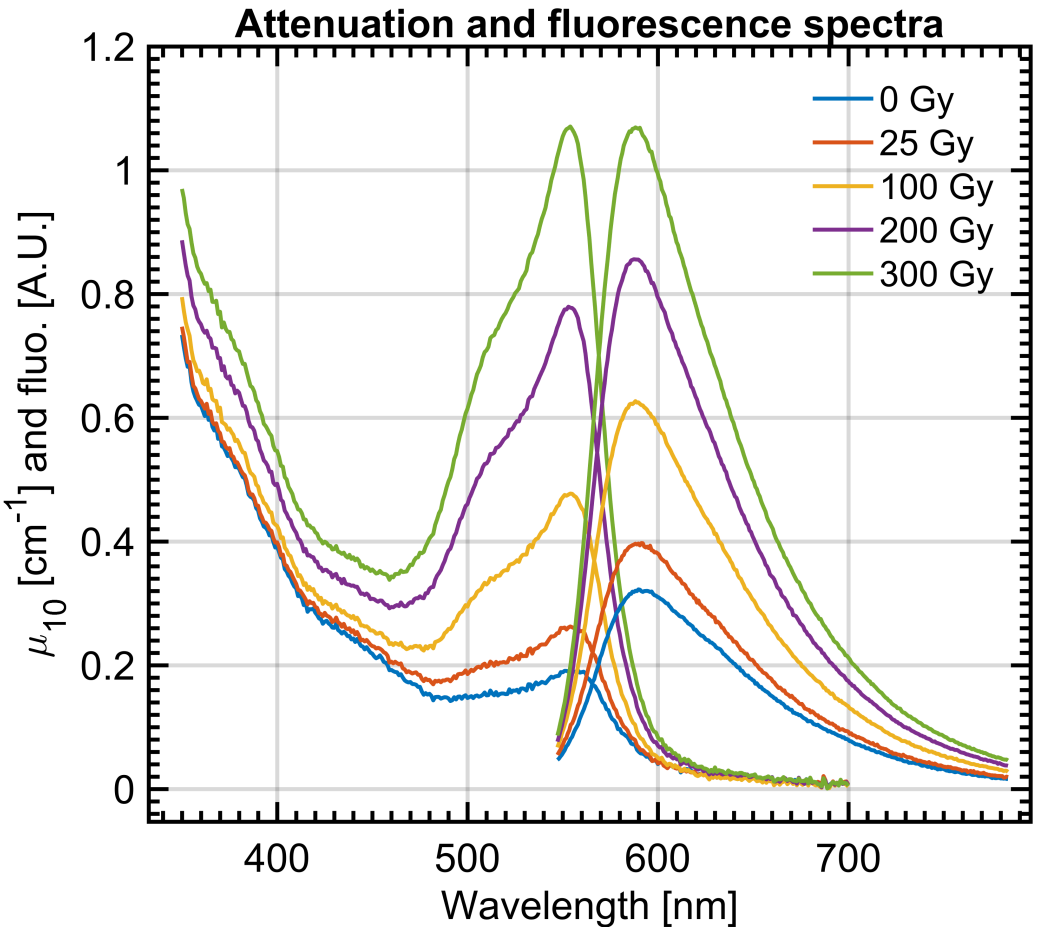

Figure 7: Absorption and fluorescence spectra of a 1 mm thick polymer sample, at different levels of irradiation.

for the excited state of the dye to decay nonradiatively into. Since the lifetime of the excited state is longer, it is more likely to decay radiatively, which means that the dye molecule is fluorescent when inside a rigid polymer.

If the polymer is flexible at the molecular level there will be a higher density of vibrational states in the surrounding polymer which the excited states in the dye can decay non-radiatively into. Because of this a more rigid polymer should have a higher fluorescence response.

On the other hand, a more rigid polymer will also exhibit decreased diffusion, so if diffusion is important for the radiofluorogenic response, a more rigid polymer may inhibit the radiation sensitivity.

The dye is exposed by breaking off a cyano group, and the exposure is made irreversible by passivation of this cyano group by other additives present in the polymer matrix. If the diffusion is too restricted in the matrix, then the cyano group may recombine with the dye molecule before it can move away or encounter a suitable passivation site or molecule. Figure 7 shows how irradiation increases the fluorescence response of the dosimeter. This increase is called a radiofluorogenic response. The absorption also increases, and this change is called a radiochromic response. Figures 8 and 9 shows a clear linearity between absorbed radiation dose and absorption and fluorescence response. Figure 10 shows that the correlation between the percentage of absorbed excitation light and the measured fluorescence is slightly better than the correlation between fluorescence and ab-

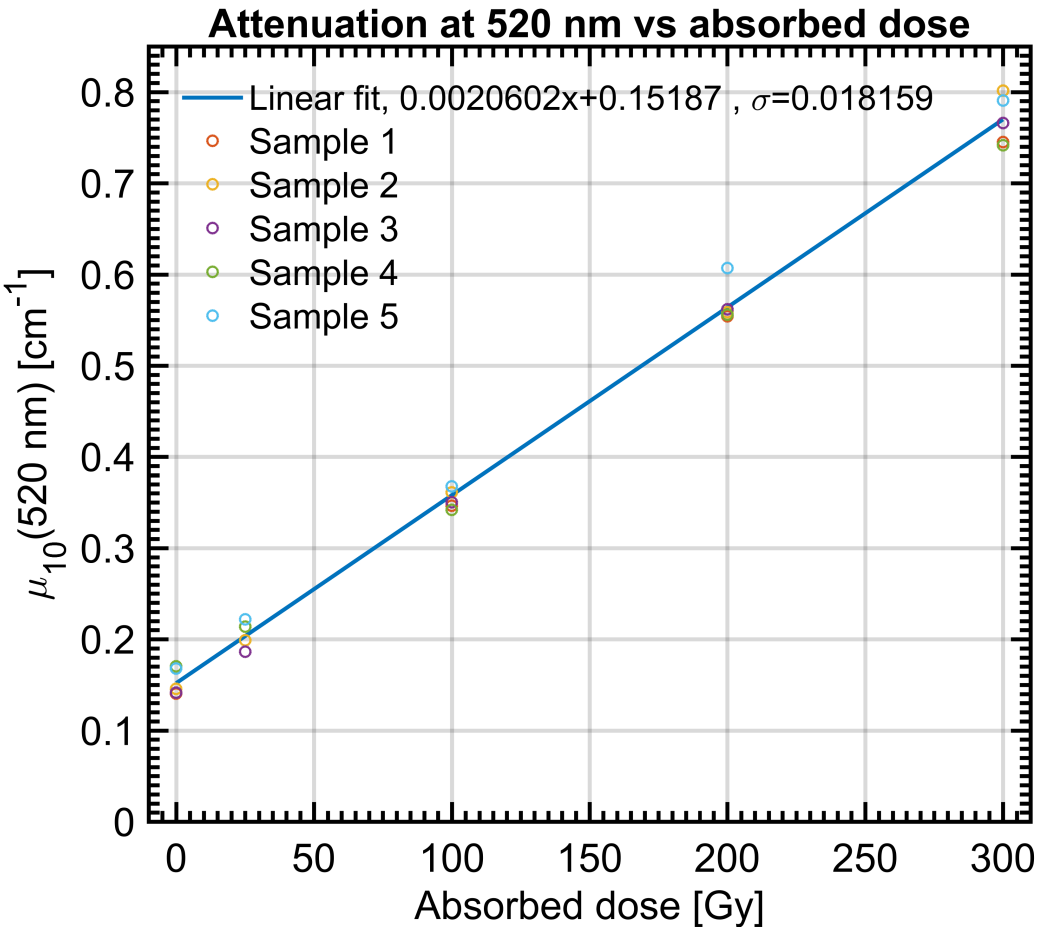

Figure 8: Linearity between absorbed dose and the decadic attenuation coefficient at 520 nm.

sorbed dose. This indicates that the fluorescence is directly linked to the absorption of the light by the dye in the sample. One curious aspect is that the trend line does not go to zero fluorescence for zero absorbed light. This is obviously impossible, but we have no explanation for this. Figure 11 shows a simplified Jablonski diagram for a fluorescent material. A photon is absorbed by the dye in the material, causing it to transition to an excited electronic state with higher energy. This excited state can then decay radiatively to a lower energy state, while emitting a photon with lower energy than the excitation photon. This decrease in energy is called the stokes shift, and it happens because there are multiple excited states and ground states available to decay into. The original excited state can decay into a lower energy excited state, and then decay radiatively. The excited state can also decay into a ground state with a higher energy than it was originally excited from. For this reason, the emission spectrum will always have a lower energy/longer wavelength than the excitation light.

The excited state can also decay entirely non-radiatively, for example through collisions with neighboring molecules. The likelihood of these two outcomes are determined by the time constants for the radiative decay and the different non-radiative decay processes.

The attenuation at $\lambda_E = 520$ nm was chosen because it is the wavelength of the laser used to excite the fluorescence in the samples.

There are some optical constants of the dosimeter material that are important for the calculation of the absorbed dose distribution from the fluorescence data, as described in section 6. These con-

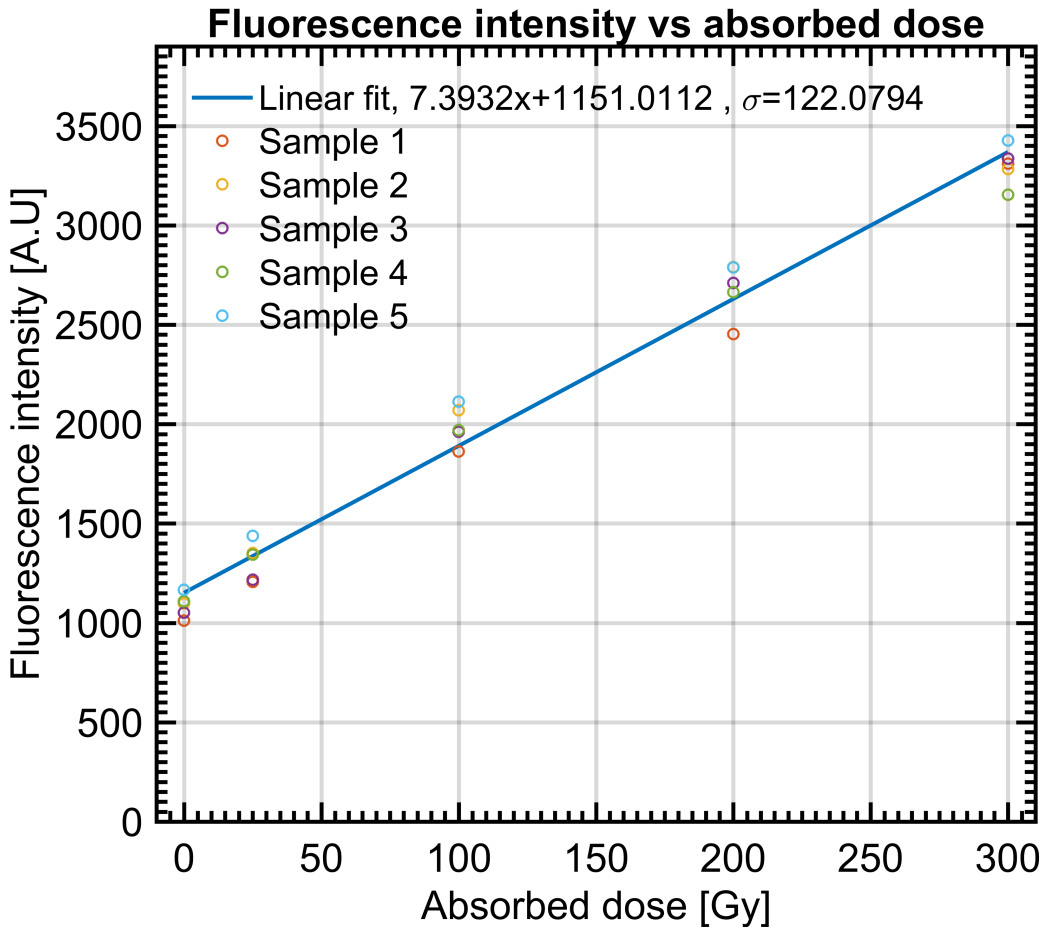

Figure 9: Linearity between absorbed dose and the fluorescence response, measured as the area under the fluorescence curve from 570 nm to 740 nm.

stants are defined in table 1. The Zero-dose attenuation, B_C, is the decadic attenuation coefficient of the dosimeter material at the wavelength of the excitation light, before the material has been irradiated. It describes how fast the excitation light is absorbed by the material.
The radiochromic response, R_C, is the change in the decadic attenuation coefficient at the excitation light wavelength in response to absorption of ionizing radiation.
The zero dose fluorescence, B_F, is the fluorescence response of the dosimeter material at zero dose, as measured by the fluorescence measurement setup described in section 4.
The radiofluorogenic response, R_C, is the change in fluorescence when the dosimeter material has absorbed ionizing radiation.
Table 2 contains the optical material constants measured for the dosimeter material formulation used in this project, colloquially known as "composition 22", along with a version of "composition 22" with 10 times less dye. There are also the preliminary constants for a composition discovered late in the project, which contains a mercapto-ester and citric acid. The optical constants for PRESAGE^{TM} were also included[1] to provide a basis for comparison. The constants measured for the "composition 22" polymer are not ideal for use in a radiofluorogenic polymer, since the background attenuation coefficient is large compared to the radiochromic response.

$$B_C/R_C = 110\text{Gy} \tag{1}$$

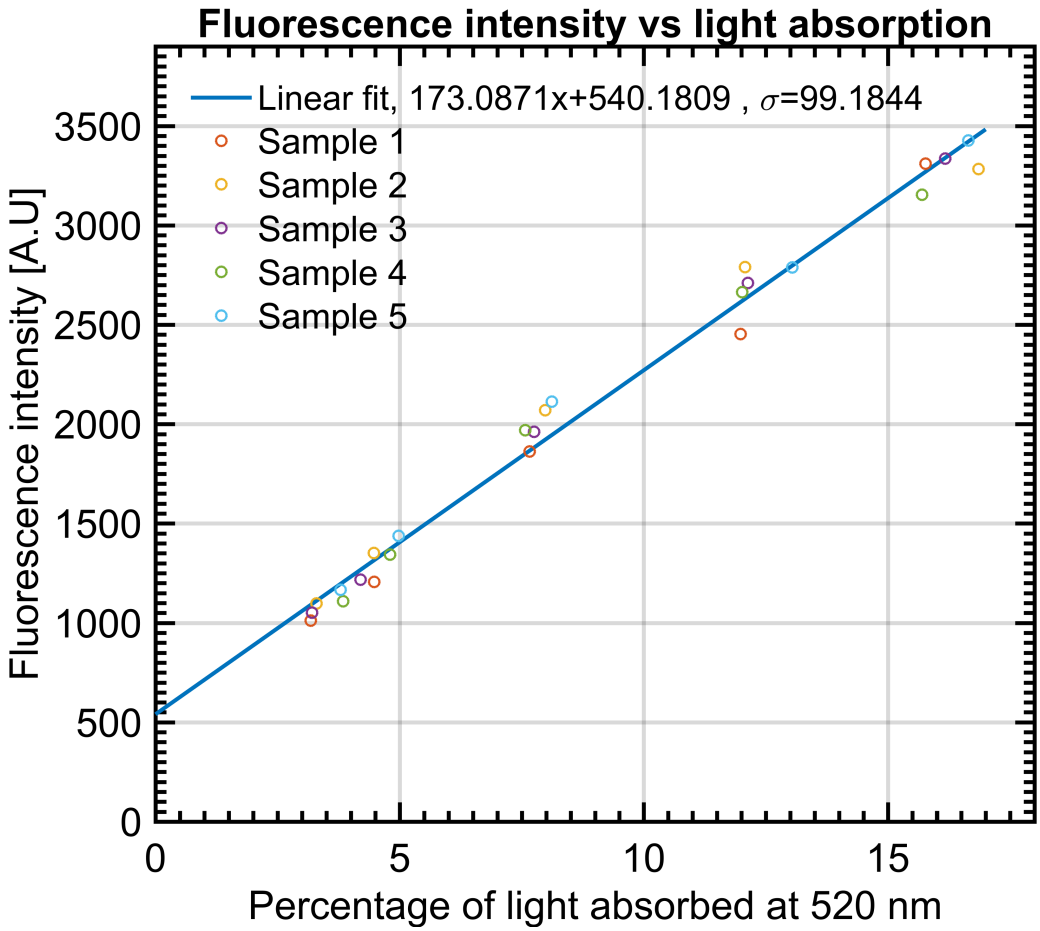

Figure 10: Linearity between percentage of absorbed light and the fluorescence response, measured as the area under the fluorescence curve from 570 nm to 740 nm.

The fluorescence background is also high compared to the radiofluorogenic response.

$$B_F/R_F = 123\text{Gy} \tag{2}$$

The zero dose attenuation is also high in absolute terms. With a decadic attenuation constant of $\mu_{10} = 0.22$ cm^{-1}, half of the excitation light will be absorbed in just 1.4 cm. With a constant of $\mu_{10} = 0.043$ cm^{-1}, it will take 7 cm to absorb half of the light, which is a more reasonable size for a clinical dosimeter.

3.1 Spectral Mapping of the Fluorescence Response

In order to select the best wavelength to excite the polymer it is not enough to know the absorbance spectrum of the irradiated polymer. It is also necessary to characterize how the fluorescence response depends on the excitation wavelength. This is because the absorbed light can excite both radiative and non-radiative states, and the relative probability of this can be wavelength dependent. There are also more than one fluorescent species present in the polymer, with different absorption and emission spectrums. One of these fluorescent species may be more sensitive to radiation than the other.
The easiest way to examine all of these properties is to measure the full emission spectrum for

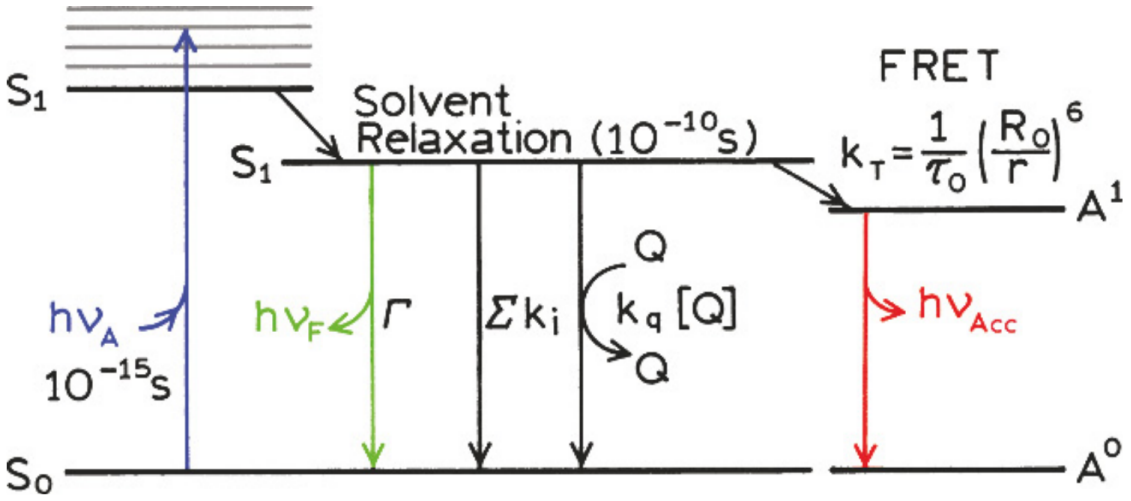

Figure 11: Jablonski diagram[14, p. 11] typical of fluorescent materials.

Table 1: Definition of important optical constants for the dosimeter material.

Constant name	definition
Zero-dose attenuation	$B_C = \mu_{10}(520\text{nm}, 0\text{Gy})$ [cm^{-1}]
Radiochromic response	$R_C = \frac{\mathrm{d}\mu_{10}(520\text{nm})}{\mathrm{d}D}$ [(cm kGy)$^{-1}$]
Zero-dose Fluorescence	$B_F = F_m(0\text{Gy})$
Radiofluorogenic response	$R_F = \frac{\mathrm{d}F_m}{\mathrm{d}D}$ [Gy^{-1}]

a range of different excitation wavelengths. This should be done with a sample before and after irradiation in order to distinguish the fluorescence from the polymer and the fluorescence from the exposed dye.
A series of measurements was performed with a Fluorolog 3 Spectrofluorometer from Horiba Jobin Yvon. The integration times varied from 20 ms to 100 ms, and the emission spectra were normalized with respect to the excitation intensity and the integration time. Figure 12 shows that a sample of composition 22 without any dye will show a clear fluorescence response when excited with 535 nm light, with a narrow emission spectrum peaking at 560 nm. This fluorescence increases by 3 million counts when the sample is irradiated. It is unknown which part of the polymer is responsible for this fluorescence. The fluorescence mapping was done within an hour of the irradiation, so it is

Table 2: Material constants for the dosimeter material. Exp. #1 and #2 were both composition 22, but performed by different people. Slight differences in curing and measurement methods probably account for the differences. The composition with 90% less dye has different constants. The composition with added citric acid and mercapto-ester seems to be better. PRESAGE$^{\text{TM}}$ was included for comparison.

Experiment \Constant	B_C [cm^{-1}]	R_C [(cm kGy)$^{-1}$]	B_F	R_F [Gy^{-1}]
Exp. #1	0.22	2.0	1142	9.3
Exp. #2	0.28	3.1	1280	8.0
90% less dye	0.125	0.7	263	1.7
merc.+c.ac.	0.043	0.024	1263	10.6
PRESAGE$^{\text{TM}}$	0.018	16.2	N/A	N/A

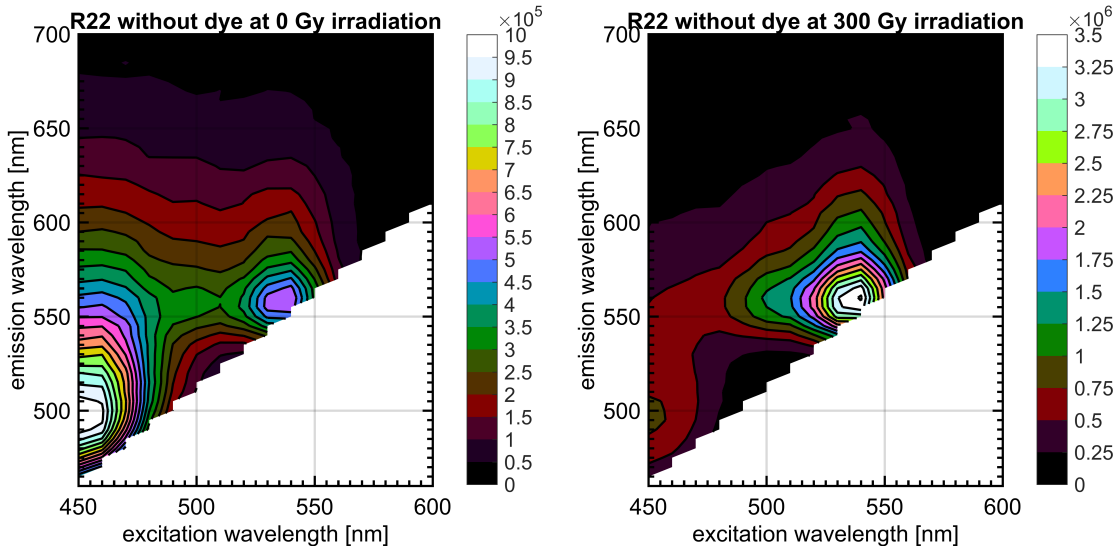

(a) 0 Gy, No dye

(b) 300 Gy, No dye

Figure 12: Fluorescence response maps for a sample without dye at 0 Gy and 300 Gy. Note the large increase in fluorescence response for excitation at 535 nm. The fluorescence excited at 450 nm is unchanged by the irradiation.

unknown, if this fluorescence comes from short-lived free radicals or from a stable chemical in the polymer. Figure 13 shows what the addition of the leuco-pararosaniline dye does to the fluorescence response. Before irradiation there is a very strong fluorescence response when excited at 450 nm, which must come from the leuco dye. After irradiation with 300 Gy, we see that the fluorescence excited at 450 nm has decreased by 10 million counts, while a new fluorescence peak of 2 million counts has appeared for excitation with 540 nm. Note that this peak is distinct from the peak observed in the sample without dye, since it has a broad emission spectrum peaking at 585 nm, in contrast to the narrow spectrum peaking at 560 nm that was observed from the sample without dye. The difference that the introduction of dye and irradiation creates has been highlighted in figure 14. It is obvious from figure 14a that the introduction of dye into the composition results in a big increase in the fluorescence excited by 450 nm light. This fluorescence probably comes from the leuco form of the pararosaniline dye. With a broad emission spectrum peaking at 520 nm, this fluorescence would probably appear as a strong green fluorescence. Figure 14b illustrates that the fluorescence excited by 450 nm has decreased by a lot, while the fluorescence excited by 540 nm has increased by a smaller amount. This is consistent with the leuco dye being broken down by the radiation, while the fluorescence from the colorful dye is limited by some other factor other than just the concentration of exposed dye.

3.2 Section Conclusions

The main conclusions in this section is that the polymer appears to have a linear radiochromic response and a linear radiofluorogenic response, which is the fundamental requirement for the intended application as a dosimeter. The material constants should be better, since the attenuation and fluorescence before any irradiation are quite high, equivalent to about ¿100 Gy of irradiation. It was also shown that using a green laser at 520 nm or 532 nm is appropriate for the 3D readout setup, since these lasers are available with high output power and good spatial mode quality. At these wavelengths, the fluorescent emissions also has a sufficient Stokes shift to be easily separable from the excitation light with an appropriate optical filter. There is also significant fluorescence from the leuco dye, when excited with light at 450 nm. This has a potential practical application,

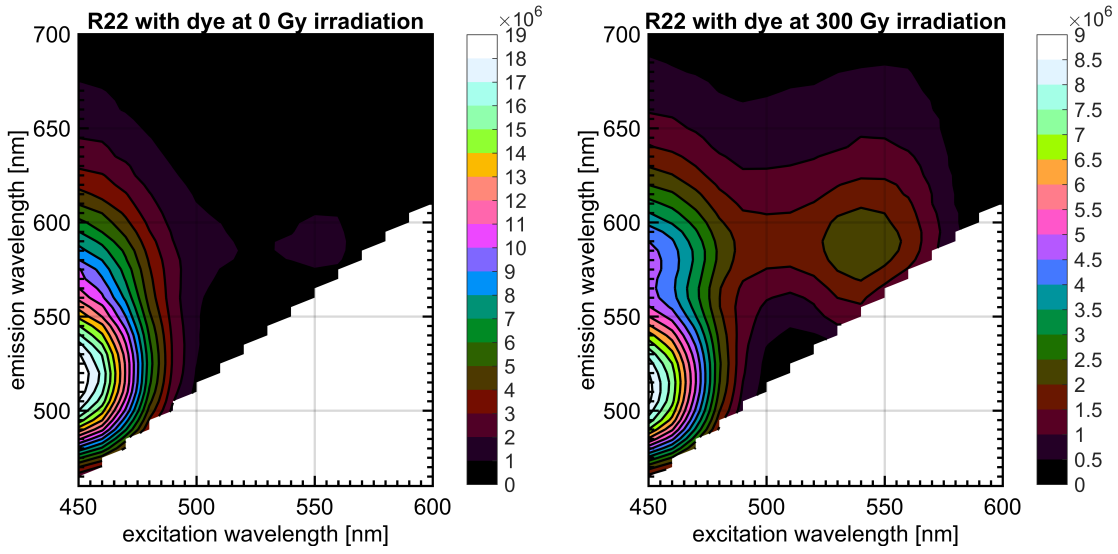

(a) 0 Gy, with dye

(b) 300 Gy, with dye

Figure 13: Fluorescence response maps for a sample with dye at 0 Gy and 300 Gy. Note the large decrease in fluorescence response for excitation at 450 nm, compared to the small increase for excitation at 550 nm.

by using the decrease in concentration of leuco dye as the dosimeter rather than the increase in exposed dye. This could merit further investigation.

4 Fluorescence Measurement Setup Introduction

To characterize the fluorescence response of the polymer, a device for measuring the fluorescence spectrum and intensity was constructed. It works by shining light at 520 nm onto a sample, and then measuring the resulting spectrum with a fiber coupled spectrometer. This section will provide a short introduction to this setup, which will be described in more detail in section 9, along with the specifications of each component.

It is important to know how the fluorescence response changes under a variety of different conditions. The main concern when measuring the fluorescence response of a sample is that the measurement conditions should be reliably repeatable. To this end a setup was prepared to measure the relative fluorescence response of a polymer sample. The setup was used in two configurations, first with a 532 nm laser and later with a 520 nm laser. Figure 15 shows an image of the fluorescence setup. This setup can be used to examine samples in the form of slides or pellets. The aluminum sample holder is used to hold the pellets. Figure 16 shows a diagram of the setup with the 520 nm laser. The laser shines onto the sample, which excites flourescence. Due to the fixed geometry of the setup, the fluorescence from different samples can be compared directly. To make the measurement more rigorous, the sample mount can be exchanged with a fluorescence reference, which provides a fixed fluorescence response. This makes it possible to compare fluorescence measurements even if the geometry of the setup has changed between measurement sessions.

The components of the fluorescence setup with the 532nm laser is listed below, along with the basic function of each component.

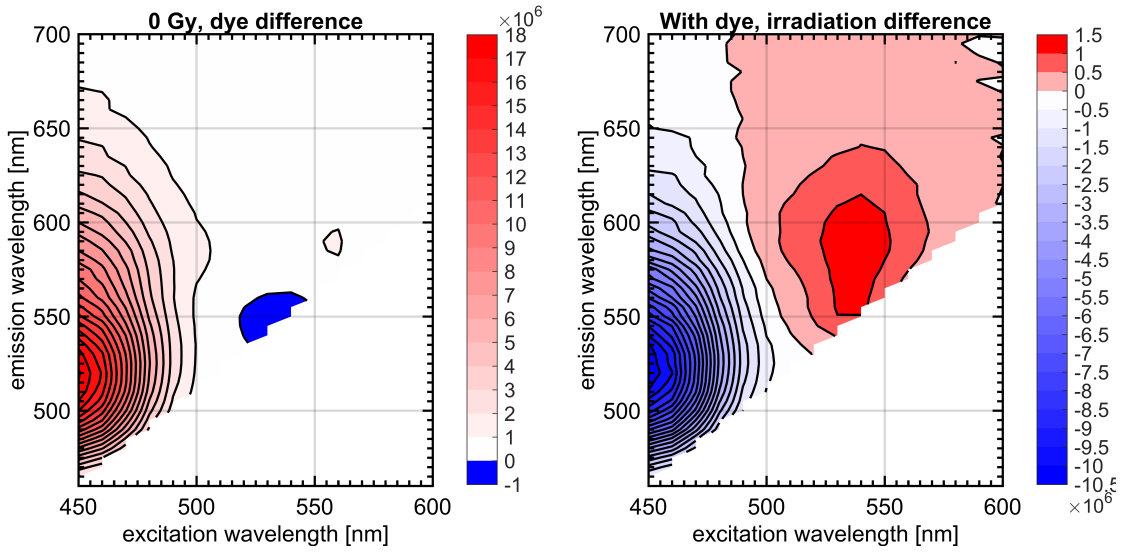

(a) Difference in fluorescence with and without dye, at 0 Gy.

(b) Difference in fluorescence at 0 Gy and 300 Gy, with dye.

Figure 14: Spectral maps of fluorescence response difference. Made to highlight the difference introduced by the addition of dye and the addition of irradiation.

1. 532 nm diode pumped Nd:YAG laser, to excite fluorescence in the sample.
2. 4 axis laser mount, to point the laser at the right spot on the sample.
3. Shortpass 600 nm filter to remove undesired emissions at 800 nm and 1064 nm from the laser.
4. Lens to defocus the laser spot on the sample, f=30mm.
5. 90:10 beamsplitter to direct a fixed percentage of the laser light towards the power meter.
6. Power meter to monitor the laser power during measurements.
7. Sample holder to position the sample in a repeatable manner.
8. Longpass or notch filter to remove the excitation light and protect the spectrometer.
9. Fiber coupling to spectrometer.
10. Ocean Optics spectrometer.

The configuration with the 532 nm laser was later superseded by a configuration with a 520 nm laser. In this the shortpass filter and the lens are not needed, since the 520 nm diode laser does not emit at any undesired wavelengths, and it has an adjustable focus lens built in. The direct diode laser also provides much better power and spatial mode stability, compared to the 532 nm laser.

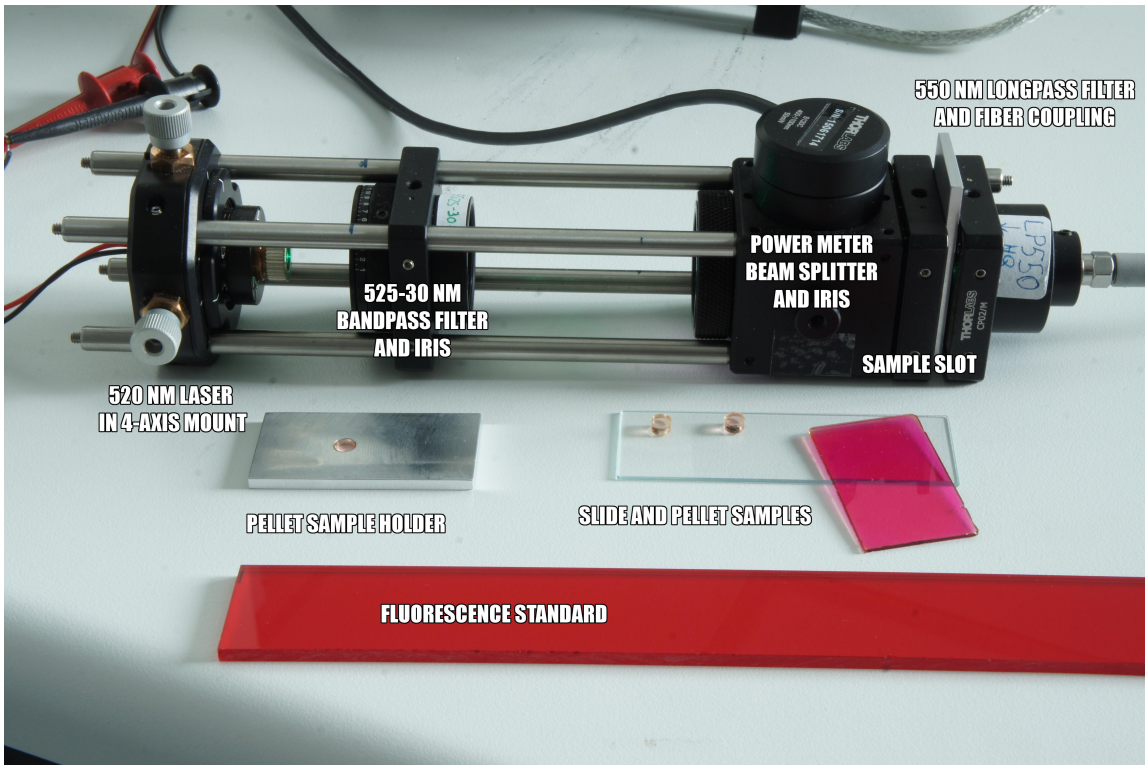

Figure 15: Image of the fluorescence setup.

1. 520 nm direct diode laser. This laser provides much better power and spatial mode stability.
2. 4 axis laser mount, to point the laser at the right spot on the sample.
3. 90:10 beamsplitter to direct a fixed percentage of the laser light towards the power meter.
4. Power meter to monitor the laser power during measurements.
5. Sample holder to position the sample in a repeatable manner.
6. 550 nm longpass to remove the excitation light.
7. Fiber coupling to spectrometer.
8. Ocean Optics QE65000 spectrometer.
9. Software to control the spectrometer and power meter.

In short, the fluorescence measurement setup enables easy comparative measurements of the fluorescence response and spectrum for different polymer samples and formulations. The components of the fluorescence measurement setup are described in more detail in section 9.

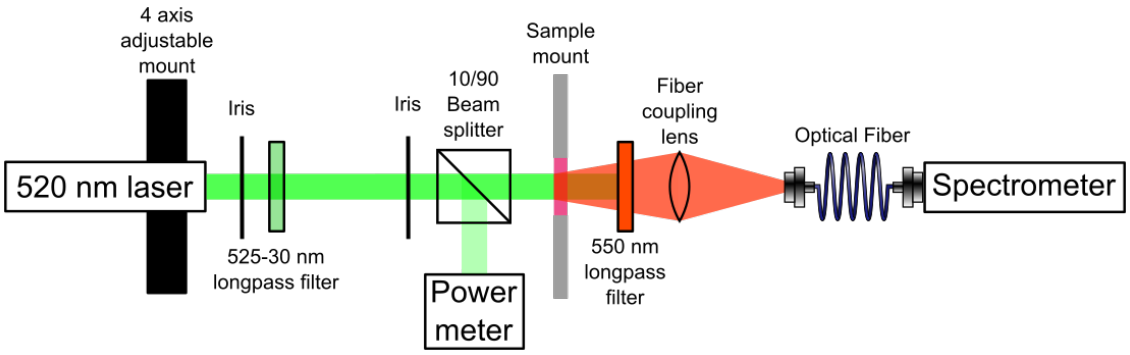

Figure 16: Diagram of the fluorescence setup components and light path. Distances not to scale. This is the version with the 520 nm laser.

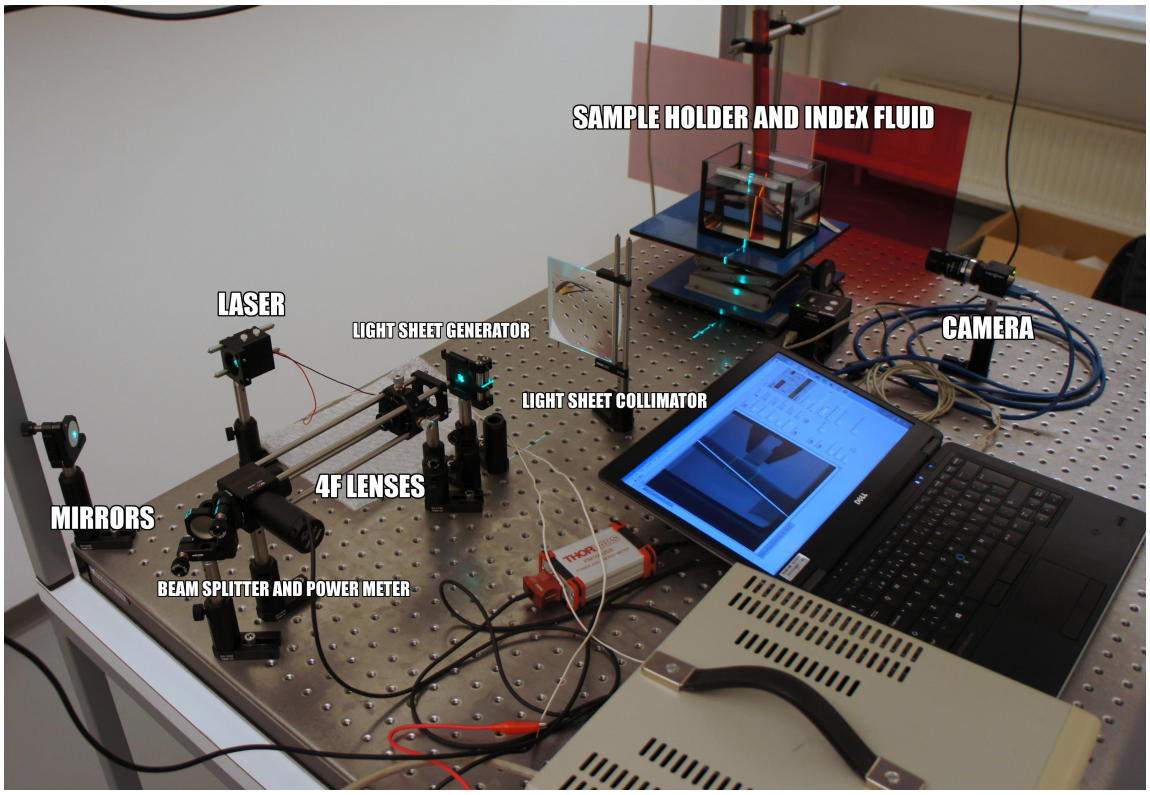

Figure 17: Annotated image of the 3D setup.

5 3D Readout Setup Introduction

The basic idea for measuring the absorbed dose in the radiofluorogenic polymer was to use optical fluorescence tomography to make images of the fluorescence response of individual slices of the sample. These images of the fluorescence response could then be translated into images of the absorbed dose distribution in those slices, and multiple slices could be assembled to make a 3D distribution of absorbed dose. This is done by using a laser beam and a special cylindrical lens to generate a thin sheet of laser light. This laser light then enters the sample, causing it to fluoresce. This fluorescence is then imaged with a camera. This is similar to light sheet microscopy[22] and particle imaging velocimetry[31], which also make use of light sheets to selectively illuminate and image thins slices of a sample.
A similar technique has been explored at the Technical University of Delft[30], only with excitation by UV lamps with emission around 383 nm instead of a laser. With the use of an incoherent light source, the thickness of their light sheet will be determined by the geometric optics of the width of the slit and the distance from the slit to the light source. This limits the spatial resolution of their setup. The group at Delft also noted the problem of attenuation of the excitation light, but did not resolve it completely[33]. A group at Aarhus university were also working on a similar setup[24], with the main differences being in the dosimetric material, the laser wavelength at 470 nm, and the use of optically stimulated luminescence rather than fluorescence. Figure 17 shows an annotated image of the setup, and figure 18 shows a closeup of the tank with the index matching fluid and a cylindrical sample in a sample holder clamp. Figure 19 shows a diagram of the setup. The laser emits a beam of green light, $\lambda = 520$ nm, which is then reflected by 2 adjustable mirrors through the middle of a 4F lens configuration. 10% of the beam is diverted by a beam splitter, into a power meter for power monitoring. The 4F lens configuration then rescales the beam and adjusts the

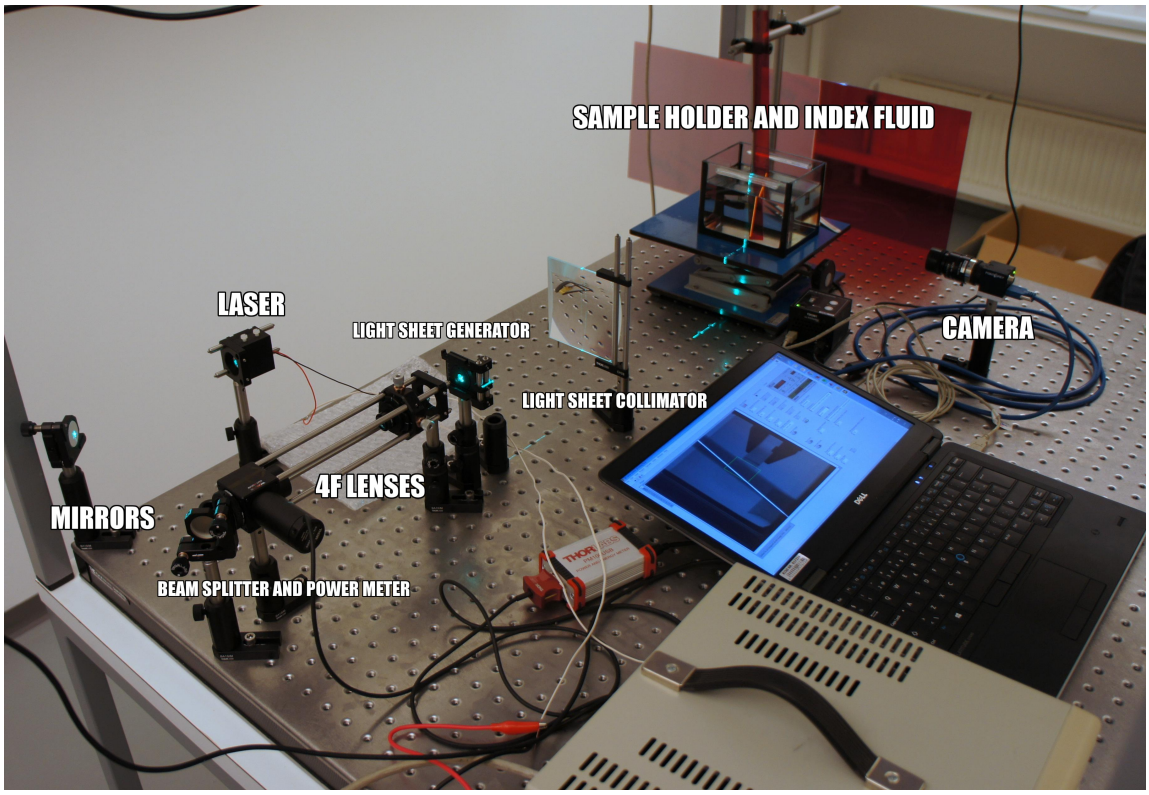

Figure 18: Closeup from the 3D setup of the tank with index matching fluid and a cylindrical sample.

focus to coincide with the sample. The laser line generator lens then defocuses the beam along the vertical axis, reshaping it into a thin flat sheet of laser light.
The components of the 3D setup are listed below, along with their basic function.

1. 520nm laser, to excite the fluorescence in the polymer.
2. Two adjustable silver mirrors, to align the position and direction of the beam.
3. Iris #1, to help align the beam.
4. Beam splitter, 10% diverted to power meter and 90% transmitted.
5. Power meter, to monitor the laser power.
6. Beam rescaling lens # 1, to rescale the beam to an appropriate diameter.
7. Beam rescaling lens # 2.
8. iris #2, to help align the beam.
9. Laser line generator lens, to shape the laser beam into a light sheet.
10. Large cylindrical lens, to collimate the light sheet into
11. Tank of index matching fluid, to prevent light from being scattered and refracted by the surface of the sample.

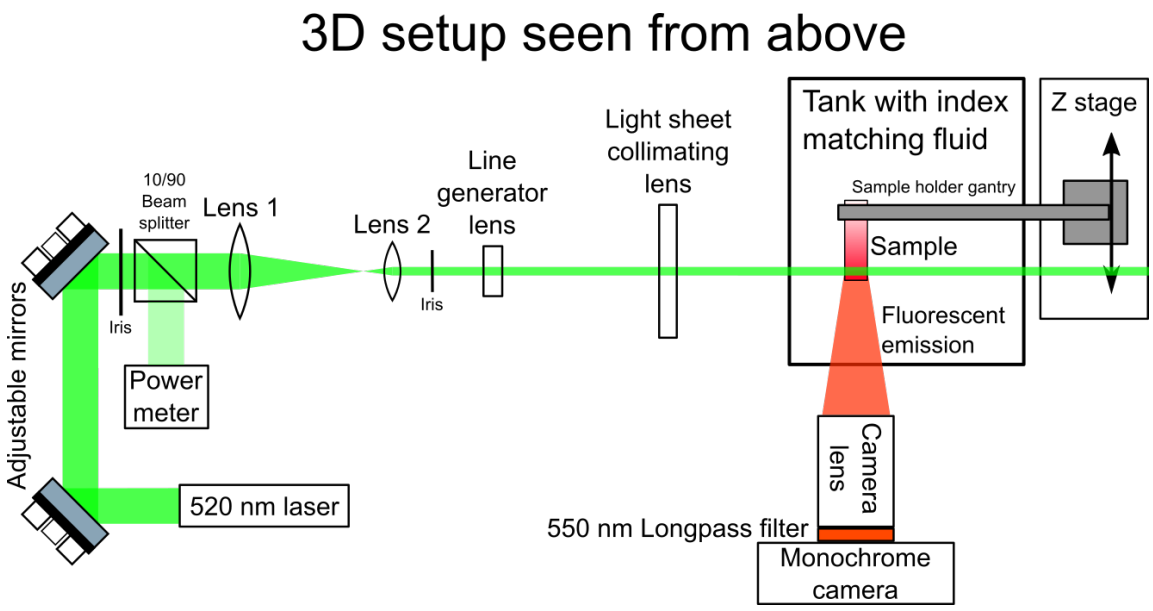

Figure 19: Diagram of the setup components and light path. Not to scale.

12. The irradiated polymer sample, which fluoresces in proportion to the received dose.
13. Fluorescence standard; A red stick of fluorescent plastic used to measure the vertical intensity profile of the light sheet.
14. The motorized sample holder, to move the sample through the light sheet/focal plane of the camera.
15. Longpass filter, cutoff at 550 nm, to prevent the green laser light from drowning out the fluorescence.
16. Camera lens to make the laser light sheet and the camera focal plane coincide.
17. Camera, to take images of the fluorescence emitted by the sample.

In short, the 3D setup can be used to read out the 3D distribution of the fluorescence response in a polymer sample. This fluorescence response can be calculated into an absorbed dose distribution with the methods discussed in sections 6 and 7. Each component in the 3D setup is discussed in more detail in section 8, along with the possible alternatives that were tested or considered.

6 2D Absorbed Dose Calculation

The fluorescence from a radiofluorogenic material can be used as a dosimeter. With a transparent sample it is possible to use this method for 3D dosimetry. The fluorescence excitation light gets absorbed by the sample, and this must be taken into account when calculating the absorbed dose distribution from the fluorescence data.
In this section, linear models for the light absorption and fluorescence response of a polymer sample are defined and used to establish a Ricatti[23] differential equation for the relationship between measured fluorescence and absorbed dose distribution. This differential equation has a solution, if a boundary condition can be imposed, in the form of a single position within the sample where the absorbed dose is known. This solution is tested with both real and simulated data to examine how the solution responds to different sources of error.

6.1 Context

A radioflourogenic polymer has been developed that exhibits a linear relationship between absorbed dose and fluorescence response and absorbance. This material is transparent, and it can therefore be used for 3D dosimetry. The 3D measurement setup works by shining a sheet of 523 nm laser light through a sample immersed in refractive index matching fluid. The laser light then excites fluorescence in the sample, which is then imaged by a camera positioned orthogonally to the light sheet. 3D information is then obtained by scanning the sample through the light sheet.

6.2 Derivation

The fluorescence that is measured in the 3D setup contains information about the absorbed dose distribution, but calculations must be performed to recover this information. The measured fluorescence, $F_m(x, y)$, depends linearly on both the local intensity of the excitation light, $I_E(x, y)$, and on the local absorbed dose $D(x, y)$. It is assumed that the excitation light enters the sample at $x = 0$ and that it propagates along the x-axis, from left to right.

$$F_m(x, y) = I_E(x, y) \cdot (R_F \cdot D(x, y) + B_F) \cdot C_{cam} \tag{3}$$

Where R_F is the radiofluorogenic response of the material, and B_F is the background fluorescence, or the fluorescence at zero dose. Both are material dependent constants that are measured experimentally. C_{cam} is a constant that contains all the camera exposure settings, as well as all other choices in the setup that affect the measured signal, such as the distance from sample to camera and the intensity of the excitation laser. The common feature is that they are all constant during the measurement. The excitation light, $I_E(x, y)$, gets absorbed by the material with an attenuation constant that depends linearly on the local dose.

$$\frac{\mathrm{d}I_E(x, y)}{\mathrm{d}x} = -I_E(x, y) \cdot \ln(10) \cdot (R_C \cdot D(x, y) + B_C) \tag{4}$$

Where R_C is the radiochromic response, and B_C is the attenuation at zero dose, both at the wavelength, λ_E, of the excitation laser. These material constants can also be measured experimentally, and are equivalent to the measured constants given in table 2.
We can combine the two equations by isolating $I_E(x, y)$ in equation 3 and inserting it into equation 4 to get

$$\begin{aligned} &\frac{\mathrm{d}}{\mathrm{d}x}\left(\frac{F(x, y)}{(R_F \cdot D(x, y) + B_F) \cdot C_{cam}}\right) \\ &= -\frac{F(x, y)}{(R_F \cdot D(x, y) + B_F) \cdot C_{cam}} \cdot \ln(10) \cdot (R_C \cdot D(x, y) + B_C) \end{aligned} \tag{5}$$

We can see that the constant C_{cam} can be multiplied out immediately, which indicates that most of our choices regarding the camera settings and setup do not matter for this calculation of the

absorbed dose distribution. This means that these settings can be optimized to improve the signal to noise of the fluorescence measurement, without needing to consider the effects on the measured data. For the differential equation 5, the left hand side can be expanded by using the quotient rule $(f/g)' = f'/g - f \cdot g'/g$ to get

$$\begin{aligned} &\frac{1}{R_F \cdot D(x,y) + B_F} \cdot \frac{\mathrm{d}}{\mathrm{d}x} F(x,y) - \frac{F(x,y) \cdot R_F}{(R_F \cdot D(x,y) + B_F)^2} \cdot \frac{\mathrm{d}}{\mathrm{d}x} D(x,y) \\ =& - \frac{F(x,y)}{R_F \cdot D(x,y) + B_F} \cdot \ln(10) \cdot (R_C \cdot D(x,y) + B_C) \end{aligned} \tag{6}$$

This can be reduced to

$$\begin{aligned} &\frac{\mathrm{d}}{\mathrm{d}x} F(x,y) - \frac{F(x,y) \cdot R_F}{R_F \cdot D(x,y) + B_F} \cdot \frac{\mathrm{d}}{\mathrm{d}x} D(x,y) \\ =& - F(x,y) \cdot \ln(10) \cdot (R_C \cdot D(x,y) + B_C) \end{aligned} \tag{7}$$

Now $\frac{\mathrm{d}}{\mathrm{d}x} D(x,y)$ can be isolated in equation 7 to obtain a differential equation for $D(x,y)$ in terms of the measured fluorescence $F(x,y)$.

$$\frac{\mathrm{d}}{\mathrm{d}x} D(x,y) = \left(D(x,y) + \frac{B_F}{R_F} \right) \cdot \left(\frac{\frac{\mathrm{d}F(x,y)}{\mathrm{d}x}}{F(x,y)} + \ln(10) \cdot (R_C \cdot D(x,y) + B_C) \right) \tag{8}$$

This is a first order and inhomogenous differential equation. It contains a term with the square of the dose. Equations of this type are known as Ricatti[23] equations. Note that the fluorescence constants can be substituted by a single constant $BR_F = {}^{B_F}/_{R_F}$. This is convenient because this fraction is much easier to measure experimentally and compare between materials/measurements. If a boundary condition of $D(x_0) = D_0$ is imposed, the solution to the differential equation 8 is given in equation 9. Ricatti did describe a solution method for Ricatti equations, but this solution was evaluated with the symbolic math programme Maple.

$$\begin{aligned} &D(x) = -BR_F + ... \\ &\frac{\ln(10)^{-1} \cdot F(x,y) \cdot 10^{x \cdot (B_C - BR_F \cdot R_C)}}{\frac{F(x_0,y) \cdot 10^{x_0 \cdot (B_C - BR_F \cdot R_C)}}{\ln(10)^{-1} \cdot (BR_F + D_0)} - R_C \cdot \int_{x_0}^{x} F(x',y) \cdot 10^{x' \cdot (B_C - BR_F \cdot R_C)} \mathrm{d}x'} \end{aligned} \tag{9}$$

The solution can be rewritten in a form that is easier to read:

$$\begin{aligned} G(x,y) &= F(x,y) \cdot 10^{x \cdot (B_C - BR_F \cdot R_C)} \\ D(x,y) &= \frac{G(x,y)}{\frac{G(x_0,y)}{BR_F + D_0} - \ln(10) \cdot R_C \cdot \int_{x_0}^{x} G(x',y) \mathrm{d}x'} - BR_F \end{aligned} \tag{10}$$

The boundary condition states that an explicit solution can be found if the absorbed dose is known at some position along each line in the image. The numerator in this solution is straightforward, with a linear dependence on the fluorescence signal and an exponential factor to account for attenuation of the excitation light. The denominator contains two terms, with the left accounting for the imposed boundary condition and the right being an integral that accounts for the internal absorbed dose distribution from x_0 to the evaluation point. Note also that there is no term in the differential equations or the solution that involves integration or differentiation with respect to the y-coordinate in the images. This means that each line in a fluorescence image are independent and need separate boundary conditions.

In the beginning of the sample, at $x = 0$, before the excitation light has been attenuated, there is direct linear relationship between the absorbed dose and the measured fluorescence. This relationship can be used to construct a boundary condition for a sample, if the constants $I_E(0,y)$, C_{cam},

B_F and R_F are known. $I_E(0,y)$ and C_{cam} can be measured with the fluorescence standard in the 3D setup.

$$\begin{aligned} F_m(0,y) &= I_E(0,y) \cdot C_{cam} \cdot (B_F + R_F \cdot D(0,y)) \\ D(0,y) &= \frac{F_m(0,y)}{I_E(0,y) \cdot C_{cam} \cdot R_F} - \frac{B_F}{R_F} \end{aligned} \tag{11}$$

The relationship in equation 11 between the initial fluorescence and the initial absorbed dose can be used to construct a boundary condition for the solution to the differential equation. The solution to the differential equation was implemented as a software program in Matlab in order to examine how it responds to different possible errors and uncertainties.

6.3 Implementation of the Solution for the Absorbed Dose

When implementing the solution in equation 9, there are a number of concerns. The measured fluorescence is in the form of images, with discrete x-positions and inherent measurement uncertainty. The propagation direction of the excitation light may also be at a slight angle relative to the pixel array. This is easy to correct in practice, either with a mechanical adjustment of the optical components or with a slight rotation of the resulting images. There is also uncertainty in the material constants and in the absorbed dose at the chosen boundary condition. The solution requires a boundary condition for each line in the image, but this may not be available. In this section, the effect of these concerns will be examined.

To examine the analytical solution in equation9, an example absorbed dose profile was defined and the resulting excitation light and fluorescence was calculated according to equations 4 and 3. The material constants used were the same as provided in table 2.

The dose profile example shown in figure 20 was not chosen to be realistic, but rather to illustrate the features and characteristics of the dose reconstruction equation, with respect to both the radiochromic and radiofluorogenic response.

Reconstructed absorbed dose profiles were then calculated with equation 9, but with illustrative errors in the boundary condition and material constants. The response to noise in the fluorescence signal was also investigated by adding many different random noise signals over the same fluorescence profile, and looking at the deviation in the resulting absorbed dose profiles. Figure 20 shows an example absorbed dose profile and the resulting fluorescence signal and decreasing excitation light intensity. The difference between the remaining excitation light and the relative fluorescence is the contrast in the fluorescence signal that is being used to calculate the dose from the fluorescence.

6.4 Realistic Dosimeter Example and Recommendations for Material Constants

As mentioned, the chosen dose example is not realistic. A more realistic dose example would be to look at a clinical dose fraction with a max. absorbed dose of 2 Gy. The length of the dose pofile could for example be 6.4 cm, to correspond to the film stack cavity in the CIRS IMRT head and neck phantom[1]. Figure 21 shows this more realistic dose profile for a single radiotherapy fraction, along with the resulting excitation light and fluorescence intensity. At the end of the profile, only 4% of the excitation light remains, and the radiofluorogenic response to the dose is almost indistinguishable from the background fluorescence. If there was any noise in the measured fluorescence, the contrast-to-noise ratio would be extremely bad. This illustrates why the composition of the dosimeter material used in this project is unsuitable for clinical dosimetry. We can also use this example to establish requirements on the material constants of an ideal dosimeter material. If the absorption of the excitation light should be less than 10% in this example, then the background attenuation should be less than $B_C < 0.007$ cm^{-1} and the radiochromic response should be less than $R_C < 0.0036$ cm^{-1}Gy^{-1}. Also, the ratio of the background fluorescence and the radiofluorogenic response should be less than ${}^{B_F}/_{R_F} < 2$ Gy. Figure 22 shows the dose example and the excitation light and

[1] CIRS product # 002HN

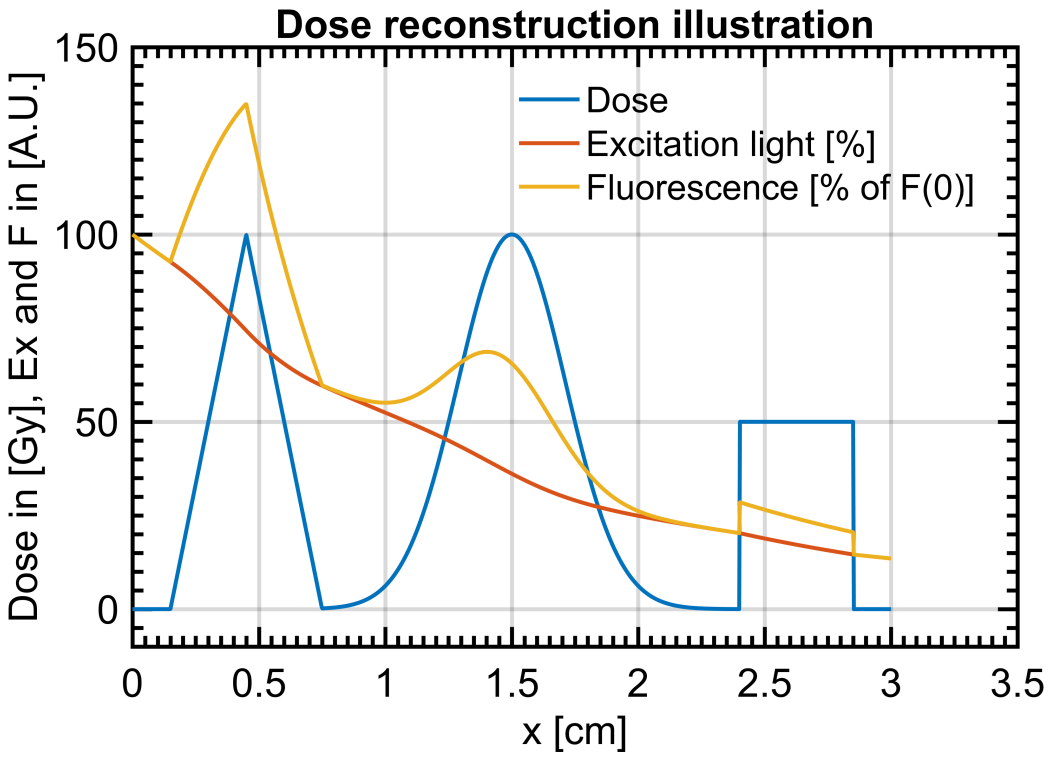

Figure 20: Dose profile example used for analysis of the solution. The resulting excitation light intensity and fluorescence profiles are also pictured, scaled to fit in the graph.

fluorescence if the requirements for the ideal clinical dosimeter were fulfilled. Only a small fraction of the excitation light is absorbed, and there is a clear difference in the fluorescence between the areas with and without absorbed dose. Another realistic option for 3D dosimetry is high dose dosimetry, with absorbed doses around 1 kGy. The application could be sterilization of medical equipment or food packaging. In this case, the radiochromic response should be low, $R_C < 0.014$ (cm kGy)$^{-1}$, and the ratio of background fluorescence and radiofluorogenic response can be higher, ${}^{B_F}/_{R_F} < 100$ Gy.

6.5 Uncertainty in the Boundary Condition

The boundary condition for the solution to the differential equation is a known absorbed dose any point along the absorbed dose profile. In practice it might not be possible to a-priori know the absorbed dose anywhere along the profile, which is a major disadvantage of this solution method. It is also possible that there is an estimate for a boundary condition, but that this estimate is wrong. Figures 23 and 24 show how the absorbed dose reconstructed from a fluorescence profile is dependent on an accurate estimate of the boundary condition dose. The error increases exponentially for every point to the right of the chosen boundary condition point, while it decreases to the left. The total effect on the absorbed dose profile is therefore larger when the boundary condition point, x_0, is further to the left, closer to the side where the excitation light enters the sample. This happens because of the exponential factor in the integral term of the denominator of the solution. The impact on the absorbed dose profile is also larger if the relative error in D_0 is larger. This happens because of the $BR_F + D_0$ term in the left term of the denominator of equation 9. If the true value of D_0 is small, any error will have a larger effect on this term. This suggests that a boundary condition to the far right will generally minimize the overall error.
A potential constraint on the boundary condition is that it should not lead to a negative recon-

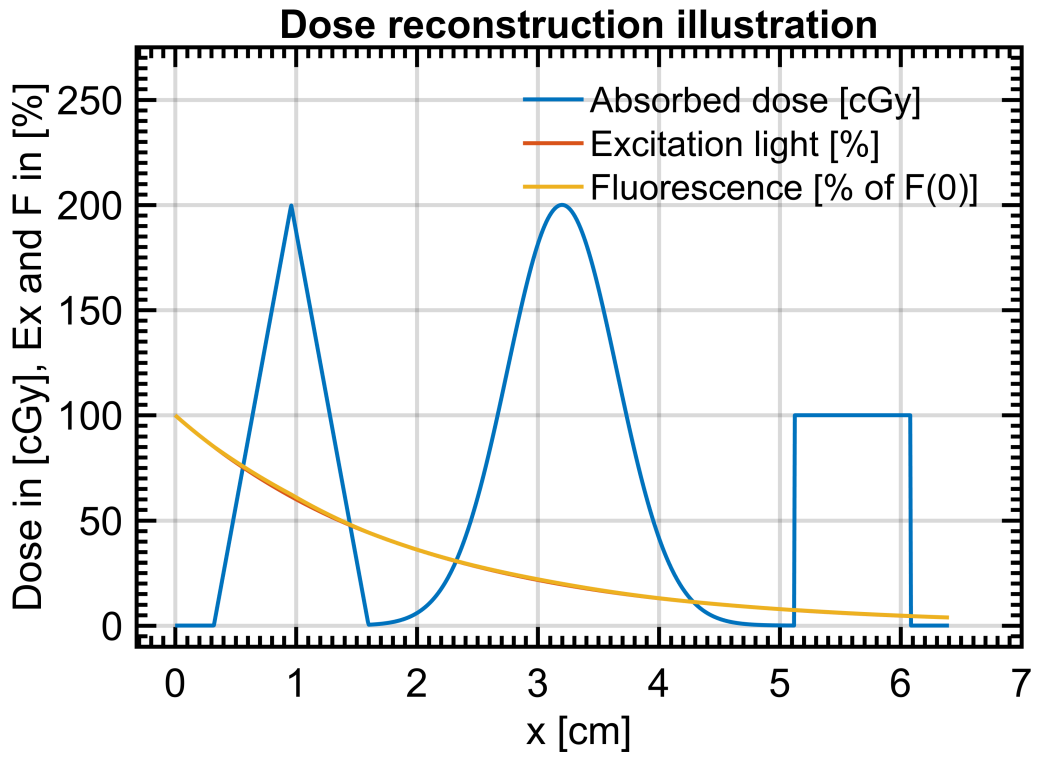

Figure 21: More realistic dose profile example. With the material constants measured for the dosimeter material used in this project, only 4% of the excitation light remains at the end of the sample.

structed absorbed dose anywhere along the profile, since negative absorbed dose should be physically impossible. This is problematic to implement in practice, since there will be noise in the fluorescence signal, which could lead to negative doses, even if the boundary condition is right. There is also the problem that the constant B_C is sensitive to the exact conditions during the curing of the polymer.

6.6 Uncertainty in the Constants

The material constants are experimentally determined values, and their values are therefore uncertain. At the time of writing, the values for the material constants are $B_C = 0.276\text{cm}^-1$, $R_C = 0.00316(\text{Gycm})^-1$ and $BR_F = 161\text{Gy}$. On measurements of different samples, prepared identically, the standard deviation on B_C and B_F is around 5%. The standard deviation on R_C and R_F is around 25%. The uncertainty is mainly from differences in the curing of the polymer samples, but also from the measurement itself. To evaluate the impact of uncertainty in the material constants, several reconstructions of the absorbed dose example were made with deliberate errors in the material constants used for the reconstruction. Figures 25 and 26 show the impact of using material constants with a 10% error for the absorbed dose reconstruction.
Due to the integral term in the solutions for $D(x)$ the error in the absorbed dose profile will tend to grow with the distance from the position with known absorbed dose or slope. This can be remedied if there are multiple positions with known properties, by using Newtons optimization[20] method to correct the constant towards new values which will make the reconstruction agree with the data in the known points.

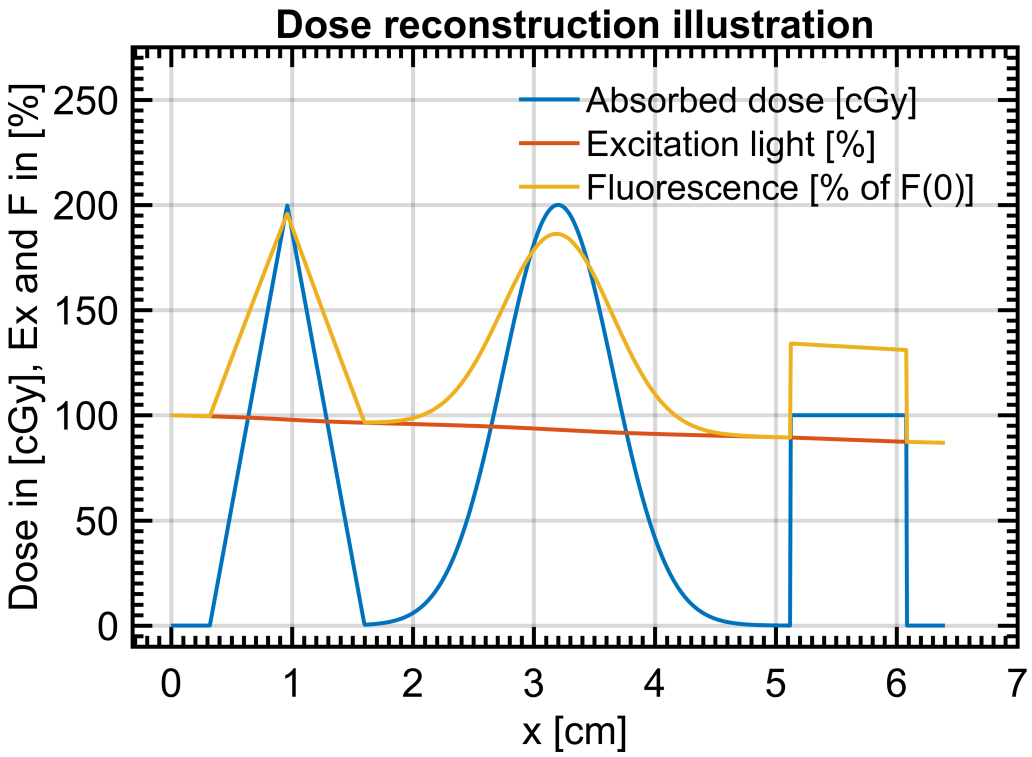

Figure 22: More realistic dose profile example. With the material constants measured for the dosimeter material used in this project, only 4% of the excitation light remains at the end of the sample.

6.7 Noise in the Fluorescence Signal

Noise in the fluorescence signal is the most obvious concern for the absorbed dose reconstruction, and it can impact the reconstructed absorbed dose in two different ways, corresponding to the two terms in the denominator of equation 9.
Any noise in $F(x_0)$ or error in D_0 will affect the left term. The right term can be affected if the noise in $F(x)$ has a consistent bias.
To investigate the impact of noise in the fluorescence signal, 10000 fluorescence profiles with random noise were generated by adding a random number to each point along the fluorescence profiles. The random numbers were distributed uniformly between -5% and +5% of the mean fluorescence value of the profile. Figure 27 shows the mean of the 10000 fluorescence profiles with uncorrelated noise, along with the standard deviation between the absorbed dose profiles. This illustrates that the standard deviation was independent of the position, as intended. Figures 27 and 28 show that a relatively small noise on the fluorescence signal leads to a relatively large error in the reconstructed dose. The majority of this error stems from a mismatch between the noisy fluorescence measurement, $F(x_0)$, at the boundary condition point x_0 and the boundary condition absorbed dose estimate D_0. This error can be minimized by replacing $F(x_0)$ with an average of F around x_0. This will only work if the absorbed dose estimate is constant in the area.

Figure 29 shows the effect of a bubble or similar artifact in a sample. The bubble scatters half of the remaining excitation light. The result is that the dose reconstruction is accurate until it encounters the artifact, at which point The results of this section are summarized in table 3. This table contains the errors on the extreme left and right sides for each of the different sources of error. It is apparent that the most important constant is the known absorbed dose D_0, with the radiochromic response $R_C$coming in second place.

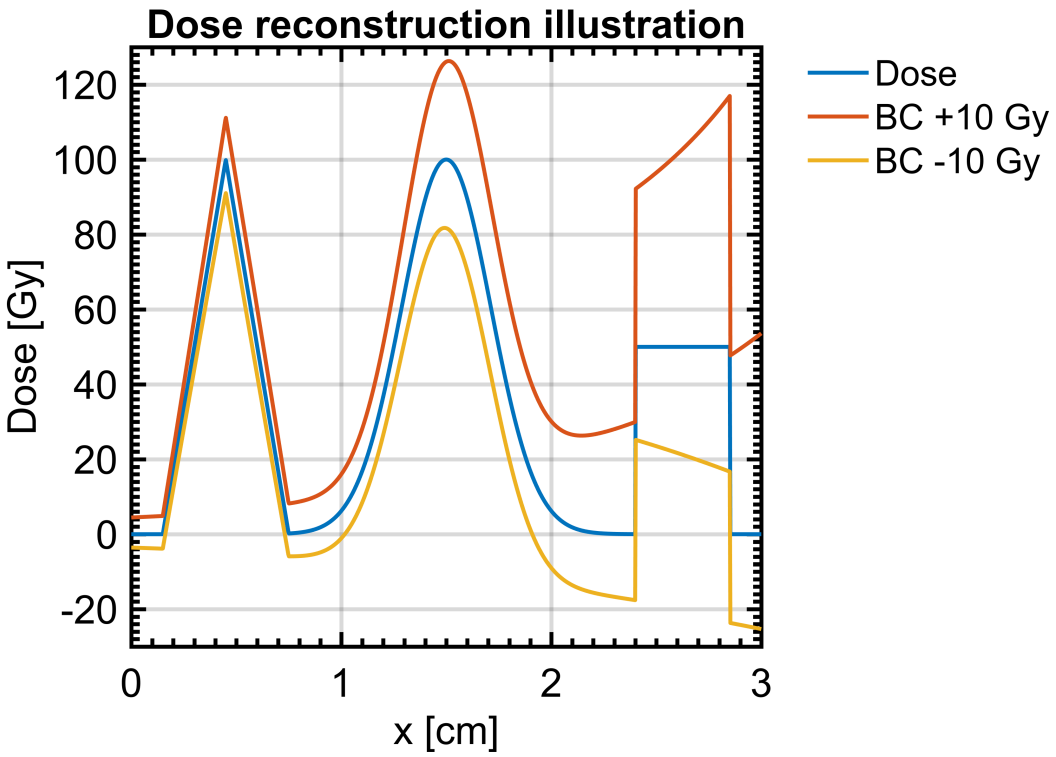

Figure 23: Dose profiles reconstructed from the fluorescence example in figure 20, but with an error added to the boundary condition. The boundary condition was the absorbed dose at the peak of the triangle.

6.8 Matlab Implementation

The solution to the differential equation was implemented as a function in Matlab, **Fluorescence2Dose2D.m**. The inputs are a fluorescence image, a scaling factor for how many mm each image pixel is, two vectors of boundary conditions containing pixel indexes, $x_0(y)$ and doses $D_0(y)$, a vector containing the material constants and an integer telling how many pixels the fluorescence should be averaged over to obtain a measure for $F_0(y)$ at $x_0(y)$. The output is an absorbed dose image of the same dimensions as the input fluorescence image.
Since the fluorescence data is given as a set of images making up a 3D volume, a function, **load_3Dsetup_images.m**, was written to load the image data into matlab, along with the metadata contained in the image file names. To transform the image data into a 3D absorbed dose distribution, a function, **ImStack2Dose.m**, was written to perform automatic generation of boundary conditions for each line in each image in the data set. The inputs are a set of images with different z-positions in the sample, a set of xyz vectors for the images, a struct containing a method designation for automatically generating boundary conditions for each line in each image, an optional scaling factor for interpolation of the processed data onto a regular xyz grid, and an optional angle for rotating the interpolated data if necessary. The outputs are the calculated absorbed dose images, along with optional interpolated and rotated absorbed dose data. The interpolation is necessary in order to plot the isosurfaces of the finished 3D absorbed dose distribution, as shown in section 11.

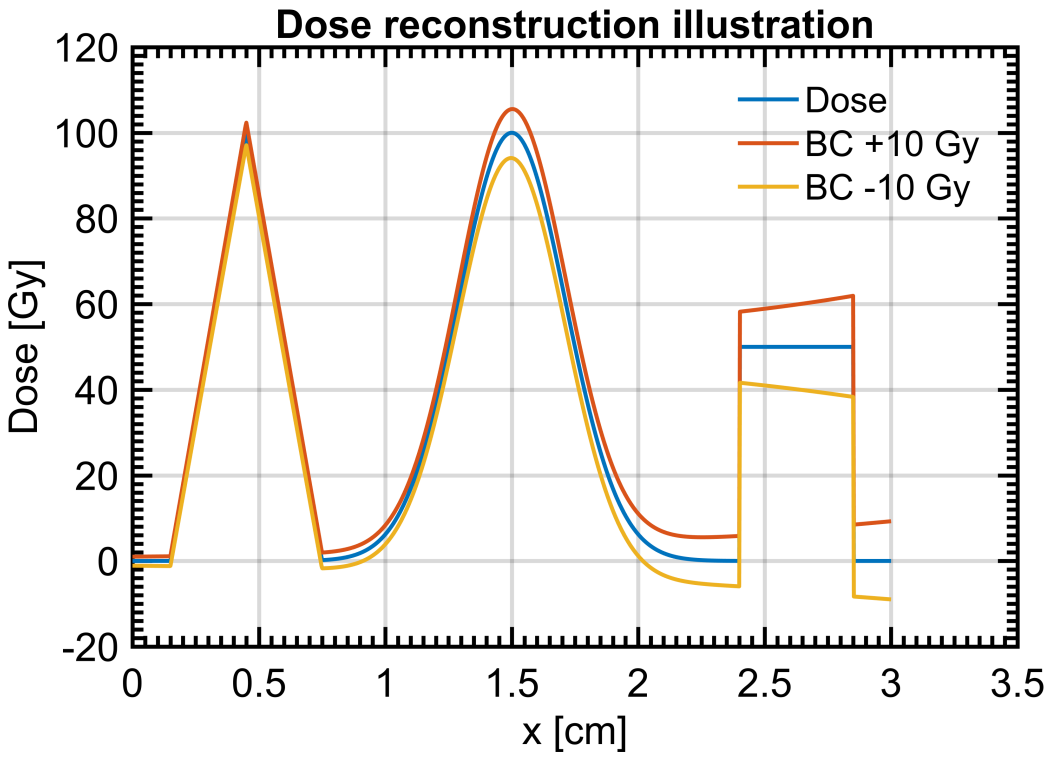

Figure 24: Dose profiles reconstructed from the example in figure 20, but with an error added to the boundary condition. The boundary condition was the absorbed dose at the flat top on the right. This shows that the impact of an error in the boundary condition depends on the position of the boundary condition.

Automatic Generation of Boundary Conditions

For a large data set with hundreds of images, each with hundreds of lines, automatic generation of boundary conditions are a necessity. There are two viable options for generating automatic boundary conditions:

1. The absorbed dose in the right end of the sample can be assumed to be zero.
2. The absorbed dose in the left end of the sample can be calculated from the vertical intensity profile measured with the fluorescence standard along with the given material constants.

The first option has three requirements: The sample must have a surface with zero absorbed dose everywhere. The sample must be placed so that this surface is on the right side of the sample in every fluorescence image. The absorbance in the sample must be low enough that the background fluorescence is still measurable without significant noise in the right edge of the sample.
The first two requirements will depend on what kind of irradiation the sample has been subjected to. The third requirement will generally be fulfilled, except in the case of extremely large doses and/or very large samples.
The second option is more interesting, since the only requirements are that the vertical intensity profile and the camera settings have been properly measured with the fluorescence standard, and that the material constants for the fluorescence of the sample are well defined and known.
The first requirement can be fulfilled by acquiring some images of the fluorescence standard immediately before and after a scan of a sample, with the same camera settings as the scan. Each line

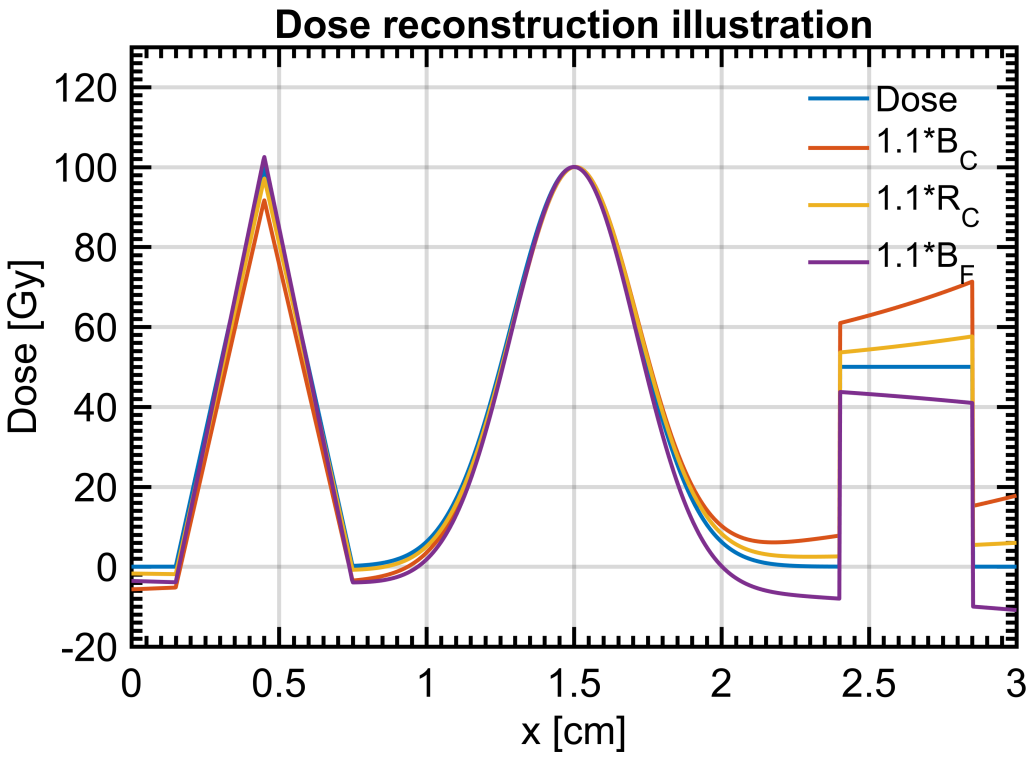

Figure 25: Reconstructed absorbed dose profiles, but with a 10% error added to the material constants. The boundary condition was the absorbed dose at the top of the Gaussian in the middle. This shows that impact of an error in the boundary condition depends on the position of the boundary condition.

in the fluorescence images can then be normalized by the excitation intensity at that y-position. The second requirement can be fulfilled by performing measurements on samples without any absorbed dose and with a known homogeneous irradiation. This characterization should be done with a sample from the same batch as the sample of interest, in order to ensure that the composition, curing method and time since curing are exactly the same.
With the complete suite of Matlab scripts, a series of fluorescence images can be loaded and calculated into a 3D absorbed dose distribution with a minimum of user input.

6.9 Special Cases of the Dose Reconstruction Equation

For some special cases, the solution to the absorbed dose reconstruction changes in notable ways. These special cases would only apply to hypothetical dosimetric materials, but they are not entirely outside the realm of possibility.

Negligible Radiochromic Response

If the radiochromic response, R_C, of the sample is sufficiently low, it can be neglected in equation 4, which means that this equation will have a solution given by equation 12.

$$I_E(x,y) = I_E(x_0(y),y) \cdot 10^{-B_C \cdot (x - x_0(y))} \tag{12}$$

Here, $I_E(x_0,y)$ is the intensity of the excitation light before it has been attenuated. This number can be measured by using the fluorescence standard. $x_0(y)$ is the position where the excitation light first enters the sample, and depending on the shape of the sample, its position may depend

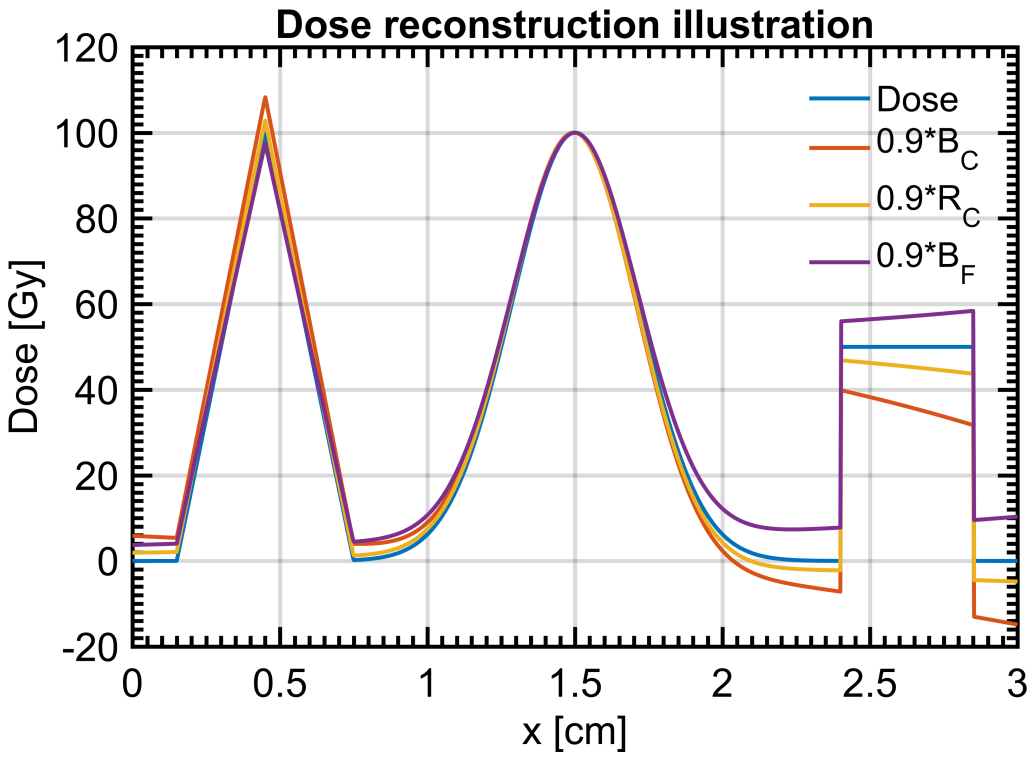

Figure 26: Reconstructed absorbed dose profiles, but with a 10% error subtracted from the material constants. The boundary condition was the absorbed dose at the top of the Gaussian in the middle. This shows that impact of an error in the boundary condition depends on the position of the boundary condition.

on the y-coordinate. This solution can be inserted into equation 3, which can then be solved to obtain an expression for the absorbed dose distribution.

$$D(x,y) = F_m(x,y) \cdot 10^{B_C \cdot (x - x_0(y))} \cdot \left(C_{cam} \cdot I_E(x_0(y), y) \cdot R_F\right)^{-1} - {}^{B_F}/_{R_F} \tag{13}$$

Using this solution in practice would be similar to the second option for generating boundary conditions described in section 6.8, with the difference that the attenuation of the excitation light can be calculated before calculating the absorbed dose distribution. This solution has the advantage that the possibility of singularities in the absorbed dose distribution in eliminated. This solution method should be applicable if the radiochromic response in a given sample contributes less than 0.5% to the attenuation of the excitation light. To be precise, if $\int_x \cdot R_C \cdot D(x')\,\mathrm{d}x' < 0.0022$ is expected, given the measured value of R_C, the size of the sample and the expected mean dose, then this solution can be used. For the absorbed dose profile in section 6.4 this would give a radiochromic response of $R_C \approx 0.17$ (cm kGy)$^{-1}$.
When developing sample materials for use in fluorescence tomography systems, fulfilment of this condition should be one of the main goals. Having a negligible radiochromic response might sound impossible, since the excitation light must be absorbed in order to excite a fluorescent emission. It would nonetheless be possible if the effect of irradiation was to increase the quantum efficiency of the fluorescence from the dye, rather than to increase the concentration of the fluorescent dye. One possible mechanism would be if the irradiation caused the material to harden, thereby decreasing the rate of non-radiative decay of the excited dye molecules[14, p. 10].

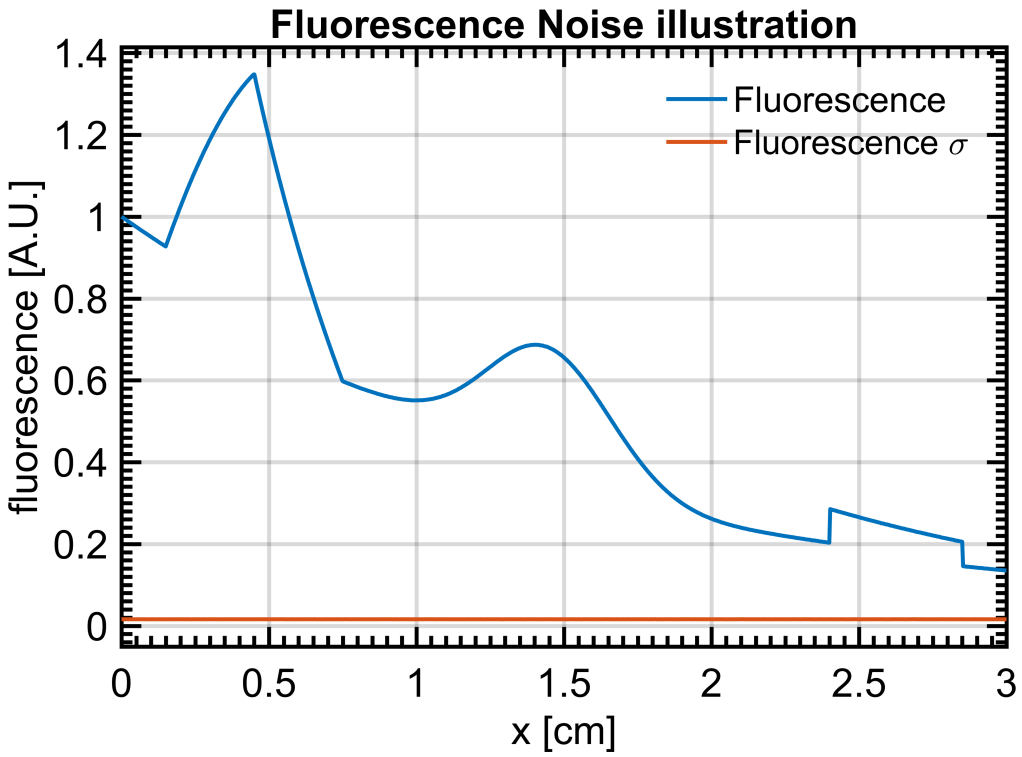

Figure 27: The mean fluorescence of the 10000 fluorescence profiles, along with the standard deviation on the fluorescence. This shows that the standard deviation is constant and relatively small, in comparison to the standard deviation on the resulting absorbed dose profiles.

There is also a solution if the boundary condition is a known absorbed dose, $D(x_0) = D_0$.

$$\begin{aligned} G(x,y) &= F(x,y) \cdot 10^{x \cdot B_C} \\ D(x,y) &= \frac{G(x,y)}{G(x_0,y)} \cdot (D_0 + {}^{B_F}/_{R_F}) - {}^{B_F}/_{R_F} \end{aligned} \tag{14}$$

Negligible Radiofluorogenic Response

If the value of R_F is negligible, there is another interesting solution for finding the dose, given in equation 15. This case is relevant if there is a radiation insensitive fluorescent dye dissolved in a radiochromic dosimeter. Due to the radiochromic property, the excitation light would be absorbed in the sample, and the local absorbed dose would be linear with the local relative change in the fluorescence.

$$D(x,y) = \frac{-1}{\ln(10) \cdot R_C} \left(\ln(10) \cdot B_C + {}^{\frac{\mathrm{d}F(x,y)}{\mathrm{d}x}}/_{F(x,y)} \right) \tag{15}$$

In this case, the radiochromic response should be tailored to the specific application, to provide enough contrast in the local attenuation of the excitation light to provide a usable signal.

$$R_C \cdot L_{\text{sample}} \cdot D_{\text{mean}} \approx 0.3 \tag{16}$$

L_{sample} and D_{mean} are the length and mean dose of the sample. The ratio of background fluorescence and radiofluorogenic response must also be very high, $|{}^{B_F}/_{R_F}| > 1000$ Gy.
This could potentially be achieved by suspending or dissolving a dye with high quantum yield, such as certain rhodamines[13] or nanocrystals[15], in a traditional radiochromic dosimeter. This

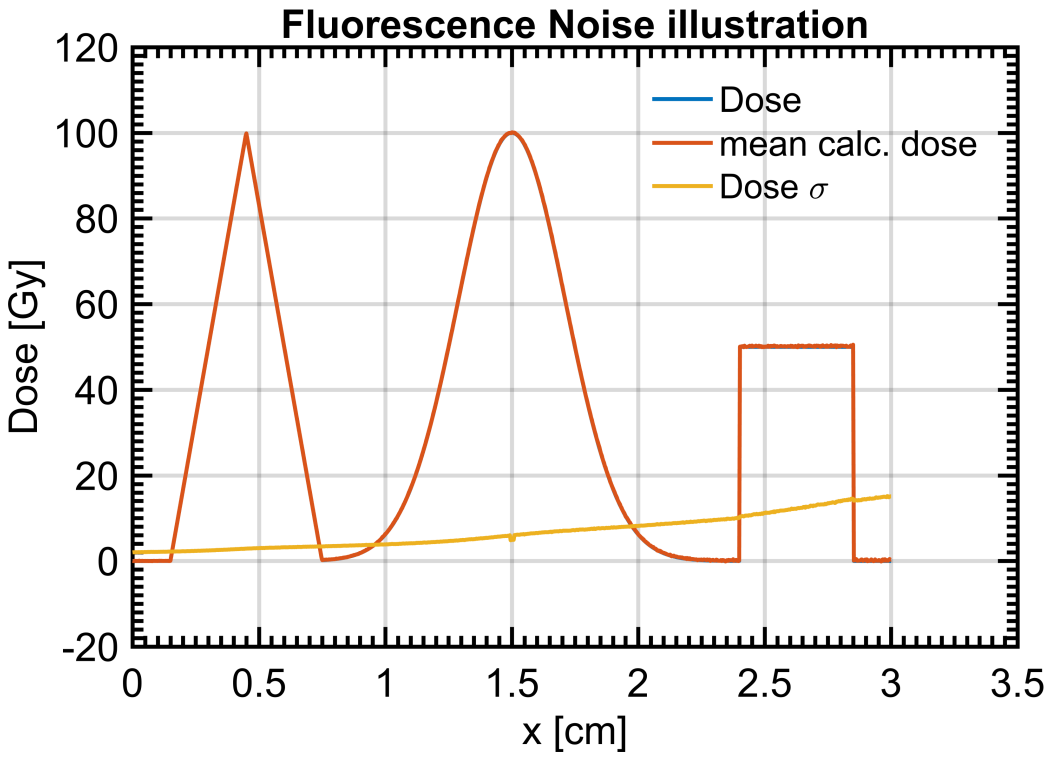

Figure 28: Mean absorbed dose profile reconstructed from the 10000 noisy fluorescence profiles, along with the standard deviation on the absorbed dose profiles. The point with zero standard deviation is the boundary condition point $x_0 = 1.5$ cm, where the absorbed dose has been defined as $D_0 = 100$ Gy. The standard deviation on the reconstructed absorbed dose is relatively larger than the standard deviation on the fluorescence used for the reconstruction.

could impart a constant fluorescence response in the sample, without increasing the absorbance or scattering very much.
This capability could potentially be incorporated into existing setups for readout of radiochromic materials. This would require an additional camera mounted beneath or above the setup, and special software to capture and interpret the fluorescent data as the laser scans through the radiochromic samples.
The ability to rotate the samples in these setups would also make this readout method very robust with respect to artifacts and imperfections in the samples. This would provide another modality for readout of the radiochromic dosimeter by reading out the local attenuation along each line. The contrast in the output signal is likely to be low, but combined with the data from a simultaneous optical CT scan, this method could provide a very good method for detecting and mitigating imperfections in the sample and artifacts from the optical CT scan. The overall accuracy of the resulting 3D absorbed dose distribution could also be improved by combining the two independent but simultaneous measurements of the same sample.

6.10 Section Conclusions

The analytical solution for calculating the dose distribution from the measured fluorescence was derived, and it was implement as a Matlab program. It successfully resolves the nonlinearity that arises from the dose-dependent attenuation of the excitation light. The solution requires boundary condition in the form of a known dose somewhere in the sample at each line in the fluorescence images. This boundary condition can be calculated by properly characterizing the dosimeter and

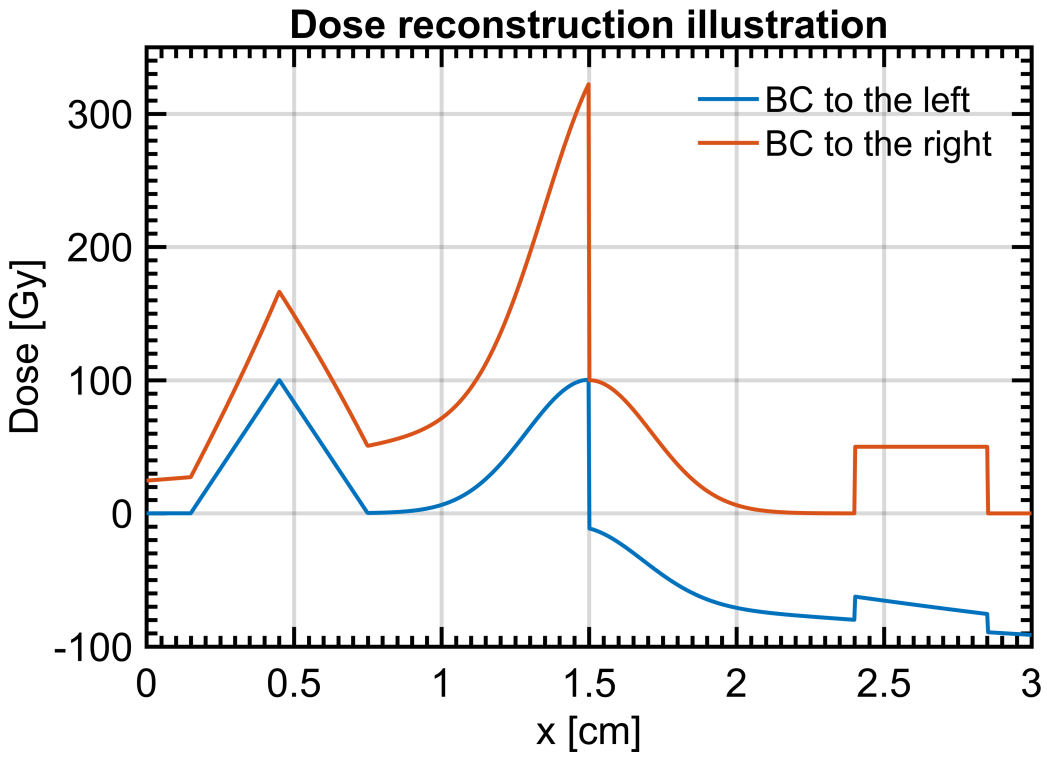

Figure 29: Dose reconstruction with a simulated artifact. At x=1.5 cm, half of the remaining excitation light is scattered. The graph shows the reconstructed dose with a boundary condition to the left and to the right of the artifact.

the vertical intensity profile of the excitation laser. Alternatively, the dosimeter samples can be prepared in a fashion such that the dose is known to be zero in a suitable region.
The solution was also tested on a hypothetical dose example, and shown to be sensitive to uncertainty in the optical constants of the dosimeter, uncertainty in the boundary condition, artefacts in the sample, and noise in the fluorescence signal.
An example of a more realistic dose profile for a clinical radiotherapy dose fraction was also used to illustrate why there are requirements on the optical constants for the dosimeter.
In the case where the radiochromic response becomes negligible, the solution becomes much more simple and stable, without the potential for singularities.
In the case where the fluorescence is strong enough for measurement, but the radiofluorogenic response is negligible, the local dose can be calculated from the local relative change in the excitation light intensity. This is of potential interest as an addition to radiochromic dosimeter setups. The requirements for the optical constants are given in table 4 The clinical case is for a dose profile with length 6.4 cm and average absorbed dose of 2 Gy. The high dose case has an average dose of 500 Gy. The special cases with negligible R_C and R_F also use the clinical dose profile.
These material constants were chosen to keep the attenuation of the excitation light below 20%, except in the negligible R_F case. This requirement is arbitrary, but is sufficient to demonstrate what order of magnitude the material constants should have for each application.

Changed constant \difference [Gy]	average magnitude	left	right
D_0+10 Gy, x_0=0.45 cm	23.9	4.5	53.6
D_0-10 Gy, x_0=0.45 cm	14.7	-3.6	-25.3
D_0+10 Gy, x_0=2.65 cm	4.7	1.0	9.3
D_0-10 Gy, x_0=2.65 cm	4.9	-1.1	-9.0
B_C·1.1	6.4	-5.7	17.8
R_C·1.1	2.4	-1.7	6.0
B_F·1.1	4.4	-3.6	-10.9
B_C·0.9	6.0	5.9	-14.8
R_C·0.9	2.3	1.9	-4.8
B_F·0.9	4.3	3.7	10.3
Artifact, x_0=0.45	48.8	0	-91.2
Artifact, x_0=2.65	37.3	24.6	0
F+noise	6.7	2.0	15.1

Table 3: Resulting Error on the left and the right sides of the example absorbed dose distribution

Table 4: Requirements for the material constants of the dosimeter, for a variety of applications and special cases.

Case \Constant	B_C [cm^{-1}]	R_C [$(\mathrm{cm\ kGy})^{-1}$]	B_F/R_F [Gy]
Clinical	< 0.007	< 3.6	< 2
High dose	< 0.007	< 0.014	< 100
Negligible R_C	< 0.007	< 0.017	< 2
Negligible R_F	< 0.007	$\approx 0.3/L_{\mathrm{sample}} \cdot D_{\mathrm{mean}}$	> 1000

7 2D Reconstruction with Fourier Components

Section 6 describes an analytical solution to the absorbed dose calculation, but this solution had some distinct disadvantages. Most notably it reguires a known boundary condition for each line in the image, and noise in the fluorescence signal can lead to large errors in the calculated dose.
These complications lead to efforts to find another way to calculate the dose, which avoids the problems of nonlinear sensitivity to noise in the measured fluorescence and discontinuity between lines in the same image. Furthermore, this method only requires one boundary condition per 2D image, given as the mean absorbed dose in the image.
This method works by generating a guess at the absorbed dose distribution, $D_C(x, y)$, and calculating the corresponding fluorescence distribution, $F_C(x, y)$. The predicted fluorescence distribution can then be compared with the measured fluorescence, and this comparison is then used to iteratively improve the guess at the absorbed dose distribution.
This solution method starts with solving equation 4 for the intensity of the excitation light:

$$I_E(x, y) = I_0(y) \cdot \exp\left(-\int_0^x \ln(10) \cdot (B_C + R_C \cdot D_C(x, y))\mathrm{d}x \right) \tag{17}$$

$I_0(y)$ is the initial intensity of the excitation light. The y-dependence represents the vertical intensity profile of the excitation beam. This is a parameter that must be measured experimentally, but it should be constant for each image series since there are no moving parts in the optical setup. In figures 30a and 30b an example of an absorbed dose distribution and the corresponding excitation light intensity is shown, calculated with a set of material parameters measured from a sample of polymer composition 22. The parameters are $B_C = 0.0565\mathrm{cm}^{-1}$, $R_C = 0.2805(\mathrm{kGycm})^{-1}$, $B_F = 1373$ and $R_F = 4.588\mathrm{Gy}^{-1}$. The structures in the absorbed dose example are a circle, a Gaussian, and two squares, chosen to illustrate the characteristics of the absorbed dose reconstruction algorithm.

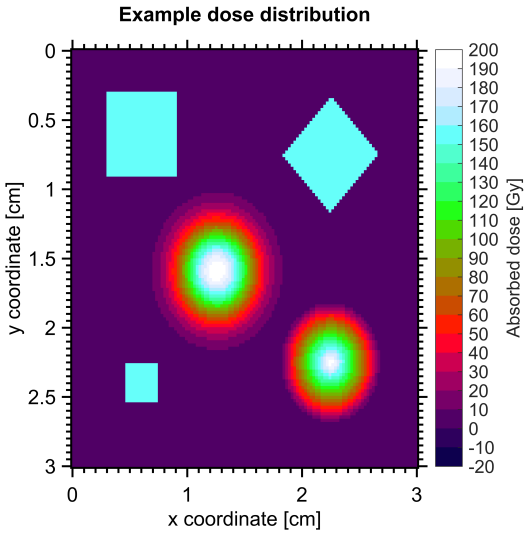

(a) Dose distribution example. This absorbed dose distribution is used to illustrate the characteristics of the recovery algorithm throughout this section.

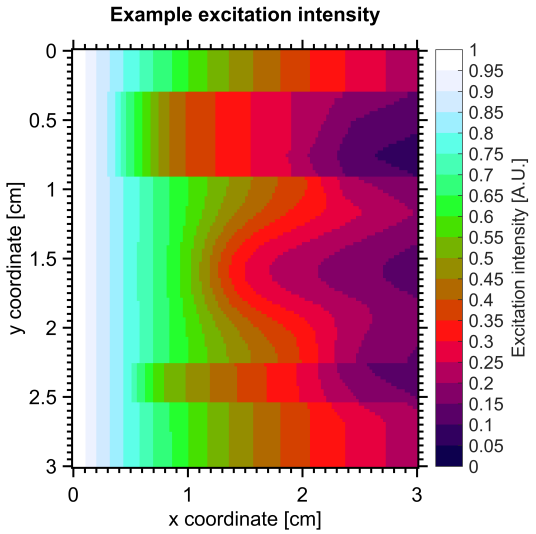

(b) Excitation light absorption resulting from the example absorbed dose distribution

Figure 30: Excitation light absorption resulting from the dose example. The light enters from the left, and gets absorbed by the sample. The attenuation constant is linear with the dose.

The solution for $I_E(x, y)$ is then inserted into equation 3, which gives us the relationship between the candidate absorbed dose distribution and the corresponding fluorescence.

$$\begin{aligned} F_C(x,y) =& I_0(y) \cdot C_{cam} \cdot (B_F + R_F \cdot D_C(x,y)) \cdot ... \\ & \exp\left(-\ln(10) \cdot \int_0^x (B_C + R_C \cdot D_C(x,y)) \mathrm{d}x \right) \end{aligned} \tag{18}$$

This equation has the advantage that it is fast and easy to compute from any given absorbed dose distribution, and that it can be readily compared to the measured fluorescence, $F_m(x, y)$. This makes the comparison a perfect candidate for the error function in a nonlinear optimization algorithm. The error function is then the sum of squares of the difference between measured and calculated fluorescence.

$$E = \int_{sample} (F_m(x,y) - F_C(x,y))^2 \mathrm{d}x\mathrm{d}y \tag{19}$$

For the sake of completeness, there is also a different way to calculate the error, which is to put the candidate distribution of the absorbed dose and the measured fluorescence into equation 8.

$$\begin{aligned} E = \int_{sample} \Bigg(& \ln(10) \cdot (B_C + R_C \cdot D_C(x,y)) - ... \\ & \frac{\frac{\mathrm{d}D_C(x,y)}{\mathrm{d}x}}{D_C(x,y) + \frac{B_F}{R_F}} + \frac{\frac{\mathrm{d}F_m(x,y)}{\mathrm{d}x}}{F_m(x,y)} \Bigg)^2 \mathrm{d}x\mathrm{d}y \end{aligned} \tag{20}$$

This definition of the error in equation 20 is unfortunately incompatible with the solution method described in this section. It contains the relative gradients of the measured fluorescence and candidate dose, but the candidate dose is represented by a subset of its Fourier components, and this representation does not replicate gradients faithfully. It is possible that this measure of the

error would be useful for a different representation of the dose distribution. Figure 31 illustrates the fluorescence that can be calculated from the absorbed dose example, using equation 18 and the previously mentioned material constants. The vertical excitation intensity profile is flat, and the camera constant has been set to one. This means that $I_0(y) = C_{cam} = 1$.
The next challenge in this solution method is how to represent the absorbed dose distribution. The measured fluorescence is discretized as pixel values in an image, and the absorbed dose distribution should therefore also be given in the same format. Trying to use the pixel values in an absorbed dose image as the free parameters in an optimization is impractical, since even a small image will have more than 10,000 pixels. The values of pixels in the same line in the image would also not contribute independently to the solution, due to the integral in equation 18. This will slow down the convergence of most optimization algorithms.
The solution to these challenges is to represent the absorbed dose distribution as a discrete 2D Fourier transform[27]. In a discrete 2D Fourier transform of an image, the Fourier components are complex numbers which represent waves with different wavelengths and spatial directions. The magnitude of each component represents the amplitude of the wave, while the complex phase represents the phase shift of the wave. Figure 32 shows an example of the Fourier transform of the dose example in figure 30a. The image shows the logarithm of the magnitude of the Fourier components, since the fourier components are complex numbers with absolute values across several orders of magnitude. The important feature is that the magnitude generally decreases with distance form the center, which implies that the central Fourier components contains most of the information about the structures on the image. The outer fourier components will therefore inly increase the resolution of the reconstructed image, without introducing new features in the dose image. The center represents the wave component with infinite wavelength, which is equivalent to a constant. Because of how Matlab calculates the 2D discrete Fourier transform it is equivalent to the mean absorbed dose in the distribution, multiplied by the number of pixels. Fourier components further from the center represent waves with steadily increasing wavelengths. Because the absorbed dose example only contains real numbers, the 2D fourier transform obeys Hermitian symmetry. This means that the Fourier components are unchanged when rotating 180 degrees about the center and flipping the sign of the imaginary values. This is useful because it reduces the necessary number of Fourier components by a factor of 2.
If you take a Fourier transform of an image, exclude all the short-wavelength components, and do an inverse Fourier transform, you will recover the original image, but at a lower resolution. The practical significance of this is that the optimization can be performed with just a limited number of Fourier components, which limits the problem to a feasible size. Figures 33a and 33b show the result of reconstructing the absorbed dose example from a limited number of Fourier Components. It is clear that the reconstruction has a lower resolution than the original image, but that the spatial features are all present. The reconstruction also fails around areas where the absorbed dose is discontinuous. This is because the Fourier representation is fundamentally unsuitable for representing discontinuities. The inclusion of discontinuities in the absorbed dose distribution example therefore represent a worst-case scenario for the algorithm.
With a suitable error function and absorbed dose distribution representation, the next challenge is to find a suitable optimization algorithm.

7.1 Optimization Algorithm

The optimization algorithm is composed of five functions that were programmed in Matlab.
The first function, I2FC.m, generates a vector of Fourier components from an image matrix, ordered by their distance from the center. The low indices contain long wavelength components, and the higher indices contain the components of progressively increasing frequencies.
The real and imaginary values of each component are split into adjacent indices, so that the optimization algorithm can work with them. The function assumes that the input matrix only contains real-valued data, so that it can take advantage of the Hermitian symmetry.
The second function, FC2I.m, takes a vector generated by I2FC.m and reconstructs an image from

the Fourier components. The overall resolution of this image is limited by the number of Fourier components in the input vector.
The third function, DFEsum.m, compares a matrix a fluorescence values against the fluorescence that can be calculated from the absorbed dose distribution described by a vector of Fourier components. It takes a vector of Fourier components, uses FC2I.m to generate an absorbed dose distribution, use equation18 to calculate the corresponding fluorescence, and uses equation 19 to compare this with the measured fluorescence. This is the objective function that is used for the optimization algorithm.
The fourth function, GradientDescent.m, is the optimization algorithm. The inputs are an objective function and a starting position for the optimization. It calculates the gradient vector of the objective function at the current position and performs a line search in the direction of the gradient. It does this iteratively until the local minimum of the objective function has been found.
The fifth function, FCGDsolver.m, is a wrapper for DFEsum.m and GradientDescent.m. The inputs are the measured fluorescence, the mean absorbed dose in the desired absorbed dose distribution, the desired number of output Fourier components, an initial vector of Fourier components, the material constants of the polymer, and some options for the convergence criteria of the optimization. The outputs are the optimized Fourier components and a history of the objective function value for each iteration in the optimization.
The code of the five functions are in appendix B.
There are three general classes of optimization algorithms that have been evaluated for use in the optimization. Second derivative methods, first derivative methods and derivative-free methods.
The second derivative methods are variations on Newton's method. They work by calculating the Hessian matrix[20] and the gradient vector of the objective function around the current solution guess, using this to generate a new solution guess.
The problem with this approach is that optimization problems with n variables will have an $n \times n$ Hessian matrix, which can become expensive in terms of memory and computation, if there are many free variables. The problem under consideration here has 45 to 2000 free variables, which is many in this context.
Having many variables will also increase the chance that the Hessian is badly conditioned, which happens if $\text{cond}(\mathbf{H}) = \max(\text{eig}(\mathbf{H}))/\min(\text{eig}(\mathbf{H}))$ is large. In plain language, this is when the second derivatives have sizes at very different orders of magnitude. A badly conditioned Hessian matrix can lead to numerical instability of the optimization algorithm.
Second derivative methods can also fail if the objective function contains saddle points or areas with negative concavity. In practice, the high number of free variables made the second derivative methods unsuitable for the optimization problem, simply because of the cost of calculating the Hessian numerically.
The other extreme was to use a derivative-free method, such as the Nealder-Mead[20] simplex method. This method performs poorly for optimization with many variables, and it converges too slowly for practical use for the optimization problem.
This leaves the first derivative methods, which work by calculating the gradient vector, and then doing a line search in the direction of this vector. Once the local minimum along the line has been found, the gradient is calculated again. No one has published a first derivative method for Matlab, so the following has been constructed:
First the gradient, $\mathbf{v}(\mathbf{x}_0)$, of the objective function is calculated. The step size is then calculated as $d = 0.1 \cdot E(\mathbf{x}_0)/sum(\mathbf{v}^2)$. This step size ensures that the first step is unlikely to go beyond the minimum of the function. The algorithm then takes steps along the gradient, $\mathbf{x}_{n+1} = \mathbf{x}_n + d \cdot \mathbf{v}$, until it has passed the minimum along the line.
The algorithm then uses the last three steps to estimate the position of the minimum, with a second degree polynomial approximation. The objective function is evaluated at this point, and the point with the highest function value is thrown away. A new minimal position is estimated with a second degree polynomial approximation.
The estimate is improved 3 times in this manner, at which point the line search has converged. When the line search has converged, a new iteration begins, with a new gradient and line search.

When the difference between iterations is sufficiently small, the optimization has converged.

7.2 Tests of the Algorithm

When doing nonlinear optimizations like this one, the algorithm must be tested in a number of ways. Does the solution converge reliably towards finite values? Does the objective function decrease for each iteration of the algorithm? Does the algorithm converge towards a single solution when different starting points are used? What is the most reasonable starting point for a given optimization problem? How does the algorithm time to convergence scale with the problem size? How does the memory use scale with problem size? How fast does the final objective function value fall, when the number of Fourier components is increased? These questions are covered in this section. Figures 34a and 34b illustrate how well the algorithm performs for 6 different initial vectors of Fourier components, with the goal being to calculate the absorbed dose example just from the measured fluorescence and information about the mean absorbed dose in the distribution. The vector of zeroes is a sensible starting point for the optimization, since it is unbiased towards positive or negative values for the individual components, and it limits the size of the initial objective function value.
The Fourier components of the measured fluorescence is another good starting point, since the high-frequency components of this must be very similar to the high frequency components of the original absorbed dose distribution. Figure 34a shows that this is indeed the case. The Fourier components of the actual absorbed dose were included to test whether these components are the optimal solution, or if they can be improved upon. The 3 random vectors were included in order to see if the optimization would converge towards a similar output in each case. They were scaled to be similar in magnitude to the fluorescence components.
Figure 34b shows that the different inputs converge with different speeds, but that they all converge towards an almost identical objective function value. The logarithm of the final objective function values only differ on the 5th decimal.
Unexpectedly, the original Fourier components were not optimal, since the optimization managed to find a slightly better set of Fourier components. The difference between the original Fourier components and the optimal solution will probably diminish as the number of Fourier components increase, since the full set of original Fourier components are the unique Fourier transform of the absorbed dose example.
The zero vector starting point converged fast, followed closely by the fluorescence components after 4 iterations. The random starting vectors converged more slowly, but still managed to arrive at the same final error. The fact that all the starting points converged to the same optimum is a good indicator that the local optimum is also the global optimum for this optimization problem. Figure 35a shows that the Fourier components output by the optimization algorithm is very similar to the Fourier components of the absorbed dose example. The objective function also had a lower value for the output than for the Fourier components of the absorbed dose example.
This is another good indication that the algorithm optimizes towards the global minimum of the objective function rather than a local minimum.
Figure 35b shows that the standard deviation on the output vector resulting from 15 different random input vector is also small. One of the inputs to the optimization algorithm is the best estimate of the mean absorbed dose in the image. This input is equivalent to the necessary boundary condition for the exact solution. In the previous examples, the actual mean absorbed dose of the absorbed dose example, 25 Gy, was used as the input. What if a wrong mean absorbed dose estimate is used as the input instead? For the reconstructed absorbed dose in figure 36a an estimated mean absorbed dose of 45 Gy, rather than the actual mean of 25 Gy was used. The resulting absorbed dose distribution still has all of the spatial features of the absorbed dose example, but there is also increasing error from left to right. This is similar to the error that happens when the wrong boundary condition is used in the exact solution.
In figures 36b and 37a this increasing error is illustrated more clearly. Figure 37b illustrates the difference in the absorbed dose distributions made by Fourier components from the optimization

output and from the original absorbed dose example. The differences appear to be larger along the edges and in the interior of the square structures. Figure 38 shows the fluorescence from the absorbed dose example but with added random noise. The noise is uniformly distributed around 0, with a mean magnitude of 1.25% of the mean fluorescence and a maximum magnitude of 5%. This is the same noise characteristics as those used in figure 38, which enables a direct comparison of the two methods. Figure 39 shows how the addition of noise to the fluorescence signal changes the calculated dose. It shows the difference in reconstructed absorbed dose between fluorescence with and without added noise. The optimization algorithm has been demonstrated to converge towards the optimal solution.

How does the optimization scale when the number of Fourier components or the image size is changed? The most computationally intensive part of the optimization is the function evaluations. If there are N_{Fc} Fourier components, then calculating the gradient takes $N_{Fc}+1$ function evaluations. The subsequent line search requires 10 function evaluations. This means that the time for each iteration is linear with N_{Fc}. The required number of iterations may increase also increase with N_{Fc}.

Figure 40a shows that the convergence time for the algorithm is linear with the number of Fourier components. We would expect the final error to decrease with increasing N_{Fc}.

Figure 40b shows that the logarithm of the final error decreases rapidly in the beginning, and the linearly as N_{Fc} increases. The rapid fall in the beginning is probably due to a minimal number of required Fourier components to place a peak at each of the features in absorbed dose example.

The time required for a function evaluation increases linearly with the number of pixels in the image. The memory usage of the algorithm is also dominated by the function evaluations, so this will also scale linearly with the number of pixels in the image.

The number of Fourier components is tied to the final maximum resolution of the image, and since a larger image takes longer to evaluate, it makes sense to rescale the input fluorescence image before running the optimization.

This algorithm could have been created to rescale the input fluorescence data to a size that matches the Nyquist frequency of the shortest wavelength Fourier components in the optimization. This would allow the optimization to converge faster and with a smaller final error. The output image would then have a size that corresponds to the highest resolution that the optimized Fourier components can resolve.

7.3 Section Conclusions

An alternative method for calculating the absorbed dose from the fluorescence was developed. It works by comparing the measured fluorescence against the fluorescence calculated from a candidate distribution of absorbed dose. This candidate dose distribution is represented by a limited number of Fourier components, and the comparison with the measured fluorescence is used to optimize these components. The only necessary boundary condition is the mean dose in the sample and the vertical intensity profile.

This method for finding the absorbed dose distribution works in theory, since the solution converges uniformly to a global minimum. The solutions also appear to be robust against noise in the measured fluorescence. Unfortunately it is too computationally intensive to be performed on a full data set with hundreds of images at full resolution. This method also requires the mean absorbed dose in each image as a boundary condition and this value is problematic to determine in practice. The method is also just as vulnerable to errors in the material constants and artifacts in the samples as the analytical solution described in section 6.

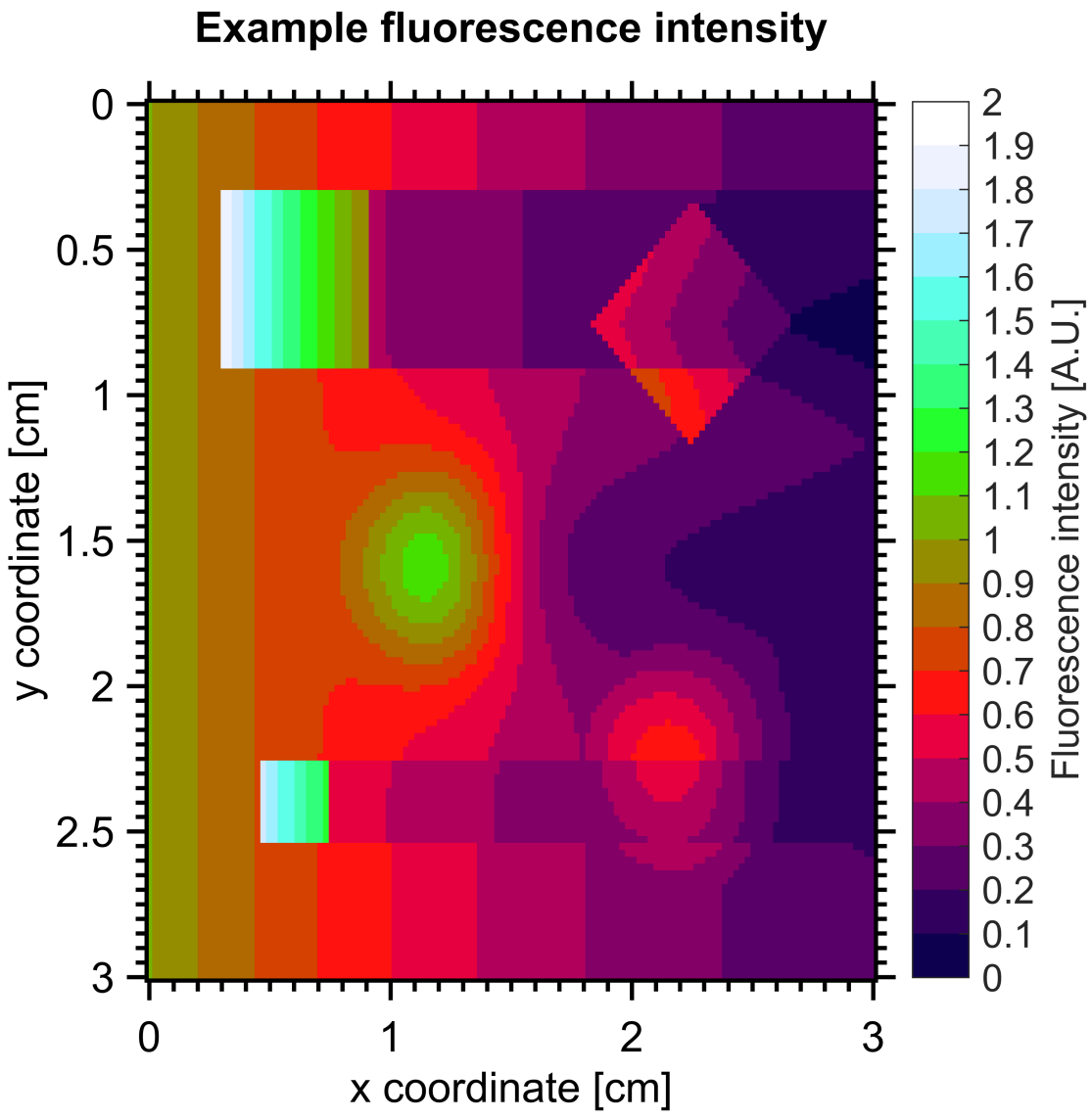

Figure 31: Fluorescence calculated from the absorbed dose distribution example. The fluorescence is linear with the absorbed dose and the excitation light intensity.

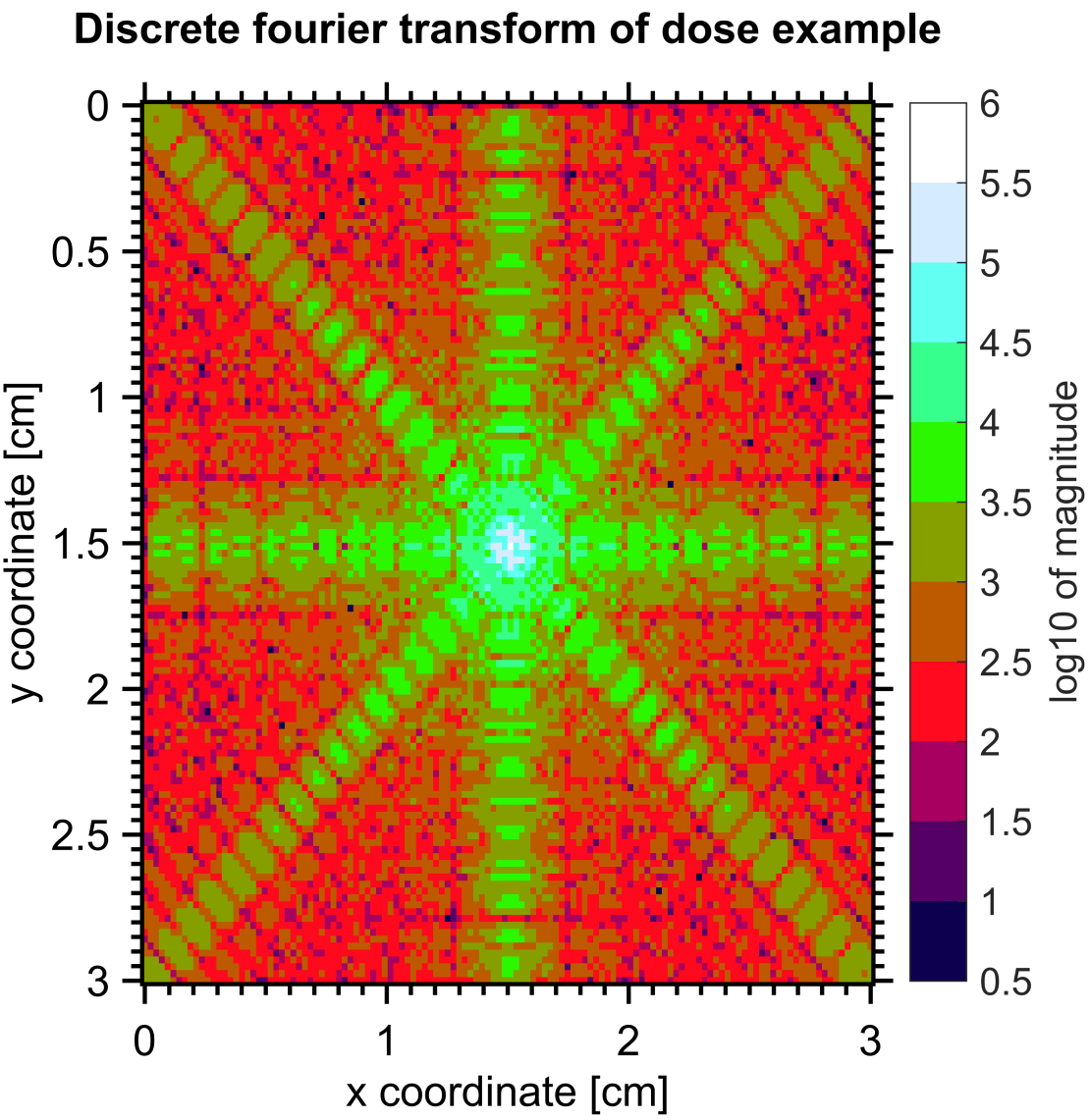

Figure 32: This image shows the logarithm of the absolute value of the Fourier transform of the absorbed dose example. Note how the size of the Fourier components decrease with the distance from the center.

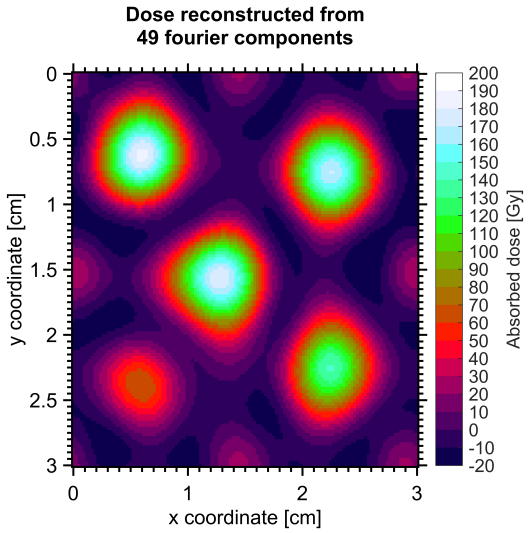

(a) Dose distribution recovered with 49 fourier components.

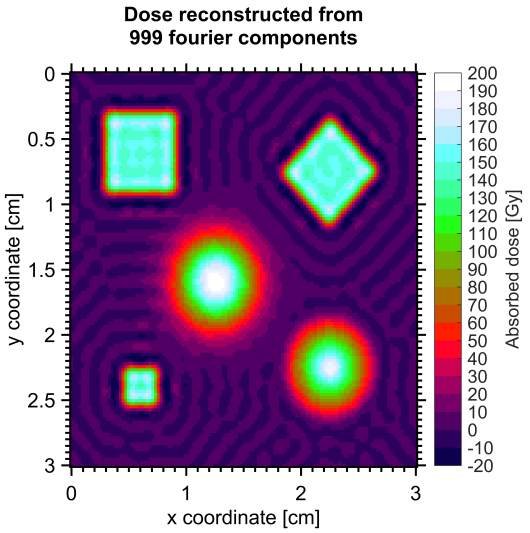

(b) Dose distribution recovered with 999 fourier components.

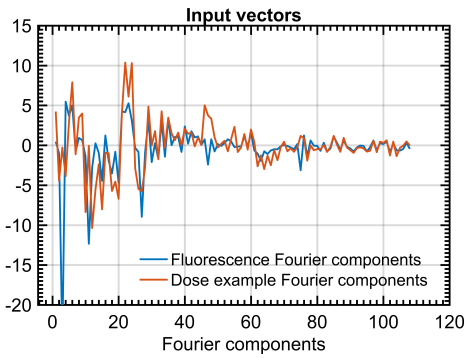

(a) Six different initial vectors of Fourier components for the optimization algorithm. Note that the Fourier components of the absorbed dose example and the corresponding fluorescence are highly correlated, especially for the high frequency components.

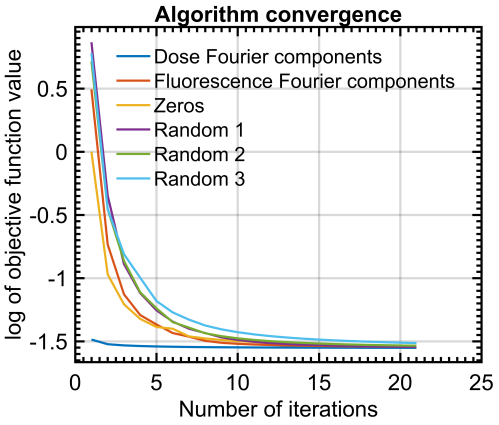

(b) Convergence of the algorithm for the different inputs. The Fourier components from the actual absorbed dose start with a low error, and converge fast. The zero-filled vector comes in second. The Fourier components from the fluorescence also perform well after the first 4 iterations. The random inputs perform worst.

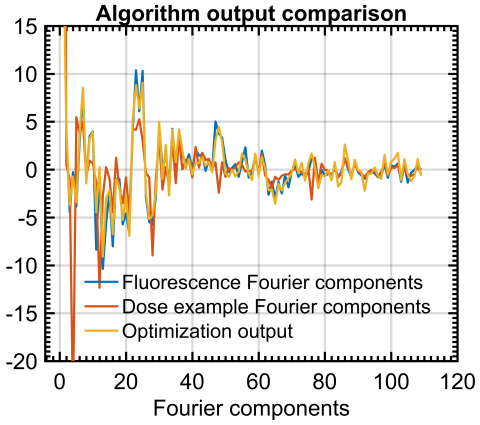

(a) Output Fourier components from the optimization algorithm and the Fourier components of the absorbed dose example. The outputs from the different inputs are visually indistinguishable but not identical. The output and the absorbed dose example are very similar.

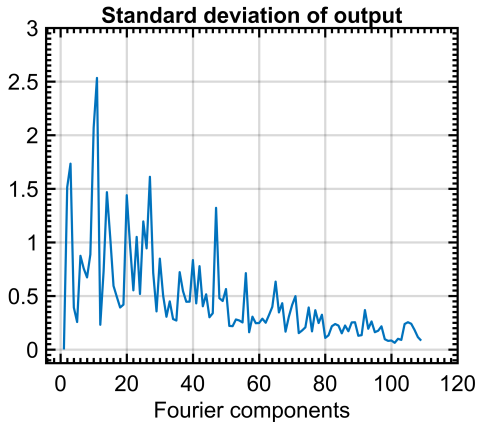

(b) Standard deviation on the output Fourier components with 15 different random input vectors.

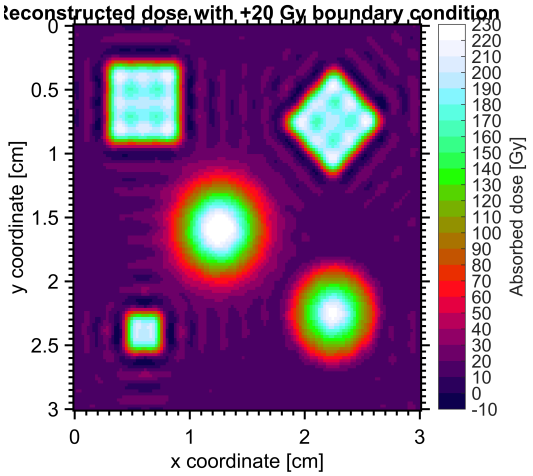

(a) Test of the algorithm output if the given mean absorbed dose is too high. Actual mean absorbed dose is 25 Gy, but the input for this optimization was 45 Gy. The spatial features in the absorbed dose example are all present, but there is an additional component on top.

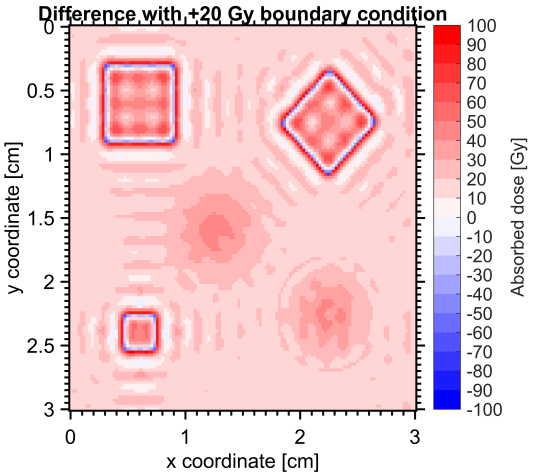

(b) Difference between absorbed dose example and the algorithm output if the given mean absorbed dose is too high. Actual mean absorbed dose is 25 Gy, but the input for this optimization was 45 Gy. The difference increases from left to right, just like if the boundary condition was wrong in the exact absorbed dose solution.

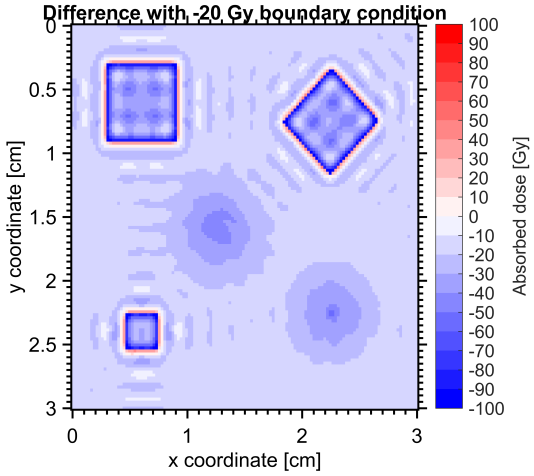

(a) Test of the algorithm output if the given mean absorbed dose is too low. Actual mean absorbed dose is 25 Gy, but the input for this optimization was 5 Gy.

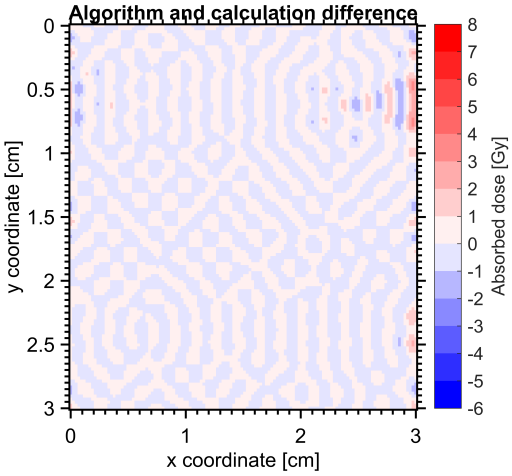

(b) Difference between absorbed dose reconstructed from 889 Fourier components from the absorbed dose example or from the optimization algorithm.

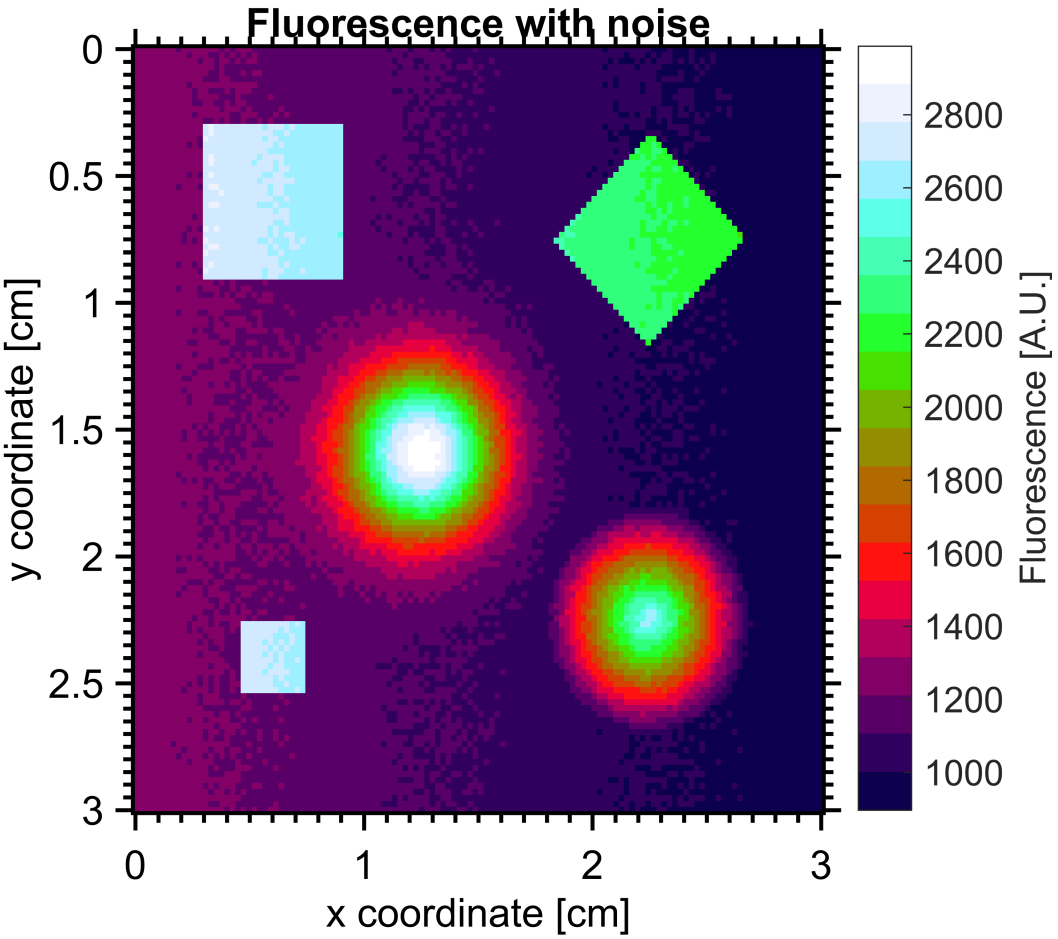

Figure 38: Fluorescence from absorbed dose example with added noise. The magnitude of the difference relatively small, and it has no apparent negative or positive bias. The magnitude does grow from left to right.

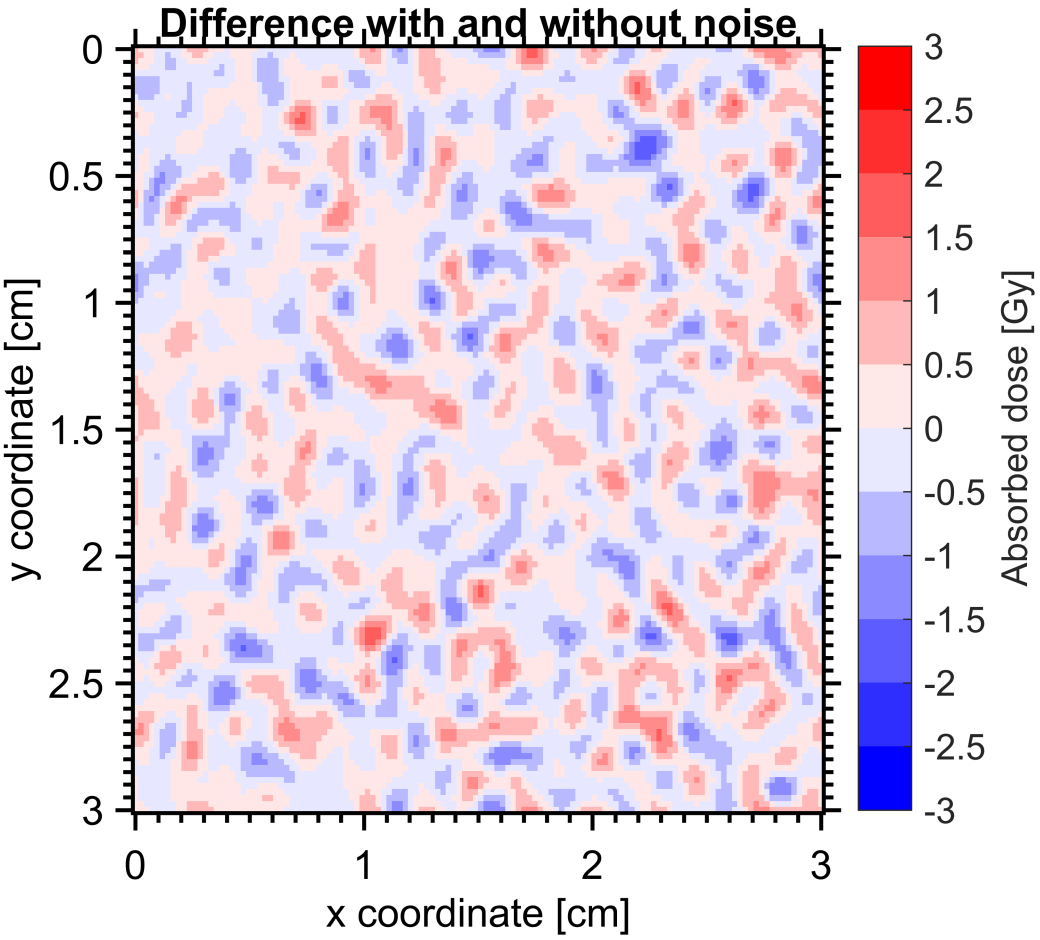

Figure 39: Difference between absorbed dose calculated from fluorescence data with and without random noise. The magnitude of the difference is relatively small, and it has no apparent negative or positive bias. The magnitude does grow from left to right.

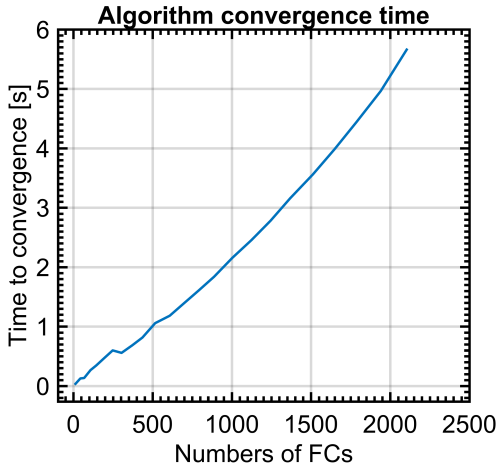

(a) Test of the algorithm convergence time. The convergence time is linear with the number of Fourier components.

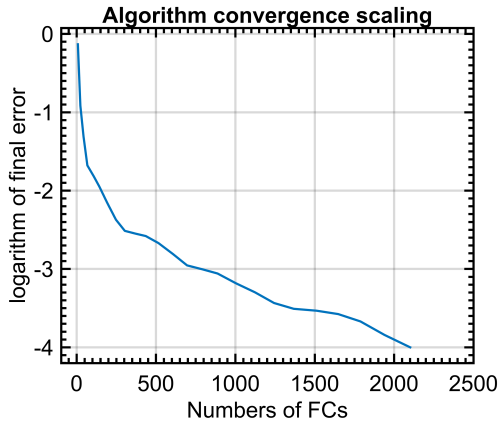

(b) Test of the algorithm final error, for increasing numbers of Fourier components.

8 Detailed Description of 3D Readout Setup Components

This section contains detailed descriptions, characterization and discussion of each component in the 3D fluorescence readout setup. For some of the components, potential alternatives will also be discussed. The components will be discussed in the order that they are listed in section 5.

8.1 532 nm Laser

The 532 nm laser uses a 808 nm diode to pump a Nd:YAG crystal, which then produces 1064 nm light, which is then frequency doubled in a periodically poled KTP crystal to produce the 532 nm light.
The choice of 532 nm was made for following reasons.
It is close to the absorption peak of the dye, and it is sufficiently far from the emission peak of the fluorescence. Furthermore, 532 nm lasers are available with higher powers and better beam quality at a better price than other lasers within the range of suitable wavelengths, which is from about 515 nm to 565 nm, as shown in section 3.
It was also considered using a fiber-coupled laser, but that would have been more expensive with no significant advantage over the mirror.
It is very important that the laser is aligned properly, so that it aims straight through the center of all the lenses, in particular the line generator lens, since this lens has a very small radius of curvature. This renders it extremely sensitive to off-axis beams.
The laser power should be at least 20 mW to assure that there is enough fluorescence for the camera to pick up.
The power stability of the laser is important to ensure agreement between the power monitoring and the fluorescence measurements.
The beam quality is important to ensure good results when generating the light sheet. In particular the wavefront distortion should be low, to ensure a collimated light sheet.

8.2 520 nm Diode Laser

Late in the project, the 532 nm Nd:YAG laser was replaced with a 520 nm direct diode laser, as this laser had better power and spatial mode stability over time.
The transverse mode is a single mode Gaussian, but the design of the diode makes the laser inherently astigmatic.[26] This means that the divergence angles, focal points and spot sizes of the x- and y-axes are different. The axis with tighter focus and therefore higher divergence angle is called the fast axis of the laser.
In other applications this difference in focal distance and spot sizes might have been a problem, but shaping the laser into a light sheet is just a very extreme form of astigmatism, so this feature of the laser was just incorporated into the setup. This was done by rotating the laser so that the fast axis is vertical and aligned with the light sheet generating lens.

Laser Beam Quality

The quality of the laser beam is an important parameter for the performance of the 3D setup. There are many different ways to quantify the quality of a laser beam, depending on the intended application, but in this case the beam should be as narrow as possible, at a distance of at least 20 cm from the nearest lens. The beam should also diverge as slowly as possible.
The general shape of a laser beam is given by a linear combination of the solutions to the Helmholtz wave equation in the paraxial approximation regime[28]. One family of solutions are the Hermite-

Gaussian beams which have the general formula:

$$\mathbf{E}_{mn}(x,y,z) = E_0 \cdot \frac{w_0}{w(z)} \cdot H_m\left(\frac{x\sqrt{2}}{w(z)}\right) \cdot H_n\left(\frac{y\sqrt{2}}{w(z)}\right) ... \tag{21}$$

$$\exp\left(-(x^2+y^2)\left(\frac{1}{w(z)} + \frac{ik}{2R(z)}\right) - i(kz + \psi(z)(m+n+1))\right)\mathbf{x} \tag{22}$$

$$w(z) = w_0\sqrt{1+(z/z_R)^2} \tag{23}$$

$$R(z) = z(1+(z_R/z)^2) \tag{24}$$

$$\psi(z) = \arctan(z/z_R) \tag{25}$$

$$z_R = \frac{\pi w_0^2}{\lambda} \tag{26}$$

Where w_0 is the beam waist radius, $w(z)$ is the spot size at longitudinal distance z from the beam waist, $R(z)$ is the wavefront radius of curvature, $\psi(z)$ is the Gouy phase shift, z_R is the Rayleigh length, $k = 2\pi/\lambda$ is the wave number and $H_k(x)$ is the k'th physicists Hermite polynomial.
In this case the fundamental mode with $m = n = 0$, also called the TEM00 or gaussian mode, is the best approximation to the beam generated by the lasers used in the 3D setup.
Because of this, the quality of a laser beam can be characterized by how much it deviates from this ideal. An appropriate method is to measure the size of the beam at the beam waist and the divergence angle of the beam far from the beam waist. The ideal beam waist can then be calculated from the divergence, and compared to the measured beam waist. Since the intensity rather than the electric field is measured, there is a need to calculate the intensity distribution for a TEM00 beam. This is given by the evaluating the Poynting vector of the electromagnetic field. This is made easier by the facts that $H_0 = 1$ and that the magnetic field is given by:

$$\mathbf{H}(x,y,z) = \mathbf{y}E_x(x,y,z)/\eta_0 \tag{27}$$

Where η_0 is the impedance of free space. With this the Poynting vector can be evaluated as

$$I(x,y,z) = \frac{|\Re(\mathbf{E}\times\mathbf{H}^*)|}{2} = \frac{|E(r,z)|^2}{2\eta_0} \tag{28}$$

$$= I_0\left(\frac{w_0}{w(z)}\right)^2 \exp\left(\frac{-2(x^2+y^2)}{w(z)^2}\right) \tag{29}$$

Measurement of the Beam Quality

A measurement of the beam quality was performed by using a Spiricon m2-200s beam scanner. The instrument used the 4σ method to determine the beam quality, but in hindsight it would maybe have been more appropriate to use the $1/e^2$ method. The 4σ method treats the beam profiles as probability density functions, from which the mean and the standard deviation can be calculated. The beam width is then 4 times the standard deviation.
In the $1/e^2$ method, the beam width is simply the distance from the beam center where the intensity has fallen to $1/e^2 \approx 0.135$ of the maximum intensity. The 4-sigma method gives a higher weight to the tails of the intensity distribution, and therefore tends to give slightly larger M^2 values.
The quality of the 532 nm diode pumped Nd:YAG laser, which was the primary laser in the 3D setup for the majority of the project, was measured. And so was the beam quality of two 520 nm direct diode lasers, to see if one of them could adequately replace the 532 nm laser in the 3D setup. One of the direct diode lasers was primarily part of the fluorescence setup, while the other was selected to replace the YAG laser in the 3D setup. The beam parameters returned by the beam scanning program are given in table 5. It can be seen that the beam qualities of all three lasers are good, with $M^2 < 1.2$ for all lasers along both the x- and y-axes. In figure 41 you can see the spot size measurements that the beam quality was calculated from. Notably, the spot sizes and angles

Table 5: Beam parameters and qualities for the different lasers for each optical axis.

Laser	w_0 [µm]	θ_d [mrad]	M^2
YAG x	296	2.68	1.17
YAG y	343	2.24	1.14
Diode 1 x	1911	0.37	1.07
Diode 1 y	1029	0.66	1.03
Diode 2 x	784	0.88	1.05
Diode 2 y	672	1.19	1.21

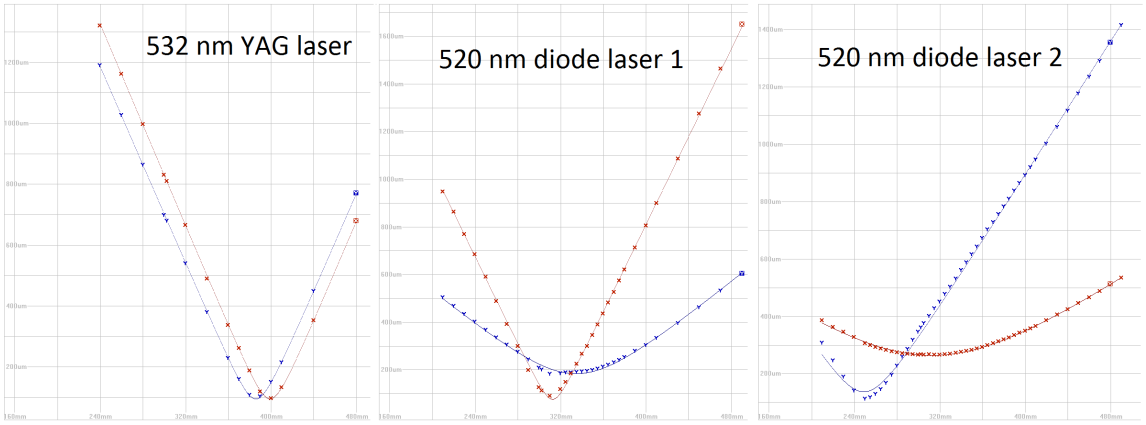

Figure 41: Spot size as function of distance for the three lasers along both x- and y-axis. The YAG laser is only slightly astigmatic, while the two diode lasers are highly astigmatic by design. This is why the beam quality must be characterized separately for each axis.

do not appear to conform to the numbers reported by the beam scanner software. This means that the actual beam quality calculation is opaque, so that the numbers provided by the program must be trusted.
The curve fitting also appears to be slightly inaccurate for the fast axis of the two diode lasers, which means that the reported beam quality may be slightly different from reality.
In conclusion, the beam quality is good for all lasers, so the direct diode laser is therefore a suitable replacement for the YAG laser in the 3D setup. This is good since the 520 nm diode laser has a much better power and mode stability over time, as shown in section 9.1.

8.3 Alignment Mirrors and Irises

The alignment of the laser was done with two protected silver mirrors on kinematic mirror mounts, all from Thorlabs. The alignment of the first mirror adjusts the position of the laser on the second mirror and the first lens. The second mirror controls the direction of the beam through the lenses. If the mirrors are too close to each other, the adjustments to the position and direction will not be independent of each other.
The alignment was checked by including two irises in the setup, positioned before and after the 4f lens configuration. The alignment procedure was:

1. Make a rough adjustment of the first mirror, so that the laser hits the middle of the second

mirror.

2. Adjust the second mirror so the laser hits the center of the second iris.
3. Adjust the first mirror to make the laser hit the center of the first iris.
4. Adjust the second mirror again to make the laser hit the middle of the second iris.
5. Repeat as necessary.

This procedure ensures that the laser goes straight through the center of all the lenses in the 3D readout setup. This is important to ensure that the beam quality of the laser remains as high as possible.

8.4 Beam Splitter and Power Meter

In the 3D setup, the power of the excitation laser was monitored. Monitoring the laser power is important in order to normalize the measured fluorescence relative to the power of the excitation laser. Even if the laser is slightly unstable, power monitoring can be synchronized to the exposure of each image, which allows each image to be normalized to the same standard.
The power monitoring was done by using a 10/90 beam splitter to split off 10% of the laser power, and this light was then measured with a Thorlabs S120C power meter. When measuring the power of a laser, the power density limitation of the power meter, 20 W/cm^2, must not be exceeded. The power meter was therefore placed sufficiently far from the beam waist of the laser.
Another possible solution is to place a convex lens with a short focal length between the beam splitter and the power meter, followed by a suitable lens tube, to make sure the intensity of the laser spot on the power meter is not too high.
The power meter was controlled by the same Labview program as the camera and the z-stage in the setup, through drivers and Labview VIs downloaded from the Thorlabs web page.
A viable alternative to the beam splitter cube would have been to use a beam sampler[2], which would have split off a smaller portion of the laser power. Using a beam sampler would also displace the beam, so it should have been placed before the mirrors in the 3D setup. The beam splitter cube was chosen because it was easier to incorporate into the cage system of the fluorescence setup and the 3D setup.

8.5 Laser Beam Rescaling

The width of the laser beam in the sample is the limiting factor for the resolution in the z-direction of the 3D scan. The laser was therefore rescaled and collimated with a 4f lens configuration.
A 4f lens configuration consists of two convex lenses with different focal lengths, f1 and f2, and it rescales the size of the beam waist by the ratio of the two focal lengths. The lenses used in the setup are achromatic doublet lenses with focal lengths of f=100 mm and f=19 mm, anti-reflection coated for 400 nm to 700 nm. The choice of these achromatic doublets enables the laser wavelength to be changed without needing to switch the lenses. Achromatic lenses also minimize spherical aberration[6], which helps to maintain the optical quality of the laser beam.
All the lenses used in the 3D readout and fluorescence measurement setups were anti-reflection coated for 400 nm to 700 nm.
The first lens is placed one focal length, f1, from the beam waist of the original beam. The next lens is placed at a distance of f1+f2 from the first lens, and the rescaled beam waist will then be at a distance of f2 from the second lens.
In the 3D setup the beam from the laser was not initially perfectly collimated, and it was not possible to position the lenses close to the laser, due to the inclusion of the positioning mirrors. The distance between the two lenses was therefore adjusted slightly so that the final beam was

[2]Thorlabs, product BSF10-A

collimated.
Due to the distances and wavelengths involved in the setup, a beam waist much og about 0.5 mm at the sample is the most practical, as shown in section 8.5.

Ray Transfer Matrix Calculation for the 4F Lens Configuration

The propagation of a Gaussian beam through an optical system can be calculated by using ray transfer matrices[28]. This is accomplished by defining a complex beam parameter.

$$\frac{1}{q} = \frac{1}{R} - \frac{i\lambda_0}{\pi n \omega^2} \tag{30}$$

where $R(z)$ is the radius of curvature for the wavefronts of the Gaussian beam, disregarding the Gouy phaseshift[28], and ω is the 1/e radius for the electric field.
If the paraxial approximation is fulfilled, as is usually the case for propagation of a laser beam, an optical system can be characterised by a ray transfer matrix. Each optical element can be represented by a 2x2 matrix, and the total ray transfer matrix is all of these matrices multiplied together.
The matrix for propagating a distance d through air is

$$M_p = \begin{bmatrix} 1 & d \\ 0 & 1 \end{bmatrix} \tag{31}$$

and the matrix for a thin lens with focal length f is

$$M_l = \begin{bmatrix} 1 & 0 \\ -1/f & 1 \end{bmatrix} \tag{32}$$

So the ray matrix for air-lens-air would be

$$M = \begin{bmatrix} A & B \\ C & D \end{bmatrix} = M_{p2} \cdot M_{f1} \cdot M_{p1} = \begin{bmatrix} 1 - \frac{d_2}{f_1} & d_2 + d_1\left(1 - \frac{d_2}{f_1}\right) \\ -\frac{1}{f_1} & 1 - \frac{d_1}{f_1} \end{bmatrix} \tag{33}$$

The Gaussian beam parameters after propagation through the system can be calculated as

$$\frac{1}{q_2} = \frac{C + D/q1}{A + B/q_1} \tag{34}$$

The optical system in the 3D measurement setup consists of a laser, followed by a 4F lens system to resize and position the beam waist, followed by a cylindrical lens that creates the light sheet. It is the beam waist after the 4F lenses that determines the thickness of the light sheet, and therefore also the z-resolution of the 3D measurements. The focal length of the cylindrical lens and the size of the sample determine at which distance the beam waist should be positioned, since the light sheet must cover the entire sample. The propagation of the beam from its origin at the laser through the two lenses and on to the sample can be calculated from a propagation matrix composed of 5 elements. air-lens-air-lens-air.
The resulting $ABCD$ coefficients for this 4F lens system have been calculated with the symbolic math program Maple, and the values are:

$$A = 1 - \frac{d_3}{f_2} - \left(d_3 + d_2 \cdot \left(1 - \frac{d_3}{f_2}\right)\right) \cdot \frac{1}{f_1} \tag{35}$$

$$B = d_3 + d_2 \cdot \left(1 - \frac{d_3}{f_2}\right) + d_1 \cdot \left(1 - \frac{d_3}{f_2} - \left(d_3 + d_2 \cdot \left(1 - \frac{d_3}{f_2}\right)\right)/f_1\right) \tag{36}$$

$$C = \frac{-1}{f_2} - \left(1 - \frac{d_2}{f_2}\right)/f_1 \tag{37}$$

$$D = 1 - \frac{d_2}{f_2} d_1 \cdot \left(\frac{-1}{f_2} - \left(1 - \frac{d_2}{f_2}\right)/f_1\right) \tag{38}$$

These coefficients can be put into equation 34 to get the new beam parameters after the lens system. The aim is to get an expression where the second and third distances are the variables, and the beam width is the output.
After evaluating this expression numerically for a range of values of d2 and d3, it is possible to find the minimum beam width for each value of d2, and the d3 value that corresponds to this beam waist. To be a viable solution, the beam waist should be around 50 cm from the second lens.
This is because the sample must be sufficiently far from the light sheet generating lens for the whole sample to be illuminated. This distance will therefore depend on the size of the sample and on the divergence angle of the light sheet after the lens.
This puts a lower limit on the focal length of the second lens, which in turn puts a lower limit on the width of the beam waist, and therefore the thickness of the light sheet at the sample. In practice, this thickness will always be thicker than predicted by this formula, since the calculations assume that the beam is purely Gaussian, with perfect beam quality, and that the optical system is entirely free of aberrations.
In practice, this calculation was only used to determine which lenses to use in the 4F system.
The initial beam parameters of the 532 nm laser were never measured, since it was very nearly collimated. The 520 nm laser was also not measured, since it had an internal adjustable focus lens. Instead, the distance between the two 4f configuration lenses was adjusted to provide the thinnest possible light sheet at the position of the sample.

8.6 Light Sheet Generating Lens

There are multiple ways to generate a sheet of laser light from a Gaussian laser beam. In this section the methods will be discussed that were considered and tried, and their relative merits will be compared.
In the most simple configuration, the light sheet generating lens is simply a cylindrical lens which spreads out the laser spot along the vertical axis. This method retains the Gaussian shape[28] of the beam, which leads to a distinct intensity profile within the sample. This intensity profile must be compensated for in the data treatment, as described in section 6.
Since the optical part of the setup has no moving parts, this compensation can be done without too many difficulties.
The angular spread of the beam is determined by the focal length of the cylindrical lens.
Another option is to use a prism-like lens called a laser line generator. This type of lens is capable of generating a light sheet with a uniform intensity profile along its entire length, which makes it easier to do the data treatment.
This method does, however, have a number of significant disadvantages.
These lenses require that the input beam has a width that is exactly correct, and they are much more sensitive to slight misalignments than the cylindrical lenses. They also require the input beam to be perfectly Gaussian to work properly. Furthermore, their intensity profile is not entirely uniform, which means that the collected data must still be normalized by the vertical intensity profile.
All the lenses used in the 3D readout and fluorescence measurement setups were anti-reflection coated for 400 nm to 700 nm.
A third option would be to use a galvo scanner and an off axis parabolic mirror to scan a linear laser beam across the sample. This could make it easy to get a flat intensity profile while maintaining a great beam quality.
This solution, however, also has a number of disadvantages. The necessary components would be very expensive, and it would introduce moving parts in the optical part of the setup. Further, the size of the sample would be limited by the width of the off axis mirror. There would also be a concern about the timing of the image exposure and the galvo scanner movement. If an image exposure started or stopped when the laser was in the middle of the image, the image would show a line at this point.
The galvo scanner would therefore have to be timed to the exposure of each camera image in order

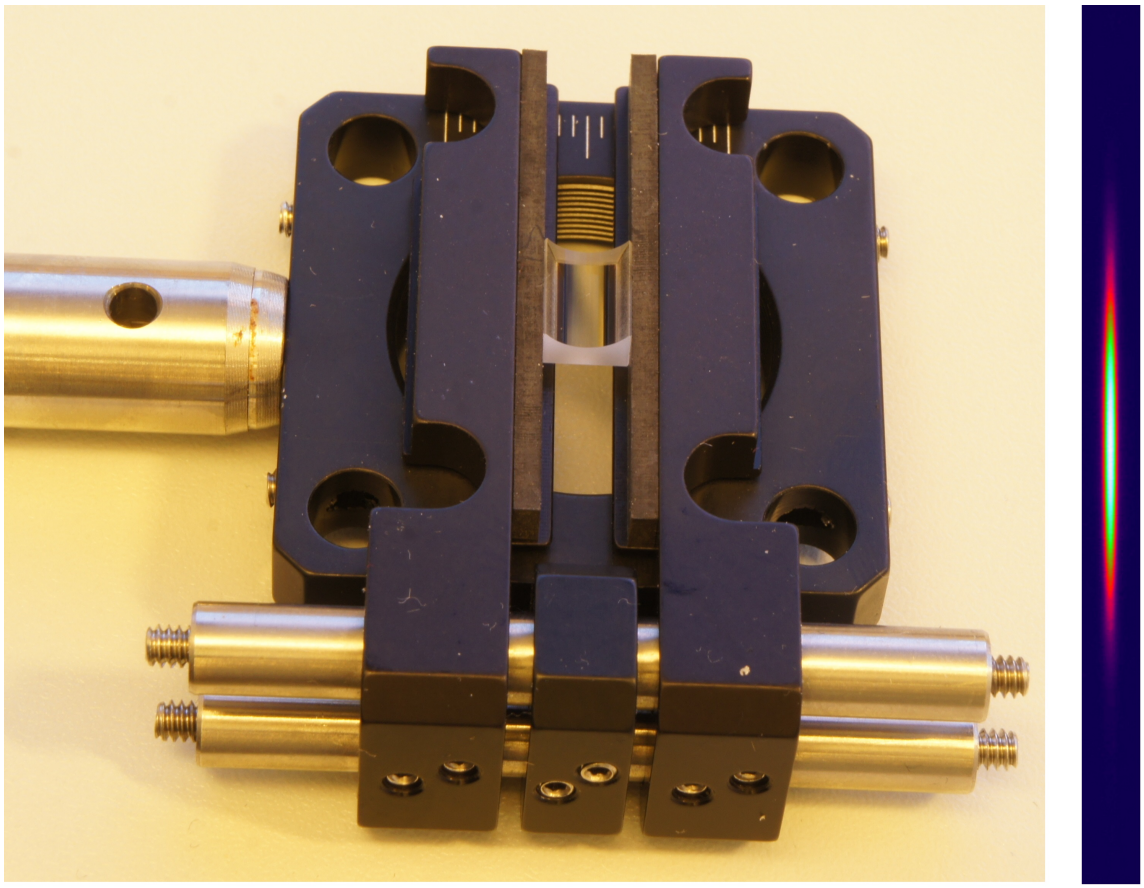

Figure 42: Image of a cylindrical lens, and the resulting line profile.

to avoid lines in the image corresponding to the position of the laser beam at the beginning and end of each exposure. The intensity profile would also not be perfectly flat, due to a nonlinear relationship between galvo scanner position and laser beam height, as detailed in section 8.6.

Cylindrical Lens

The first method was to use a plano-cylindrical lens with a focal length of f=-6 mm, Thorlabs product # LK1087L1-A. This lens spreads the Gaussian beam along the vertical axis, while preserving the collimation along the other axis. The beam still has a Gaussian intensity profile in both directions. The angular spread of the light sheet depends on the focal length of the lens. Lenses with shorter focal lengths will give a wider spread.
There is a choice to use a lens with a negative or positive focal length. It was decided to use a lens with a negative focal length, since this minimizes the angle between the light rays and the lens interface, which also minimizes potential aberrations of the beam profile. The lens with negative focal length was also slightly easier to mount, and decreased the overall length of the optical setup by 2 times its focal length.

Fast Axis Collimator

The angular spread from the cylindrical lens is determined by the focal length, and the focal length of the available lenses was not quite short enough to accommodate samples larger than 1 cm without making the light path excessively long. One solution is to use a fast axis collimator lens, which

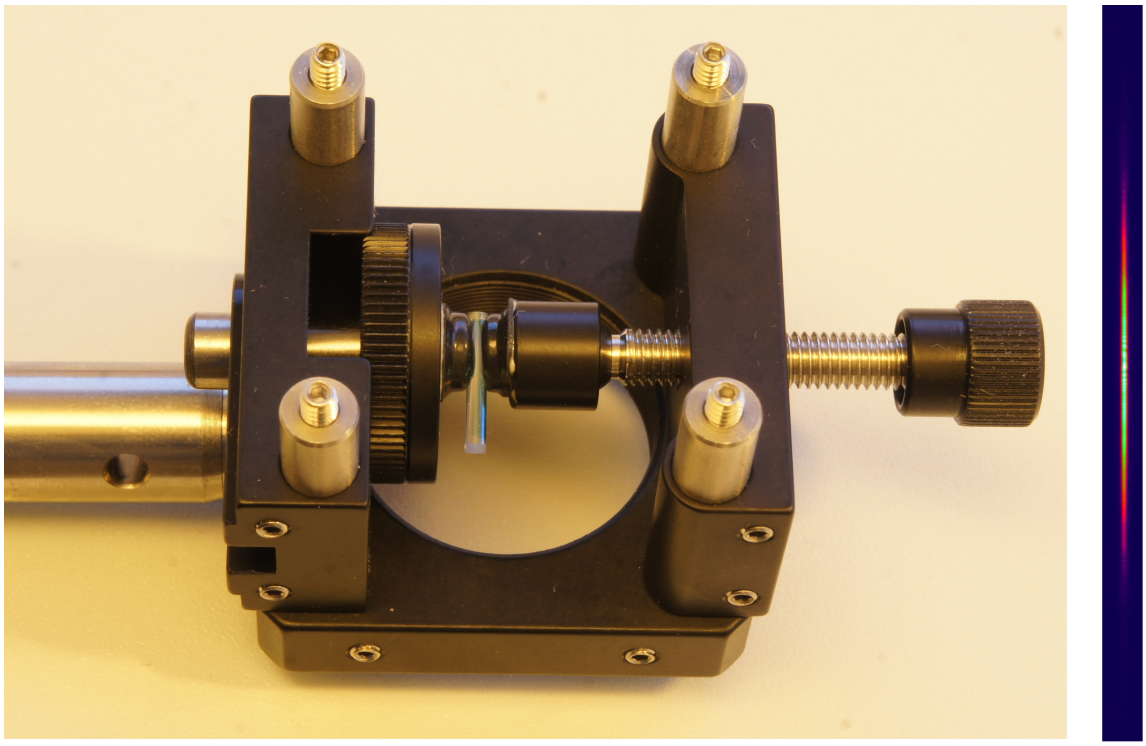

Figure 43: Image of a fast axis collimator lens, and the resulting line profile. Note the interference fringes, which appeared because the beam was wider than the lens.

is basically just a tiny aspherical cylindrical lens with a very short focal length. These lenses are normally used to collimate the output from laser diodes. One of these lenses was tried out in the setup, but the height of the lens was actually smaller than the initial width of the Gaussian beam, which lead to interference fringes in the resulting light sheet, just like what would be seen in a single slit interference experiment.

Laser Line Generator Lens

There are lenses specifically designed to generate laser lines from Gaussian beams, but they require the initial beam to have highly specific parameters in order to generate lines with approximately flat angular profiles. The advantage is that they can generate light sheets with a high angular spread, which allows for illumination of large samples. By choosing a suitable rescaling of the initial laser beam it was possible to generate a satisfactory laser beam with one of these lenses, and the best version of the 3D setup uses one of these lenses.

Light Sheet Collimating Lens

One overarching problem with the use of a single cylindrical lens to generate the light sheet is that the rays in the resulting light sheet are not strictly parallel. This can be a problem when the absorbed dose is calculated from the fluorescence, since this calculation uses line integrals along the light rays. Because of this a large cylindrical lens, LJ1895L1-A from Thorlabs, was included in the setup. It was plano-convex and AR-coated, with a focal length of 15 cm and a height of 10 cm. The height is important, since it limits the height of the resulting light sheet, and thereby also the potential sample size. The lens was placed with its focal point at the line generator lens, in order to collimate the light sheet after the lens.

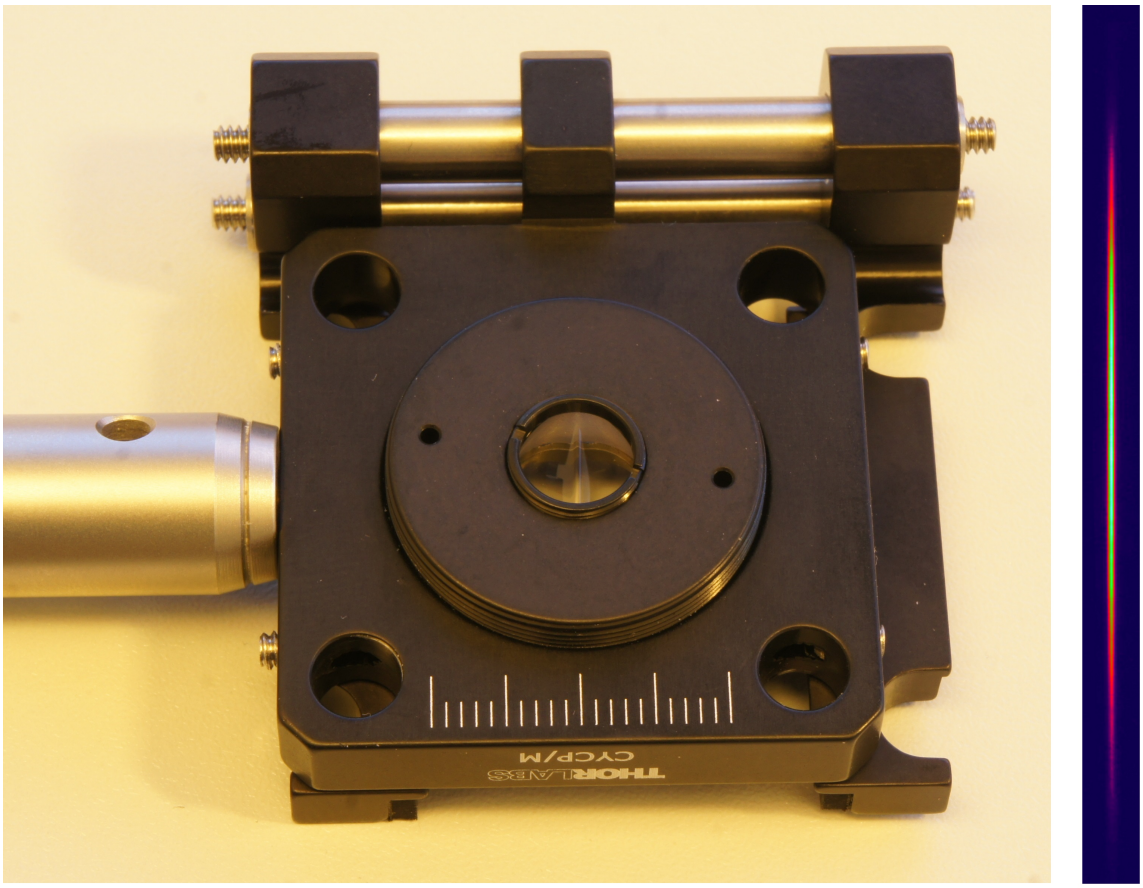

Figure 44: Image of a mounted line generator lens and the resulting line profile.

Off Axis Parabolic Mirror and Galvo Scanner

Another solution to the problem of parallel rays is to use a galvo scanner and an off axis parabolic mirror.
With this approach, the sample would be illuminated by a laser beam that rapidly scans through the sample. The galvo scanner would be mounted at the focal point of the off axis parabolic mirror. This approach would generate perfectly parallel rays, and would allow greater control over the scanning process by adjusting the scan parameters of the galvo scanner. However, there are also a number of serious drawbacks, which is why an implementation of this approach was never tried out.
The scanning of the laser beam would have to be synchronized to the image capture. If the laser beam was in the middle of the sample and moving up at the start of an image exposure, then the upper part of the image would be brighter than the lower part. The same holds for the position of the beam at the end of the exposure. The end result would be an image with three horizontal bands of different brightness.
With a representative triangle wave scan rate of 50 Hz and an image exposure of 1 second, the difference in brightness could be up to 4 percent. If the exposure time is shorter, the difference in brightness will be larger.
There would also be a gradient of brightness in the image, since the galvo scanner would change the beam angle into the off axis mirror at a constant rate, which means that the vertical position of the beam would not change at a constant rate. This gradient depends on the exact configuration

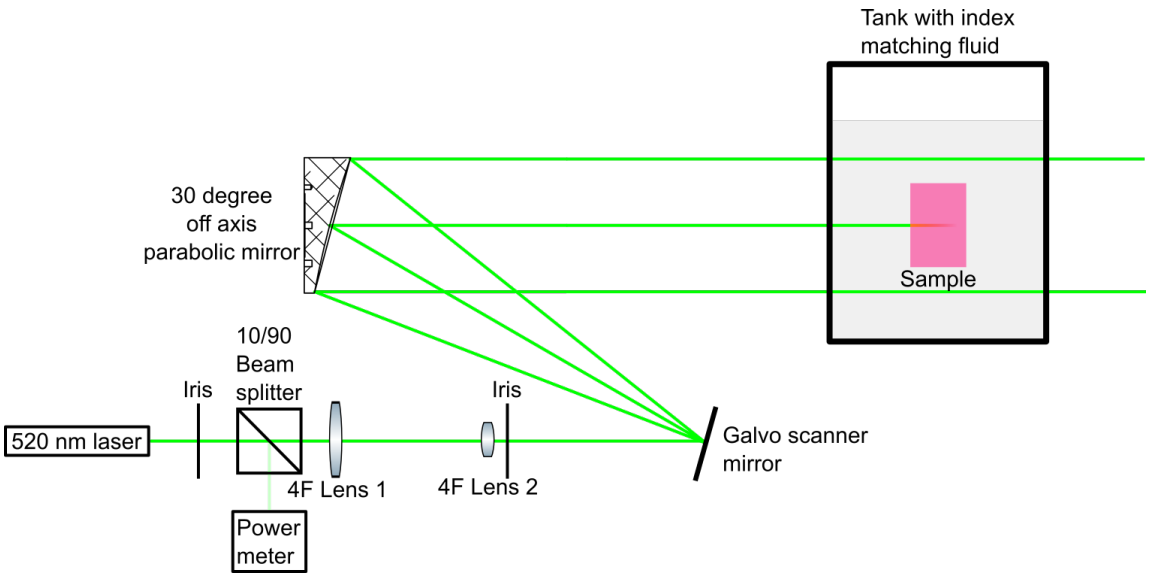

Figure 45: Diagram of hypothetical setup with galvo scanner and an off axis parabolic mirror. The parts with the off axis mirror and the galvo scanner is to scale, the rest is not.

of the setup.
To give a practical example, Edmund Optics sells a 30 degree off axis parabolic mirror with a diameter of 101.6 mm and a parent focal length of $f_p = 304.8$ mm[3], which would be viable in this hypothetical setup. Figure 45 shows how this mirror would be mounted above the initial beam path so that its focal point would be on the beam path. The galvo scanner would then be mounted at the focal point where it could reflect the collimated laser beam onto the mirror. The vertical intensity profile of the illumination provided with the galvo scanner would not be completely homogeneous, even if the mirror scans with a constant rate, as shown in appendix 13. This means that the vertical intensity should still be characterized.

8.7 The Index Matching Fluid

The inclusion of index matching fluid in the 3D readout setup is crucial to prevent the excitation light from being reflected, refracted and scattered at the surface of the sample. It also makes it possible to use samples with arbitrary shapes, which opens up for a large range of applications.

Figure 46 shows the fluorescence from a sample that has been immersed in water, to illustrate the consequences of poor index matching. Water has a refractive index of 1.33 while the sample has an index of 1.49, which means that the excitation and emission light can be refracted and reflected at the surface of the sample. There are also forbidden angles for the excitation light, which means that some regions of the sample are not illuminated at all.

In order for a fluid to be viable as an index matching fluid, it has to fulfil some requirements. The index matching fluid must be transparent and clear to the wavelengths of the excitation light and the spectrum of the emitted fluorescence. The fluid must have a refractive index that is as close as possible to the index of the dosimeter material. The refractive index of the fluid should also be slightly higher rather than slightly lower, to eliminate the possiblity of total internal reflection of the emitted fluorescence light. This requirement can be complicated somewhat if there is a large difference in the dispersion of the two materials.

Figure 48 shows the internal reflection of the emitted fluorescence, as function of its angle relative to the surface of the sample, and the index mismatch between the fluid and the polymer. The white

[3]Product number 83-968

area is the angles with total internal reflection, which is undesired. This is why the index matching fluid should have a refractive index that is slightly higher than the dosimeter material. In most cases, the refractive index of the chosen fluid can be adjusted by mixing it with a different fluid.
The fluid should not react chemically with the dosimeter material, or dissolve it over time. The index matching fluid should be non-toxic to touch, since it is almost impossible to avoid getting into contact with it when working with it. It should not give off any toxic gases.
For dosimeters with refractive index between 1.33 and 1.47, a mixture of propylene glycol or glycerol with water is often suitable, due to the availability and ease of use of these materials. Unfortunately the dosimeter material used in this project has a refractive index around 1.49, and it is also hygroscopic. Because of this a silicone fluid was used as the index matching fluid instead.
The silicone fluid we chose was Dow Corning 550(r) fluid, with CAS 63148-52-7. It is a Poly(dimethylsiloxane-co-methylphenylsiloxane), with a molecular weight of 550 g/mole and a viscosity of 125 centistokes. It has a refractive index of 1.4977 at 20 degrees and an Abbe number of 38. This Abbe number translates into an average dispersion of $^{dn}/_{d\lambda} - 7.6e - 5$ nm^{-1}. It is chemically stable, not toxic, not volatile at room temperature and not hygroscopic.
The refractive index of the polymer was difficult to measure accurately, but it was around 1.49±0.01, with an Abbe number of 52, corresponding to average dispersion of $^{dn}/_{d\lambda} - 5.5e - 5$ nm^{-1}. This should have made the silicone fluid almost perfect for the intended application. Unfortunately, the index matching was not perfect, so several attempts to find a fluid that is miscible with the silicone fluid were made. Figure 49 shows the emulsion that results when two different silicone fluids are shaken together. The two fluids will separate over time. Attempts with water, glycerol and ethanol yielded similar results.
Late in the project, it was discovered that olive oil and Tibelly® baby oil are miscible with the DC550 silicone oil. The baby oil is perfect in this case, because it is clear, colorless, non-fluorescent and it has a refractive index of 1.440, with an Abbe number of 62.

Interference Patterns in Cylindrical Samples

A surprising problem appears when cylindrical samples are put into the setup. The laser light is refracted slightly at the interface between the sample and the index matching fluid, and this refraction causes the laser light to interfere with itself within the sample. These interference fringes are then visible as a pattern in the fluorescence from the sample, caused by destructive and constructive interference of the excitation light. In figure 50 we see such a pattern. These patterns can only appear because a coherent light source is used, and because the refractive index of the sample is very close to that of the index matching fluid.
An attempt was made to remove this interference pattern by inserting a depolarizer[4] into the optical setup. The depolarizer was intended to randomize the otherwise linear polarization of the laser light, which should prevent it from interfering with itself. In order to maximize the randomization of the polarization and to prevent optical damage to the depolarizer, the depolarizer should be positioned to maximize the area of the laser spot on it. Therefore, it was positioned immediately after the line generator lens,. This did not have the intended effect of removing the interference, as can be seen in figure 51, but it did indirectly reveal another interesting optical property of the sample. The fluorescence from the sample was observed to follow the same pattern as the horizontal stripes in figure 51. This is interesting since the stripes come from differences in polarization direction rather than intensity. A possible explanation is that the fluorescent emission from the dye is not isotropic, but that it has a slight preference for being either parallel or orthogonal to the polarization of the excitation light.
The dye molecules are oriented randomly within the sample, so any polarization dependent anisotropy in the emission would have to arise from a polarization dependence in both the excitation of, and the emission from, the individual dye molecules. In effect, a dye molecule with the correct orientation relative to the polarization of the excitation light should be more likely to be excited, and the resulting emission should also have an anisotropic intensity distribution[21].

[4]Thorlabs Microretarder Depolarizer Array, DPP25-A

Table 6: FWHM of the horisontal intensity profiles from the 3 light sheet lenses

Lens	FWHM [mm]	50% width [mm]
Cylindrical lens	0.70	0.51
Fast axis collimator	0.71	0.58
Laser line generator	0.70	0.50

This effect is not usually seen with fluorescent molecules in solution, since the timescale of molecular rotation, 40 picoseconds, is orders of magnitude faster than the typical lifetimes of organic fluorophores, which are 10 ns to 100 ns[14, sec. 1.4.2].
The polarization of the excitation laser also makes a difference for the interference pattern. This was investigated by putting a half-wave plate into the setup and using this to turn the polarization of the excitation laser. When the polarization was turned by 90 degrees, the interference pattern changed, and the new pattern was anti-correlated with the old pattern. This is shown in figure 52.

8.8 Fluorescence Standard

The fluorescence standard is a piece of red plastic[5] that fluoresces orange when excited with green light. The fluorescence response of this plastic is assumed to be constant, although the ambient temperature may make a difference. This makes it a consistent reference against changes in the camera aperture, exposure time and gain settings, as well as changes to the vertical intensity profile of the excitation laser light sheet. Figure 53 shows an image of the fluorescence standard as it is used in the 3D setup. In equation 11, the camera settings and vertical intensity profile would be equivalent to C_{cam} and $I_E(0, y)$ respectively. In theory, this should make it possible to determine the absorbed dose at the beginning of the sample.
The surface of the plastic has good optical quality, but the plastic itself is easy to scratch. The optical quality is important when trying to measure the vertical intensity profile. The refractive index of the plastic is close to that of the index matching fluid. This helps to eliminate losses to reflection and scattering at the surface of the fluorescence standard. This makes the standard more reliable. Figure 54 shows that the emissions spectrum is not dissimilar to the emission spectrum of the dye in the dosimeter. This is another reason why it was chosen for this application. The fluorescence standard is also used in the fluorescence setup to standardize the measurements of the material constants against potential changes in the spatial mode of the excitation laser. To measure the vertical intensity profiles generated by the different light sheet lenses described in section 8.6, the fluorescence standard was suspended vertically from the 3D setup gantry into the field of view of the 3D setup camera. The fluorescence standard was angled 45 degrees with respect to the light sheet/camera image plane, to allow for a measurement of the thickness/horisontal profile of the light sheet. The scaling in the image plane was measured by lowering a ruler into the image plane of the camera and capturing an image. Figure 55 shows the light sheet profiles for the cylindrical lens, fast axis collimator lens and the laser line generator lens. Figure 56 shows that the vertical profiles are considerably less smooth than anticipated. This means that it is absolutely necessary to normalize the fluorescence data from a sample with respect to the vertical intensity profile of the excitation light sheet. Figure57 shows that the horisontal profile/thickness of the light sheet is mostly unaffected by the choice of light sheet lens. The thickness of the light sheet can be characterized by the FWHM of the horisontal profile. Another measure is the width containing 50% of the intensity. These values are in table 6.

[5]Oroglas Aquarelle Red 35%, ref# 800-01170, from RIAS A/S

8.9 The Sample Holder and Z-Stage

Because of the index matching fluid, the samples could potentially be cured into any shape. The samples used in this project were all cured in 1x1x3 cm cuvettes or 1.8 cm diameter cylinders, as shown in figure 58. The samples were mounted in a clamp in such a way that the clamp did not obstruct path of the excitation light sheet or the view of the camera. This clamp was hanging from a gantry mounted on a motorized z-stage[6]. The z-stage was controlled by the 3D setup control software. The fluorescence standard was also mounted in a clamp on the gantry, allowing it to be moved into the path of the light sheet without any manual handling. Figure 59 shows the how the z-stage, gantry and sample holder clamp.
When putting a new sample into the index matching fluid, there are sometimes bubbles sticking to the sample after immersion. These bubbles can be removed with a bit of careful agitation of the sample holder. When the sample is in the light sheet, the fluorescent emission is clearly visible as an orange glow.
The most important aspects of this part of the setup is that the clamp should not obstruct the cameras view of the sample, the gantry should be stable, and the length of the motorized z-stage should be longer than the length of the samples. Due to the movement of the sample, the tank with index matching fluid must be more than twice as long as the samples.

8.10 3D Setup Longpass Filter

Even the small amounts of laser light scattered by imperfections in the sample can confound the emitted fluorescence, partly because most camera CCDs are optimized for green wavelengths. Therefore the laser light must be removed with an optical filter. The cutoff wavelength should be at 550 nm in order to maximize the amount of fluorescence that gets through, while minimizing the laser light.
Optical wavelength filters can be made with colored glass or with thin-film interferometric coatings. Interference filters can be designed to have their cutoff wavelengths wherever desired, but the cutoff will also depend on the angle of incidence. This angular dependence is not a concern, since the camera is positioned relatively far from the sample, so the light from the setup will have shallow angles.
Some filters sold by Thorlabs were considered for these purposes. The available colored glass filter with the right cutoff wavelength were FGL550M and FGL590M, and they were only OD1 and OD2 at 532 nm respectively and this optical density was insufficient for use in the 3D setup.
For this reason, an interference filter was chosen. The filter was FELH0550, also from Thorlabs, with OD5 at 532 nm.
Alternatively, it could have been possible to use an interferometric notch filter at the laser wavelength, but that would require a notch filter for each laser wavelength used in the setup, with no real advantage.
Some optical filters can display autofluorescence when struck by intense light. This is not a concern in this setup, since the filter is only hit by scattered laser light.

8.11 Camera

The camera in the 3D setup was a FL3-U3-32S2M-CS from Point Grey, with a resolution of 2080 x 1552, pixel pitch of 2.5 micrometers, and sensor format 1/2.8".
The camera should be greyscale, without a Bayer filter, because a Bayer filter would block approx. three quarters of the incoming light. It should have high sensitivity and low readout noise. It should be capable of exposures up to at least 1 second, to allow measurements with low levels of fluorescent emission from the sample. The camera should also have good software driver support from the manufacturer, to allow full control over the internal exposure settings from third party

[6]Thorlabs, KMTS50E/M

gain \exposure time	63 ms	250 ms	1000 ms
0	2.7	2.8	3.0
12	6.3	4.4	5.3
24	12.0	10.8	12.7

Table 7: Mean camera dark noise for different integration times and gain settings.

software. This is important since the actual image capture must be coordinated with the movement of the sample stage, which means that both the camera and the stage must be controlled in the same program.
The light gathering ability of the camera was determined to be linear with the exposure time. The gain setting goes from 0 to 24 and the light sensitivity of the camera doubles with every 6. The dark noise of the camera is low, as shown in table 7. This table was generated by acquiring images with the lens cap in place in a dark room, and then counting the average image values for different exposure times and gain settings. These numbers are relative to a maximum of 4096.

8.12 3D Setup Control Program

To simultaneously control the camera, z-stage and power meter in my setup, a program was written in labview.
The program structure is: hardware initialization and configuration - concurrent loops with different purposes - hardware shutdown. The concurrent loops are and their purposes are:

- power meter config: Executes changes in power meter integration time and calibration wavelength.
- z-stage loop: Monitors z-stage position and listens for and executes changes in desired position or velocity of z-stage.
- camera config: Executes changes in camera exposure time and gain.
- power meter readout: Continuously reads the power meters.
- camera image update: updates the image shown as each exposure becomes available.
- image saving: saves an image as black and white PNG when requested. File name contains relevant metadata about the image.
- slow sweep start: sweep across a range of z-positions in the desired number of steps and saving an image for each position.
- fast sweep start: start a continuous sweep across the desired range, while saving the desired number of pictures. Sweep velocity is tailored to the sweep range, number of images and image exposure time.

Figure 60 shows a block diagram of the 3D setup control program. The boxes are the different loops in the program, and their contents describe what they do. The circle contains the important global variables, and the arrows show whether the loops write or read these variables.

PT Grey Camera Start

To ensure optimal performance from the camera, a number of settings must be correctly configured when the camera is started.

1. Auto exposure must be set to off.
2. Auto acquisition framerate must be off.

3. Auto gain must be off.

4. Videomode must be set to 2x2 binning. This typically reduces the read-out noise at the hardware level, at the cost of potential spatial resolution. It also allows us to use a higher framerate for the camera.

5. The pixel format must be set to Mono 12 packed, to get sufficient bit depth for the images. Mono 16 will cause and error.

6. Output image type must be set to grayscale (U16).

7. TriggerSelector: Frame Start.

8. TriggerMode: Off.

9. TriggerSource: Software.

10. ExposureMode: Timed.

Image Update

This function retrieves the latest image from the camera and displays it on the front panel.

Camera Exposure Configuration

This function controls the camera exposure through a Sub-Vi function. The inputs are the camera reference, the framerate (1-21 HZ) and the gain (0-24). The exposure time must be calculated as 999/framerate, or an error will occur. Increasing the gain by 6 will double the image brightness, at the cost of increased image noise. The gain, exposure time and framerate are updated simultaneously to avoid errors. An exposure factor, $EF = \text{Framerate}/2^{\text{Gain}/6}$, is calculated from the gain and the framerate. The saved images can be multiplied with their exposure factor to evaluate their brightness relative to an image with framerate=1 Hz and gain=0. This does not take the brightness of the excitation laser or the aperture of camera lens into account. The aperture opening is evaluated relative to full opening and the excitation laser power is monitored continuously and saved in the file name of each picture.

Z-Stage Control

This function monitors the current z-stage position and whether the stage is currently moving. It also registers changes in the position and movement speed of the z-stage and executes these changes.

Power Meter

This function changes the power meter configuration and reads out the latest power measurement. The settings are the averaging time, 30 ms to 1000 ms, and the calibration wavelength, 400 nm to 1100 nm. The sensitivity is wavelength dependent, so the power meter must be calibrated to the wavelength of the excitation laser.

Image Saving

This function saves the latest image with a name that contains a user defined name along with the z-position, power meter reading, exposure time, framerate, gain and exposure factor. The images will be saved in a parent folder chosen by the user. This loop also automatically creates a new folder, when the user defined image name is changed.

Slow Sweep

The user can define a sweep that goes from one z-stage position to another in a number of discrete steps, and this function will execute the sweep while saving an image at each step. At each step the stage will move to the new position, wait for the stage to stop moving, wait for one exposure time, and then save the acquired image.

Fast Sweep

This function takes the sweep parameters from the slow sweep, and use them to define a fast sweep, where the z-stage moves continuously while saving images whenever the stage reaches a new step. The velocity of the z-stage will automatically be changed to allow enough time for one exposure for each step. To ensure that the z-stage speed is consistent throughout the sweep, the sweep is initiated and stopped 2 mm beyond the first and last steps. This allows the z-stage to accelerate to a constant speed before the first image is captured.

Program Limitations

Due to the necessity of direct simultaneous control of the camera, z-stage and power meter, the program uses Labview drivers to control the devices. Unfortunately, the camera control drivers were poorly documented, so it was not possible to use the full potential of the camera. The framerate is locked to the exposure time, due to a bug/undocumented feature in the labview drivers, and the framerate is locked between 1 Hz and 21 Hz, even though the camera is capable of 60 Hz in its native program. I also had to use 2x2 pixel binning in order to get to 21 Hz. This has the effect of improving the image noise at the cost of reduced resolution.

Program Development

During development, the design of the program underwent a few iterations. In the first iteration, the structure of the program was basically initialization-¿ main loop-¿ shutdown. In the main loop, commands to each of the devices were executed sequentially. The sequence was motor positioning, power meter readout, camera image read, optionally save an image. In the current structure each of the devices are executing their functions on independent loops. This makes the program a lot more responsive, and it is easier to program new features, since measurements and commands can be done with local variables.

8.13 Section Conclusions

The beam quality of both lasers used in the 3D setup is close to perfect. This means that the width of the laser light sheet is generally limited by the optical design of the setup and/or by the quality of the optical elements.
The use of a 520 nm direct diode laser is best for the 3D readout setup. It has high power, good power stability, good beam quality and good spatial mode stability. The only downside is the inherent astigmatism, which requires the fast axis to be aligned with the light sheet lens in the setup. In contrast, the 532 nm Nd:YAG laser had poor power stability and spatial mode stability.
The mirrors should be positioned so that, mirror 2 is close to iris 1, and mirror 1 is far from mirror 2. This will ensure that mirror 1 controls the positioning of the beam on the lenses, while mirror 2 controls the angle through the lenses. The mirrors should also be adjusted so that the beam passes through the center of the lenses in the setup.
The power meter monitors the power output of the laser during scanning of the samples. These power measurements are necessary to normalize the images of the fluorescence from the samples and the fluorescence standard.
The 4f lens configuration was used to rescale the laser beam. After the rescaling, the beam should have a waist size of between $w_0 = 0.12$ mm and $w_0 = 0.41$ mm, which will give a Rayleigh lengths

of about $z_R = 0.1$ m and $z_R = 1$ m. The distance between the 4f lenses is adjusted to position the beam waist at the position of the sample in the setup.
For the light sheet, the laser line generator lens is the best of the three lenses that have been evaluated. With this lens, the vertical intensity profile is homogeneous within +/- 10% across the field of view of the camera. This inhomogeneity means that the vertical intensity profile must be characterized. There was an unexpected problem with the use of a light sheet, namely the appearance of interference fringes in cylindrical samples, as described in section 8.7. This self-interference of the excitation light would be avoided if a setup with a galvo scanner and an off-axis parabolic mirror was used instead. This solution would make the setup and the setup software more complicated. The galvo scanner would need to be synchronized to the image acquisition to avoid stripes in the images.
The refractive index matching with DC550r fluid is not perfect, and the addition of baby oil to lower the refractive index of the silicone oil did not help. It appears as if the index of the dosimeter material is higher than the index matching fluid for red wavelengths and lower for green and blue. This might happen because the DC550 fluid has a fairly high dispersion. The imperfect matching is not high enough to visibly refract the excitation light, but it does lead to total internal reflection of the emitted light.
This internal reflection disappears if the sample is angled so that the emitted light does not hit the surface of the sample at angles below 15 degrees on the way to the camera.
There are also interference patterns in the cylindrical samples. These patterns did not appear to change with different concentrations of baby oil. This means that the interference is probably not caused by refraction of the excitation light at the surface, but rather by bending of the excitation light due to a gradient in the refractive index of the polymer sample.
This implies that the refractive index of the polymer could depend on something in the curing process. If the refractive index is not well-defined at the micrometer scale of the polymer, then this could also cause the internal reflection of the emission.
Such an ill-defined refractive index would also explain why the refractive index of the polymer could not be measured with a refractometer, despite using samples with flat surfaces and high optical quality. There is another Polyphenyl-methylsiloxane fluid, CAS 63148-58-3, with more phenyl groups than DC550 fluid, which has a higher refractive index around 1.55. It is available with a range of different viscosities, and the lowest viscosity is probably easier to work with in terms of bubbles and potentially for mixing. This fluid might be a candidate for testing as an index matching fluid with the dosimeter material.
The fluorescence standard makes it possible to characterize the vertical intensity profile and changes in the camera settings. This characterization is easy and reliable to perform. This means that the collected fluorescence data for a sample can be normalized with respect to the vertical intensity profile, and that a boundary condition for the absorbed dose reconstruction can be calculated rather than assumed/guessed, if the material constants of the sample are known and the dosimeter material has been characterised.
The motorized stage must have a travel that is longer than the length of the samples. The tank with index matching fluid must be more than twice as long as the samples. The clamp holding the samples must not obstruct the view of the sample from the camera. The optical filter should be a longpass interference filter with a cutoff wavelength at least 10-15 nm above the wavelength of the excitation laser, depending on the quality of the filter. For large or highly irradiated samples, the cutoff wavelength can also be chosen to minimize the spectral overlap between the absorbance spectrum of the polymer and the emission spectrum of the fluorescence. This would eliminate the potential problem of re-absorption of emitted fluorescence in the sample.
The camera had no problem imaging the fluorescence fluorescence emitted by the samples. This suggests that there is no pressing need to invest in cameras with better sensitivity. The camera has low level of dark noise, which mostly depends on the gain level. At high gain levels, there are hot pixels that can lead to artefacts in the images. These hot pixels should be identified and calibrated for. A better camera could potentially be swapped in, particularly if it has better software support.
The setup control software coordinates the movement of the z-stage, the acquisition of fluorescence

images, and the monitoring of the excitation laser power. There were aspects of the camera control which were never fully understood and could potentially be improved upon. The exposure time could never be increased beyond 1 second or below 1/21 second. It was also necessary to use 2x2 pixel binning to get the maximum framerate up to 21. Improving or rewriting the camera controls should be a priority if the project is continued.

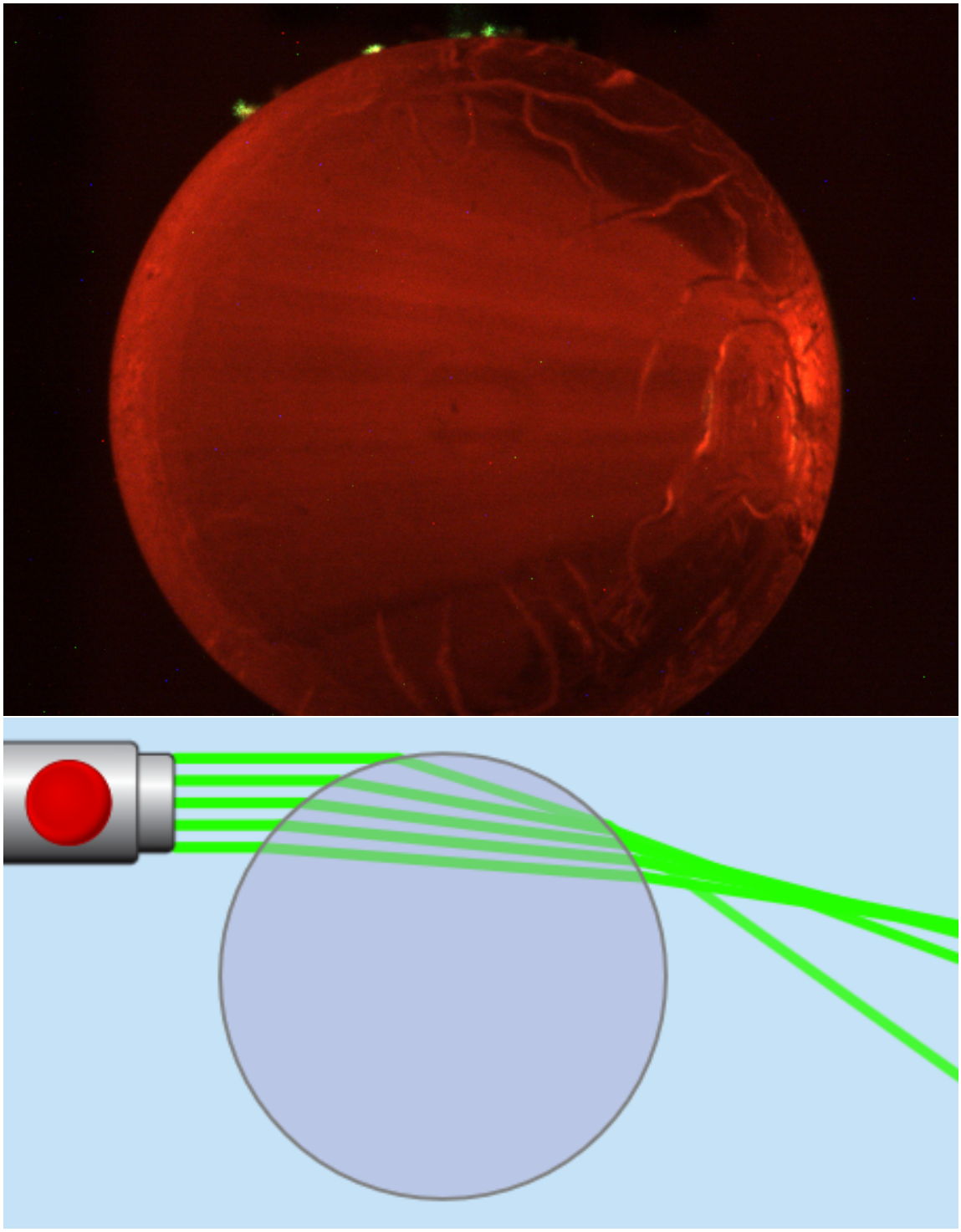

Figure 46: A sample immersed in water with a light sheet being refracted through it, along with a ray-tracing diagram showing the same situation. Note the refraction of the excitation light.

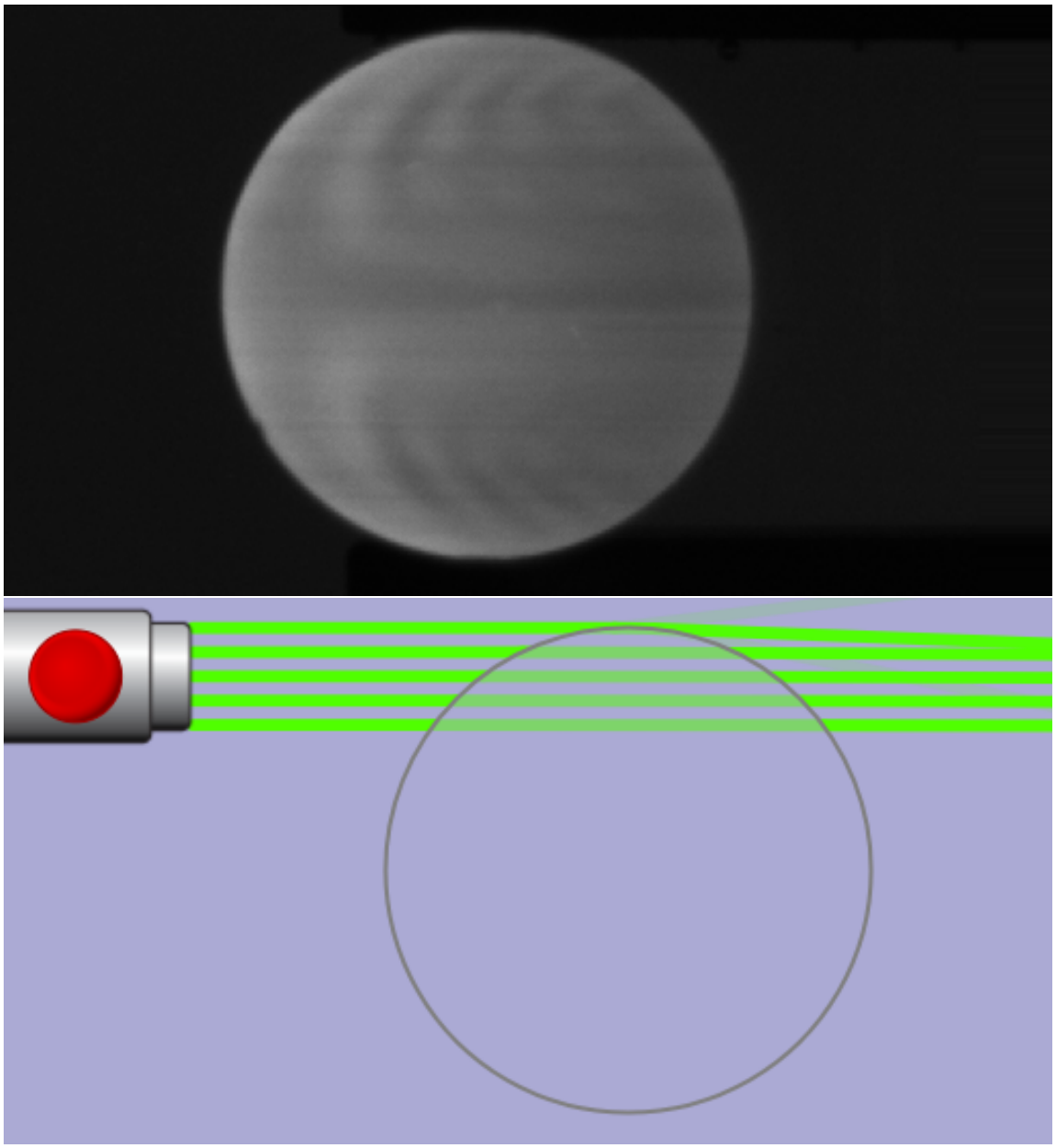

Figure 47: A sample immersed in index matching fluid with a light sheet being refracted through it, along with a ray-tracing diagram showing the same situation. Note the almost non-existent refraction and the lack of forbidden angles. The interference pattern happens because the coherent laser excitation light is refracted slightly and therefore can interfere with itself.

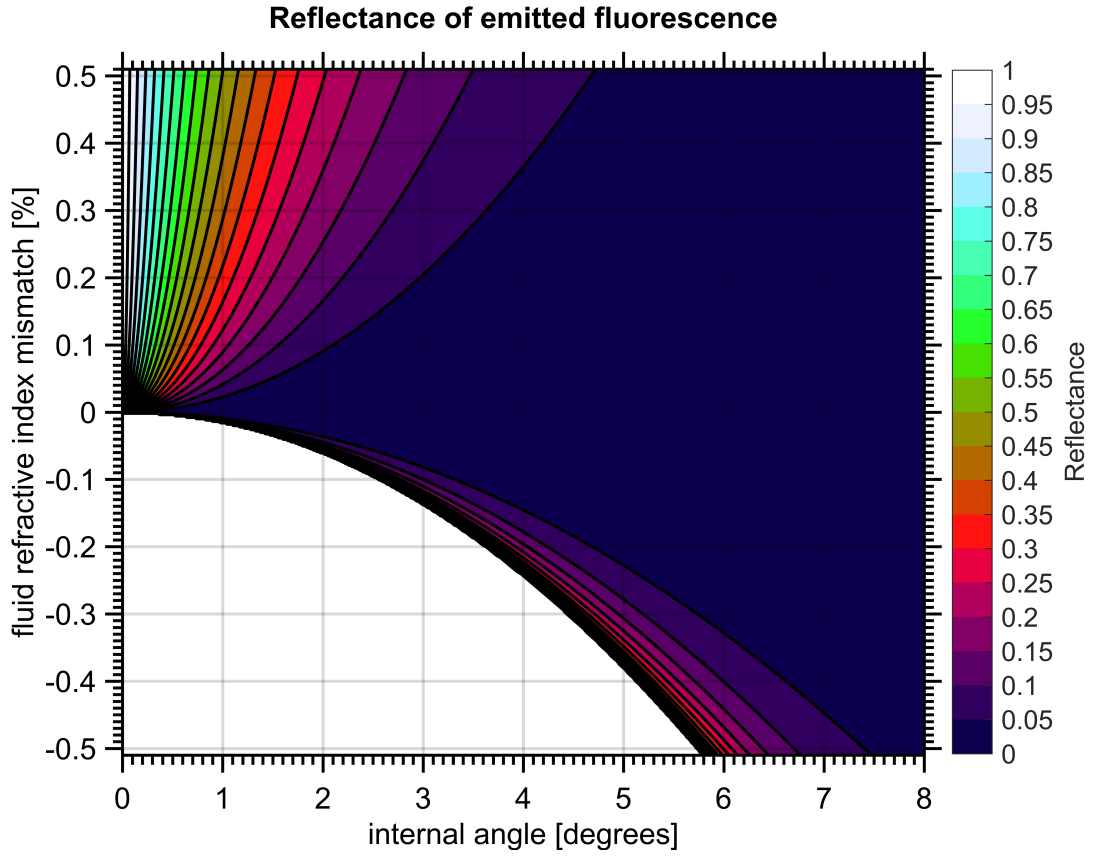

Figure 48: The internal reflection of the emitted fluorescence, as function of its internal angle and the index mismatch between the fluid and the polymer . The white area represents total internal reflection, which is why the index matching fluid should have an index that is slightly higher than the polymer.

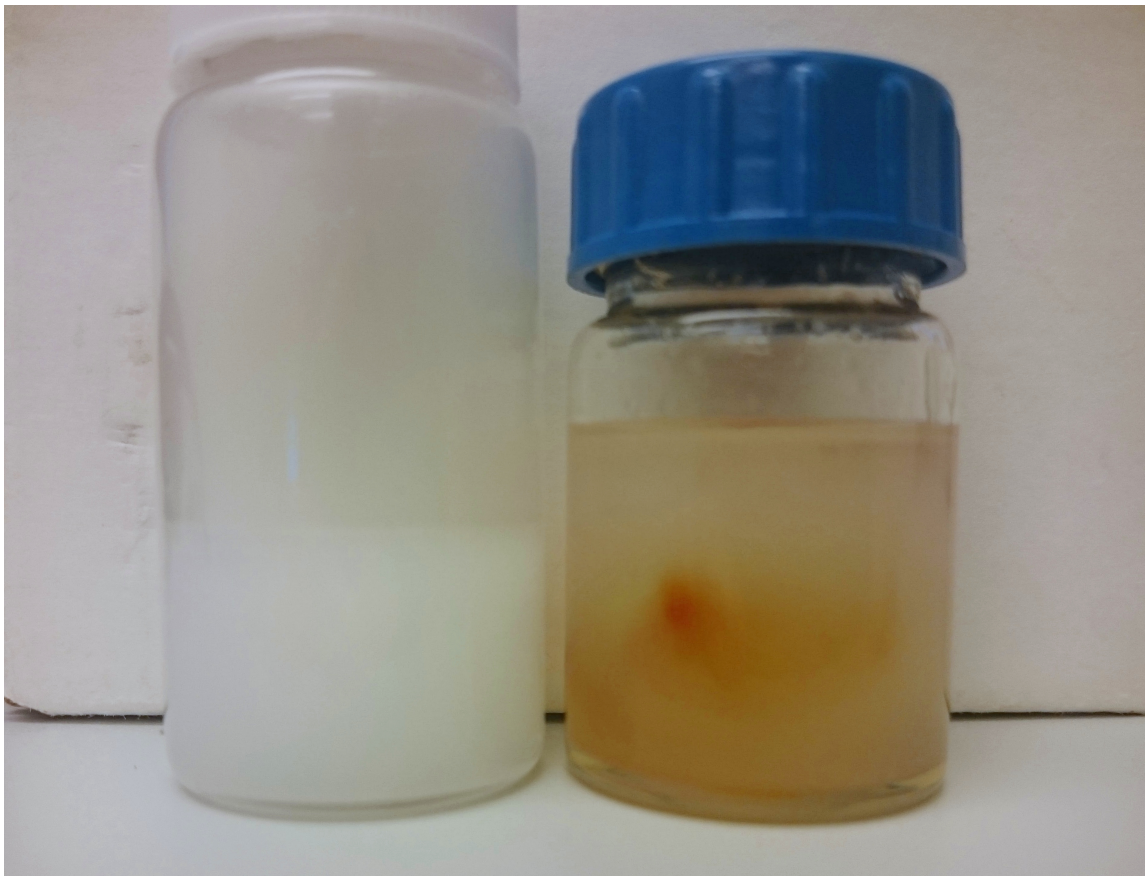

Figure 49: The result of attempting to mix the DC550 fluid and a polydimethylsiloxane silicone fluid. They are immiscible, leading to the light scattering seen in the images.

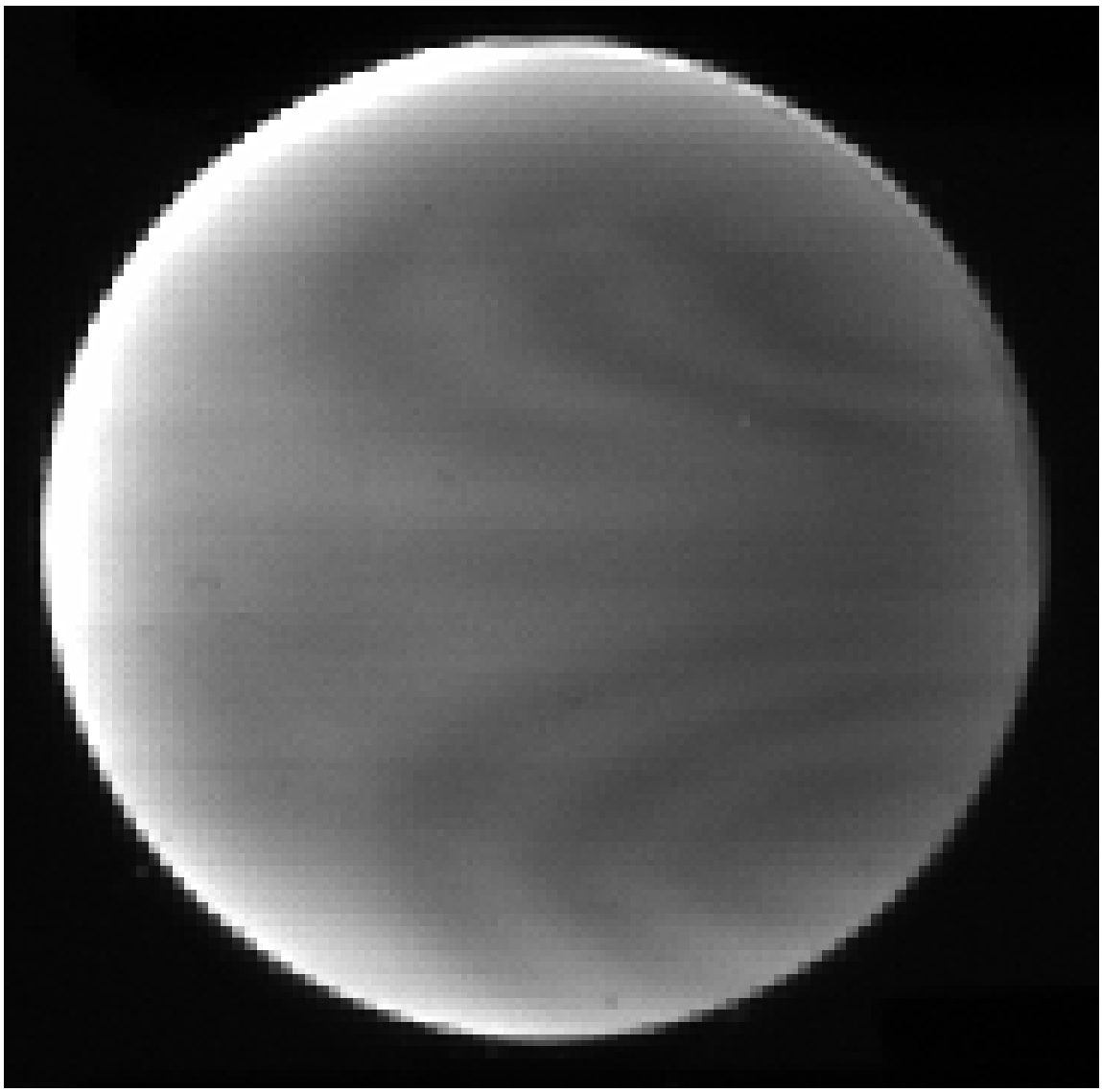

Figure 50: The interference pattern observed in a cylindrical sample still unexposed to radiation. Other samples show similar interference patterns. The pattern is independent of the rotation of the sample, which shows that it comes from the excitation light rather than the sample.

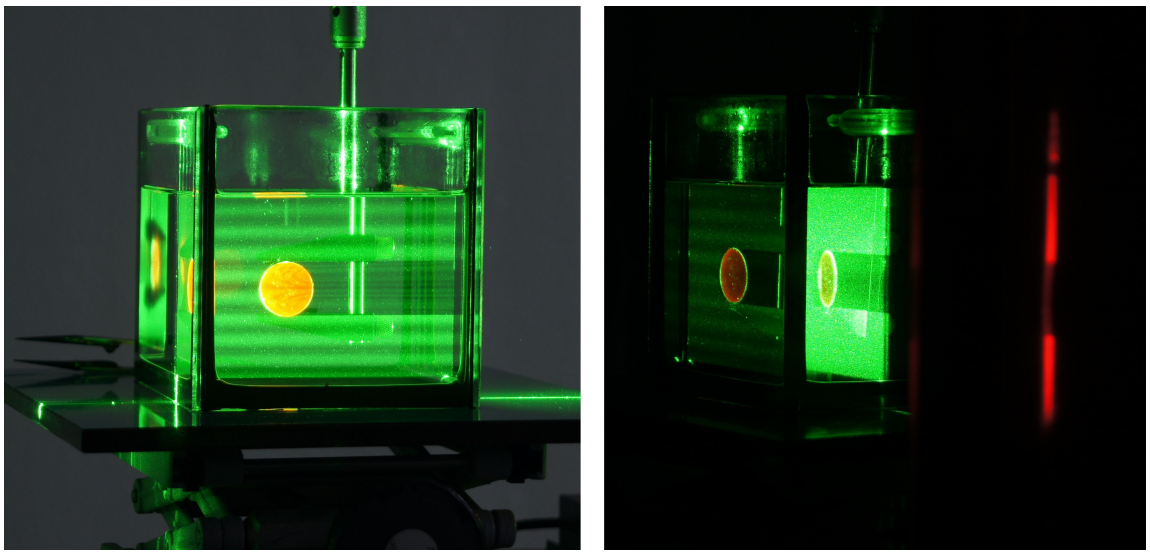

Figure 51: The effect of putting a depolarizer into the setup. The depolarizer is not randomizing the polarisation, but is merely making it spatially dependent in a predictable manner. The interference within the sample remains, but it can also be seen that the light scattered by particles in the index matching fluid is polarization dependent. The view through the other facet of the tank, along with the red flourescence from the fluorescent screen to the right, shows that the horizontal stripes are not variations in intensity but in polarization.

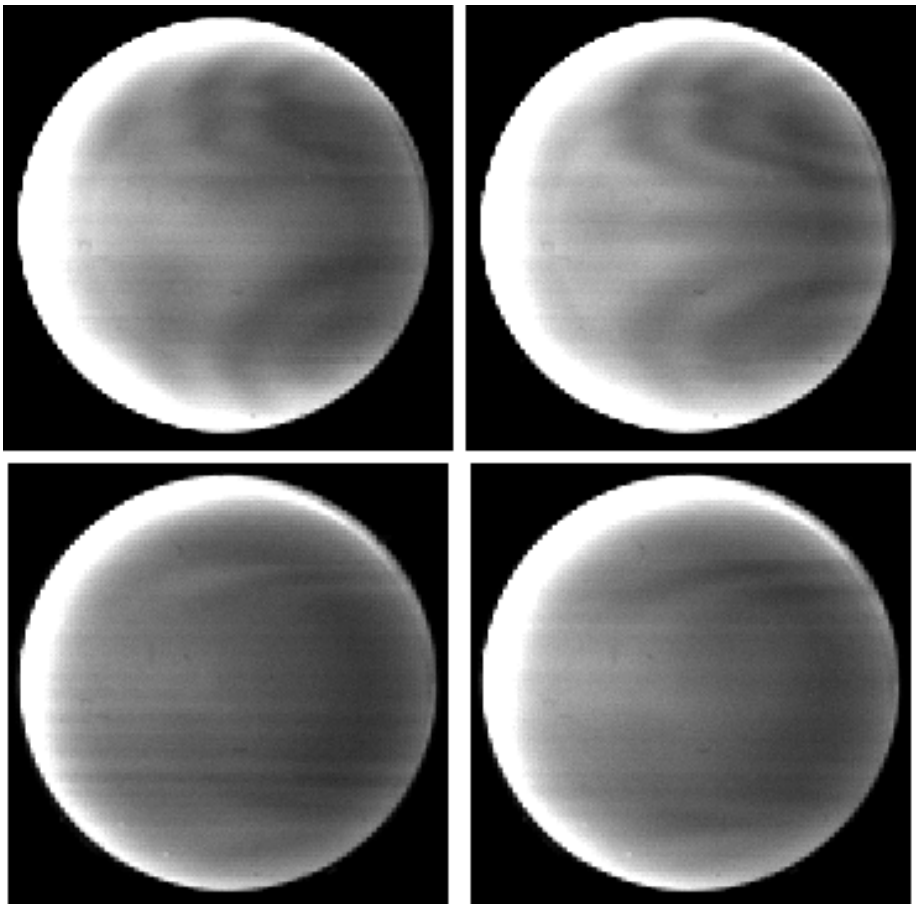

Figure 52: Two examples of what happen to the interference pattern when the polarization of the excitation light is changed. A half-wave plate was used to turn the polarization of the excitation light by 90 degrees, and the resulting interference patterns in the cylindrical smaples are anti-correlated. It is unknown exactly why this happens.

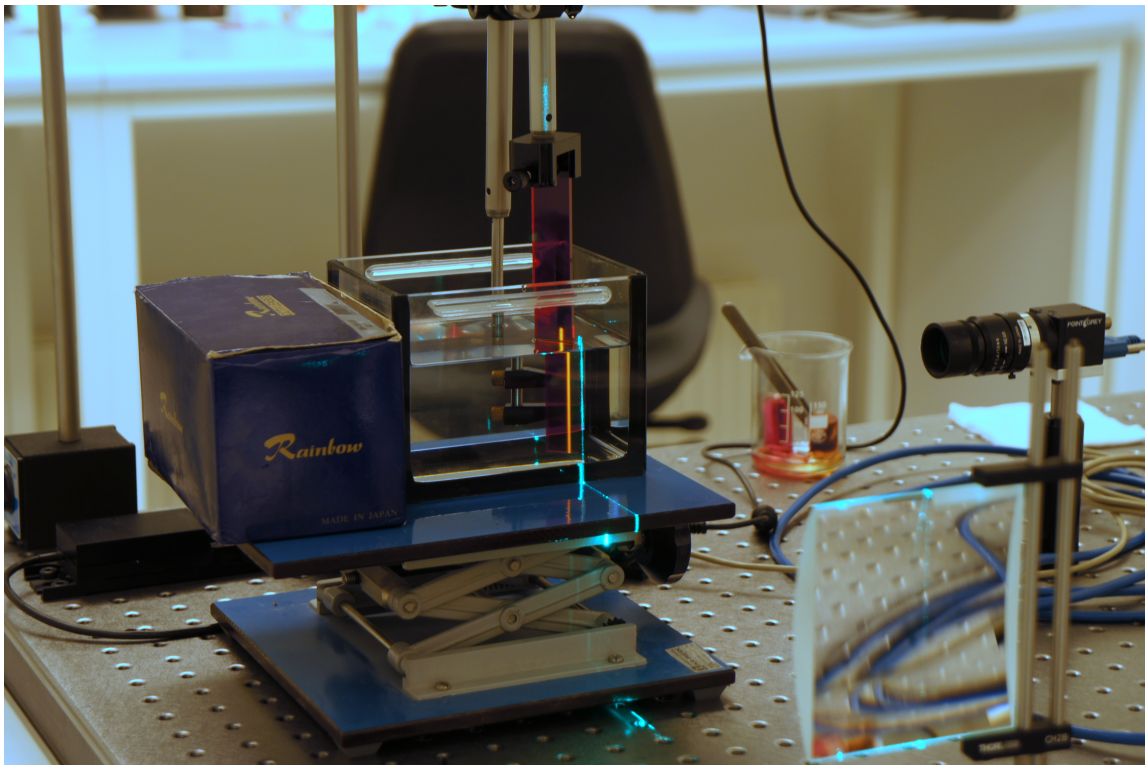

Figure 53: Picture of the of the fluorescence standard in the 3D setup.

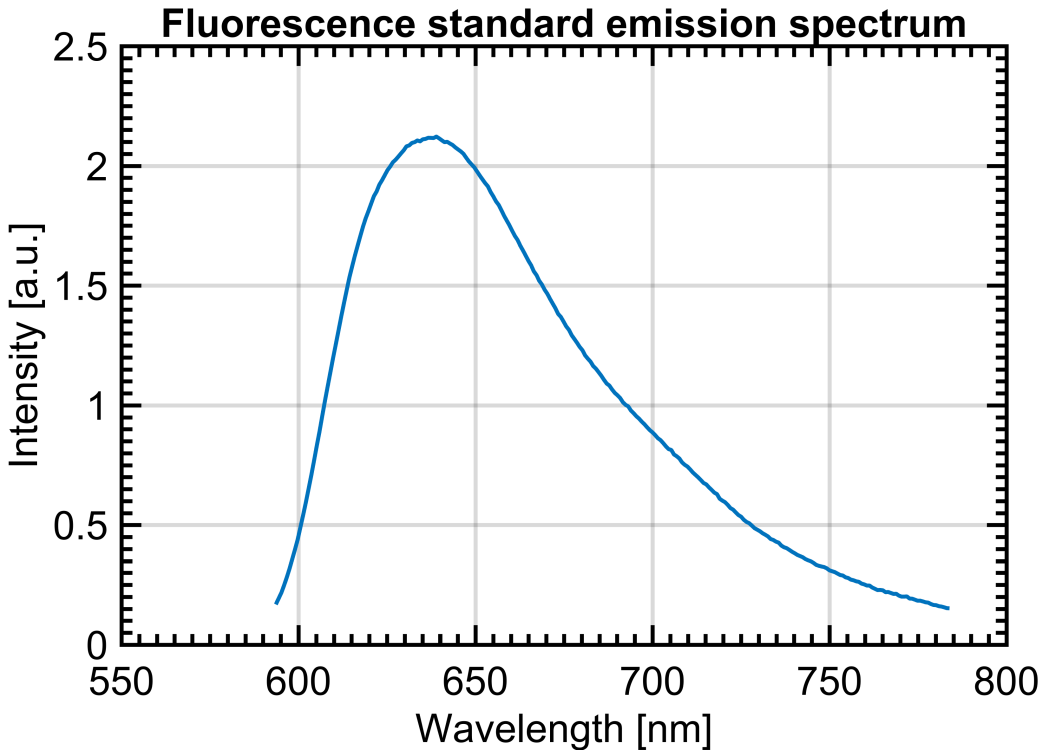

Figure 54: Graph of fluorescence standard emission spectrum.

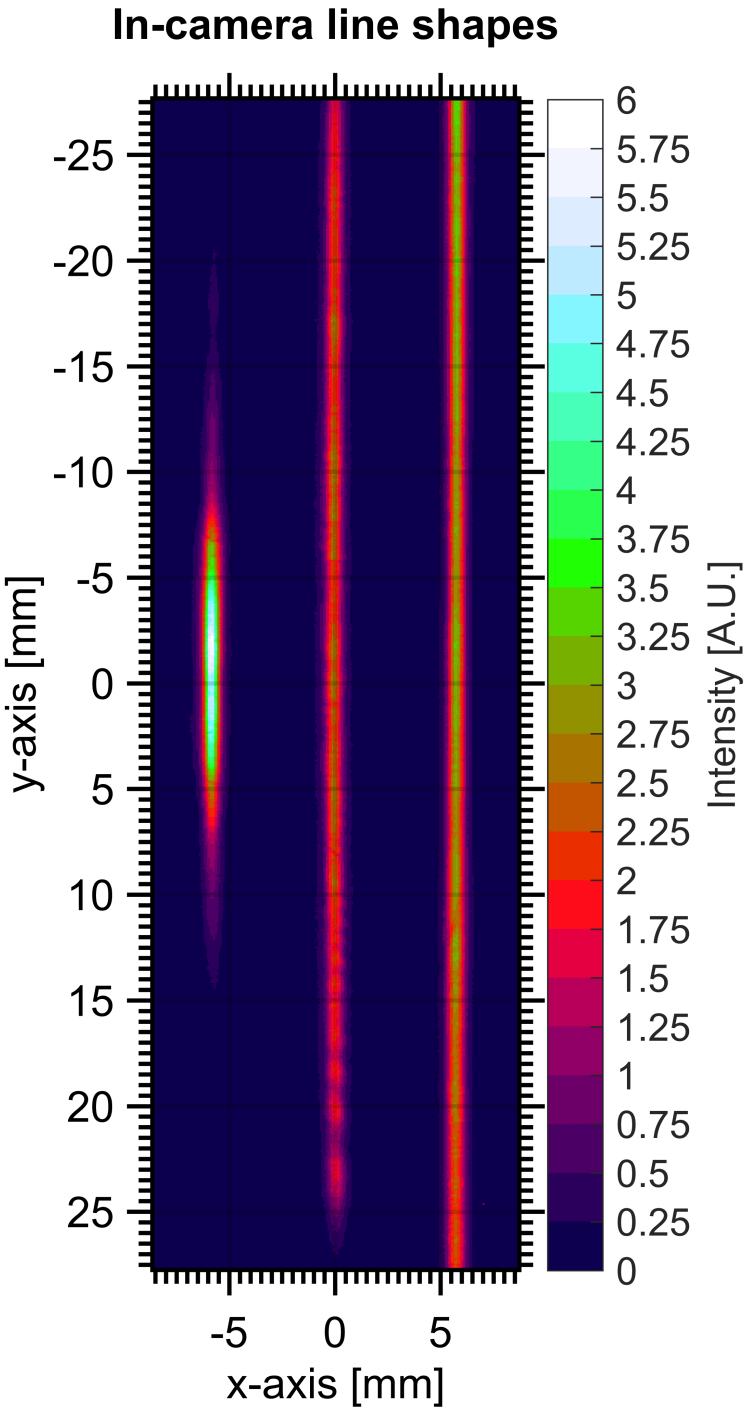

Figure 55: Examples of vertical intensity profiles from the different light sheet lenses, imaged as fluorescence from the standard captured by the 3D setup camera.

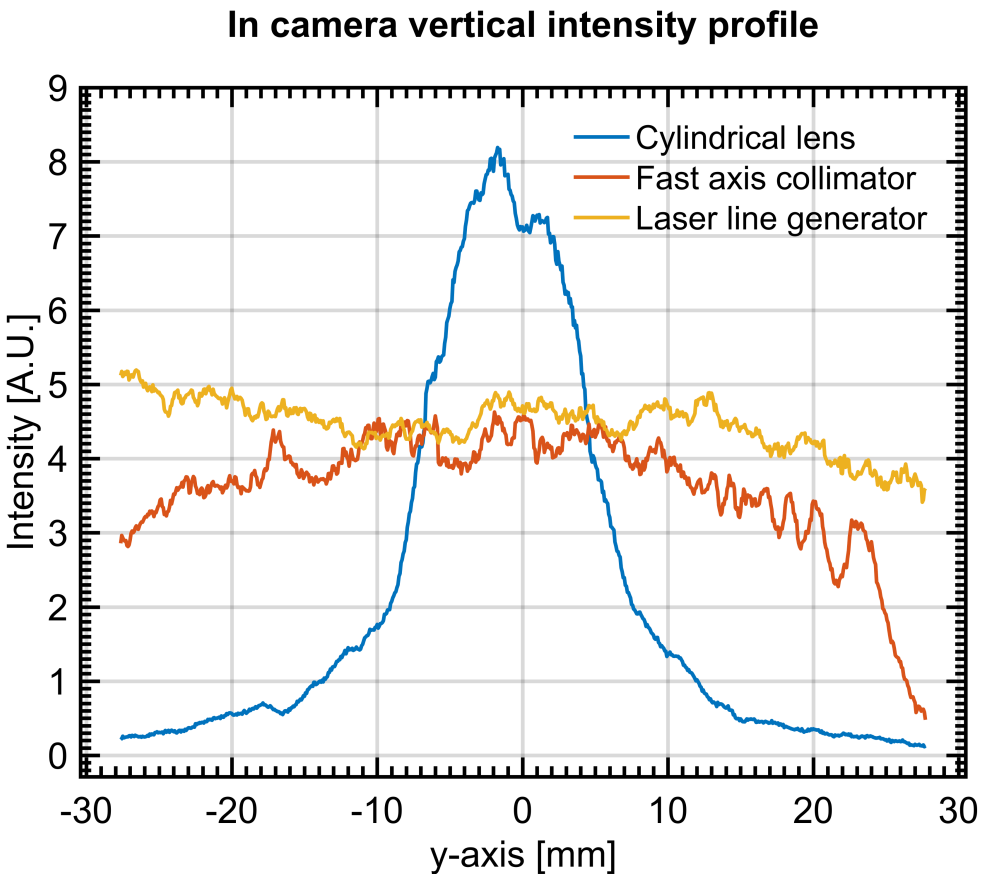

Figure 56: The vertical intensity profiles from the 3 lenses. The vertical profiles are not as smooth as anticipated.

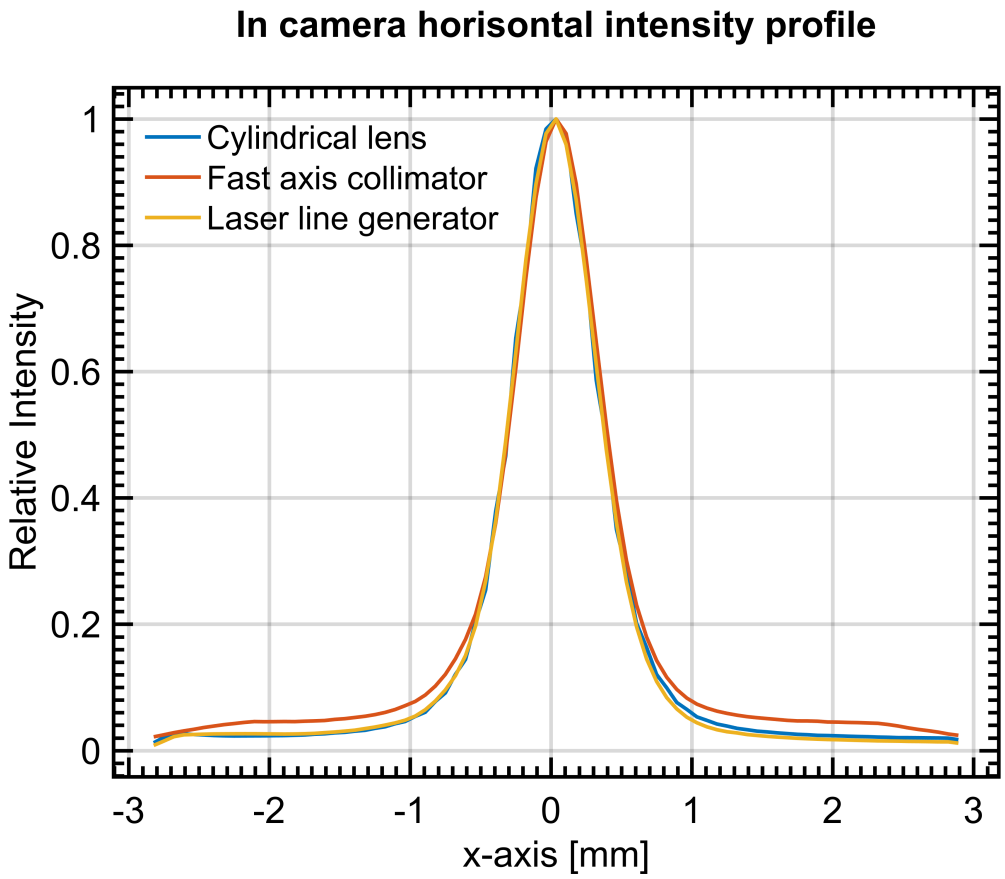

Figure 57: Examples of vertical intensity profiles from the different light sheet lenses, imaged as fluorescence from the standard captured by the setup camera.

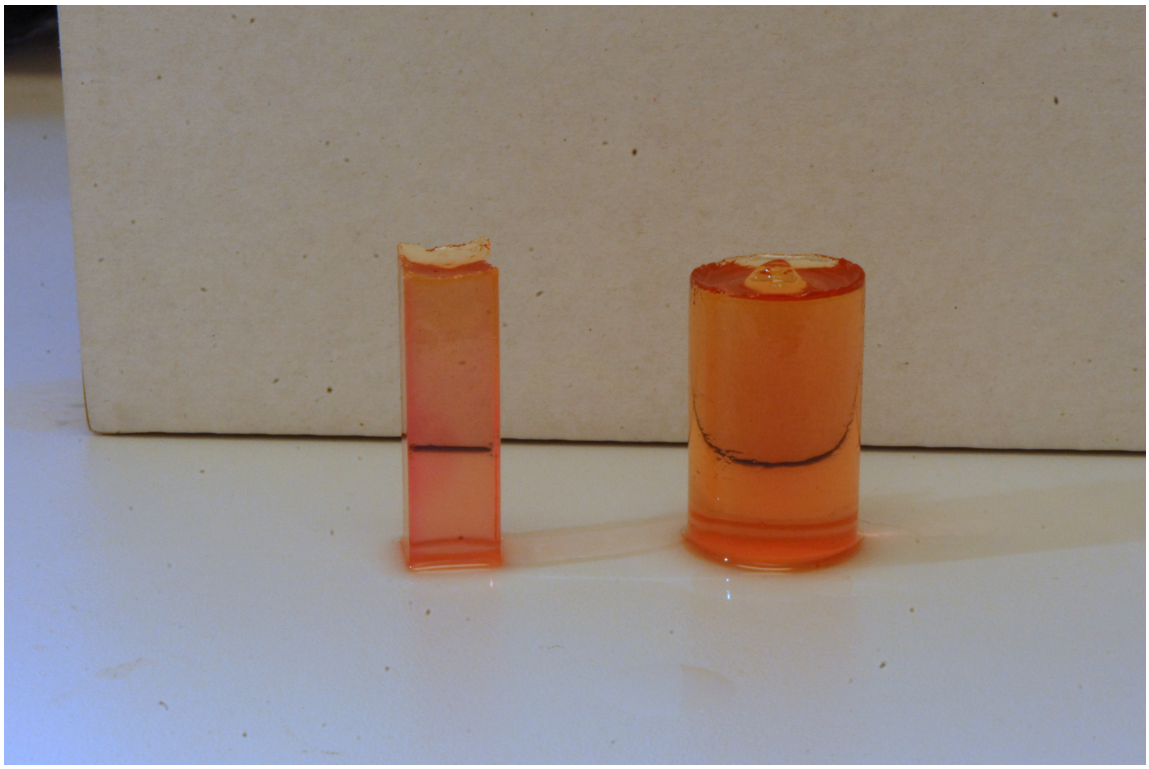

Figure 58: Cuvette and cylindrical samples. The cuvette on the left has been irradiated with about 100 Gy of 50kV x-rays through a circular aperture, and the radiochromic response is faintly visible. The cylinder is not irradiated, but is colored because it was cured slowly with cooling.

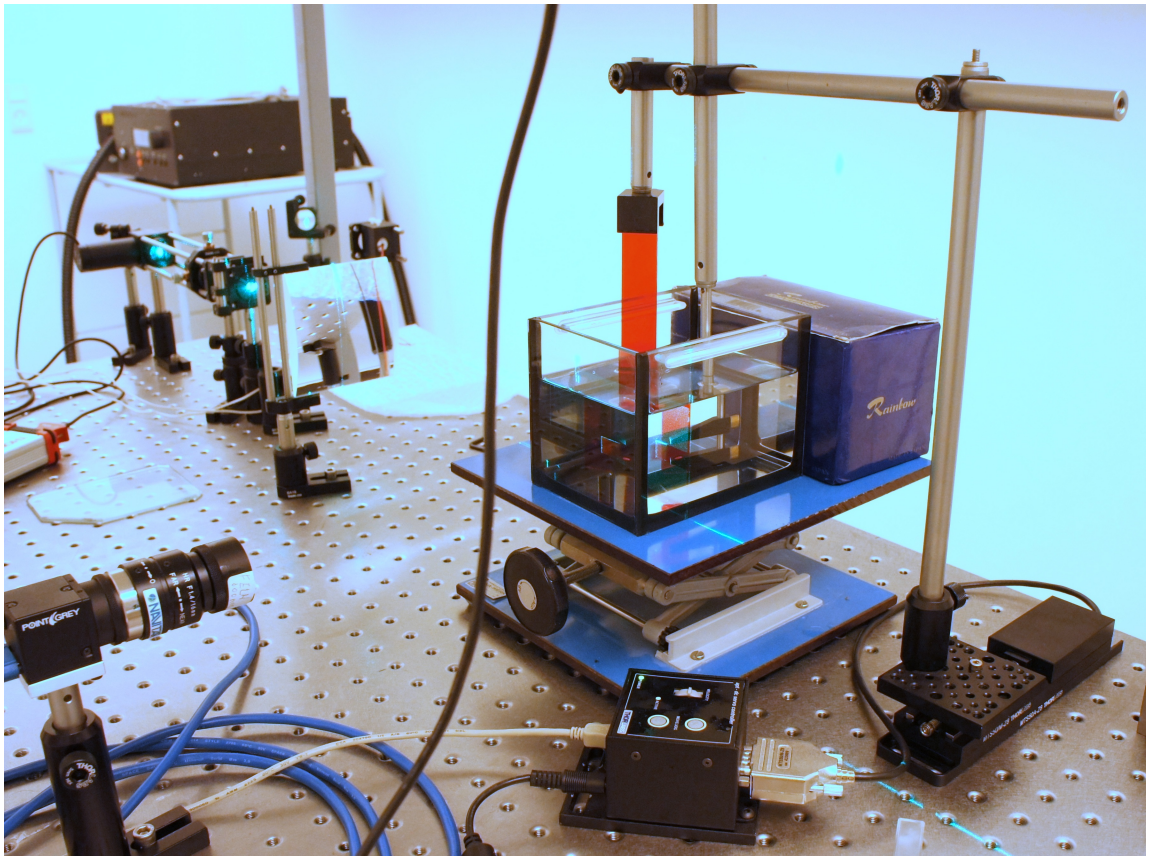

Figure 59: Image of the motorized z-stage, the gantry and the clamp holding and moving the dosimeter samples. The fluorescence standard is also mounted on the gantry.

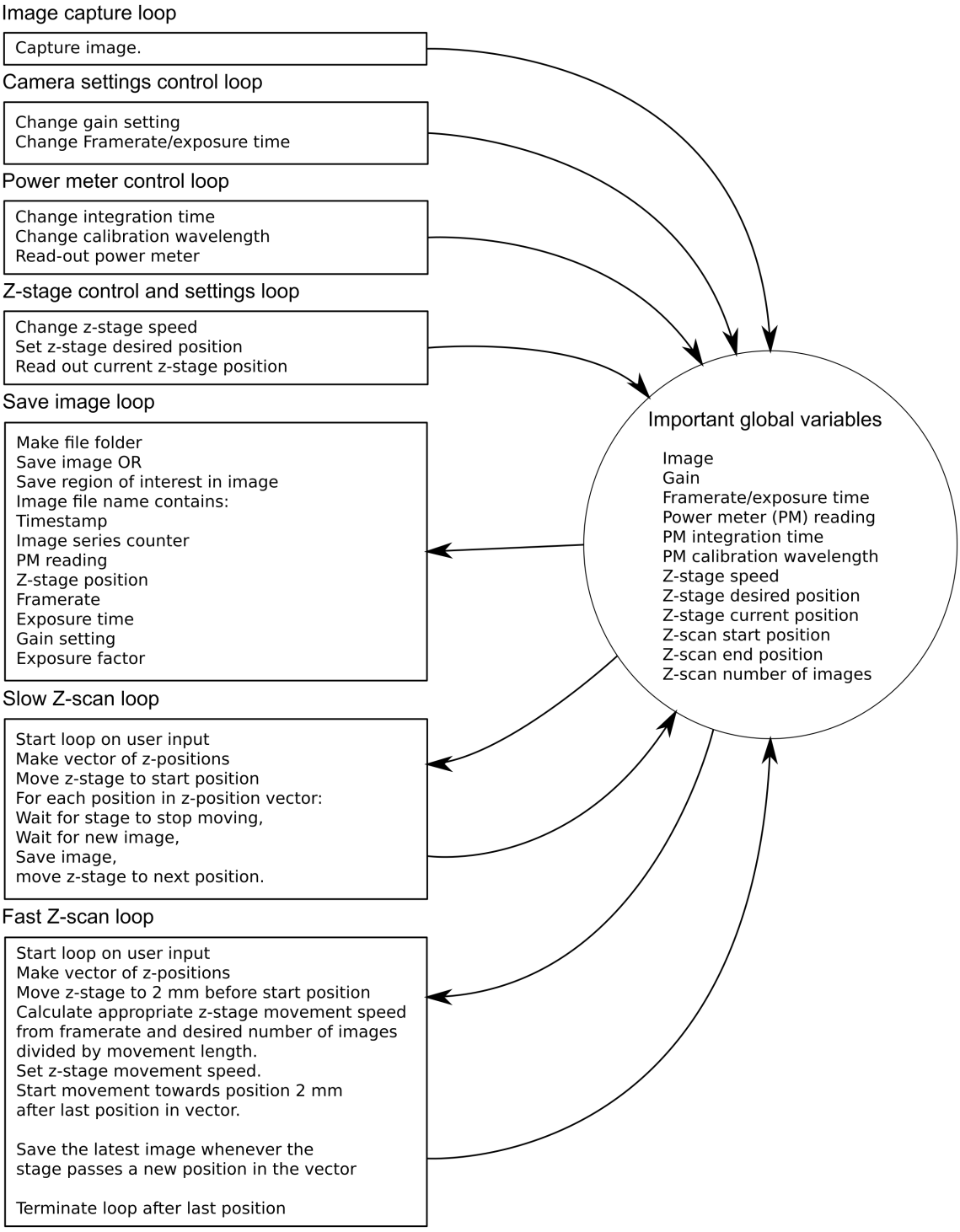

Figure 60: Block diagram of the 3D setup control program.

9 Detailed Description of Fluorescence Setup Components

This section contains detailed descriptions, characterization and discussion of the components in the fluorescence measurement setup. The components will be discussed in the order that they are listed in section 4.

9.1 Fluorescence Setup Excitation Laser

Two different lasers were used in the fluorescence setup. In both cases the lasers were mounted in a 4-axis laser mount, to allow the beam spot to be placed on the optimal position on the sample in the field of view of the fiber coupling.
Initially, a 532 nm Nd:YAG laser was used, but it had issues with power and spatial mode stiblity, so it was replaced with a 520 nm direct diode laser, which was much more stable.
The 532 nm laser works by having a 808 nm diode pumping a Nd:YAG crystal, which causes it to emit light at 1064 nm. This light goes into a KTP crystal, where it undergoes frequency doubling to become 532 nm light. These conversion processes are not perfect, so the laser also emits some of the light at 808 nm and 1064 nm, which is why the first optical filter must be included.
The conversion processes are also highly temperature sensitive, which means that the power output of the laser can be unstable, especially close to the lasing threshold.
More importantly, the transversal output mode can also be unstable, leading to a mismatch between the power measured by the power meter and the intensity of excitation light on the sample.
In contrast, the 520 nm diode laser is more stable, but the measured fluorescence response is slightly different from the value measured with 532 nm light.
To illustrate this, an IVPF (current-voltage-power-fluorescence) characterization of both lasers was performed. This is done by controlling the current supplied to the laser, then measuring the corresponding voltage, laser power output and fluorescence response of the fluorescence standard. This is done for a range of different input currents.
The fluorescence is measured within the field of view of the fiber coupling, which is very narrow.
The output power of the laser is measured by the power meter, which captures the full beam.
This means that any changes in the spot size or mode shape of the laser will lead to a change in how much fluorescence is measured at any given output power. Figure 61 shows how the stability of the spatial mode of the two lasers is different. The 520 nm laser is far more stable and consistent.
Figure 62 shows how the power efficiency of the two lasers differ. The 520 nm laser is more consistent and more efficient.

9.2 Fluorescence Setup Power Monitoring

The power monitoring is an essential part of the fluorescence setup, since the measured emission should be directly proportional to the laser power. The power monitoring was particularly important early in the project when a 532 nm YAG laser was used, since it had an unstable power output, especially at the low output powers that were used in this setup.
Just like in the 3D setup, the power is monitored by splitting off 10% of the light with a BS025 beamsplitter cube from Thorlabs, and measuring this light with a S121C PM100 USB power meter from Thorlabs.
The proportionality between the laser power and the measured emission is not entirely linear, so the standard procedure is to always measure the emission spectrum with the same laser power, and to compare the emission against a measurement of the fluorescence standard made during the same session.

9.3 Fluorescence Setup Sample Holder

Comparisons of the fluorescence response from different polymer samples rely on consistent positioning of the samples in the setup.
For this reason, a sample holder was made. It is a block of aluminum with a hole in the middle, as

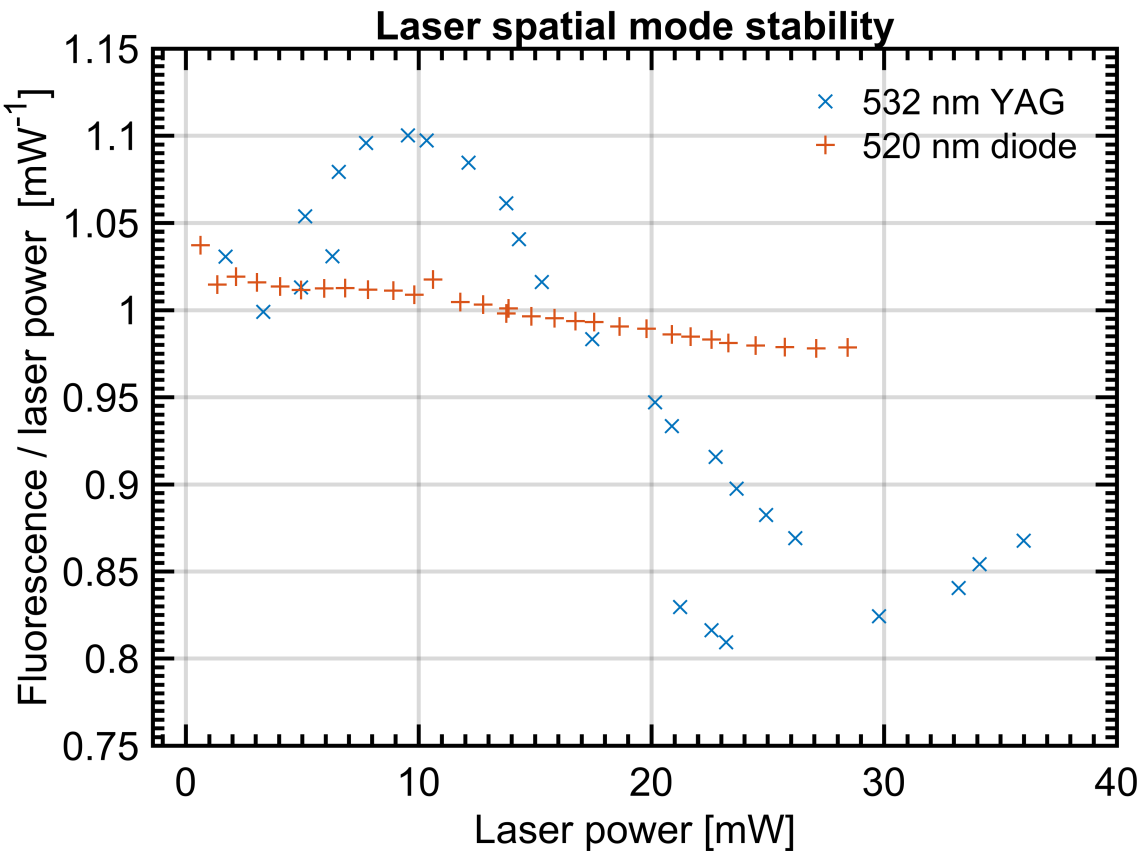

Figure 61: Normalized fluorescence from the fluorescence standard as function of the laser output power. The 520 nm diode laser is stable within 5%, while the 532 nm Nd:YAG laser is very unstable and power dependent.

shown in figure 15. The hole is made to fit the polymer pellets shown in figure 63. The dimensions of these pellets were chosen so they would fit into a setup for measuring EPR signals. The sample holder can be removed and replaced easily, and the cage rods in the fluorescence setup makes it easy to position it consistently.
In earlier versions of the setup there was no specific sample holder, and slides of cured polymer were simply placed into the slot. The slot is also wide enough to accept the fluorescence standard. The slide samples were prepared by forming a mould with glass plates, putting in the liquid polymer, putting a glass lid on top, and then curing with the UV lamp.
The mould for the pellet samples was a machined aluminum block on top of a glass plate, as also shown in figure 63.
The optical quality of the surface of the samples must be perfect in order to obtain consistent measurements of the fluorescence response, which is why glass was used as the top and bottom surfaces for the mould. Glass does have the disadvantage that the cured polymer sticks to it, making it difficult to remove. For future developtment, a hard UV-transparent plastic with a suitably smooth and flat surface could be investigated as a practical alternative.

9.4 Fluorescence Setup Longpass filter

The optical longpass interference filter with cutoff wavelength at 550 nm is identical to the one described in section 8.10.

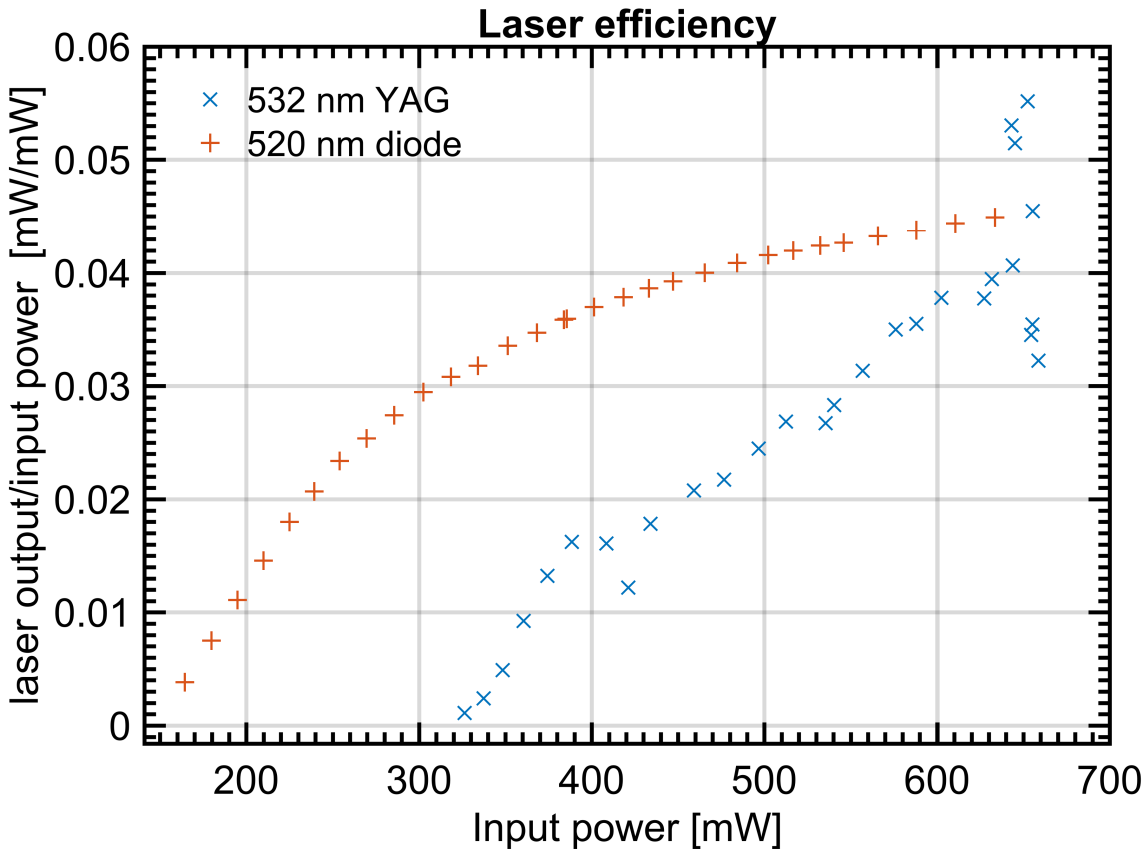

Figure 62: The power efficiency of the two lasers. The effficiency of the 520 nm diode laser changes in a predictable and stable manner, while the 532 nm Nd:YAG laser is unstable and unpredictable.

An optical filter of high quality is crucial in this setup, since the optical fiber coupling is directly in the beam path of the laser. This means that the filter is necessary to prevent saturation of and potential damage to the photodetector in the spectrometer.

9.5 The Fiber Coupling

The emission from the sample is isotropic, so the best and easiest way to collect the light into the spectrometer is to place a fiber coupling as close to the sample as feasible.
The fiber coupling in this setup is an Ocean Optics patch cord model QP600-2SR, with a numerical aperture of 0.22. The fiber coupling picks up light from a very narrow cone of about 3 degrees across. This makes the positioning of the laser spot on the sample very critical which is why the laser in the setup is mounted on a 4-axis mount.
The direction and spatial mode of the laser should be stable, otherwise the ratio of the measured laser power and the measured fluorescence could change.

9.6 Spectrometer

The spectrometer used in the fluorescence setup was an Ocean Optics QE65000. It has a spectral range from 200 nm to 1100 nm. The detector quantum efficiency is highest at wavelengths from 400 nm to 900 nm, which is suitable for our application. During measurements, the detector was cooled to -6°C by an internal Peltier cooler, in order to reduce the dark current. The Spectrometer

Figure 63: Images of the slide and pellet samples, along with one of the alanine pellets that the pellet samples were shaped after. On the right is a photo of the pellet curing process.

was controlled through a Labview program, described in section 9.7, with the drivers and Labview plugins provided by the Ocean Optics web page.

9.7 Fluorescence Setup Control Program

A program to control the Ocean Optics QE65000 spectrometer and the Thorlabs S121C power meter was written. This was necessary to synchronize the measurements of the spectrum and the laser power, so that the measured fluorescence response can be normalized by division with the laser power.
The structure of the program is concurrent loops that repeatedly measure the power from the power meter and the spectrum from the spectrophotometer. Similarly, the program also allows the user to continually change the exposure parameters for the spectrophotometer and the power meter.
The intensity of the excitation light needs to be stable on both the sample and the power meter. This means that the spatial mode of the laser needs to be stable.
Since the power meter and the spectrometer measure at the same time, it is not strictly necessary for the laser power to be stable, but sudden changes in the laser power are usually accompanied by fluctuations in the spatial mode.
For this reason, the laser should be operated sufficiently above the lasing threshold that it does not fluctuate.
During a series of fluroescence measurements, the output power of the laser should be kept consistent. This is because a change in the laser power might also change the spatial mode of the laser slightly, which would change the ratio of the fluorescence emitted by the sample and the power measured by the power meter.
The reason for using the 520 nm diode laser is that it is more stable, both spatially and temporally, than the 532 nm Nd:YAG laser.
Power stability is not essential, since the setup contains a power meter that continuously monitors and corrects for the laser power, but the spatial stability is very important since the field of view of the fiber coupler is smaller than the laser spot. This means that the power meter reading can potentially remain constant while the laser intensity in the field of view of the fiber coupler changes significantly. Figure 64 shows a block diagram of the Labview program, similar to the diagram shown in figure 60. The boxes are the different loops in the program, and their contents describe what the loops do. The circle contains the important global variables, and the arrows show whether the loops write or read these variables.

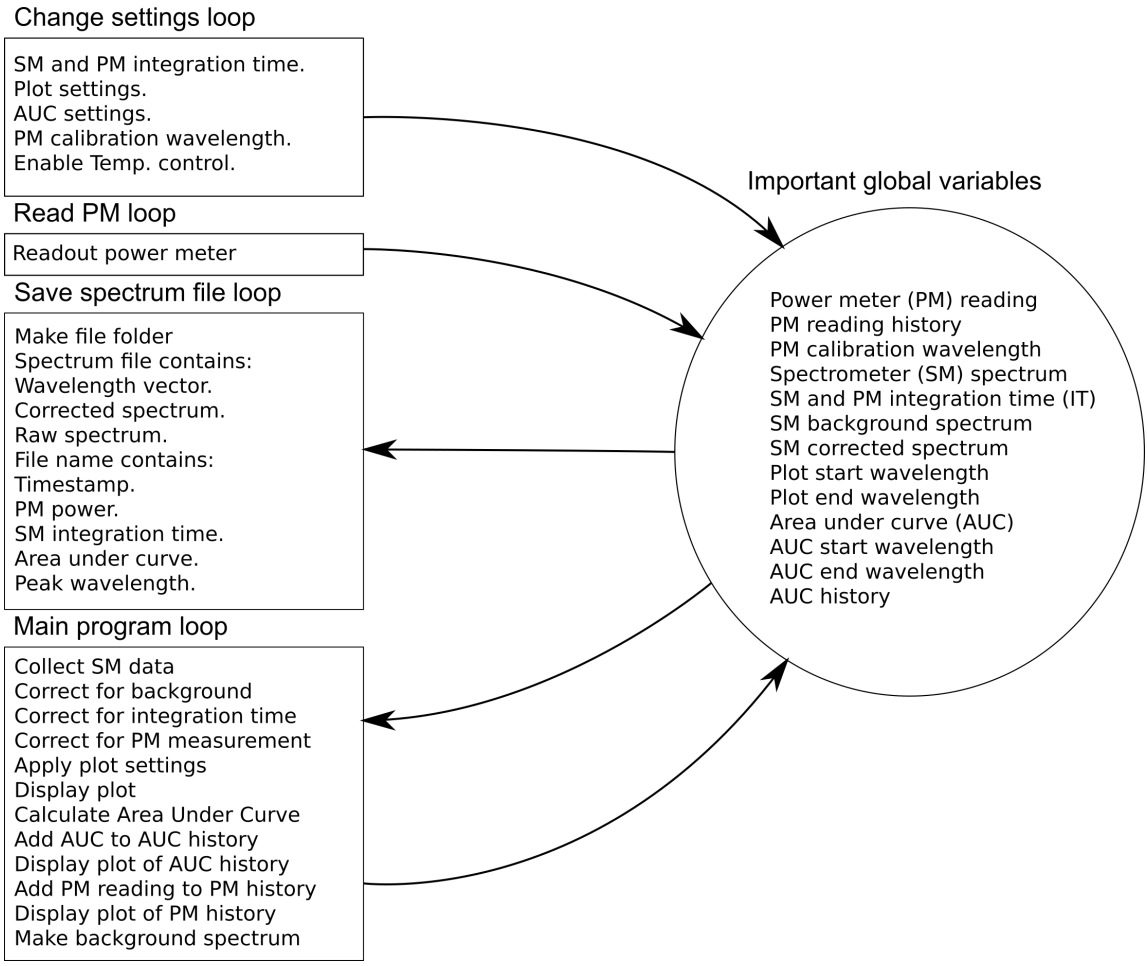

Figure 64: Block diagram of the fluorescence setup control program.

9.8 Section conclusions

Compared to the 532 nm Nd:YAG laser, the 520 nm direct diode laser is much more stable in output power and spatial mode, which makes it much better for use in the fluorescence measurement setup. The power monitoring works in conjunction with the measurement of the fluorescence standard to provide a reference of the laser power for every measured fluorescence spectrum. This combination, along with a laser with stable spatial mode, makes it possible to compare the fluorescence response of different samples directly.

The samples must be positioned in a stable and repeatable way, and the optical quality of the sample surfaces must be nearly perfect.

For the fluorescence setup, the quality of the longpass filter is more important than in the 3D readout setup. This is because the excitation laser aims directly into the fiber coupling to the spectrometer.

The fiber coupling only picks up light from a narrow field of view, so the positioning and spatial mode of the excitation laser must be stable.

The fluorescence setup control program streamlines the process of measuring and comparing the fluorescence response of different samples. There is still room for improvement in the program. For example by using a measurement of the fluorescence standard to normalize the measurements of the samples directly in the program, instead of applying the normalization manually in the subsequent

analysis of the spectral data. The program can also be difficult to get working on a new computer, due to drivers issues with the spectrometer and the power meter. Using, modifying and compiling this program will require some knowledge of Labview.

10 The Solid-State Polymer Dosimeter

The dosimeter samples used in the 3D readout setup were all composed of "composition 22", as described in section 3. Unfortunately, the dosimeter material that was available was ultimately not suitable for use as a clinical dosimeter. It had a number of properties that made it very difficult to construct a reliable absorbed dose distribution from the 3D fluorescence data acquired by the 3D readout setup.
First of all, the photo-curing reaction that hardens the polymer matrix is exothermic. If the sample is too large, it can become hot enough to melt or even carbonize a plastic container. If the sample is allowed to become too hot during curing, it will expose some of the dye in the middle, increasing the zero-dose attenuation and fluorescence. Such an inhomogeneous dye exposure before irradiation makes it impossible to calculate the dose accurately after irradiation and 3D readout.
For this reason, an ice bath was used to cool the polymer during the 2 minute curing of the cuvette samples. Late in the project, a setup for cooling the cylindrical samples during curing was devised. These cylindrical samples were larger, and were therefore more difficult to keep cool. Any samples cured over 20 minutes at low UV intensity tended to become fully exposed, due to an unknown chemical reaction. This aspect of the polymer chemistry was never fully explored.
Even when perfectly cured, the zero-dose attenuation and fluorescence of the polymer is high, compared to the radiation response, as noted in section shown in table 2.
Any surface of the polymer exposed to air during the curing will tend to remain fluid, with a thin layer of uncured monomer. This is because oxygen in the air interferes with the reaction of the photo-initiator in the polymer. In order to be useful in a 3D readout setup the polymer should have the following material properties.

- The surface of a cured sample should be hard and have good optical quality.
- Before irradiation, the polymer should be as transparent as possible at the absorption and emission wavelengths for the fluorescent dye.
- The radiochromic response should be linear and as small as possible.
- The fluorescence response should increase linearly with the radiation dose.
- The radiofluorogenic response should be high compared to the fluorescence at zero absorbed dose.
- The material constants should be constant over time.
- The material constants must be homogeneous within a sample.
- The influence of the curing process on the material constants should be well understood and characterized.

The polymer does not fulfil these requirements so it is necessary to characterize how it diverges from the hypothetical "perfect dosimeter". The development and characterization of the polymer was not a part of this project, but some measurements of the characteristics and material parameters of the polymer were performed nonetheless.

10.1 Bubbles in the Cured Samples

Figure 65 shows the bubbles that sometimes appear in the samples. They have the effect of blocking the exciation light sheet and also the emitted fluorescence if they are between the light sheet and the camera. In the processing of the resulting fluorescence images, bubbles and the subsequent reduction in excitation light intensity will lead to artifacts in the reconstructed images. Making samples without bubbles and/or particles is therefore a necessity. With the samples used in the project, there were more bubbles if the samples were cured faster. It is unknown if the bubbles

Table 8: Constants from the exponential fit

Fit \Constant	c_1 [cm^{-1}]	c_2 [cm^{-1}]	c_3 [hours]	r
After curing	0.249	-0.144	8.01	0.9999
After irradiation	1.363	0.366	4.35	0.9999

come from gas dissolved in the polymer liquid, or from gas developed during the curing. It would be interesting to experiment with using a vacuum to de-gasify the polymer before curing it.
In the processing of the resulting fluorescence images, bubbles and the subsequent reduction in excitation light intensity will be interpreted as an area with very low exposure. If the boundary condition is to the right of the bubble, then the fluorescence to the left of the bubble will be interpreted as abnormally high exposure. This divergence will grow exponentially with the distance from the bubble, as shown in figure 29.

10.2 Polymer Stability over Time

One of the main problems with the polymer was that it is not stable over time. To characterize this, it was measured how the absorbance spectrum of a 10 mm thick sample of polymer changed over time.
A sample was cured in a 1 cm cuvette and then removed from the cuvette. A few drops of index matching fluid were put in the cuvette, and the sample was put back in. This was done to minimize the number of optical interfaces from 4 to 2, and to eliminate the possible influence of changes in the optical quality of the sample surfaces.
As soon as possible after curing the sample cuvette was put into the spectrophotometer, which was programmed to collect one full absorbance spectrum every 10 minutes. This measurement series was run overnight for a total of 100 spectra. After this the same sample was exposed to 500 Gy of gamma radiation from Cobalt-60, in gamma cell 3. After irradiation the sample was put back into the spectrophotometer and another 100 spectra were collected overnight at 10 minute intervals.
Between each measurement in the overnight series, this sample would be exposed to low intensity UV light at 430 nm, which could have an effect on the dye. To act as a control, in case the process of repeated absorbance measurements had an effect on the sample, another sample was prepared identically to the primary one. This sample was only measured 4 times, at the start and end of each measurement series for the primary sample.
The efforts to control the losses at the optical interfaces were undercut somewhat by the observation that a few tiny bubbles had appeared in the samples during the first measurement series. The effect of these bubbles was to scatter some of the light, which added a small wavelength independent offset to the absorption spectrums. This had to be corrected for in the data analysis. Figure 66 shows how the absorbance spectra changes after curing and after irradiation. It is clear that changes in the dye concentration is the only significant contributor to dosimeter color change over time frames of a few days. Figure 67 shows how the peak of the of the absorption spectrum changed after curing and after irradiation. After curing, the attenuation coefficient at the peak of the dye absorption band, $\lambda = 555$ nm, was increasing. After irradiation the attenuation coefficient at the peak decreased exponentially in a similar fashion. These changes were fitted to an exponential approach:

$$\mu(t) = c_1 + c_2 \cdot \exp(-t/c_3) \tag{39}$$

The values from these exponential fit are presented in table 8. In both cases the exponential equation was a good fit to the measured data. The exponential approach towards a value is perfectly consistent with a gradual approach towards a chemical equilibrium. To be within 1 percent of the final value, at least 5 times the time constant must pass. For the increase after curing this is about 40 hours. This means that a sample should not be used until 2 days after it has been cured. The 4 hour time constant for the decrease after irradiation means that a sample should ideally not be evaluated until 24 hours after it has been irradiated.

Another problem is that considerable differences in the final color of un-irradiated samples have been observed, depending on how they were cured. It is unknown if the time constant is the same, but it is likely that samples which have been cured more will be harder and have lower diffusion, which could give a higher time constant.
All of these factors combine to make the polymer unsuitable for use as an accurate dosimeter. To clear up these questions, an experiment was done to clarify how much influence the curing parameters have on the polymer stability over time.

10.3 Influence of Curing Time and Intensity on Polymer Stability

The presently unpublished measurements and results presented in this section were made by M.R. Bernal-Zamorano, who developed the polymer composition. The results have been included here, because they contain information that is important for understanding the polymer. A series of exploratory measurements were performed to ascertain the effects of varying the curing time and intensity, and the subsequent time stability of the polymer.
2.78 mm thick pellets of polymer composition 22 were cured under a 385 nm UV diode with 4 different curing methods with 4 pellets for each method. Before starting the experiment a current-voltage-power characterization of the diode was performed. The power output was proportional to the current, all the way to the 10 A current limit of the power supply. The experiments highlighted some interesting disparities in how the absorbance and the fluorescence change over time after curing and irradiation. The experiment also shows that the curing method has a significant impact on the optical properties of the cured polymer.

Figure 68 shows how the 4 different curing methods affect the absorbance peak of the dye, before irradiation of the pellets. The main difference is the offset of the dye absorbance. If it is assumed that the underlying curve is an exponential approach with a time constant of 8 hours, as observed in section 10.2, then the second value should be within 5 percent of the final value. This means that the 16 pellets are not headed for the same endpoint for the chemical equilibrium of the dye concentration. The fact that the slope is similar despite different starting points indicates that the chemical equilibrium is determined by something other than the dye concentration. Figure 69 shows how the 4 different curing methods affect the absorbance peak of the dye, when the pellets are irradiated with 50 Gy in a Co-60 source. The curing method has no impact on the absorbed dose response of the absorbance, but the starting points are very different, ranging from 0.08 to 0.17, which is a factor of 2. This dependence on the curing method is problematic, since the absorbance at 0 Gy is one of the material constants that is used for calculating the absorbed dose from the fluorescence.

Figure 70 shows how the 4 different curing methods affect the absorbance peak of the dye, after the pellets have been irradiated with 50 Gy in a Co-60 source. It is interesting that this experiment shows a slow increase in absorbance after irradiation, while the experiment in the present project with 500 Gy irradiation showed a gradual decrease, with a time constant of 251 minutes.

Figure 71 shows how the 4 different curing methods affect the fluorescence of the pellets before irradiation. It appears that the initial fluorescence is very dependent on the curing method, but that this difference mostly disappears over time. It goes down from 1100 to 200. The endpoints for the fluorescence also depend on the curing method, with values ranging from 120 to 180. This is in contrast to the absorbance, which increased by a factor of 2. The fact that the initial fluorescence decreases by a factor of five while the absorbance increases by a factor of 2 seems to indicate that the observed fluorescence is not limited by the amount of exposed dye, but rather by something else. This could for example be local changes in the polymer around the dye molecules, since the quantum yield of the fluorescence from the dye could be highly dependent on condition of the polymer matrix. Figure 72 shows how the 4 different curing methods affect how the fluorescence of the pellets are changed by irradiation. The differences in how much the fluorescence increases do not appear to be significant. This is similar to the radiation induced response of the absorbance, which was also unaffected by the curing method.

10.4 Changes in Fluorescence

The fluorescence been observed to change over time after curing and after irradiation. Unfortunately, the characterization of the fluorescence response was also complicated by the observation that the excitation light can quench the fluorescence at high intensities.

Figure 73 shows how the fluorescence response decreases when a slide sample is subjected to excitation with the laser at high power. When the laser power is decreased, the fluorescence response recovers, suggesting that this change is reversible. This quenching of the fluorescence response means that all characterization of the fluorescence response should be done with a low and consistent laser power, to minimize its influence.

To investigate precisely how the fluorescence changes over time, a series of experiments were performed to measure this change while it was happening. For all of these measurements, the laser power in the setup was a relatively low 2.9 mW, in order to minimize the fluorescence quenching shown in figure 73. In the first experiment, a pellet of polymer was cured and placed in the fluorescence measurement setup as fast as possible. The pellet was left in the setup for several hours while the spectrum was measured every second. The fluorescence intensity was calculated as the mean intensity around the fluorescence peak, from 580 nm to 660 nm. Figure 74 shows how the fluorescence intensity changed over time in this experiment. The increase in fluorescence is interesting, since it indicates that the polymer continues to change after the curing light is turned off. The low diffusion rate means that any such changes could take a relatively long time to complete. Another interesting aspect is that this increase in fluorescence is not tied to any visible change in the sample color. This is another indication that the change in fluorescence is due to changes in the local environment of the dye molecules, rather than changes in the dye concentration.

The aim of the second experiment was to find out how the fluorescence develops after the polymer is irradiated. To test this, another three pellets were cured at the same time, and then left for some days in order for them to reach equilibrium. They were then irradiated with 300 Gy in the Co-60 gamma cell. Immediately after irradiation they were placed in the fluorescence setup. Figure 75 shows that the illumination in the setup appears to have a pronounced effect on the initial increase in fluorescence. The increase for pellets #3 and #1 was clearly accelerated when they were put into the setup. When pellet #2 was replaced into the setup, it was at a lower value than when it was taken out, which indicates that at least some part of the increase is reversible in the short term.

The experiment was meant to look at the long term changes after irradiation, so one of the samples was placed into the setup and left overnight. Figure 76 shows how the fluorescence of this sample decreased over time. In contrast to the curve seen in figure 74, the decrease appears to be linear rather than exponential. The reason for this quickly became apparent when the sample was removed, as seen in picture 77. In this context, it should be noted that the readout process in the 3D setup will only illuminate each z-position in the sample for a maximum of 2 seconds, and the intensity of the excitation laser is on the same order of magnitude. Therefore there is no risk of bleaching a sample during the 3D readout process. The intense green light in the setup had bleached the dye in the sample, which is the reason for the decrease in observed fluorescence. This calls the results from figure 74 into question, since bleaching of the dye would not be apparent in an un-irradiated sample. The decrease observed in that case is probably a combination of multiple processes, with bleaching being a minor but not insignificant factor. Figure 77 also shows us the shape and position of the laser beam in the sample. This position was chosen to maximize the fluorescence signal, so this position is also where the field of view of the spectrometer fiber coupler is.

10.5 Quantum yield of the fluorescence from a polymer sample

To estimate how much room for improvement there is in the design of the polymer material, a rough estimate of the quantum yield of the fluorescence from a polymer sample was made. An estimate for the fluorescence standard was also made. A camera was set on tripod, pointing at the sample and the fluorescence standard. The polymer sample was highly exposed, to ensure that all of the

laser light was absorbed. Grayscale images of the fluorescence standard and a polymer sample were acquired, with different exposure times to acquire at least 1 image without saturation for both. A piece of white tissue paper was positioned directly in front of the fluorescence standard, to keep the distance to the camera the same. Images of the laser light being scattered from the piece of paper were then acquired, again with a variety of exposure times to avoid saturation of the image. The fluorescent emission from the sample and the fluorescence standard is assumed to be isotropic, while the laser light scattered by the paper is distributed across a half sphere. The images were then normalized by their exposure time and their aperture, to allow for direct comparison. The approximate intensity of the emitted fluorescence and the scattered laser light was then defined as the sum of image brightness across the width of the laser line, averaged over a representative vertical span of the laser line. The intensity of the polymer sample, relative to the scattered laser light, was found to be 0.25%, and for the fluorescence standard it was 0.55%. No attempt was made to account for the variation in how the camera translates photons of different wavelengths into image brightness, so this rough estimate of the quantum yield is probably only accurate within a factor of 3. The low value of the quantum yield suggests that there is room for improvement in this aspect of the radiofluorogenic material. If a material with a significantly higher quantum yield is developed, the dye concentration could be lowered enough to make the radiochromic response negligible without affecting the radiofluorogenic response, which would open up for the possiblity discussed in section 6.9. Samples could be made very transparent without impacting the measured fluorescence if a radiofluorogenic material with a higher quantum yield is developed.

10.6 Section conclusions

The polymer material used in this project is not suitable for dosimetry in the clinical dose range. While the polymer is sensitive to radiation, it is not sensitive enough, compared to the background absorption and fluorescence at zero dose. Further, the dye in the polymer is also sensitive to a lot of factors that are difficult to control, such as the internal temperature during curing, how fast it is cured, and the time elapsed since the curing. These things could potentially be characterized and controlled through further work.

The main problem with the polymer is that it is exothermic during curing, and the developed heat tends to expose the dye. This means that the exposure at zero absorbed dose is inhomogeneous in the sample, and there is no obvious method to control for that. Simultaneously, samples that are cured slowly tend to become highly exposed after curing, for reasons that are not yet understood. Therefore, accurate clinical dosimetry through optical fluorescence tomography cannot work with this particular composition of the dosimeter material. Therefore, further work is needed on the dosimeter material. Currently, the dosimeter material is suitable for high dose applications in the kilo-Gray region.

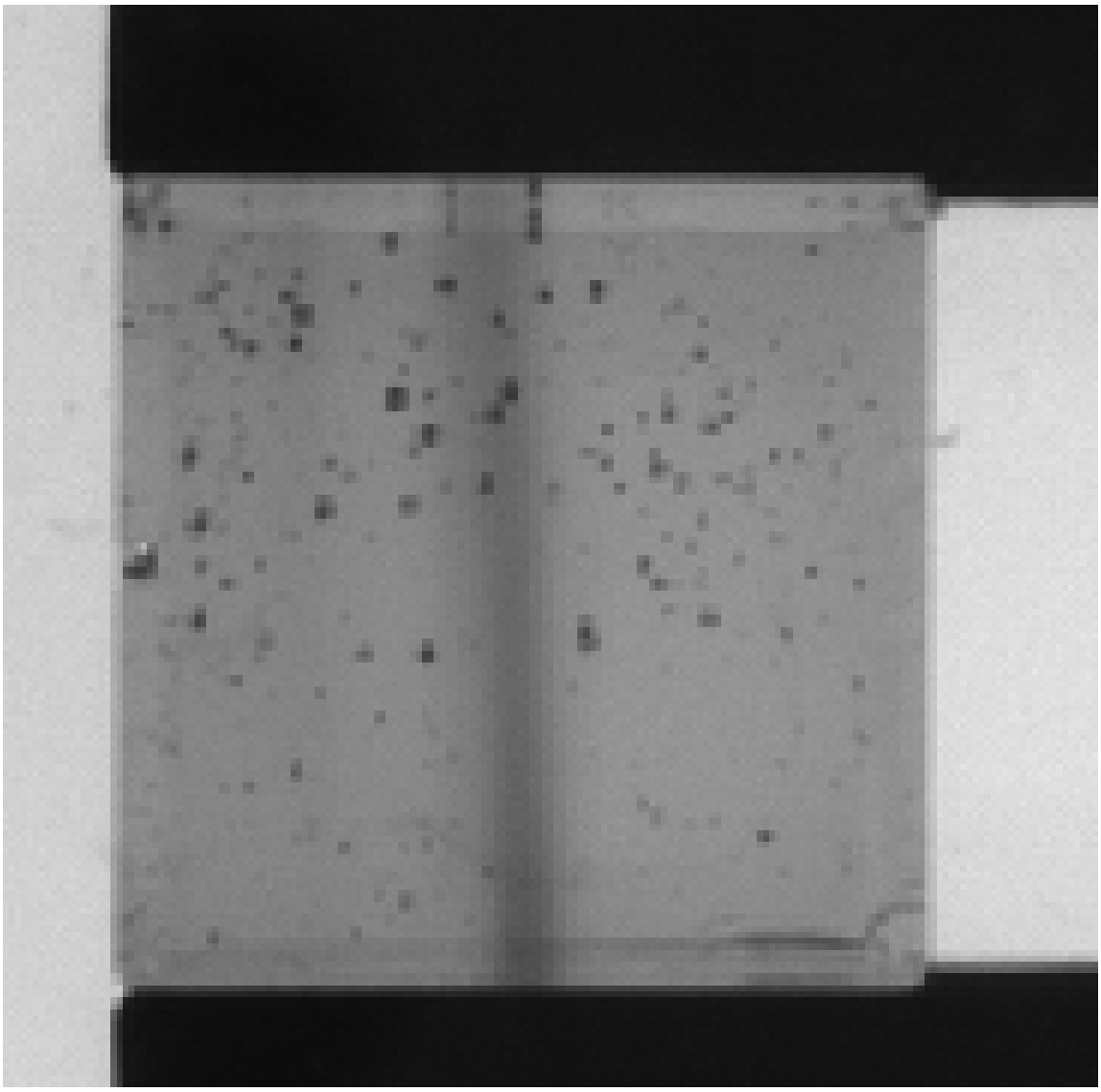

Figure 65: Bubbles in a polymer sample. The light is coming from behind and is being scattered by the bubbles.

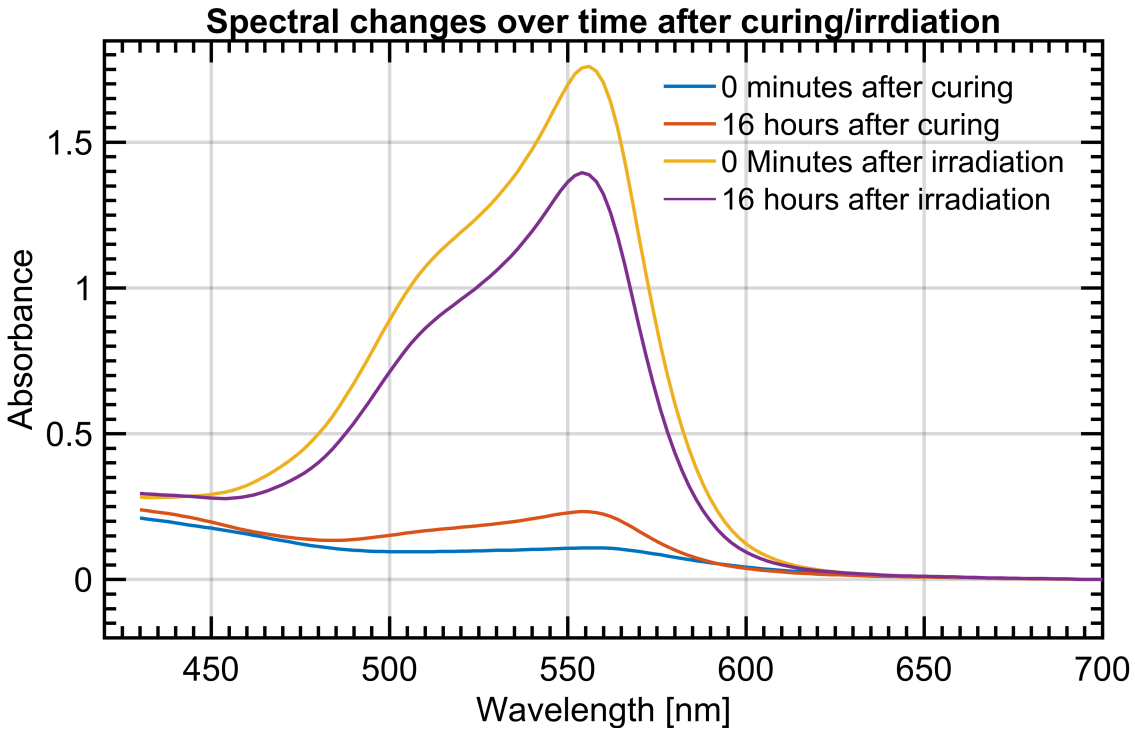

Figure 66: Qualitative changes in the absorption spectrum over time, after curing and after irradiation. It is clear that the change in absorbance comes from a change in the dye concentration.

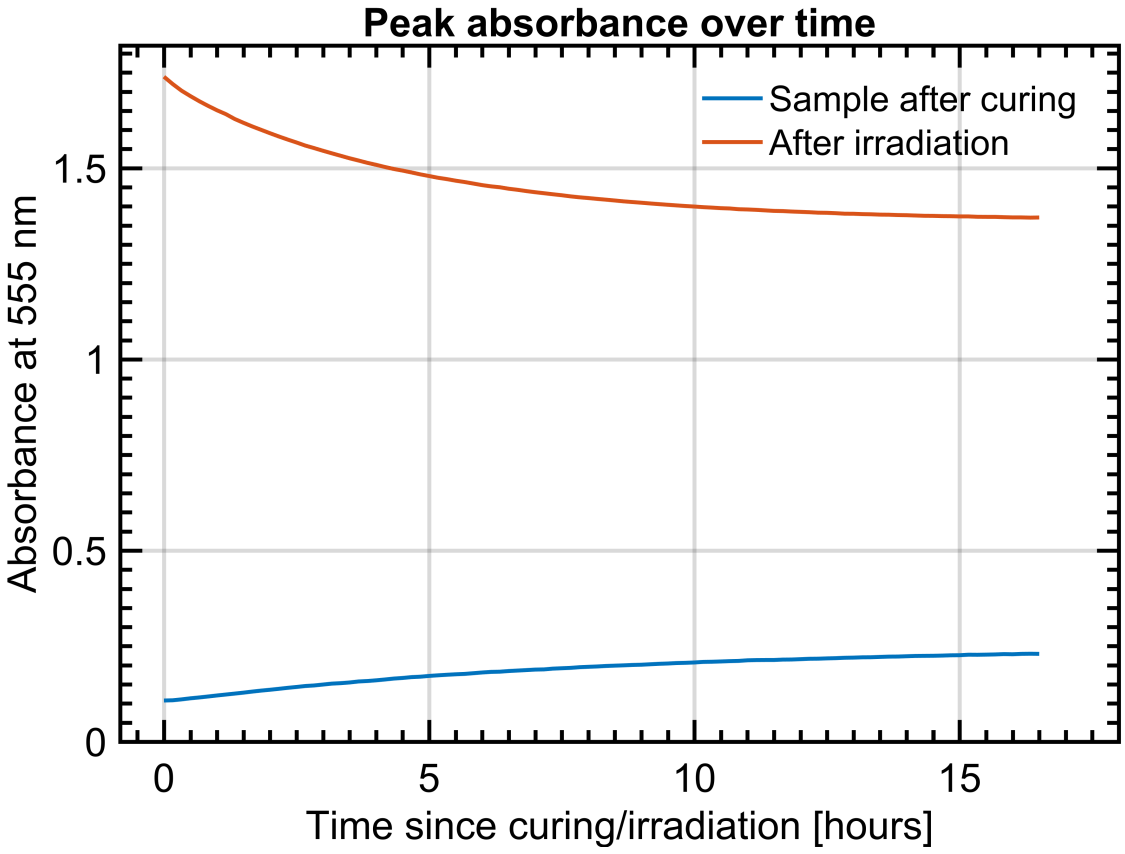

Figure 67: Absorbance at 555 nm over time. After curing it increases towards a new equilibrium. After irradiation it decreases. In both cases the change is consistent with an exponential approach towards some equilibrium value.

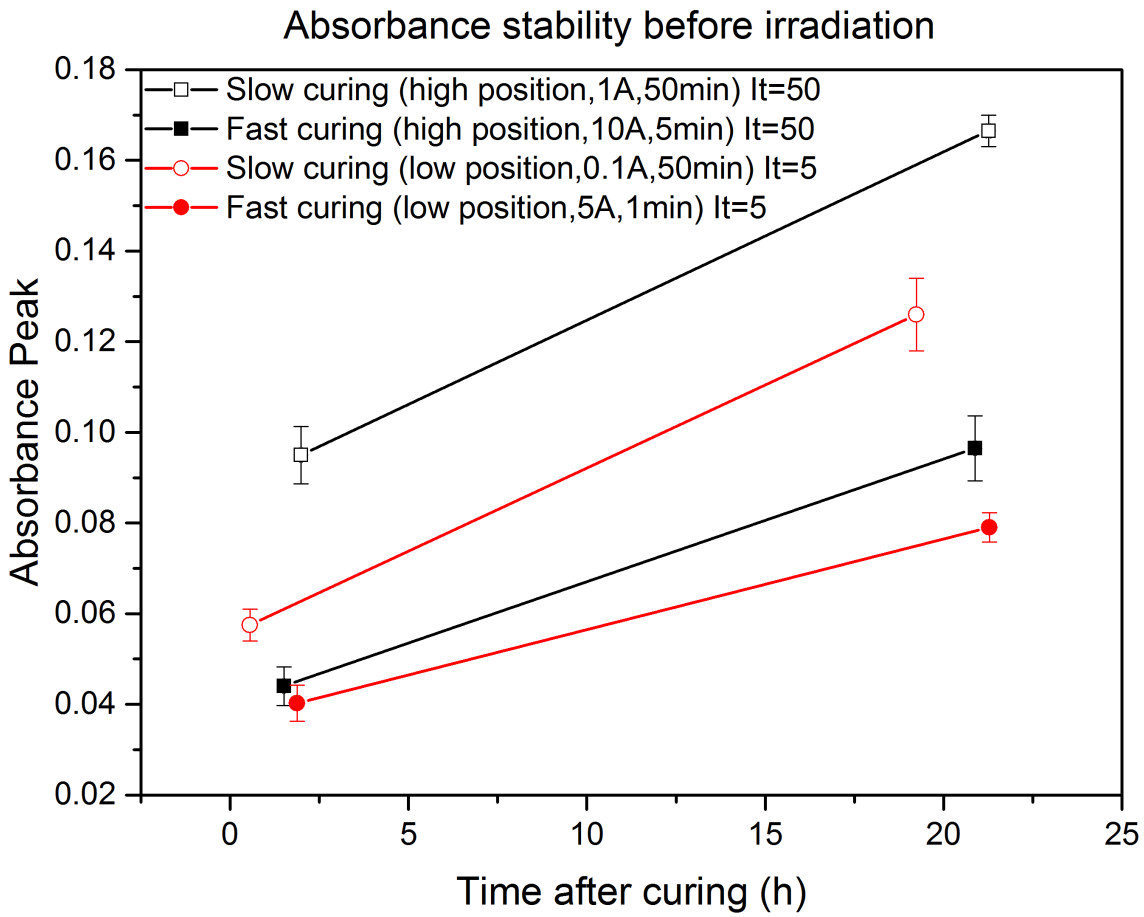

Figure 68: Graph showing how different curing methods affect the stability of the absorbance from the dye, before irradiation. The curing method mostly affects the offset, with faster and longer curing giving a smaller offset. The differences in the slopes are smaller than the error bars and therefore not statistically significant.

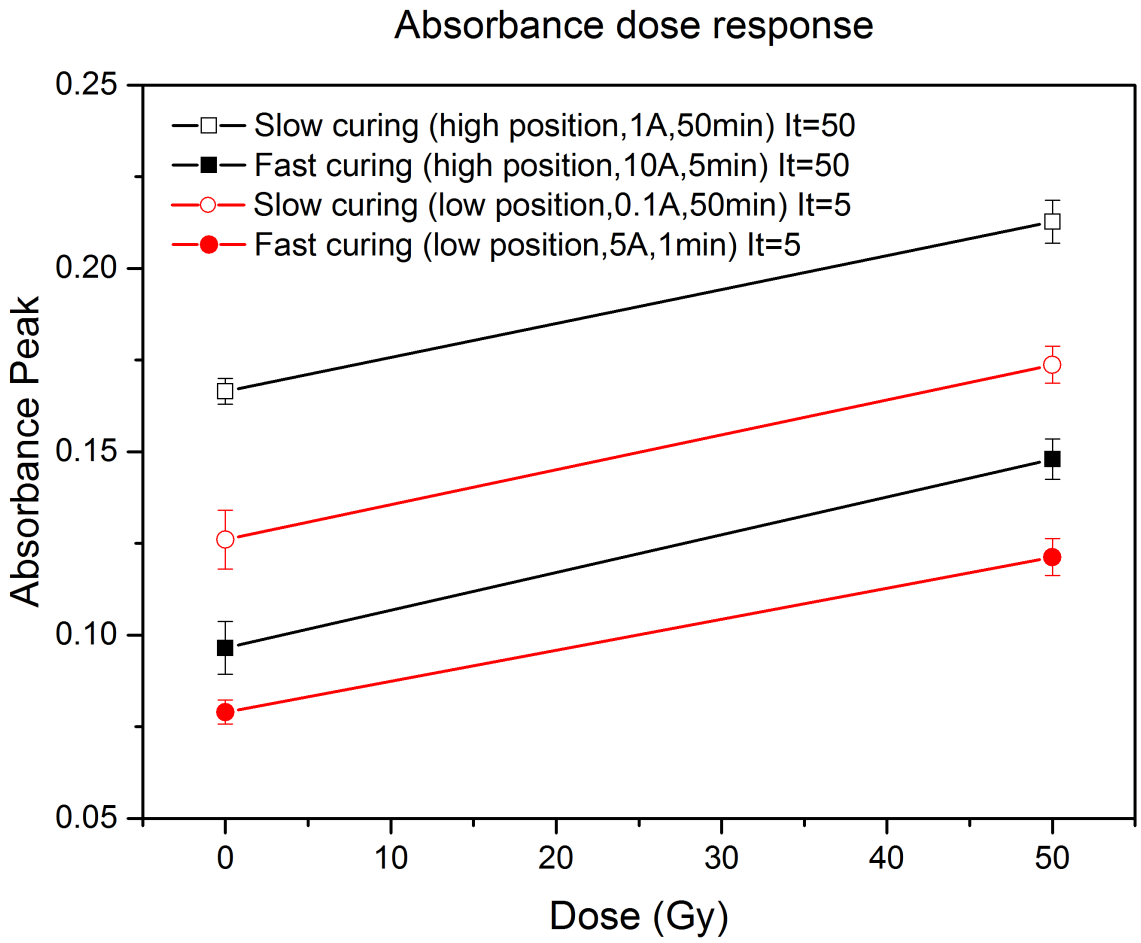

Figure 69: Graph showing how different curing methods affect the absorbed dose response of the absorbance from the dye, after irradiation with 50 Gy in a Co-60 source. The starting point depends on the curing method, but the slopes are identical.

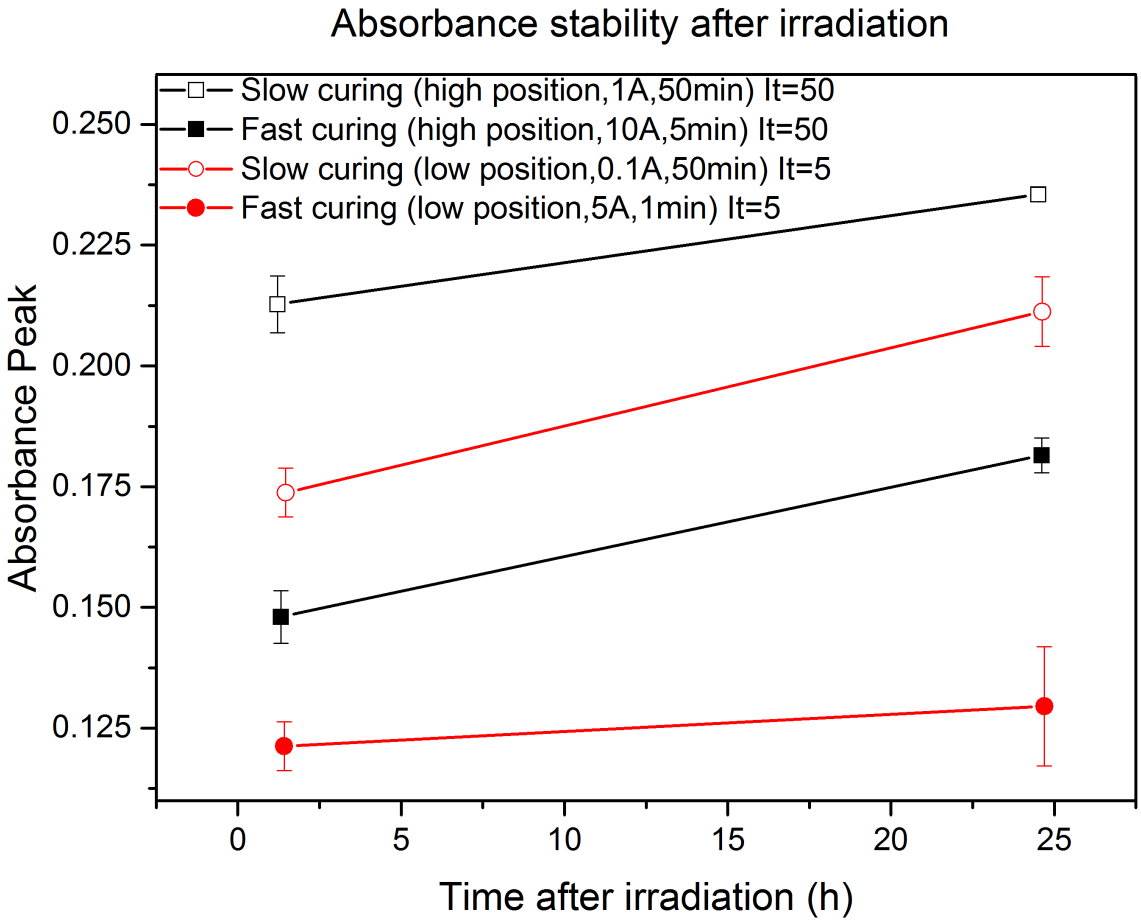

Figure 70: Graph showing how different curing methods affect the stability of the absorbance from the dye, after irradiation with 50 Gy in a Co-60 source. Like before irradiation the curing method mostly affects the offset, with faster and longer curing giving a smaller offset. The differences in the slopes are again smaller than the error bars and therefore not statistically significant.

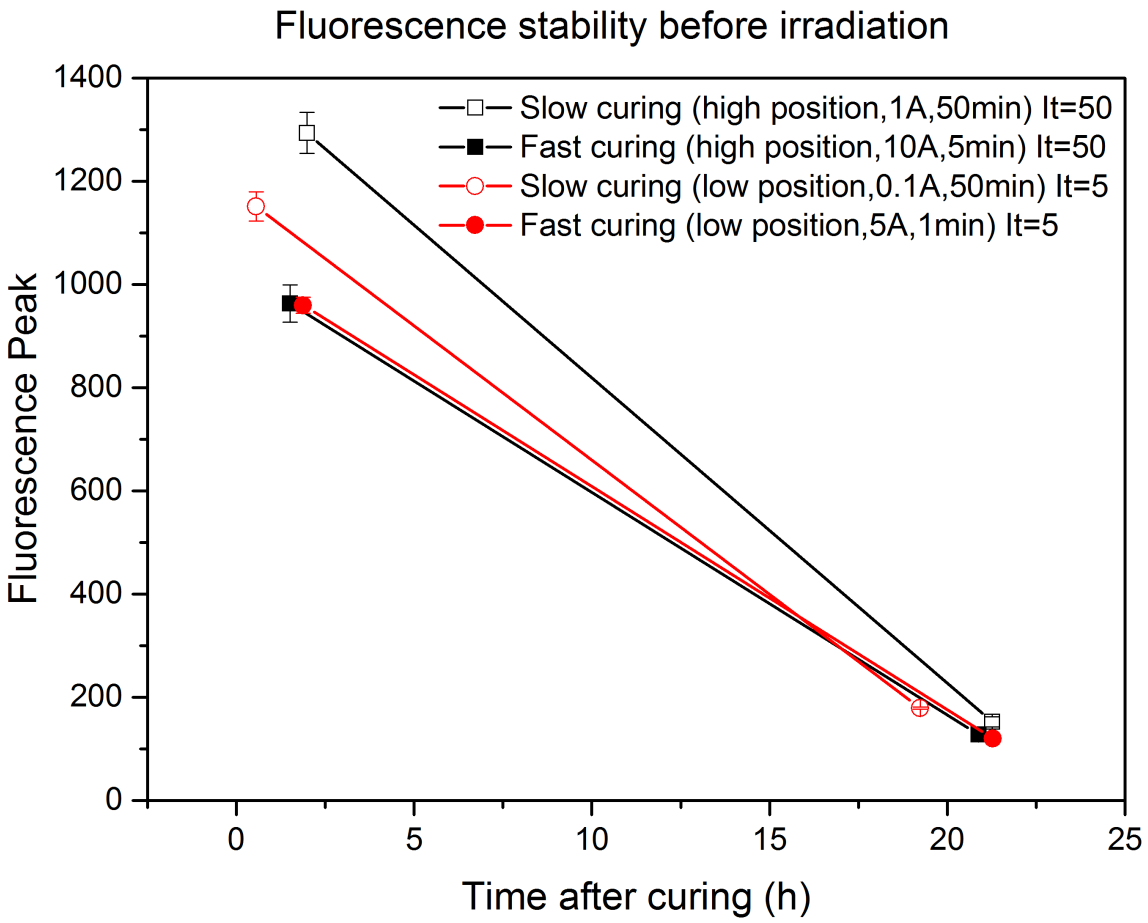

Figure 71: Graph showing how different curing methods affect the stability of the fluorescence from the sample, before irradiation. The curing method has a large effect on the initial fluorescence. After 24 hours the initial fluorescence has almost entirely disappeared.

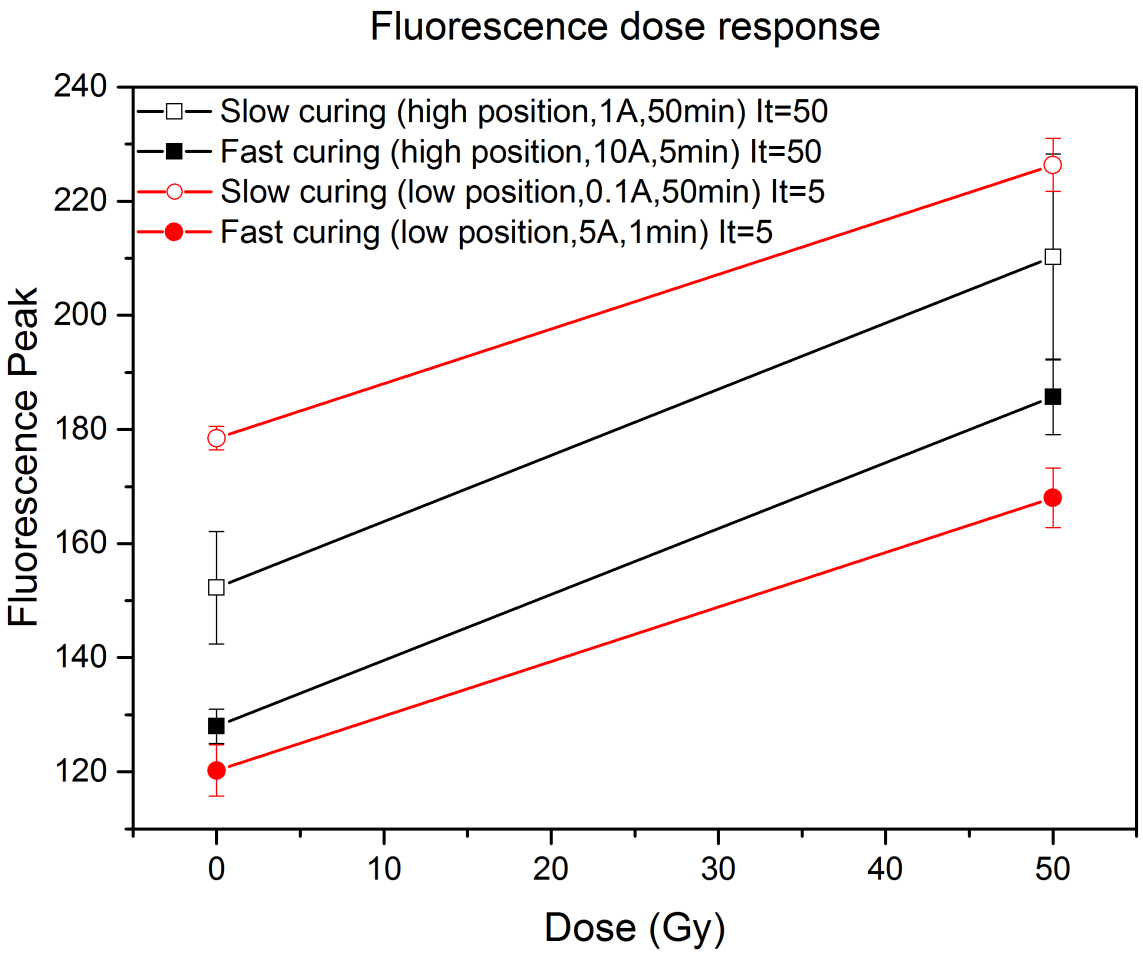

Figure 72: Graph showing how different curing methods affect the absorbed dose response of the fluorescence from the pellets. The differences in the slope are not statistically significant.

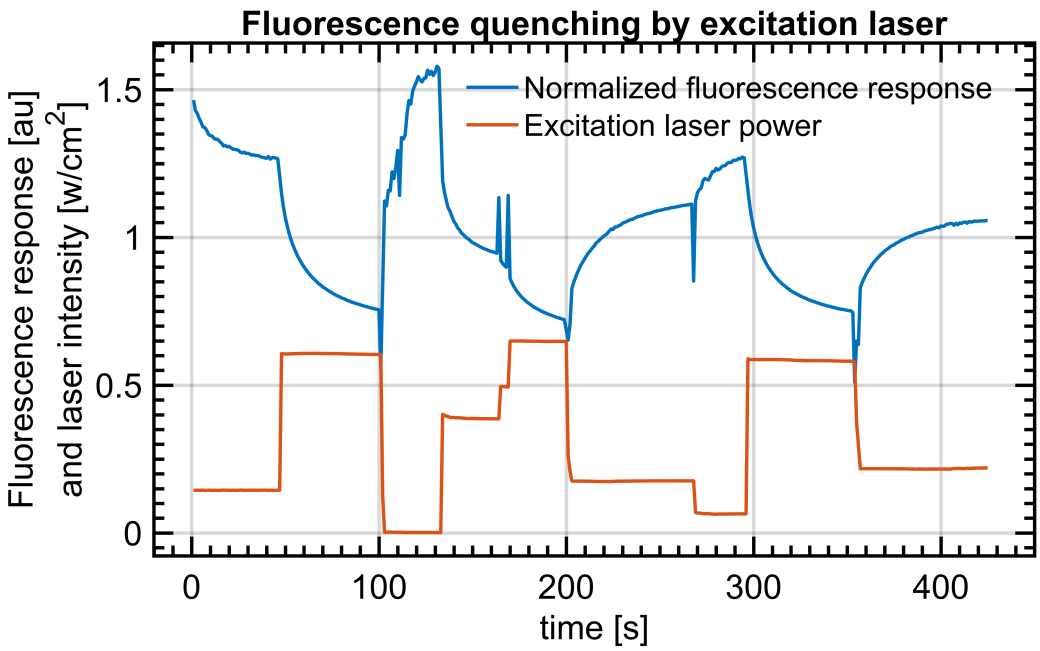

Figure 73: Graph showing how the fluorescence response of a slide sample changes when the excitation laser power is changed. At each stationary laser power, the fluorescence response makes an exponential approach to a new stationary value.

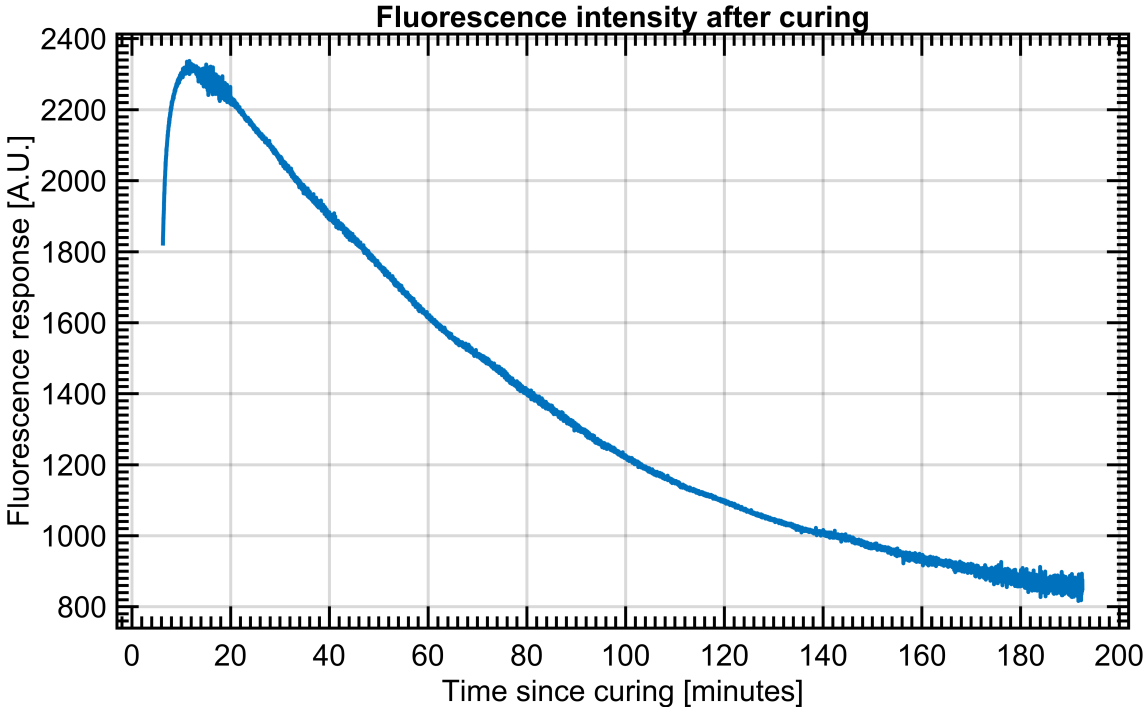

Figure 74: Fluorescence response of a polymer pellet after curing. Note that the fluorescence increases in the beginning, and then appears to decrease exponentially afterwards.

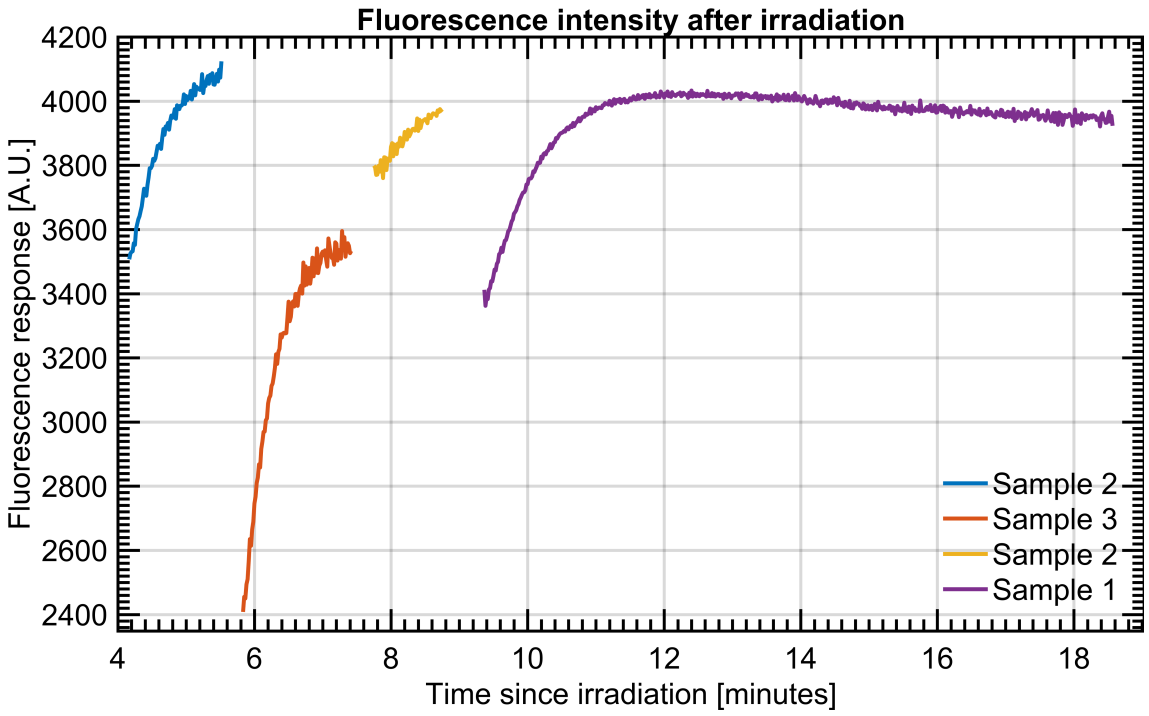

Figure 75: Fluorescence increase of 3 polymer pellets after irradiation. Note that the fluorescence increase seems to be accelerated by the illumination from the setup.

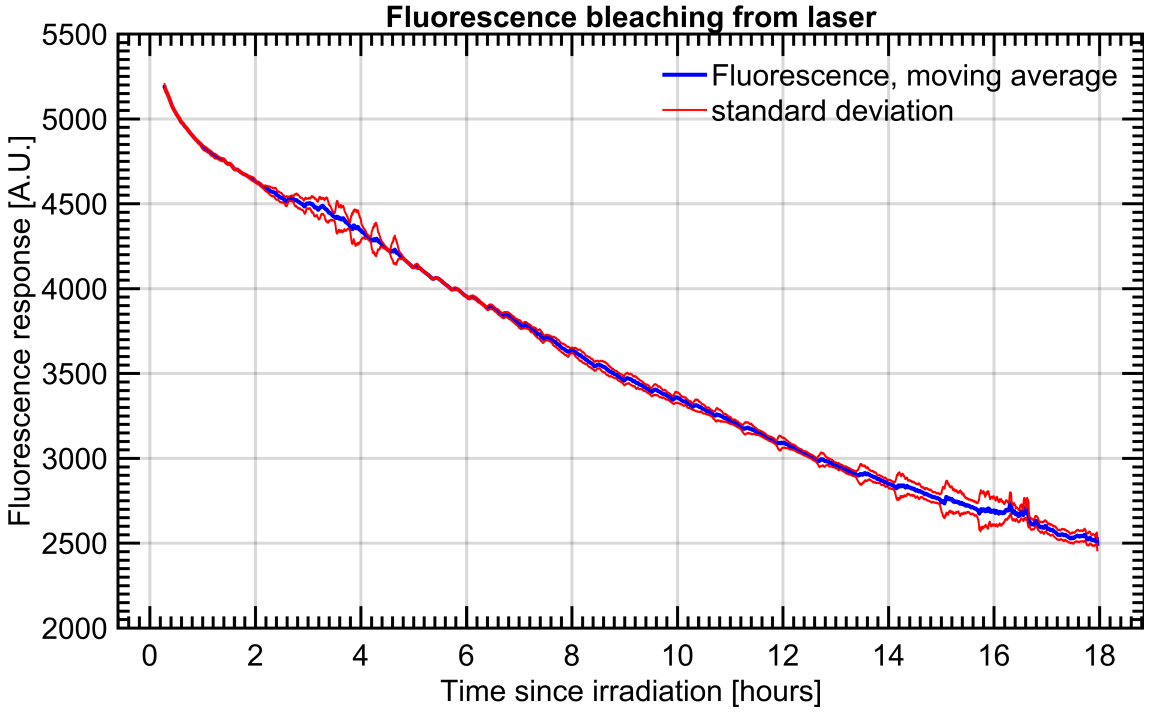

Figure 76: Fluorescence decrease after irradiation. The decrease appears to be linear rather than exponential.

Figure 77: Bleaching of dye due to long term exposure to intense green light.

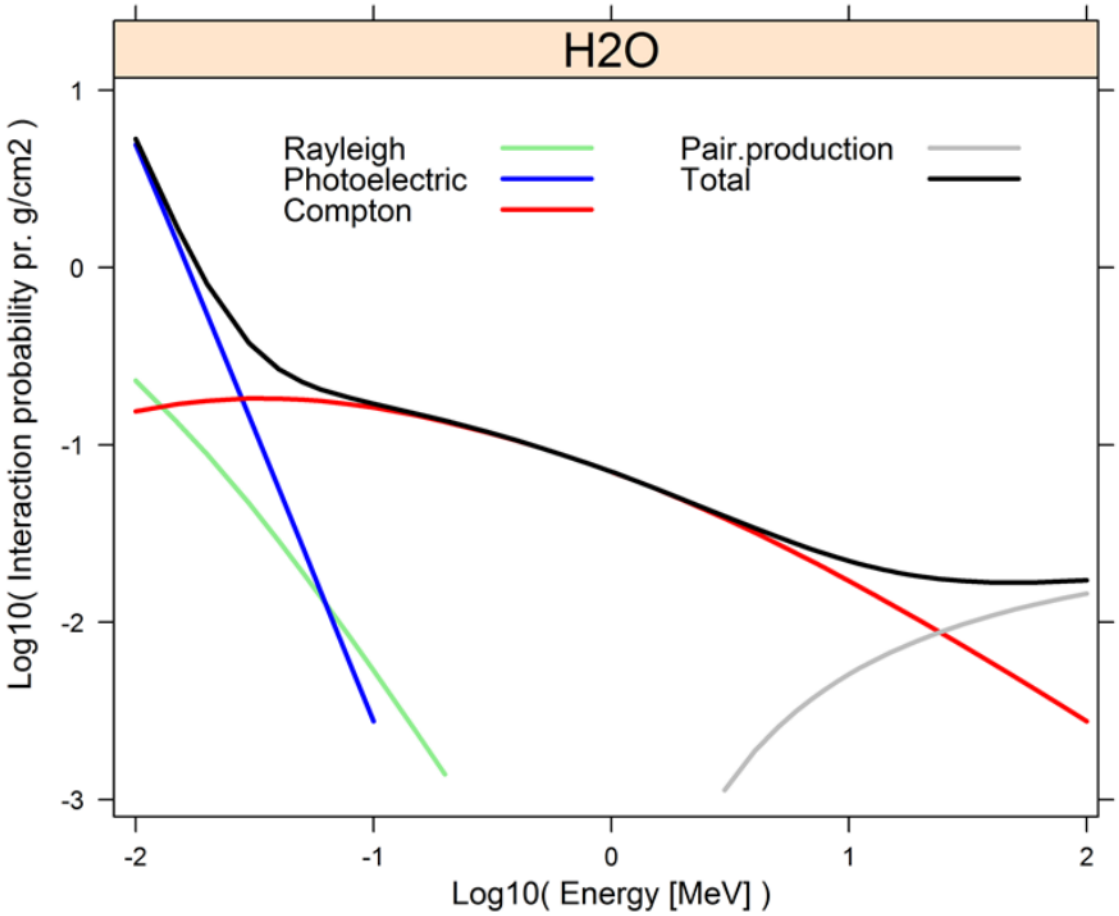

Figure 78: The importance of different interactions between water and photons with different energies. Figure from course materials by C.E. Andersen.

11 Experimental Results

The 3D setup was tested with samples that had been exposed with different kinds of radiation, including 50kV X-rays, 18MeV protons and even two-photon Absorption from a pulsed laser at 600 nm. The idea was to test the reaction of the dye in the polymer to the different kinds of interactions that ionizing radiation can have, such as the photoelectric effect, compton scattering and pair production. For proton beams, the interactions are energy loss through coulomb interactions with the outer electrons, and scattering off the atomic nuclei. The secondary electrons set into motion through these interactions typically have ranges less than 1 mm, so the energy from interactions is deposited locally. Figure 78 shows the interaction probabilities between water and photons with different energies. The production of experimental results was complicated by the fact that it was difficult to prepare samples without internal bubbles. It was also impossible to produce samples larger than 1x1 cm without internal exposure due to overheating, even with external cooling during the curing process. The data were processed with the method described in section 6.8. The material constants were taken from table 2, except for the samples exposed with two-photon absorption, which required modified optical constants to produce a sensible output. The boundary condition was generally an assumption of zero absorbed dose in the right side of the samples, except when otherwise noted, since boundary conditions to the right will minimize the expected error, as shown in section 6. The results from the successful experiments are presented in the following sections.

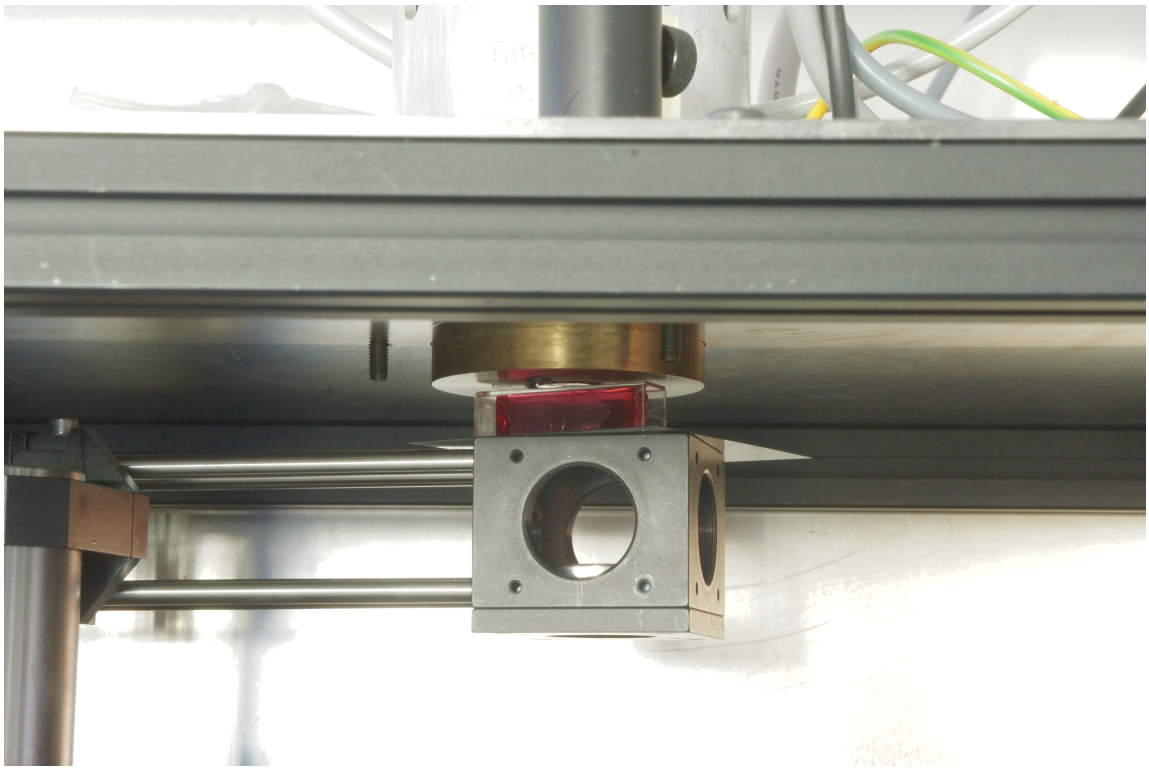

Figure 79: Image of a 1x1x3 cm cuvette sample in position for irradiation with 50kV x-rays through a 15 mm wide aperture.

11.1 50kV x-Rays through Aperture

The irradiation was done with 50kV x-rays through a 15 mm diameter aperture into two samples with different concentrations of dye. The aperture left some of the sample unirradiated, which was useful for generating the boundary condition for the dose reconstruction.
The fluorescence was measured in the 3D fluorescence setup with illumination from 2 different directions. Afterwards, the reconstruction algorithm discussed in section 6.8 was used to find the absorbed dose from the fluorescent images. The absorbed dose in both images was somewhat consistent, but not satisfactorily so. To show the results of the dose reconstruction in 3D, it was plotted as selected iso-dose surfaces, using Matlab. Figure 79 shows how the samples were irradiated with 50kV x-rays. The samples were placed off-center beneath the 15 mm diameter aperture of an x-ray apparatus. The face of the samples closest to the aperture are named as the "top". Figure 80 shows 4 examples of the fluorescence from a scan of a 1x1x3 cm sample that has been irradiated with 50kV x-rays through the aperture. Figure 81 shows the result of a 3D reconstruction of the absorbed dose made from the scan of the sample exemplified in figure 80. The figure shows 4 selected iso-dose surfaces of the 3D volume data. The material constants used for the reconstruction were from line 1 of table 2. There is some uncertainty regarding the the accuracy of these material constants for any given sample, so the calculated absorbed dose may not be accurate. The boundary condition was placed in the left side of the sample, with a best guess at the absorbed dose calculated as described in section 6.8 Figure 82 shows selected isosurfaces from the 3D volume of fluorescence data that the data in figure 81 was calculated from. This illustrates how the calculation is not a simple linear mapping of fluorescence to dose, and why such a linear mapping could be problematic. Figure 83 shows 4 examples of the fluorescence from a second scan of the same sample as in figures 80, 81 and 82. This time, the sample was oriented differently, in order to test the difference between different

boundary conditions in the absorbed dose reconstruction algorithm. Figure 84 shows the absorbed dose reconstructed from the second scan. The material constants were the same as mentioned before, but this time the boundary condition was an assumption of zero absorbed dose in the right side of the sample. This comparison shows that two different scans with different orientations and boundary conditions for the reconstruction can give similar results. The differences between the absorbed dose reconstructed from the two scans is probably due to uncertainty in the boundary condition calculation of the first scan. Figure 85 shows selected isosurfaces from the 3D volume of fluorescence data from the second scan. It illustrates how the orientation of the sample will influence the fluorescence that is measured.
A different sample with 10 times less dye was prepared in the same manner as the previous sample, and scanned 2 times. Both scans had the same sample orientation. Figure 86 shows 4 examples of the fluorescence from the first scan of the low dye sample. The sample was oriented to put the zero absorbed dose region on the right side of the images. In the absence of bubbles and other artifacts in the samples, this boundary condition is the best and most reliable option. Due to the low dye content the fluorescence response, background attenuation and attenuation absorbed dose response is lower. Figure 87 shows the 3D absorbed dose reconstructed from the first scan of the low dye sample. The background attenuation and the attenuation absorbed dose response were the values given in line 3 of table 2. The 3D absorbed dose isosurfaces show clear artifacts from imperfections in the sample. The reconstruction results are still largely similar to the result of the scans of the first sample. Figure 86 shows 4 examples of the fluorescence from the second scan of the low dye sample. This scan had a 6 times longer exposure time for the camera, which should give better signal to noise for the fluorescence data. Increasing the exposure time and/or gain runs the risk of saturating the camera sensor. The orientation of the sample was the same as the first scan. Figure 87 shows the 3D absorbed dose reconstructed from the second scan of the low dye sample. The material constants and boundary condition were the same as for the first scan. The result is nearly identical, which illustrates that the results of scanning are reproducible, and that the artifacts in the reconstruction stem from imperfections in the sample, rather than from noise in the fluorescence signal.

11.2 Proton Beam Experiment

One of the main motivations for 3D dosimetry is to perform research into the absorbed dose distribution of particle beams, such as proton beams or carbon-ion beams. One of the challenges for measurement of such beams is the high absorbed dose rate and high LET that these particles have, particularly at the Bragg peak. Figure 90 shows how the stopping power of protons in water increases as the proton energy decreases. Since the energy loss per cm increases as the proton loses energy, there will be a short range where the proton will lose its remaining energy. This range is called the Bragg peak. To investigate the behavior of the radiofluorogenic polymer under these conditions, we irradiated a range of samples with a proton beam, and imaged the resulting samples in the 3D setup. The accelerator was normally used for production of medical radionuclides, so the energy was a relatively low 18 MeV, while the absorbed dose rate was extremely high. The first samples were burned by by the beam, until the accelerator current was turned down below its monitoring threshold. Therefore, the absorbed dose delivered to the sample is unknown. Most of the samples were overexposed, rendering them completely opaque at the Bragg peak and therefore unsuited for readout in the 3D setup. Only one sample, with its dye concentration at 10% of normal, was suitable for readout after the irradiation. The material constants used for the reconstruction were taken from table 2, line 3. The images were acquired with a different camera lens that allowed for closer zooming on the samples, and therefore better spatial resolution in the xy-plane. Figure 91 shows 4 examples of the fluorescence images from a scan of the proton irradiated sample. The The curve in the second image is a dimple in the bottom of the cuvettes that we cure the samples in. The lines in the third and fourth image are from reflection of the emission light by the interface between the sample and the index matching fluid. Figure 92 shows the absorbed dose reconstructed from the first image in figure 91. The sample starts at x=0, but continues beyond

the bragg peak. The absorbed dose goes to zero after the bragg peak. Note how the side straggling increases with depth. Figure 93 shows the absorbed dose reconstructed from the second image in figure 91. The bragg peak follows the curve of the dimple in the sample. Figure 94 shows selected iso-value surfaces of the absorbed dose distribution. The curve of the surfaces is due to the dimple in the bottom of the cuvettes that the samples were cured in. The proton beam from the cyclotron was not monochromatic nor was the spatial distribution of the proton fluence rate well defined. Both of these characteristics can reduce the relative height of the Bragg peak. An experiment with a monochromatic beam and a well defined aperture would allow a better characterization of the Bragg peak and lateral straggling of the protons due to nuclear interactions.

11.3 Determination of Setup Spatial Resolution

To test the XY spatial resolution, a sample with a sharp discontinuity in the absorbed dose distribution was needed. The contrast provided by the Bragg peak in the sample irradiated with protons was suitable for this. In particular, the dose distribution shown in figure 92 was used to determine an upper limit on the XY plane spatial resolution of the 3D readout setup. Figure 95 shows how an upper limit for the XY spatial resolution in the dosimeter was calculated from figure 92. Line profiles across the Bragg peak were made, and then the distance from 75% to 25% of the peak value was calculated. The distribution of these distances from all the lines in figure 92 are shown on the right. The mean of this distribution is 85 μm and the minimum is 75 μm.
The spatial resolution in the Z-direction should be limited by the thickness of the laser light sheet. To test this, the dose distribution in figure 100. Figure 95 shows the distribution of Z direction spatial resolution in the dosimeter as calculated from 100. The mean of this distribution is 0.8 mm, and the minimum is 0.2 mm. This puts the upper bound for the spatial resolution around 0.8 mm, which is slightly higher than the expected value of 0.5 mm. This discrepancy may be because the dose contrast in the chosen 3D absorbed dose distribution is not as sharp as it could be.

11.4 Two Photon Exposure Experiment

It would be useful to be able to mark the polymer samples in a way that allows us to determine their exact orientation and position solely from the fluorescence data. One way to do this would be to expose small spots within the samples in a controlled fashion.
With 4 exposed points with known positions, the spatial orientation and scaling of the sample in a 3D fluorescence data set could be determined unambiguously, which would be critical for any clinical application of the dosimetry system.
One possible way to achieve controlled exposure inside a sample would be two-photon absorption. The dye used in the polymer has previously been observed to be sensitive to UV light around 270 nm to 340 nm[18]. This has been corroborated by subjecting pellet and slide samples to sunlight, which causes a visible color change within a few seconds. At the same time, the dye is also insensitive to the visible light typically used indoors, along with the 395 nm UV light used to cure the samples. Therefore it should be possible to use two-photon absorption, a non-linear optical effect, to expose the dye in the samples. This process might have a practical application, by exposing small spots at pre-defined locations within a sample, in order to provide a reliable reference for the location, orientation and scaling of the sample in the final 3D fluorescence data.
Exposure of small spots could be achieved by focusing a pulsed laser into the sample, similar to a method used for 3D microfabrication[17] through photo-polymerization.
Since the strength of two-photon absorption scales with the square of the light intensity[3, p. 880], the dye exposure should be localized to a small spot at the focus of the laser.
The first attempt to do two-photon exposure of a sample was performed with a nanosecond laser at 532 nm. The pulse energy was high enough to leave scorch marks on the surface of the samples, where the beam was still unfocused. When the beam was attenuated it was still powerful enough to vaporize polymer and create bubbles on the inside of the samples, instead of exposing the dye. There was no level of attenuation that successfully exposed the samples without destroying the

polymer at the focus.
The reason for this is that the wavelength of the pulsed laser was at the peak of the absorption band of the exposed dye. Therefore, any dye exposed by a two-photon process would also absorb highly at 532 nm, leading to local destruction of the sample at the focus of the laser. At the 532 nm laser wavelength, any laser intensity high enough for two-photon exposure will also be high enough to damage the polymer material.
At a later date the experiment was repeated with a tunable femtosecond laser. It was a femtosecond optical parametric amplifier, pumped by a femtosecond amplifier[7]. The pulse length and energy was 50 fs and 40 μJ, with a pulse repetition rate of 1 kHz.
With this laser it was possible to try other wavelengths, particularly outside the absorption band of the dye. It was determined that the best wavelength for producing the two-photon exposure is around 610 nm, because the dye is transparent at this wavelength, while it is also sensitive to the 305 nm photons that the two-photon process produces in the sample. 532 nm photons do not work, because they get absorbed by the exposed dye, which protects the interior of the sample from the effect. A sample was exposed to pulses of 600 nm light from a femtosecond laser. The sample immediately changed colors when exposed to the laser pulses. This shows that the sample was exposed through a two-photon process, since the polymer is not normally sensitive to light in the visible wavelengths. Figure 97 shows isosurfaces from a 3D reconstruction of a scan of this sample. The constants used for the reconstruction were from table 2 line 1, except for $B_C = 0.43$ cm^{-1} and $R_C = 4.7$ cm^{-1}kGy^{-1}.
The laser had been focused with an f=100 cm lens, and the sample was placed as close to the focues as possible. Three distinct beams are visible, with the focal point being inside the sample for at least the bottom left one. The less-exposed areas are from movements of the sample through the beam.
The initial exposure of a sample revealed that the laser was powerful enough to expose the polymer within fractions of a second. It was also found that the focus of the laser could damage the sample, by evaporating microscopic bubbles inside it. Figure 98 shows the lase mode after being disrupted by such bubbles in a sample. The output of the femtosecond laser was tunable in wavelength, so several different samples were exposed to 10 seconds of illumination with wavelengths ranging from 580 nm to 640 nm. This was done to determine the wavelength at which the polymer is most sensitive to the two-photon process, while still being outside the absorption band of the exposed dye. It is apparent from figure 99 that the optimal wavelength is somewhere between 600 nm and 620 nm. A 3D scan was performed on one of the samples, and figure 100 shows selected isosurfaces from the exposure reconstruction. The constants used for the reconstruction were from table 2 line 1, except for $B_C = 0.40$ cm^{-1} and $R_C = 3.0$ cm^{-1}kGy^{-1}. Attempts to create more localized spots in the samples were made. The f=100 cm lens was replaced by an f=10 cm lens, and a sample was positioned as close to the focus as possible. It was moved around multiple times in attempts to improve the positioning. Figure 101 shows the exposure reconstruction of this sample. The constants used for the reconstruction were from table 2 line 1, except for $B_C = 0.39$ cm^{-1} and $R_C = 3.5$ cm^{-1}kGy^{-1}. The exposed point in the middle represents a successful attempt to place the focus fully inside the sample. An attempt to make an even more focused spot was made.
The laser was focused with a f=2 cm lens, and a sample was placed to put the focus inside. This time, the strong focusing of the laser lead to huge light intensity at the focus, which gasified the polymer locally instead of merely exposing it, leading to microscopic bubbles in the polymer. After attenuating the laser even further, it was difficult to determine if the sample was being exposed or not. Figure 102 shows the reconstructed exposure from one of the samples placed at the focus of the 2 cm lens, after attenuation of the laser. The constants used for the reconstruction were from table 2 line 1, except for $B_C = 0.44$ cm^{-1} and $R_C = 4.0$ cm^{-1}kGy^{-1}. The spot on the right was probably exposed by the laser. The exposure in the middle of the sample is because the sample was cured too quickly and without sufficient cooling.
For some reason, the samples used for these measurements had a higher background attenuation and a higher radiochromic response than for the other experiments. The higher background can partially

[7]TOPAS and Spitfire XL from Spectra Physics.

be explained by longer time between curing and exposure and readout. The higher radiochromic response is harder to explain. It may be the case that it should have been the radiofluorogenic response, R_F, that was lower for the exposure with two-photon absorption.

11.5 Section conclusions

These experiments show that the absorbed dose reconstruction algorithm can be used on data from the real world setup, if the material constants are known and consistent, and the samples are free of imperfections. Further, the scans of the same sample from different directions show that the result of readout scans and reconstructions can be reproducible.
The samples are sensitive to irradiation with protons, but the Bragg peak was lower than expected. It is unclear if the lower-than-expected Bragg peak is due to quenching at high absorbed dose rates, nonlinearity at high doses for the polymer, or something else.
This proton beam data set shows that the 3D setup might be useful to study off-axis straggling and other aspects of the absorbed dose distribution of proton irradiation.
The spatial resolution in the xy-plane was determined to be be limited by the camera optics, with an upper bound of 85 μm. The spatial resolution in the z-direction is also expected to be limited by the thickness of the light sheet, and an upper bound of 0.8 mm was established.
It was determined that the dye in the dosimeter can be exposed through two-photon absorption of light with wavelengths in the 580 nm to 640 nm range. The optimal wavelength for two-photon exposure was determined to be in the range from 600 nm to 620 nm.
A tentative confirmation that localized exposure can be achieved with a focused pulsed laser was also made. Such localized exposure can potentially be used to make reference points or lines in larger samples.

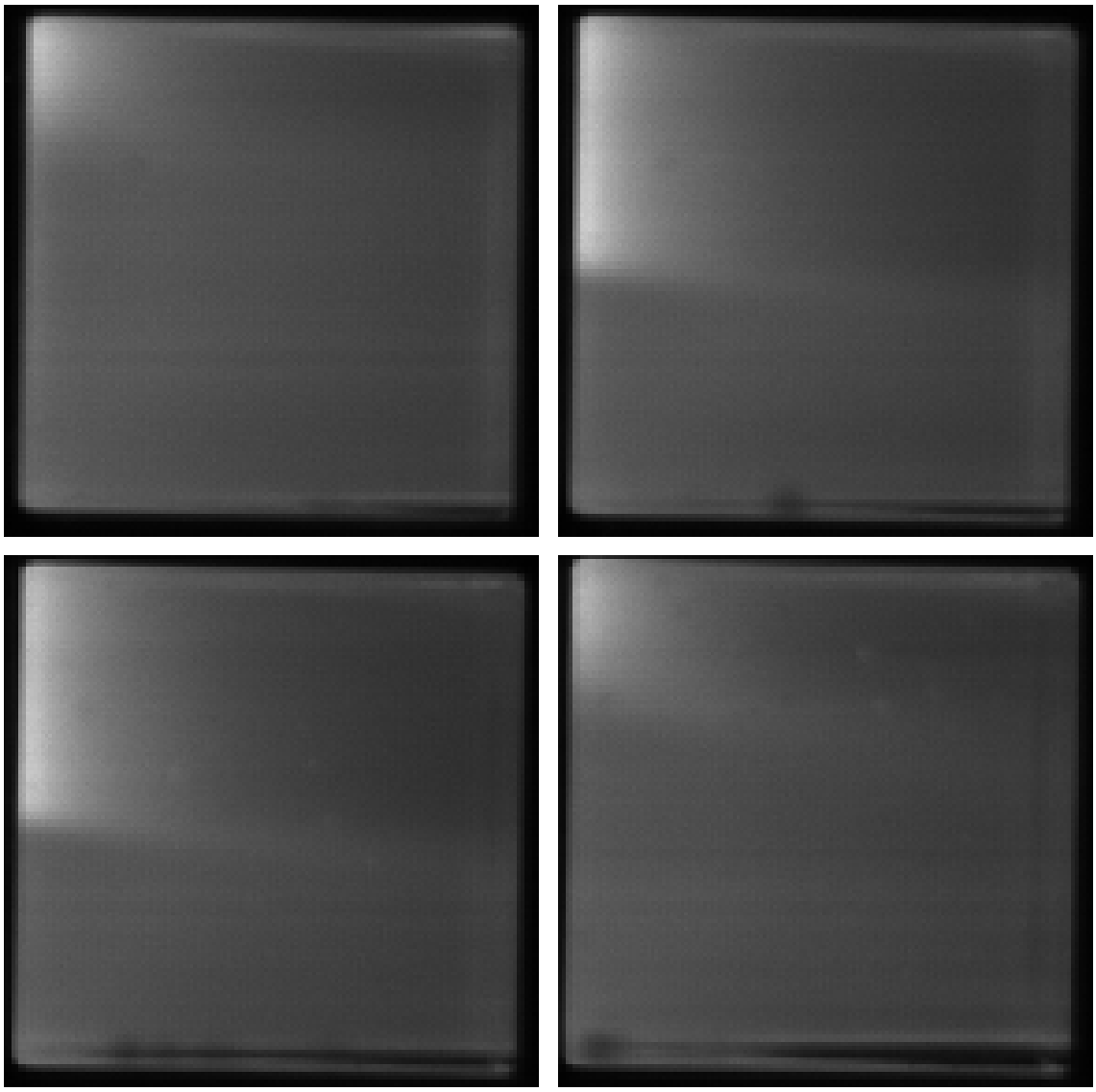

Figure 80: Fluorescence from a 1x1x3 cm cuvette sample irradiated with 50kV x-rays through a 15 mm wide aperture. The "top" of the sample is facing left.

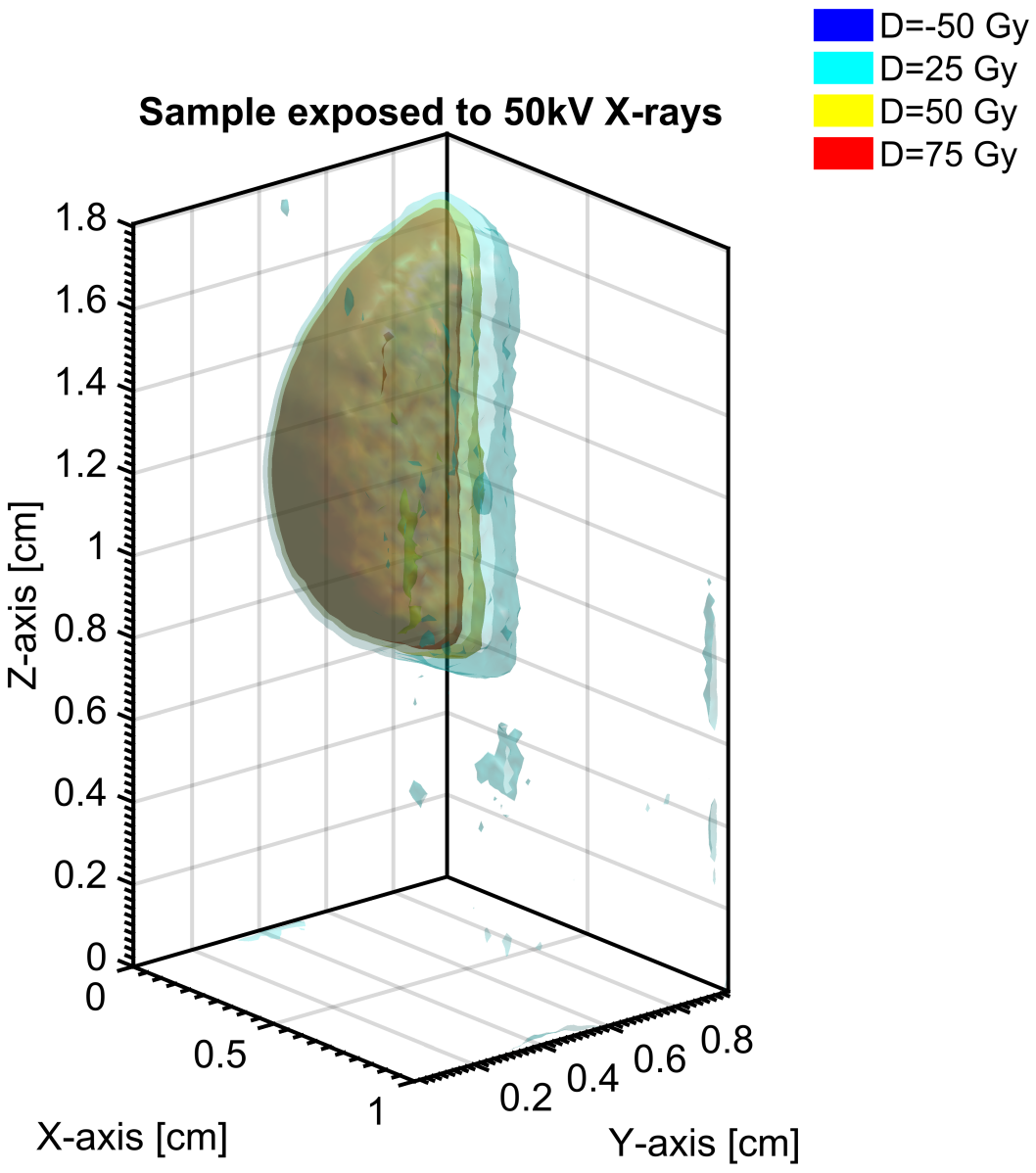

Figure 81: 3D absorbed dose distribution in a sample sample irradiated with 50kV x-rays.

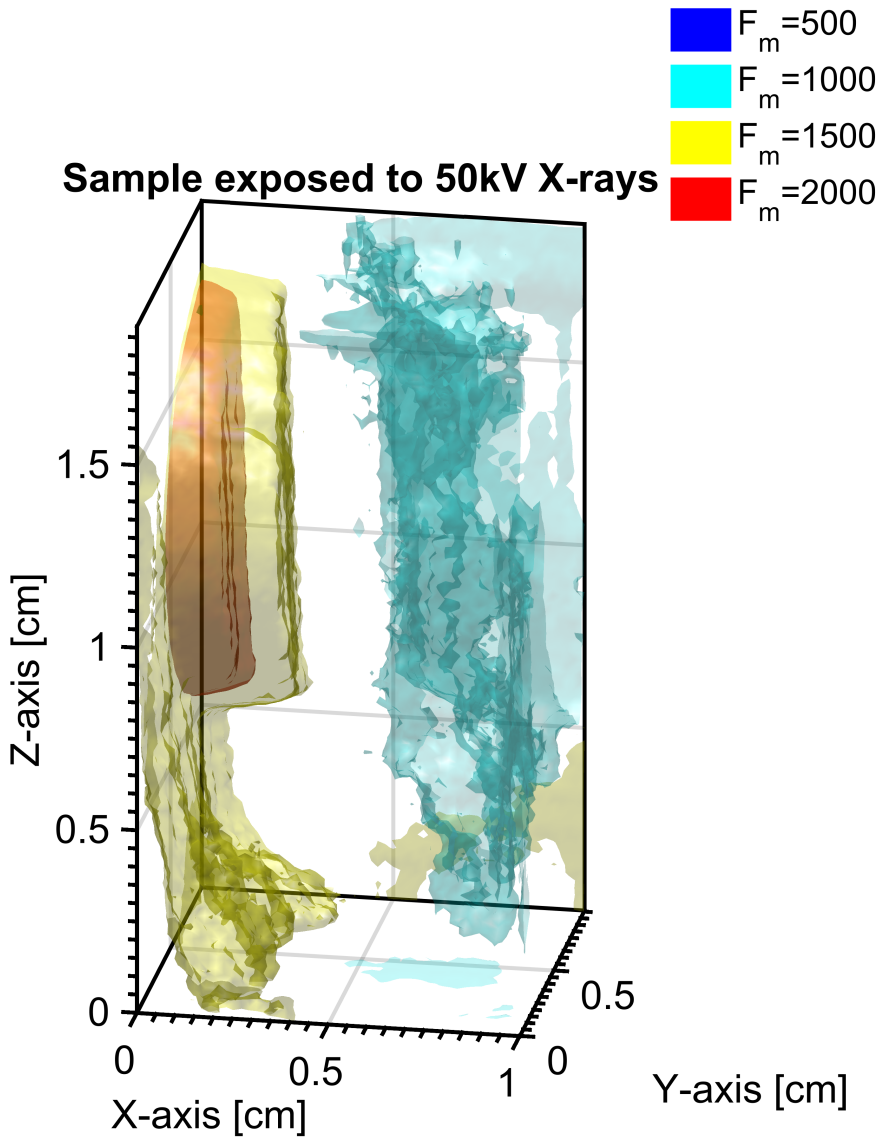

Figure 82: 3D fluorescence from a sample irradiated with 50kV x-rays.

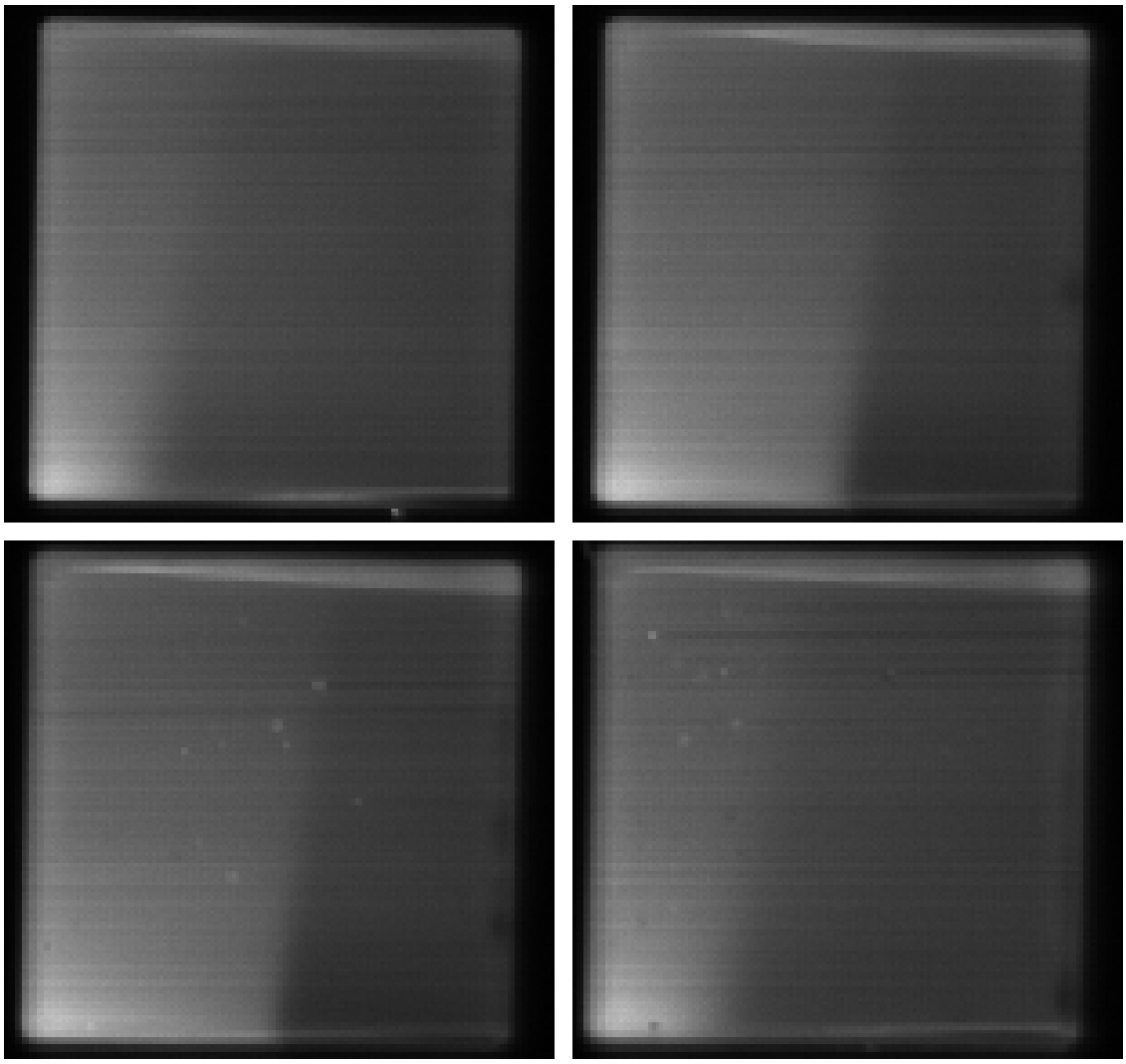

Figure 83: Fluorescence image examples from a 1x1x3 cm sample irradiated with 50kV x-rays through an aperture. The "top" of the samples is facing down in these pictures.

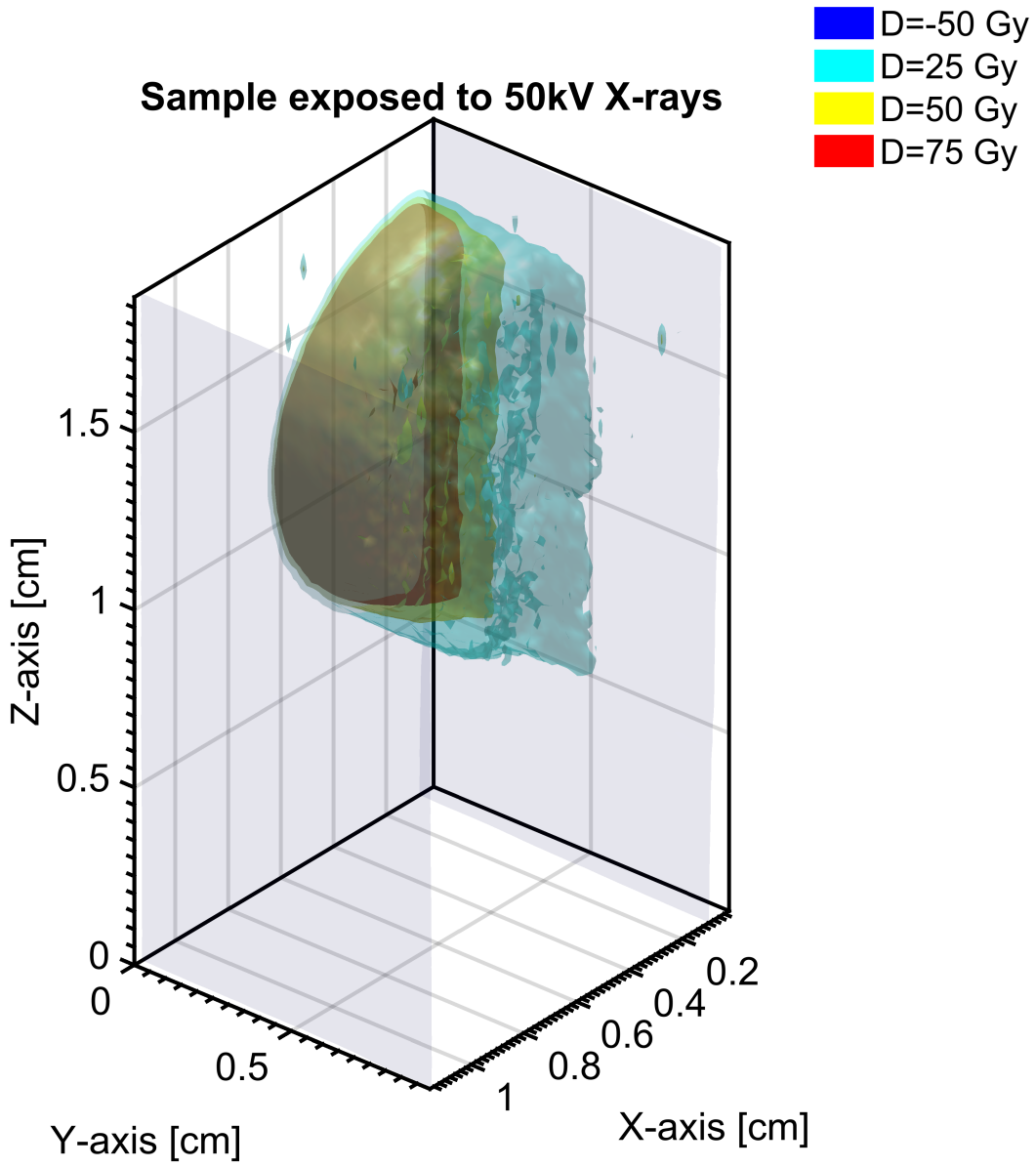

Figure 84: 3D absorbed dose distribution in a sample sample irradiated with 50kV x-rays.

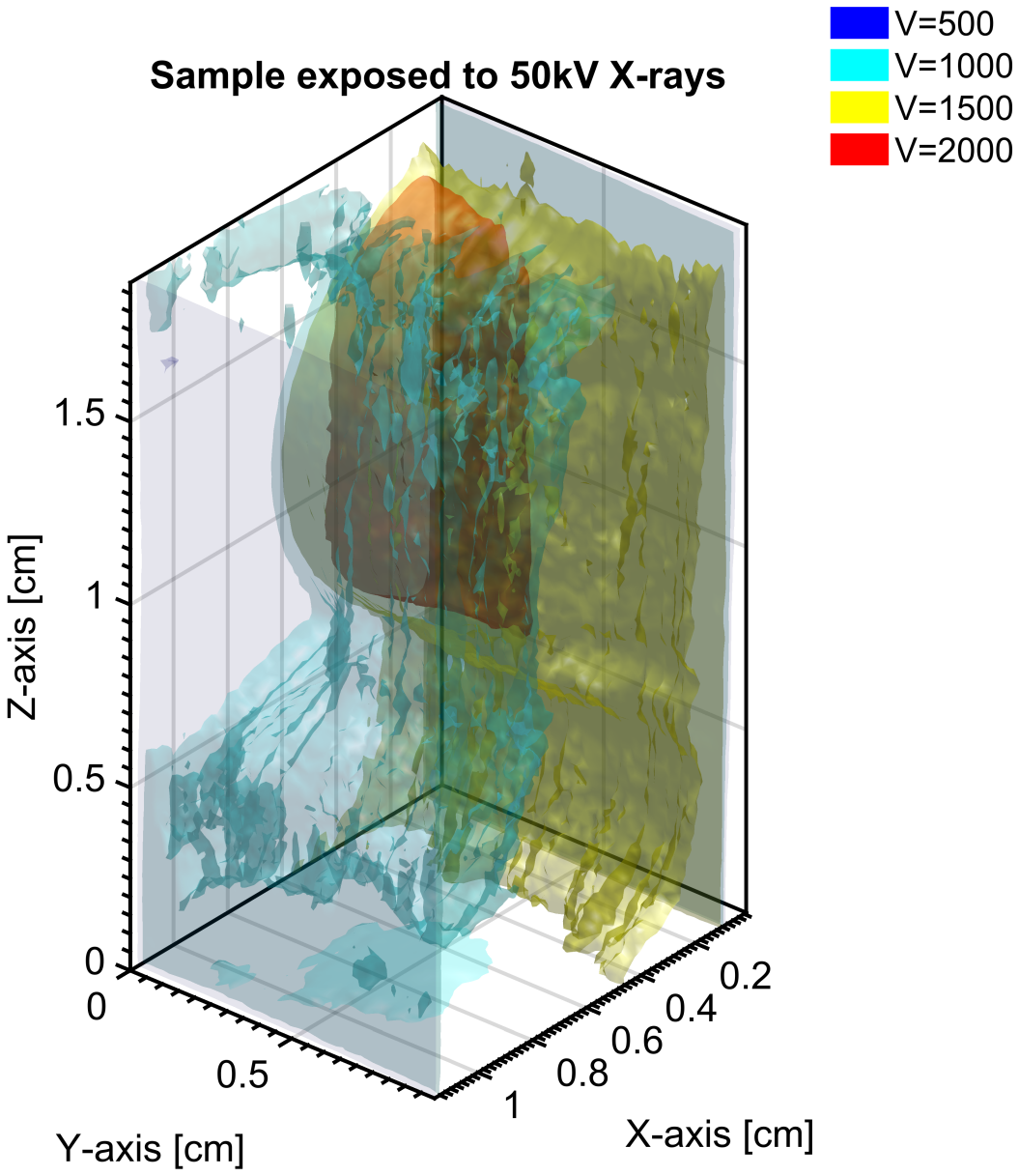

Figure 85: 3D fluorescence from a sample irradiated with 50kV x-rays. The x-rays

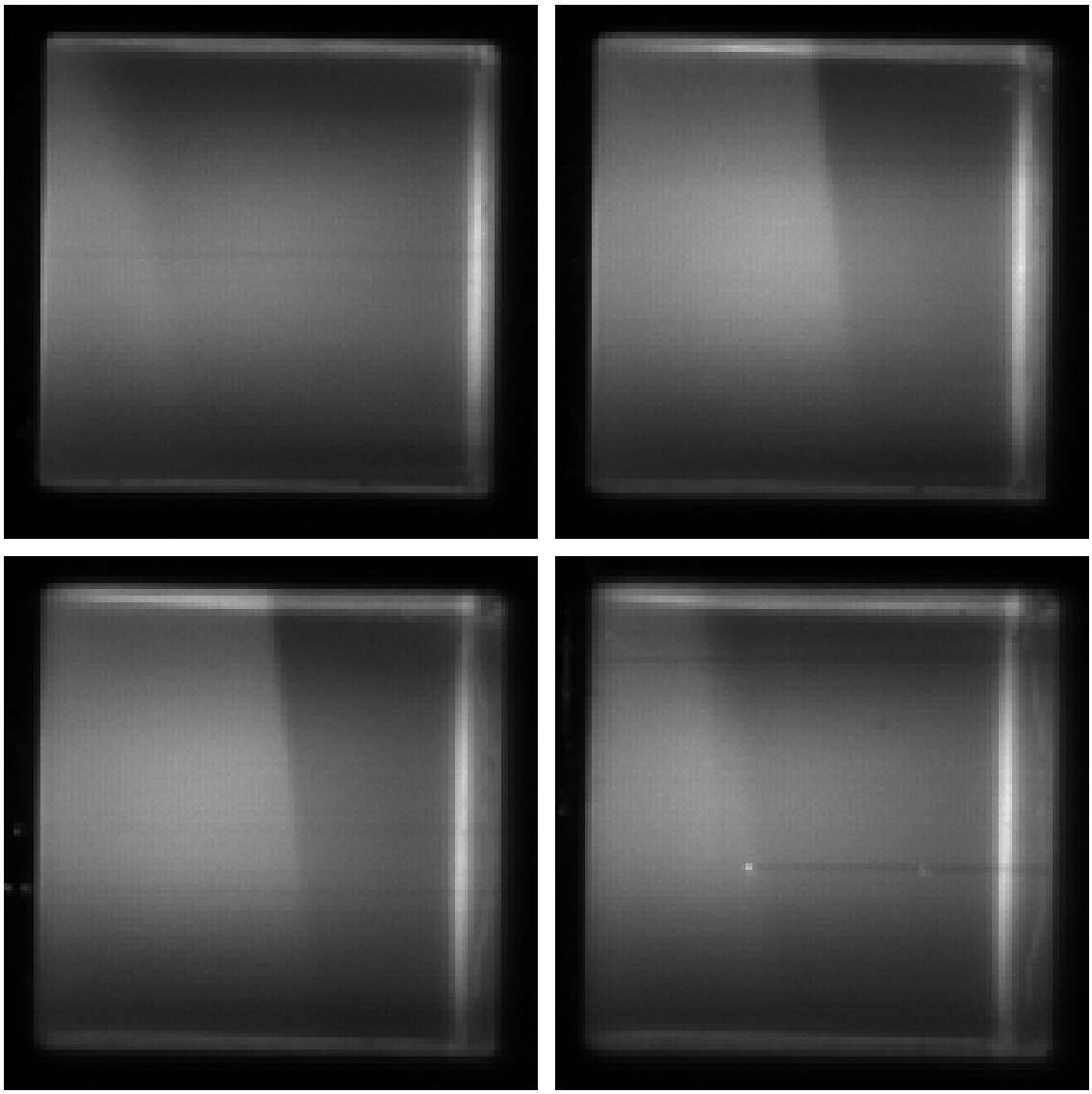

Figure 86: Fluorescence image examples from a 1x1x3 cm low dye sample irradiated with 50kV x-rays through an aperture. The "top" of the samples is facing up in these pictures.

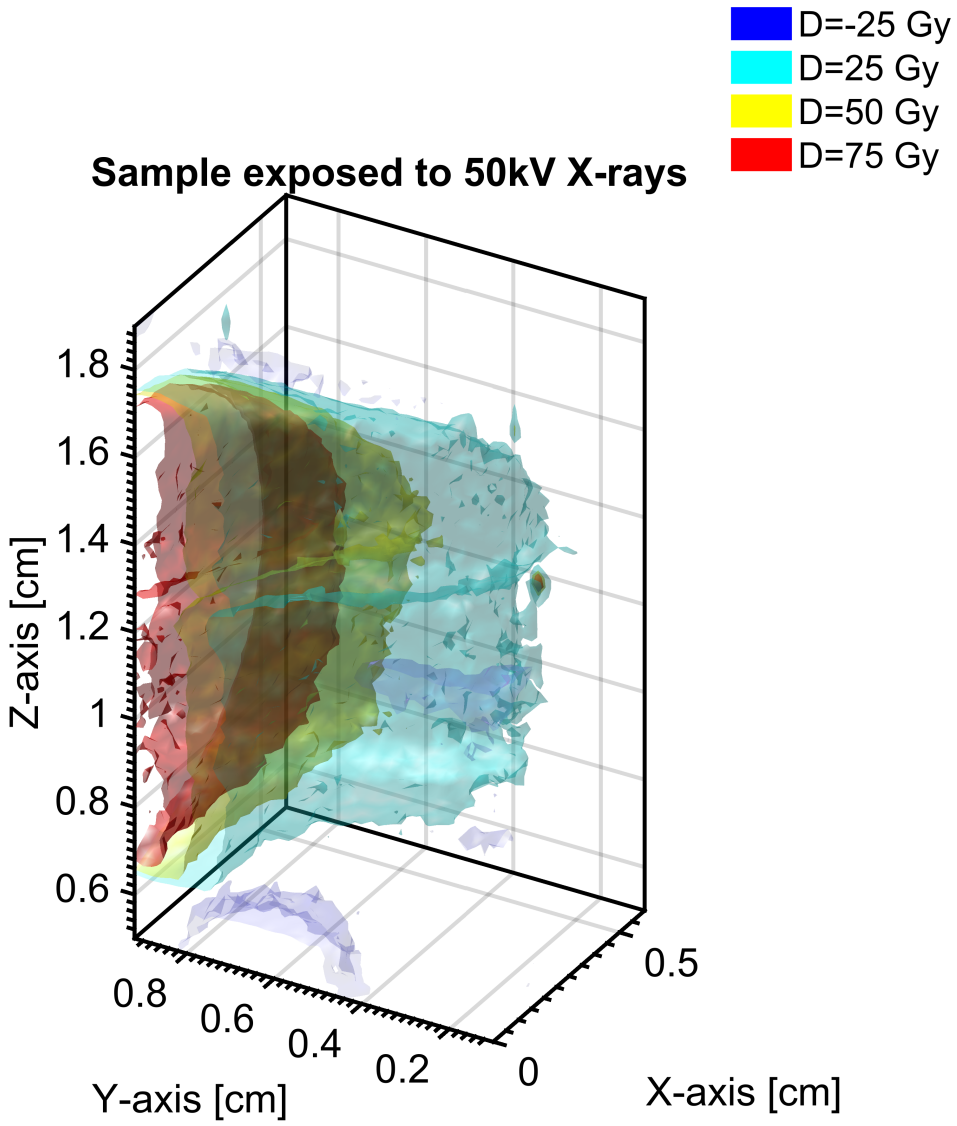

Figure 87: 3D absorbed dose distribution in a low dye sample sample irradiated with 50kV x-rays.

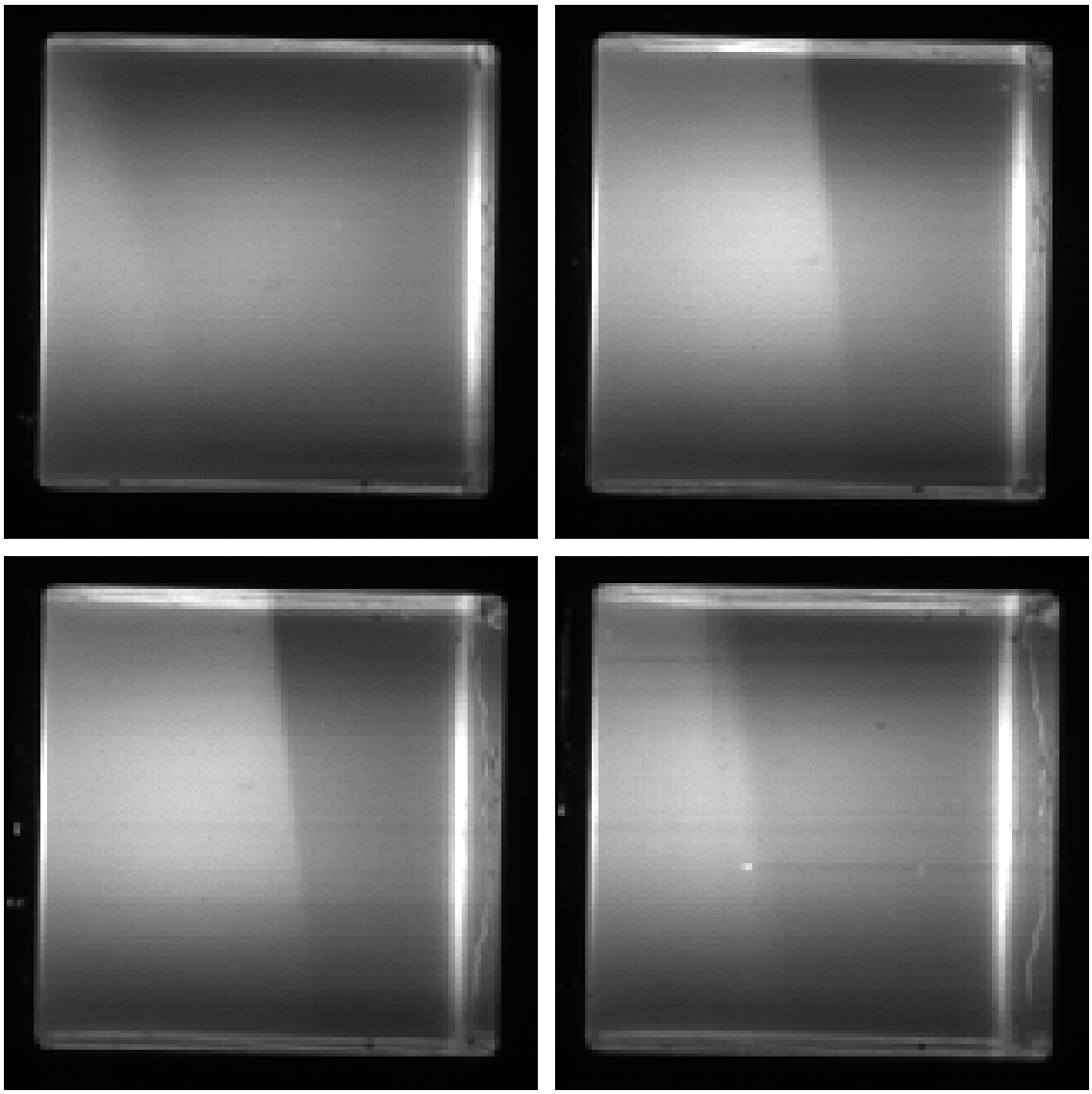

Figure 88: Fluorescence image examples from a 1x1x3 cm low dye sample irradiated with 50kV x-rays through an aperture. The "top" of the samples is facing up in these pictures.

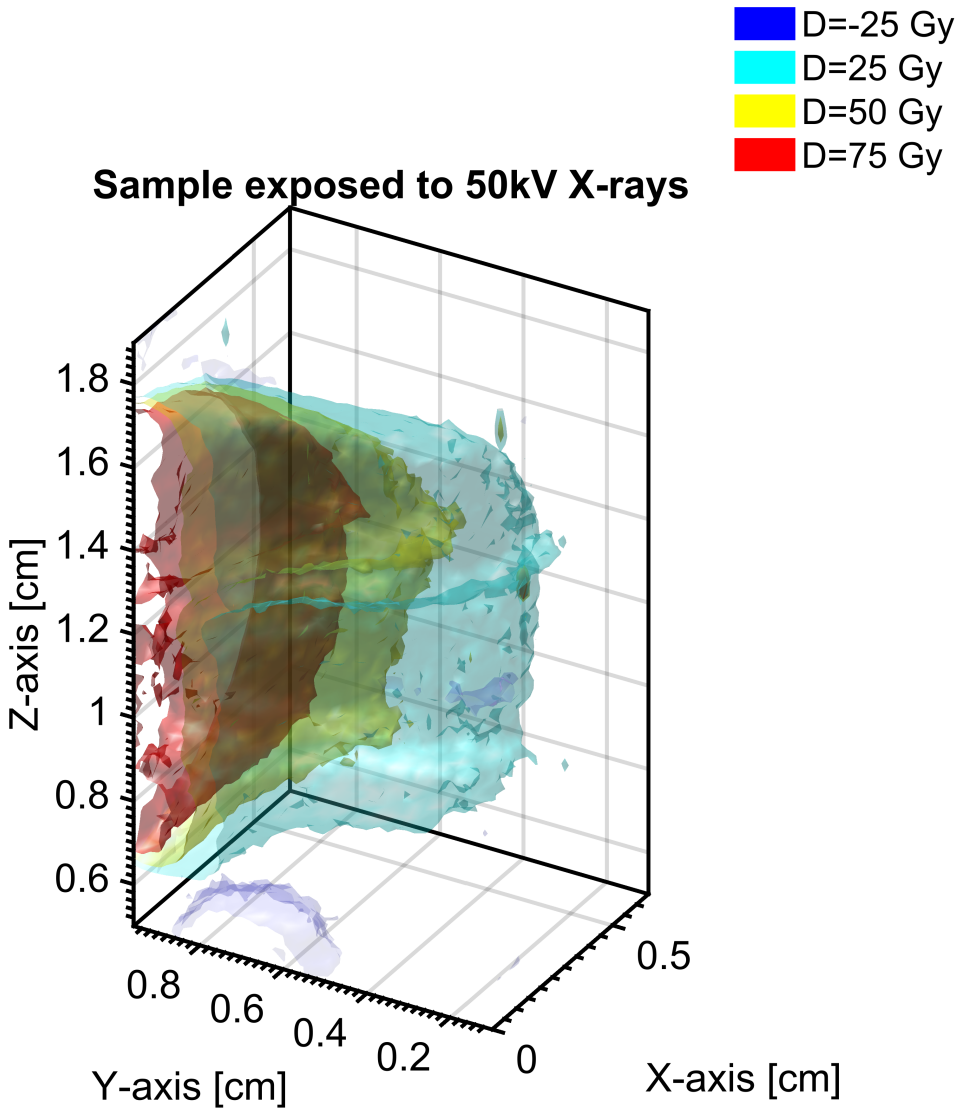

Figure 89: 3D absorbed dose distribution in a low dye sample sample irradiated with 50kV x-rays.

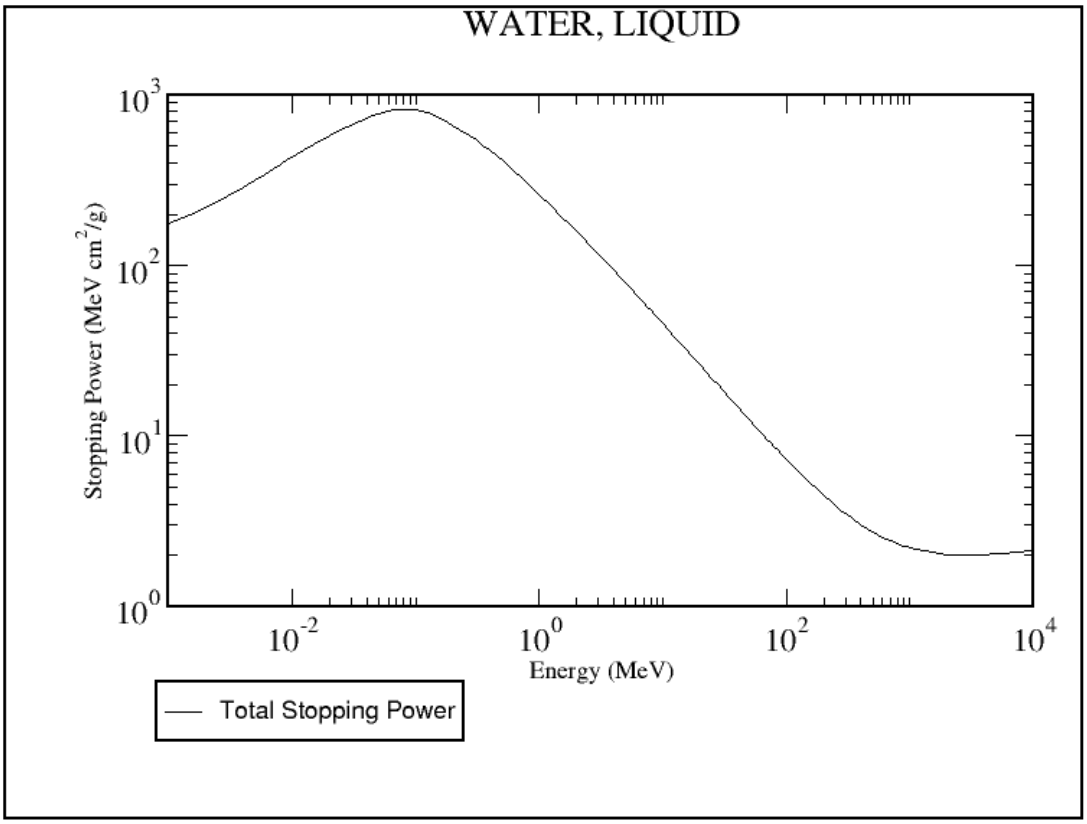

Figure 90: How the stopping power of protons in water increase as the proton energy decreases. Generated from the NIST PSTAR database web page.

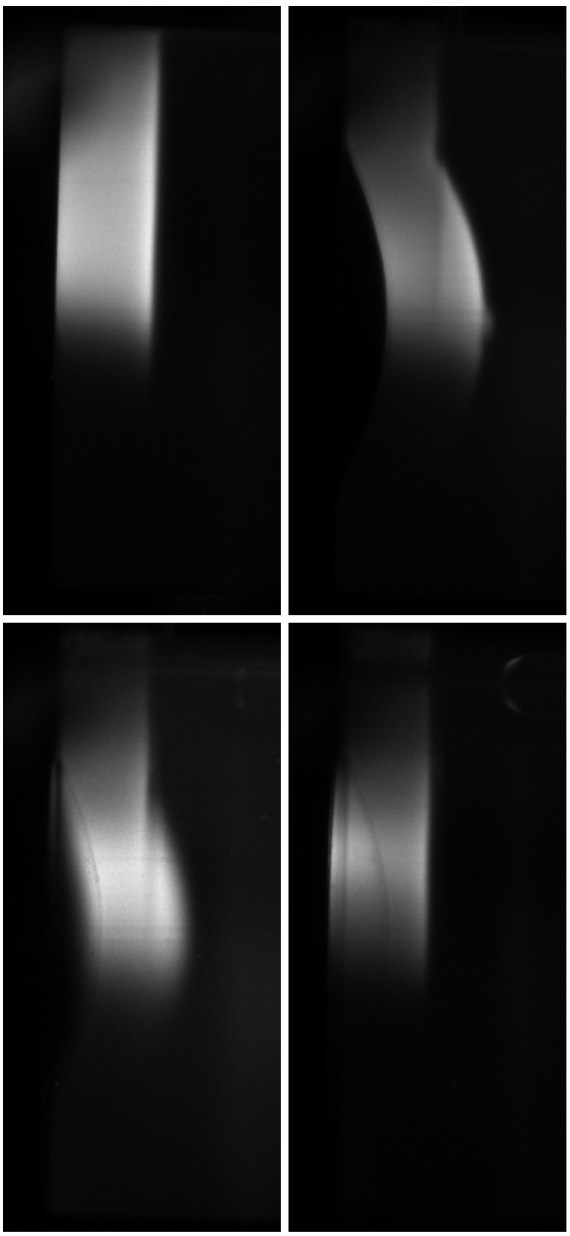

Figure 91: Images of the fluorescence from a sample irradiated with 18MeV protons.

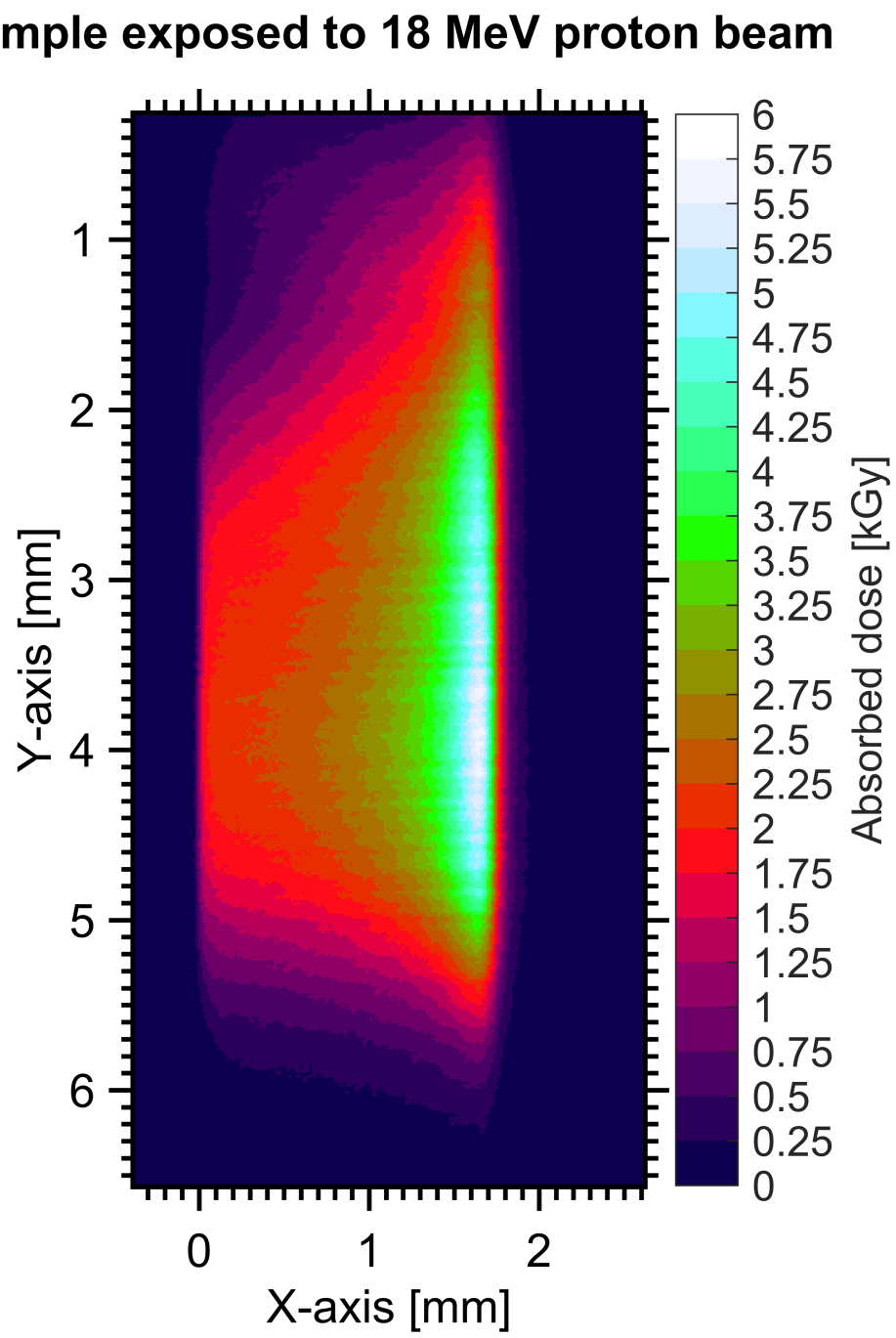

Figure 92: Image of the transverse absorbed dose distribution. Note how the straggling increases with depth.

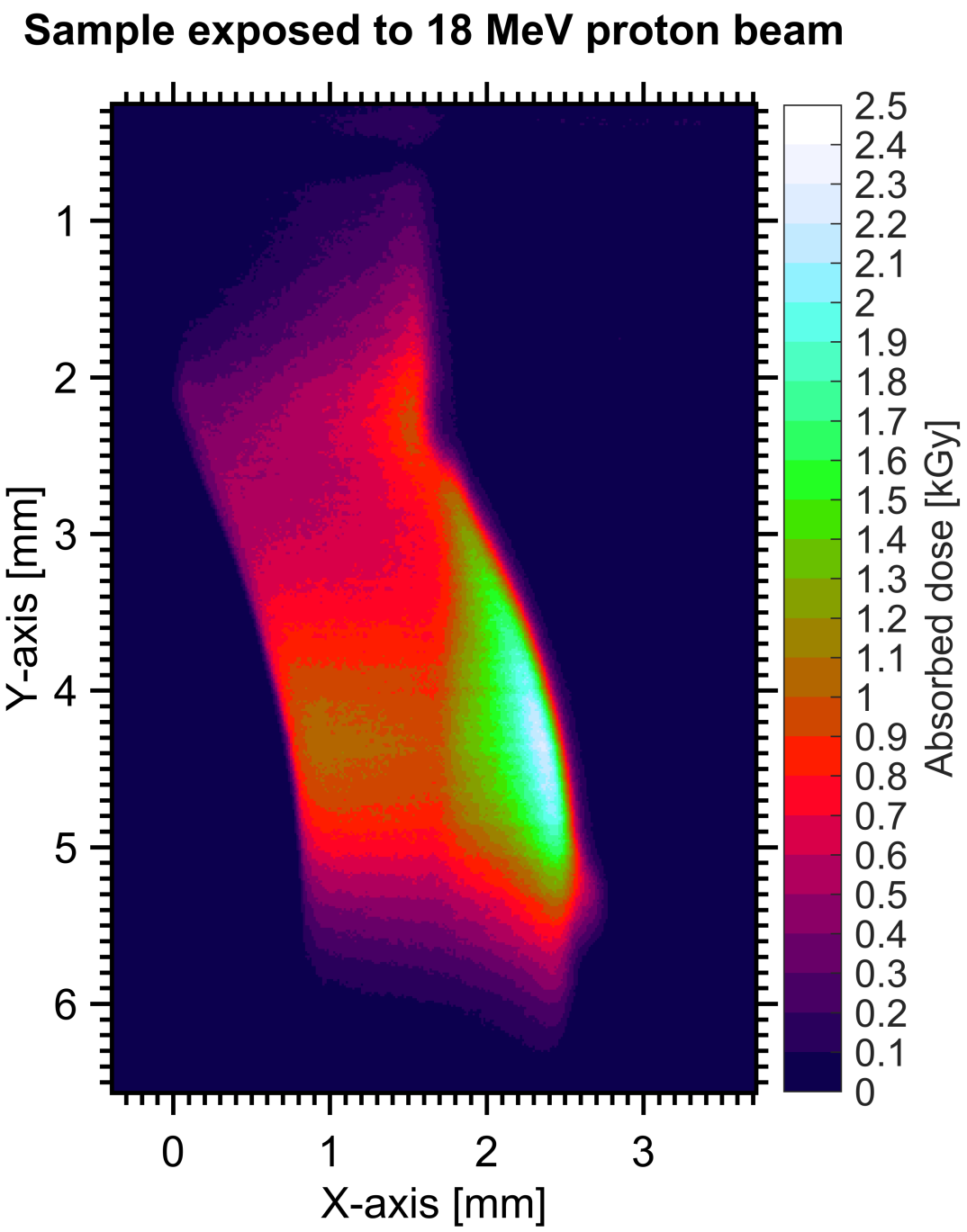

Figure 93: Image of the transverse absorbed dose distribution. Note how the straggling increases with depth.

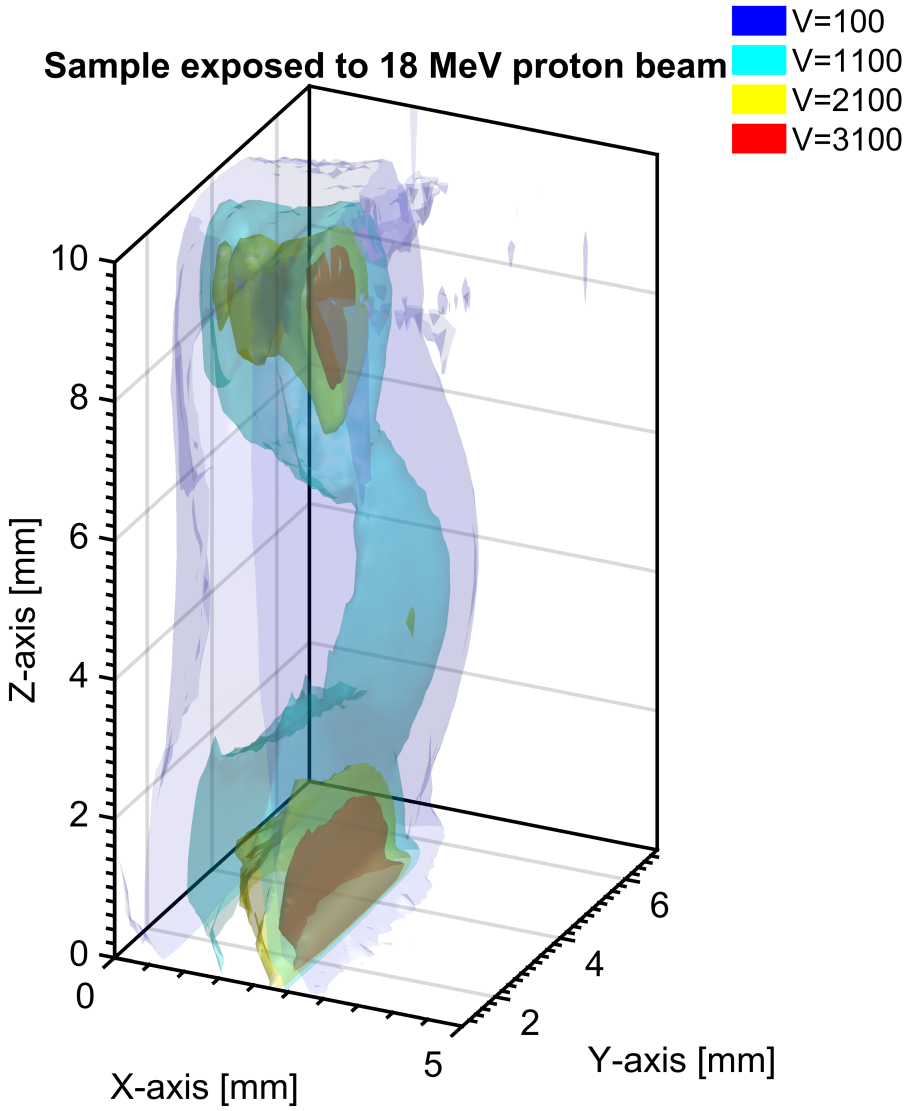

Figure 94: Image of the 3D absorbed dose distribution from the protons. This shows a Bragg peak within the sample. The peak is less intense than expected, probably due to saturation of the material response for particles with high linear energy transfer (LET). It may also be due to saturation at high absorbed dose rates.

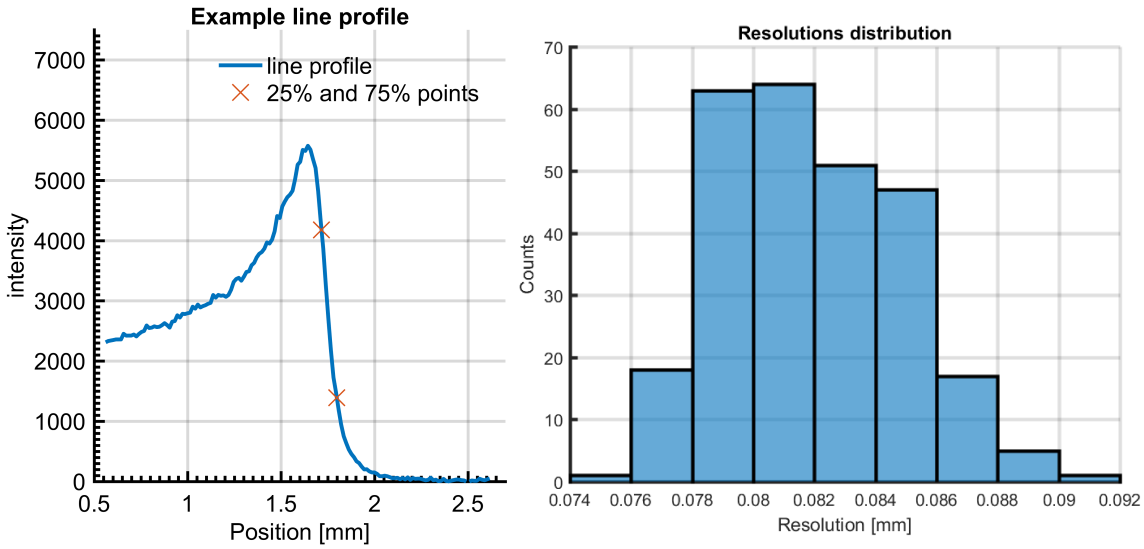

Figure 95: An example of a line profile across the Bragg peak in figure 92, along with points at 25% and 75% of the peak value. The resolution is defined as the distance between the 25% and 75% points. On the right is the distribution of resolutions for all lines in figure 92.

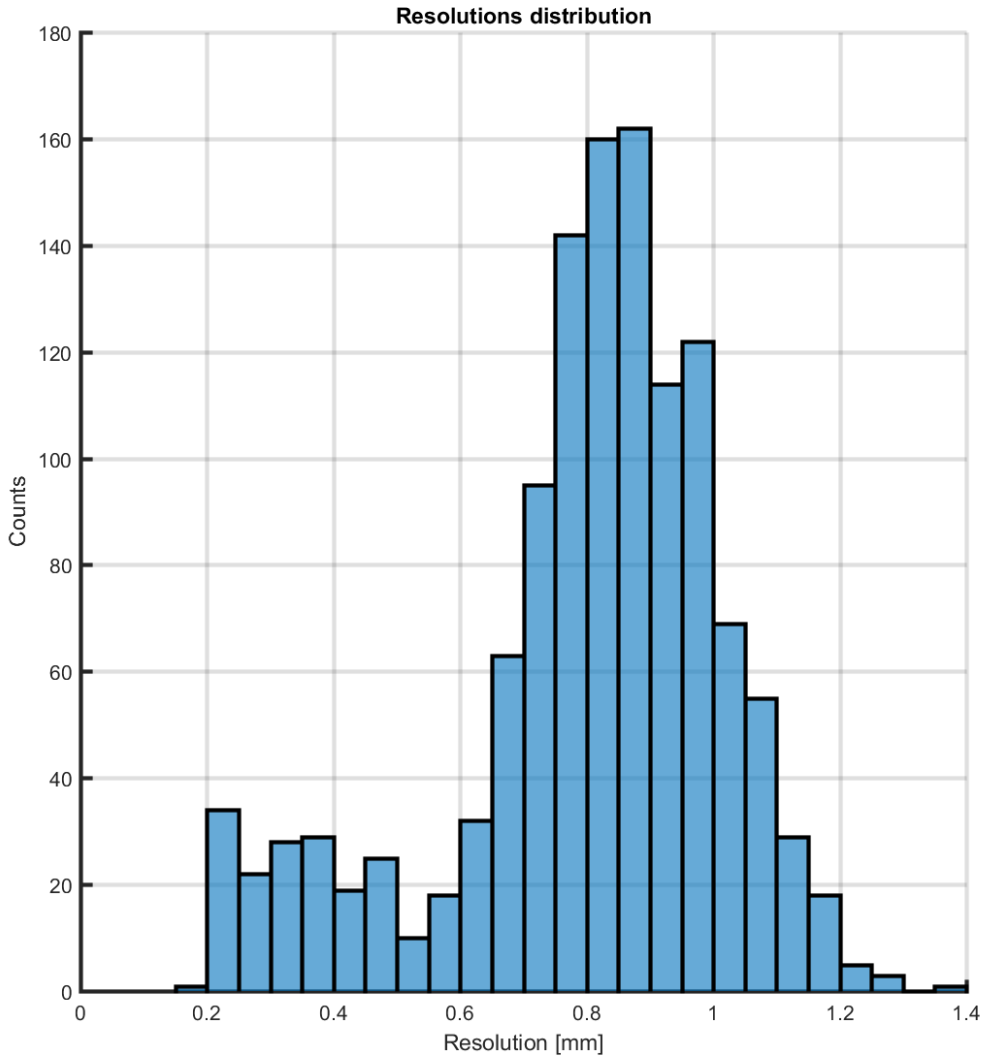

Figure 96: Distribution of Z-resolutions calculated from the dose distribution in figure 100. Only line profiles with an exposure maximum above 200 were used.

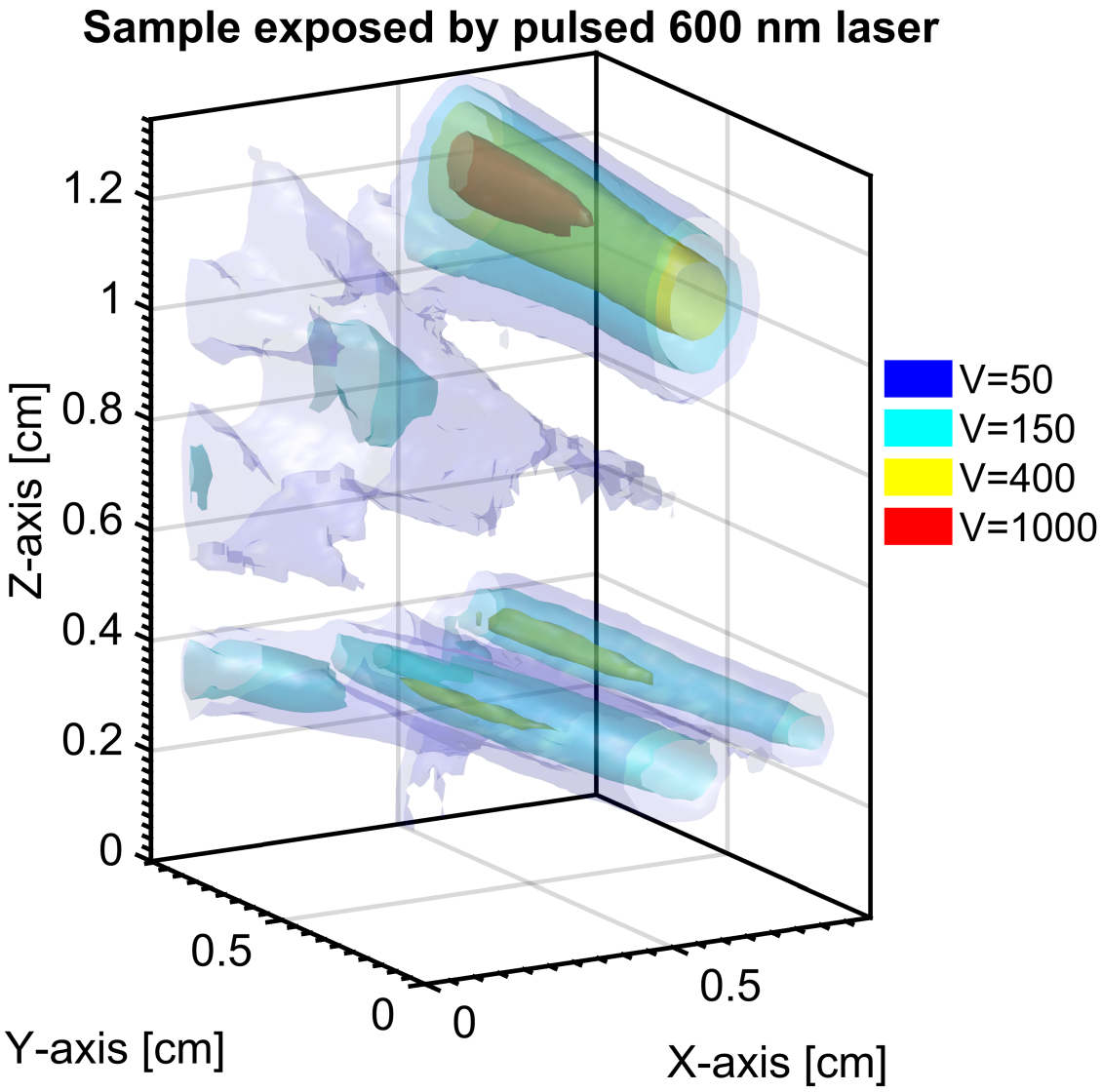

Figure 97: Isosurfaces from a 3D scan of a sample exposed with a femtosecond laser at 600 nm. This confirms that the polymer can be exposed by a two-photon process, since the polymer is not at all sensitive to red light under normal conditions.

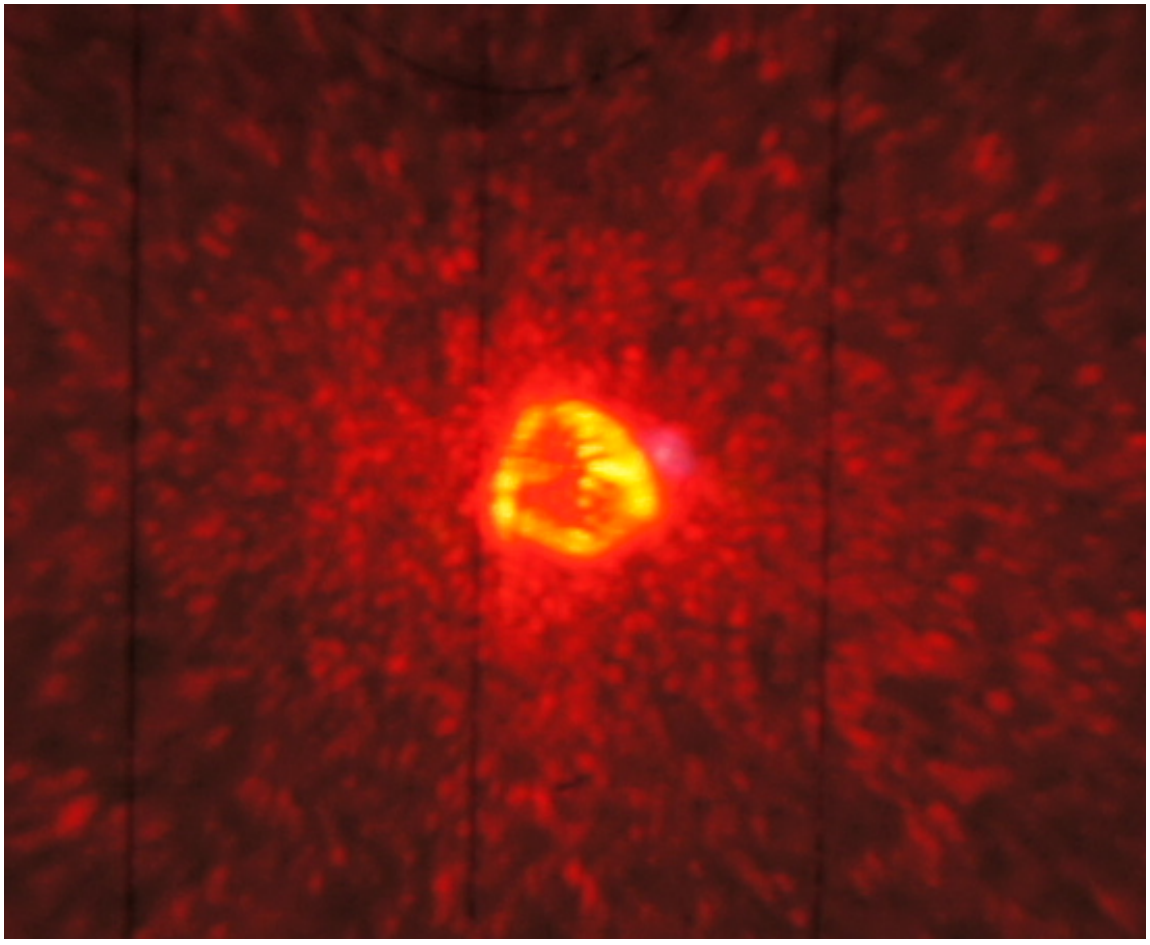

Figure 98: The effect of sample surface damage on the laser mode.

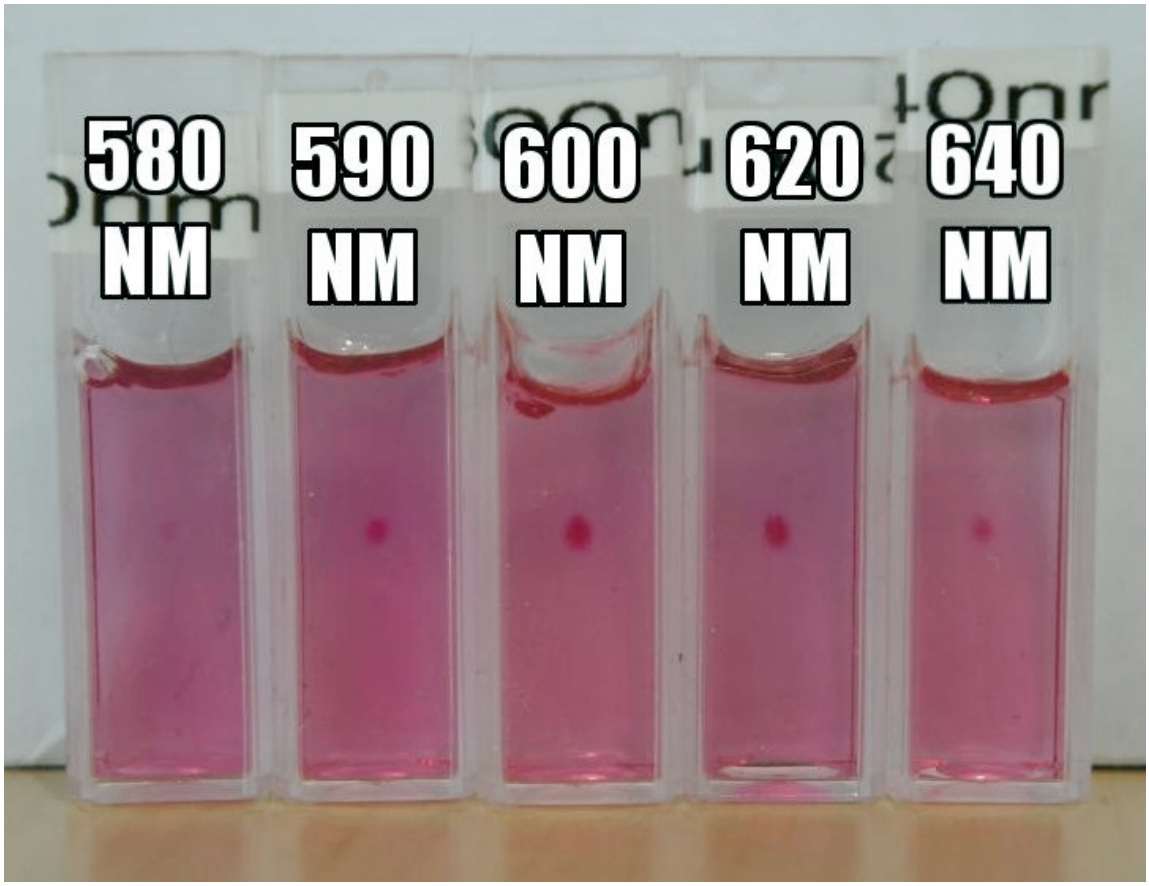

Figure 99: 5 samples exposed for 10 seconds with a femtosecond laser, at different wavelengths. It appears that the polymer is most sensitive to a wavelength between 600 and 620 nm.

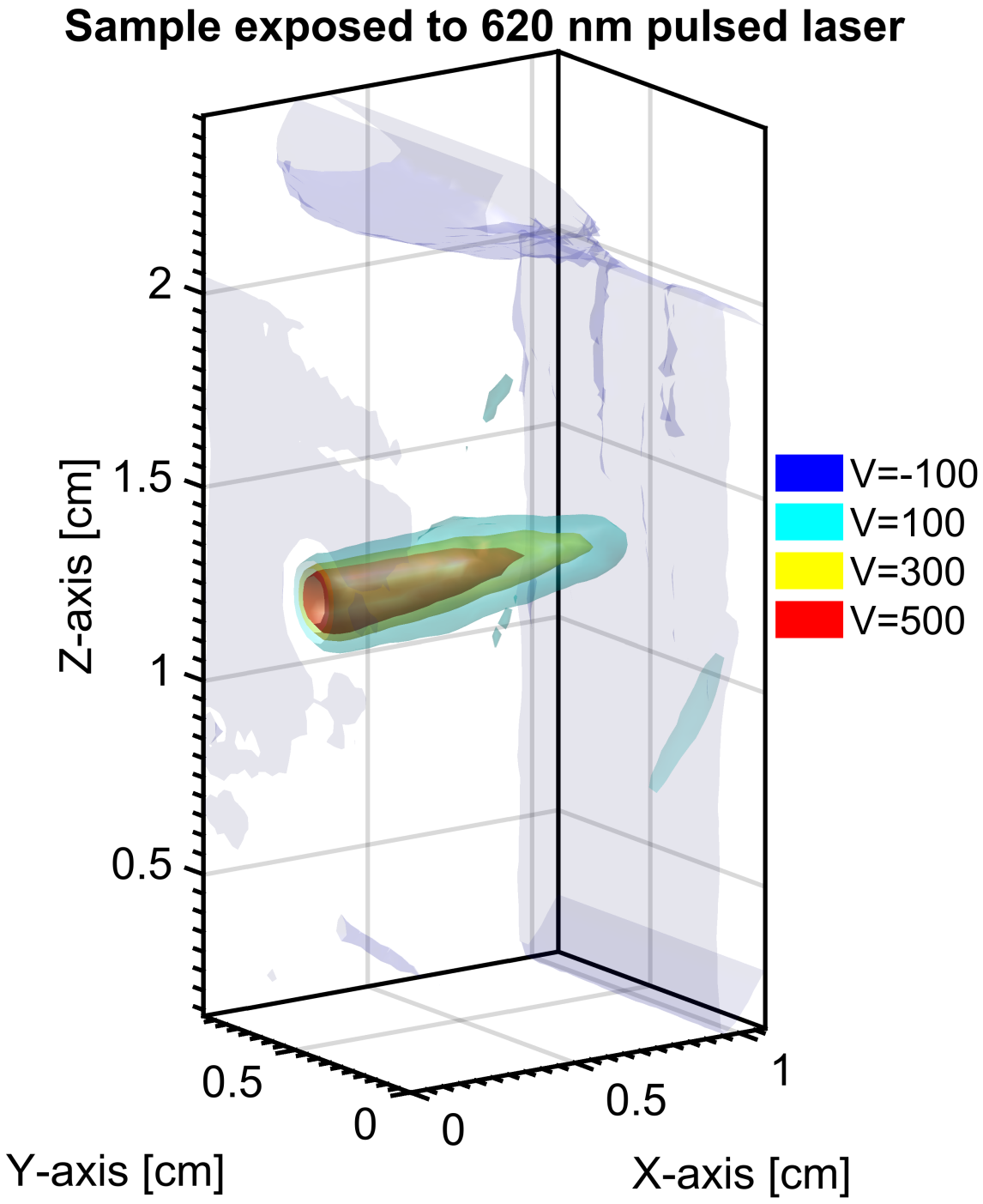

Figure 100: Isosurfaces from 3D scan of the sample exposed with 620 nm light.

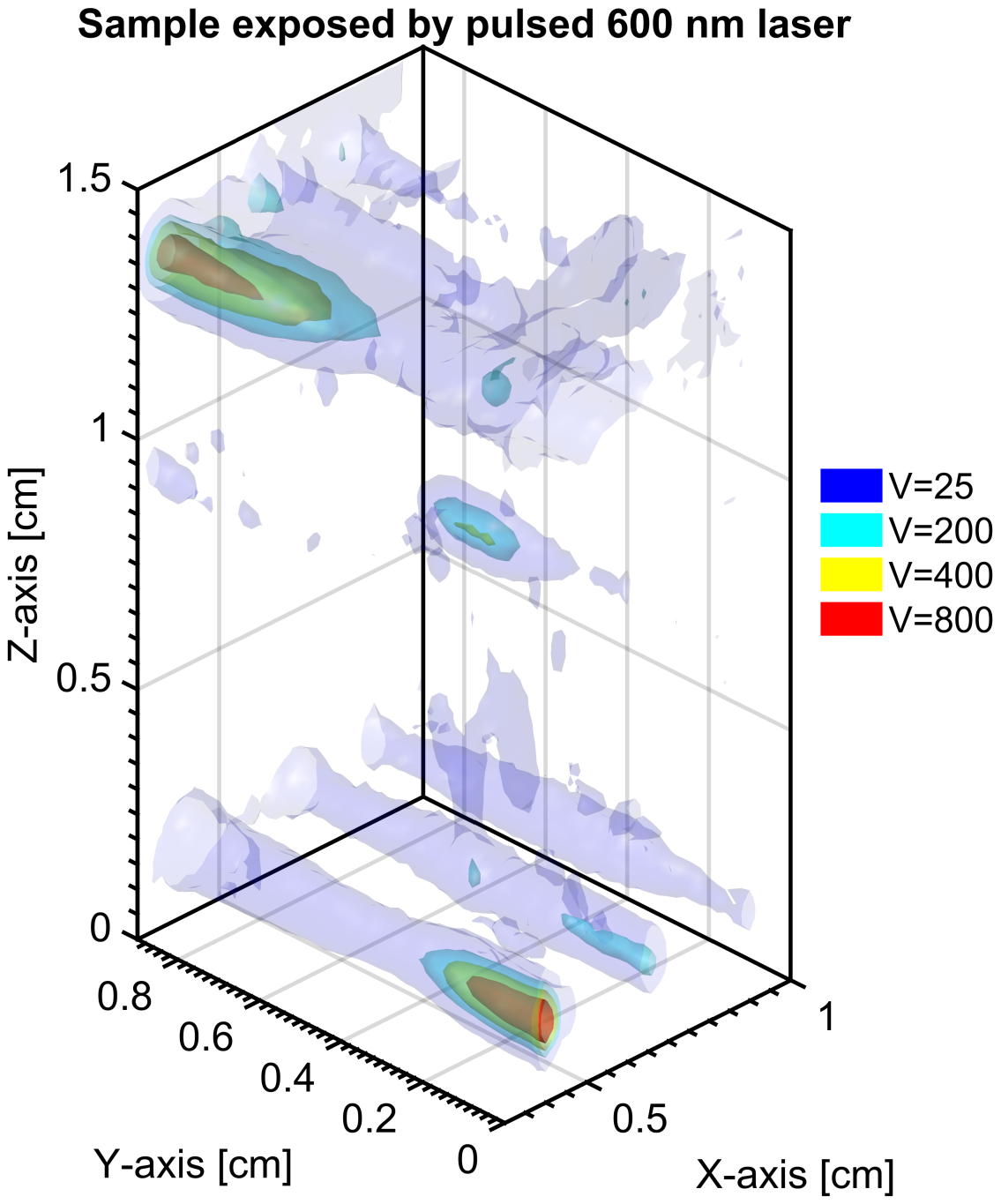

Figure 101: Sample exposures from a 600 nm femtosecond laser focused with an f=10 cm lens.

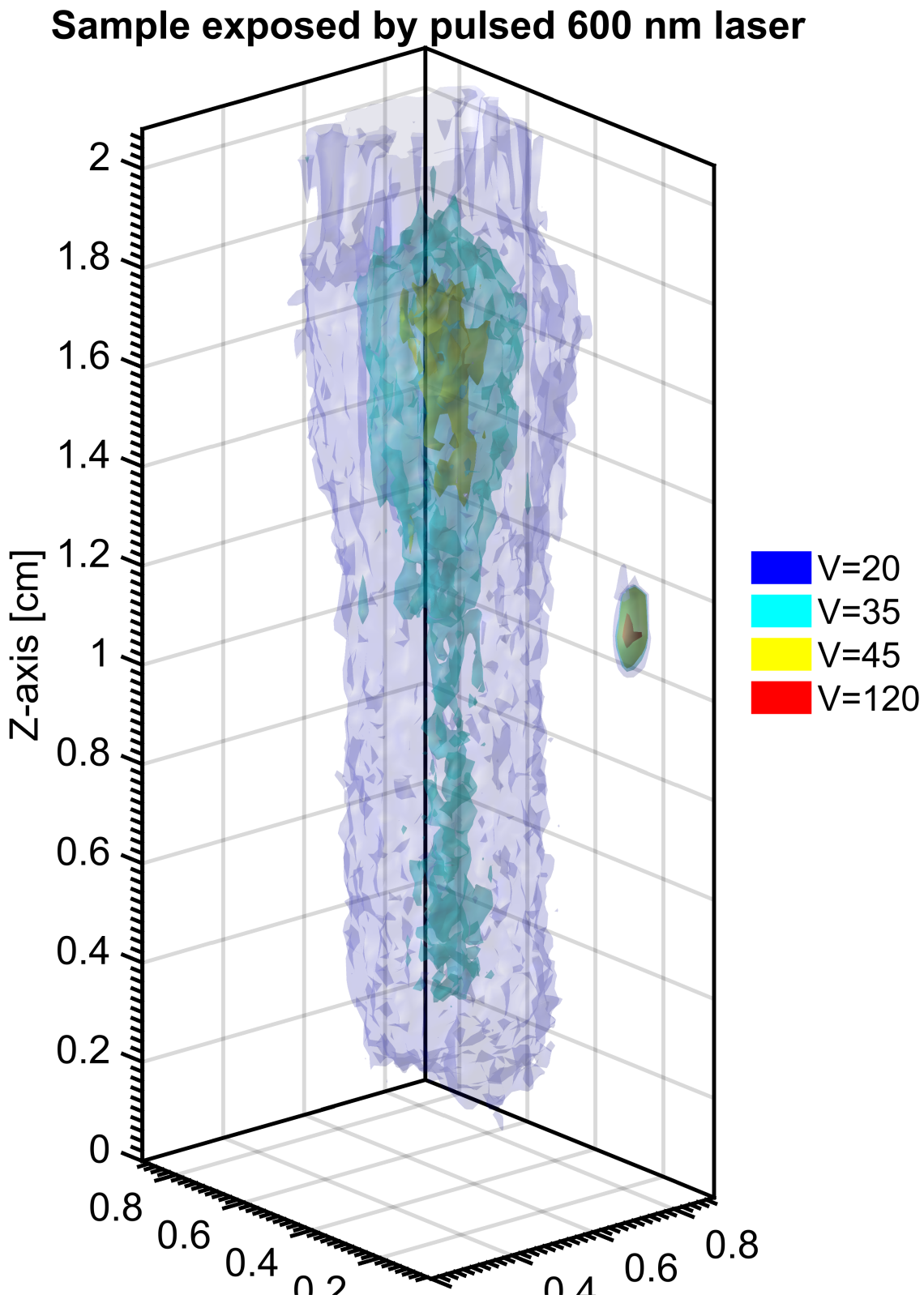

Figure 102: Sample exposures from a 600 nm femtosecond laser focused with an f=2 cm lens.

12 Conclusion

It has been investigated whether 3D dosimetry could feasibly be achieved with a measurement method based on optical fluorescence tomography of a radiofluorogenic dosimeter.
If a suitable dosimeter material is developed, then it should be possible to use optical fluorescence tomography to read out the 3D distribution of the absorbed dose in a dosimeter sample, in a manner that is fast, convenient, reliable and accurate.
A setup and method for measuring the 3D distribution of fluorescence from such a dosimeter has been designed, implemented and tested.
A list of design considerations and recommendations has been made for the 3D readout setup.
A setup for characterizing the fluorescence response of the dosimeter material has been designed, implemented and used to characterize the different dosimeter material candidates developed as part of a different project.
A list of design considerations and recommendations has been made for the fluorescence setup.
An analytical solution for analysing the data from the 3D readout setup has been developed and its sensitivity to a variety of errors has been characterized.
An alternative algorithmic analysis method has also been implemented and tested for its convergence characteristics and noise sensitivity. This solution method is more computationally expensive, but it requires fewer boundary conditions and it is less sensitive to noise in the fluorescence signal.
Some characterizations of the dosimeter material used during the project were made, and a list of requirements for the optical, chemical and mechanical properties of an ideal dosimeter has been made.
Some measurements of the 3D fluorescence from samples exposed to 50kV x-rays, protons and two-photon absorption were made. The analytical solution to the data analysis was tested on these samples, demonstrating that it can be used on measured data from the experimental setup.
Of these, the three main results from this thesis are:

- The analytical solution for calculating the absorbed dose distribution from the fluorescence data
- The design recommendations and considerations for a 3D readout setup using optical fluorescence tomography
- The requirements on the dosimeter material for the different applications.

Data Analysis Solution

The analytical solution for the relationship between the measured fluorescence and the absorbed dose is presented in equation 10. This solution takes the dose dependent attenuation of the excitation light into account. The analytical solution assumes that both the local attenuation of the excitation light and the local fluorescence response are linear with the absorbed dose. If the relationship is more complicated than this, there is no guarantee that an analytical solution exists, but a numerical solution can still be developed. The analytical solution requires a boundary condition to be defined for each line of each image in the data set. This represents a major obstacle for implementation of this technique. One possible method to define the boundary condition is given in equation 11. In the beginning of the sample, none of the excitation light has been absorbed, and the relationship between absorbed dose and measured fluorescence is simple. This method requires a fluorescence reference within the 3D readout setup to measure the vertical intensity profile of the excitation light, and the camera settings represented by the constant C_{cam}. The analytical solution is highly sensitive to errors in the boundary condition and in the material constants, so the dosimeter material must be well-characterized.
There was an interesting special case for the analytical solution, if the radiofluorogenic response is negligible, but the fluorescent response is still significant enough to be measured. This would be equivalent to having a fluorescent dye with high quantum yield dissolved in a traditional radio-

chromic dosimeter, and then using the fluorescence as another readout modality for the absorbed dose distribution. This could be incorporated into existing optical CT readout systems, since the camera would be placed orthogonally to the existing beam path in the system.
The alternative algorithmic solution was developed in an attempt to mitigate the need for many separate boundary conditions. Candidate 2D distributions of the absorbed dose distribution are used to calculate the resulting fluorescence, and this fluorescence is then compared against the actual measured fluorescence. The candidate distribution of the absorbed dose is represented by a limited number of Fourier components, and gradient descent is then used to change these Fourier components to improve the agreement between the calculated fluorescence and the measured fluorescence. This algorithm was shown to converge reliably towards the optimal solution. It also only requires one boundary condition for each fluorescence image, and it is less sensitive to noise in the fluorescence signal. The implementation of the algorithmic solution in this project was too slow to be used in practice on full 3D data sets.

3D Readout Setup Design

For the 3D readout setup, the most important recommendations are:

- A laser should be used instead of an incoherent light source.
- The power and spatial mode stabilities of the laser are very important.
- 520 nm direct diode lasers are much better than 532 nm Nd:YAG lasers for this setup
- To avoid interference patterns of the excitation light in the sample, a laser scanning setup should be used instead of a light sheet.
- The refractive index matching fluid should have an index that is matched to the dosimeter material at the emission wavelength, but slightly higher to avoid total internal reflection of the emission.
- The setup must include a fluorescence reference to characterize the vertical intensity profile of the excitation light and the camera sensitivity.
- The dosimeter material should be characterized in the 3D setup, for direct comparison against the fluorescence reference.
- The camera should be black and white, without a Bayer filter in front of the sensor.

Experimental irradiations with 50kV x-rays and 18MeV protons were performed, and it was shown that the data analysis methods derived for the material could be applied successfully to data from the 3D measurement setup. Software to automatically determine and/or apply the required boundary conditions for 3D data was developed. It was shown that the spatial resolution of the dosimeter and the 3D readout is limited by the camera optics and sensor in the xy-plane, and by the thickness of the excitation laser light sheet in the z-direction. An upper bound for the inherent spatial resolution of the dosimeter was established as 0.085 mm.

Dosimeter Requirements

The material properties for the dosimeter depend on the intended application. Numerical values for the optical constants are given in table 9. The clinical case is for a dose profile with length 6.4 cm and average absorbed dose of 2 Gy. The high dose case has an average dose of 500 Gy. The special cases with negligible R_C and R_F also use the clinical dose profile. These material constants were chosen to keep the attenuation of the excitation light below 20%. This requirement is arbitrary, but is sufficient to demonstrate what order of magnitude the material constants should have for each application.
The material constants must also be homogeneous throughout each sample of the dosimeter mate-

Table 9: Requirements for the material constants of the dosimeter, for a variety of applications and special cases.

Case \Constant	B_C [cm^{-1}]	R_C [(cm kGy)$^{-1}$]	$^{B_F}/_{R_F}$ [Gy]
Clinical	< 0.007	< 3.6	< 2
High dose	< 0.007	< 0.014	< 100
Negligible R_C	< 0.007	< 0.017	< 2
Negligible R_F	< 0.007	$\approx {}^{0.3}/_{L_{\text{sample}} \cdot D_{\text{mean}}}$	> 1000

rial. Additionally, the dosimeter material should not scatter the excitation or emitted light. The relationship between the curing process and the material constants should be characterized, and the stability of the material over time should also be characterised.
The dosimeter used in this project did not live up to these requirements. For the clinical application the background attenuation and the noise to contrast ratio for the fluorescence signal was about 50 times too high. For the high dose application, the radiochromic response was about 100 times too high. The dosimeter material was also unstable over time, highly sensitive to its temperature during curing and highly exothermic during curing. Therefore, curing times of more than 5 minutes with active cooling was necessary for samples larger than 1 cm in diameter. On the other hand, curing times of more than 10 minutes lead to higher baseline concentration of the dye in the dosimeter, which precludes the curing of samples larger than 2 cm in diameter.
Overall, a 3D readout setup with a scanning laser beam, a reliable fluorescence reference and a suitable dosimeter material could be used for clinical dosimetry in a practical and reliable way, and the resulting data could be analysed with the analytical solution described in this thesis.

List of Publications and Presentations

The author of this thesis is co-author on the following related papers:

1. **"Radiochromic and Radiofluorogenic 3D Solid Polymer Dosimeter: Initial Results for High Doses"**; M.R. Bernal-Zamorano, N.H. Sanders, L. Lindvold, C.E. Andersen. *Journal of Physics: Conference Series, 2017, DOI:10.1088/1742-6596/847/1/012016*

2. **"Radiochromic and Radiofluorogenic 3D Solid Polymer Dosimeter: Effect of the Photoinitiator"**; M.R. Bernal-Zamorano, N.H. Sanders, L. Lindvold, C.E. Andersen. *Rad. Meas. Vol. 106, Nov. 2017, Pages 192-195, DOI:10.1016/j.radmeas.2017.03.012*

3. **"Radiochromic and Radiofluorogenic 3D Solid Polymer Dosimeter; a third signal: Electron Paramagnetic Resonance (EPR)"**; M.R. Bernal-Zamorano, N.H. Sanders, L. Lindvold, C.E. Andersen. *In preparation for Radiation Measurements.*

Preliminary reports have been presented at the following conferences and meetings:

1. **35th Annual Meeting of the European Society for Radiotherapy and Oncology**; Poster on "Novel Material for High Resolution Dosimetry, Utilizing Radiation Induced Changes in the Fluorescence Response", N.H. Sanders, M.R. Bernal-Zamorano

2. **18th International Conference on Solid State Dosimetry**; Presentation on "3D Dosimetry Using a Fluorescent Polymer", N.H. Sanders, M.R. Bernal-Zamorano

3. **Aarhus workshop on dosimetry research in Denmark**; Presentation on "Challenges in 3D Dosimetry with Fluorescence", N.H. Sanders, M.R. Bernal-Zamorano

4. **5th Öresund Workshop on Radiotherapy**; Presentation on "Recovering Dose Distribution from Fluorescence Data", N.H. Sanders, M.R. Bernal-Zamorano

Acknowledgements

I would like to thank all the people who helped me during this project.
Special thanks goes out to:
My fellow PhD-student Rocío Bernal-Zamorano, who developed the dosimetric polymer.
My supervisor Lars Lindvold for always making time for me.
My co-supervisor Claus E. Andersen for his incisive advice and critical eye.
DTU Nutech secretaries Pia Elhauge and Merete Holmegaard Larsen, for bearing my forgetfulness with grace and patience.
The director at DTU nutech, Jens-Peter Lynov, for personal advice and support.
Amit Kumar Prasad who introduced me to the fluorescence spectrometer.
Mark Bailey and Arne miller who helped with gamma irradiations of the dosimetric polymer.
Binbin Zhou and Morten Bache who provided access and help with the femtosecond laser for two-photon exposure.
Dennis Elema Ringkøbing who performed the proton beam irradiations.
Ole Bjarlin Jensen who helped with the characterization of the laser beam qualities.
Lasse Høgstedt for being a good friend and for advice on the 3D readout setup.
Kristina Ankjærgaard for always bringing the party.
Thomas Roholm for being a good friend and a genuinely good person.
Tiantian Yao and Michal Sadel who worked on similar optical systems, which proved to be important touchstones for comparisons with my own system, even if I never met them.
Nikola Markovic for lifting my spirits when I was lost in the dark.
Martin Autzen for keeping me in good company when I was working late, and for inspirational discussions.
Grichar Valdes Santurio for dragging me to the Friday Bar, despite my protestations.
Susanne Bekke for good company during the late lunches.
My sister Eline, Her husband Rasmus, and their children Jonatan and Ronja, just for being their perfect selves.
My parents, to whom goes all the honor and the credit.

References

[1] J. Adamovics and M. J. Maryanski. Characterisation of PRESAGE^{TM}: A new 3-d radiochromic solid polymer dosemeter for ionising radiation. *Radiation Protection Dosimetry*, 120(1-4):107–112, jun 2006.

[2] Admin. Interaction of chemotherapy and radiation, 2015.

[3] Malvin Carl Teich Bahaa E. A. Saleh. *Fundamentals of Photonics*. John Wiley & Sons, 2013.

[4] Harrison H. Barrett. *The Radon Transform and Its Applications*, pages 217–286. Elsevier, 1984.

[5] James L Bedford, Young K Lee, Philip Wai, Christopher P South, and Alan P Warrington. Evaluation of the delta4phantom for IMRT and VMAT verification. *Physics in Medicine and Biology*, 54(9):N167–N176, apr 2009.

[6] Julie Bentley and Craig Olson. *Field Guide to Lens Design*. Society of Photo-Optical Instrumentation Engineers, 2012.

[7] M.R. Bernal-Zamorano, N.H. Sanders, L. Lindvold, and C.E. Andersen. Radiochromic and radiofluorogenic 3d solid polymer dosimeter: effect of the photoinitiator. *Radiation Measurements*, mar 2017.

[8] M.R. Bernal-Zamorano, N.H. Sanders, L. Lindvold, and C.E. Andersen. Radiochromic and radiofluorogenic 3d solid polymer dosimeter: initial results for high doses. *Journal of Physics: Conference Series*, 847:012016, may 2017.

[9] Cyrus Chargari, Nicolas Magne, Jean-Baptiste Guy, Chloé Rancoule, Antonin Levy, Karyn A. Goodman, and Eric Deutsch. Optimize and refine therapeutic index in radiation therapy: Overview of a century. *Cancer Treatment Reviews*, 45:58–67, apr 2016.

[10] S J Doran. How to perform an optical ct scan: an illustrated guide. *Journal of Physics: Conference Series*, 444:12004, Jun 2013.

[11] Kevin Jordan. Review of recent advances in radiochromic materials for 3d dosimetry. *Journal of Physics: Conference Series*, 250:012043, nov 2010.

[12] S S Korreman. Semi- and virtual 3d dosimetry in clinical practice. *Journal of Physics: Conference Series*, 444:012007, jun 2013.

[13] R.F. Kubin and A.N. Fletcher. Fluorescence quantum yields of some rhodamine dyes. *Journal of Luminescence*, 27(4):455–462, dec 1982.

[14] Joseph R. Lakowicz. *Principles of Fluorescence Spectroscopy*. Springer US, 2007.

[15] Julien Laverdant, Willy Daney de Marcillac, Carlos Barthou, Vu Duc Chinh, Catherine Schwob, Laurent Coolen, Paul Benalloul, Pham Thu Nga, and Agnès Maître. Experimental determination of the fluorescence quantum yield of semiconductor nanocrystals. *Materials*, 4(12):1182–1193, jun 2011.

[16] Daniel Low. The importance of 3d dosimetry. *Journal of Physics: Conference Series*, 573:012009, jan 2015.

[17] Shoji Maruo, Osamu Nakamura, and Satoshi Kawata. Three-dimensional microfabrication with two-photon-absorbed photopolymerization. *Optics Letters*, 22(2):132, jan 1997.

[18] A. Miller, W. Batsberg, and W. Karman. A new radiochromic thin-film dosimeter system. *International Journal of Radiation Applications and Instrumentation. Part C. Radiation Physics and Chemistry*, 31(4-6):491–496, jan 1988.

[19] Wayne D Newhauser and Rui Zhang. The physics of proton therapy. *Physics in Medicine and Biology*, 60(8):R155, 2015.

[20] J. Nocedal and S. J. Wright. *Numerical Optimization*. Springer, 1999.

[21] Lukas Novotny. *Principles of Nano-Optics*. Cambridge University Pr., 2012.

[22] Rory M Power and Jan Huisken. A guide to light-sheet fluorescence microscopy for multiscale imaging. *Nature Methods*, 14(4):360–373, mar 2017.

[23] J. Ricatti. Observations regarding differential equations of the second order. *Actorum Eruditorum quae Lipsiae publicantur Supplementa*, 8, 1724.

[24] M Sadel, E M Høye, P S Skyt, L P Muren, J B B Petersen, and P Balling. Three-dimensional radiation dosimetry based on optically-stimulated luminescence. *Journal of Physics: Conference Series*, 847:012044, may 2017.

[25] L J Schreiner. True 3d chemical dosimetry (gels, plastics): Development and clinical role. *Journal of Physics: Conference Series*, 573:12003, Jan 2015.

[26] Haiyin Sun. Laser diode beam basics. In *SpringerBriefs in Physics*, pages 27–51. Springer Netherlands, 2015.

[27] Duraisamy Sundararajan. *Discrete Fourier Transform, The: Theory, Algorithms and Applications*. World Scientific Publishing Company, 2001.

[28] Orazio Svelto. *Principles of Lasers*. Springer, 5th edition, 2010.

[29] Jan Vandecasteele and Yves De Deene. Evaluation of radiochromic gel dosimetry and polymer gel dosimetry in a clinical dose verification. *Physics in Medicine and Biology*, 58(18):6241–6262, Aug 2013.

[30] J.M. Warman, M.P. de Haas, L.H. Luthjens, A.G. Denkova, O. Kavatsyuk, M.-J. van Goethem, H.H. Kiewiet, and S. Brandenburg. Fixed fluorescent images of an 80mev proton pencil beam. *Radiation Physics and Chemistry*, 85:179–181, apr 2013.

[31] Jerry Westerweel, Gerrit E. Elsinga, and Ronald J. Adrian. Particle image velocimetry for complex and turbulent flows. *Annual Review of Fluid Mechanics*, 45(1):409–436, jan 2013.

[32] E. Wieslander and T. Knoos. Monte carlo based verification of a beam model used in a treatment planning system. *Journal of Physics: Conference Series*, 102:012027, feb 2008.

[33] T. Yao. *3D Radiation Dosimetry Using a Radio-Fluorogenic gel*. PhD thesis, TU Delft, 2016.

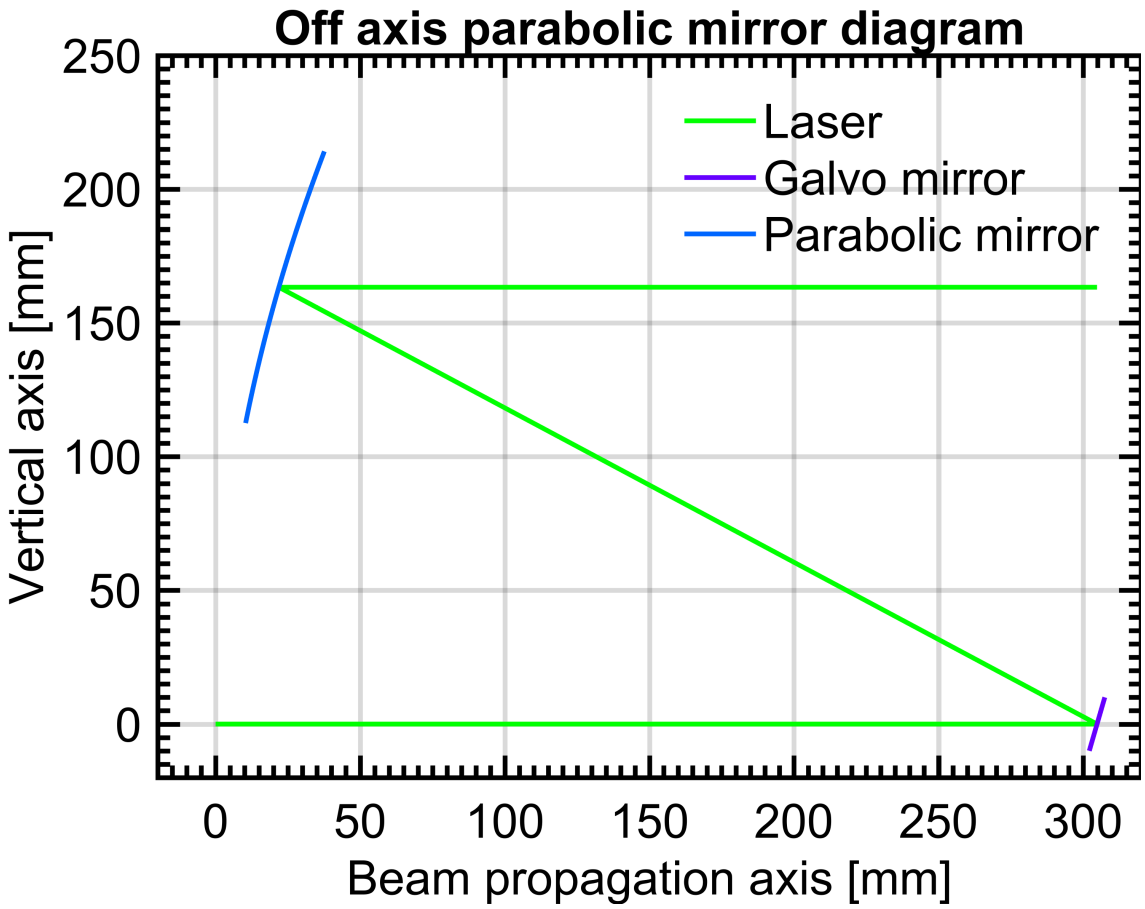

Figure 103: Diagram of a setup with a galvo mirror and a 30 degree off axis parabolic mirror.

13 Appendix A

The illumination provided by the galvo scanner would not be equal at all heights, since the laser beam would move up and down with different speeds depending on its position on the mirror. Looking at figure 103, the initial angle of the laser beam is 0 degrees. If the galvo scanner mirror is at an angle of $\theta_{gs} \in [0; \pi/2]$ then the reflected beam will have an angle of $\theta_1 = 2 \cdot \theta_{gs}$. In the coordinate system, the "bottom" of the parabolic mirror is at the origin and the shape of the parabolic mirror is given by.

$$x = \frac{y^2}{4 \cdot f_p} \tag{40}$$

The laser beam after being reflected by the galvo scanner can be described by the line

$$y = (f_p - x) \cdot \tan(2 \cdot \theta_{gs}) \tag{41}$$

If the intersection of the beam line and the mirror curve is found, the relationship between the height of the beam after the parabolic mirror and the angle of the galvo scanner can be determined.

$$y = 2 \cdot f_p \cdot \frac{\sqrt{\tan(2 \cdot \theta_{gs})^2 + 1} - 1}{\tan(2 \cdot \theta_{gs})} \tag{42}$$

The differential of this with respect to the galvo mirror angle describes how the height of the beam will not change at a constant rate, if the galvo scanner changes angle with a constant pace.

$$\frac{\mathrm{d}y}{\mathrm{d}\theta_{gs}} = 4 \cdot f_p \cdot \frac{\sqrt{\tan(2 \cdot \theta_{gs})^2 + 1} \cdot \left(\sqrt{\tan(2 \cdot \theta_{gs})^2 + 1} - 1\right)}{\tan(2 \cdot \theta_{gs})^2} \tag{43}$$

14 Appendix B

Many Matlab scripts were written during the course of this project, and quite a few of them are specific to the thesis at hand. These are included in the zip file "Appendix_B_Matlab_scripts_NISA_Thesis.zip". If this file was not included with the version you received or downloaded, feel free to contact the author. The most important scripts are listed below:

ImStack2Dose.m Calculates the 3D absorbed dose distribution from a data set of fluorescence images. Several options for boundary condition calculation. Can interpolate and rotate 3D distribution after calculation.

Dose2Fluorescence.m Calculates fluorescence from absorbed dose distribution and material constants.

Fluorescence2Dose.m Calculates absorbed dose distribution from fluorescence, material constants and boundary conditions.

FC_GD_solver.m Calculates absorbed dose distribution using the algorithmic method with Fourier Components and gradient descent described in the thesis.

load_3Dsetup_images.m Loads images acquired by the 3D readout setup into Matlab, along with the metadata in their file names.

Load_fluorescence.m Loads fluorescence spectra data from the fluorescence measurement setup into Matlab.

15 Appendix C

The control software for the 3D readout setup and for the fluorescence measurement setup were made in Labview, which is a visual conding environment. The scripts are included in the file "Appendix_C_Labview_scripts_NISA_Thesis.zip". If this file was not included with the version you received or downloaded, feel free to contact the author.